LBL-24604

Proceedings of the Second Workshop on Experiments and Detectors for a Relativistic Heavy Ion Collider (RHIC)

Lawrence Berkeley Laboratory
May 25–29, 1987

LBL--24604

DE88 008389

Jointly sponsored by

Nuclear Science Division
Lawrence Berkeley Laboratory
University of California
Berkeley, CA 94720

and

Brookhaven National Laboratory
Upton, New York 11973

Edited by

Hans Georg Ritter
Asher Shor

This work was supported by the U.S. Department of Energy
under Contract No. DE-AC03-76SF00098

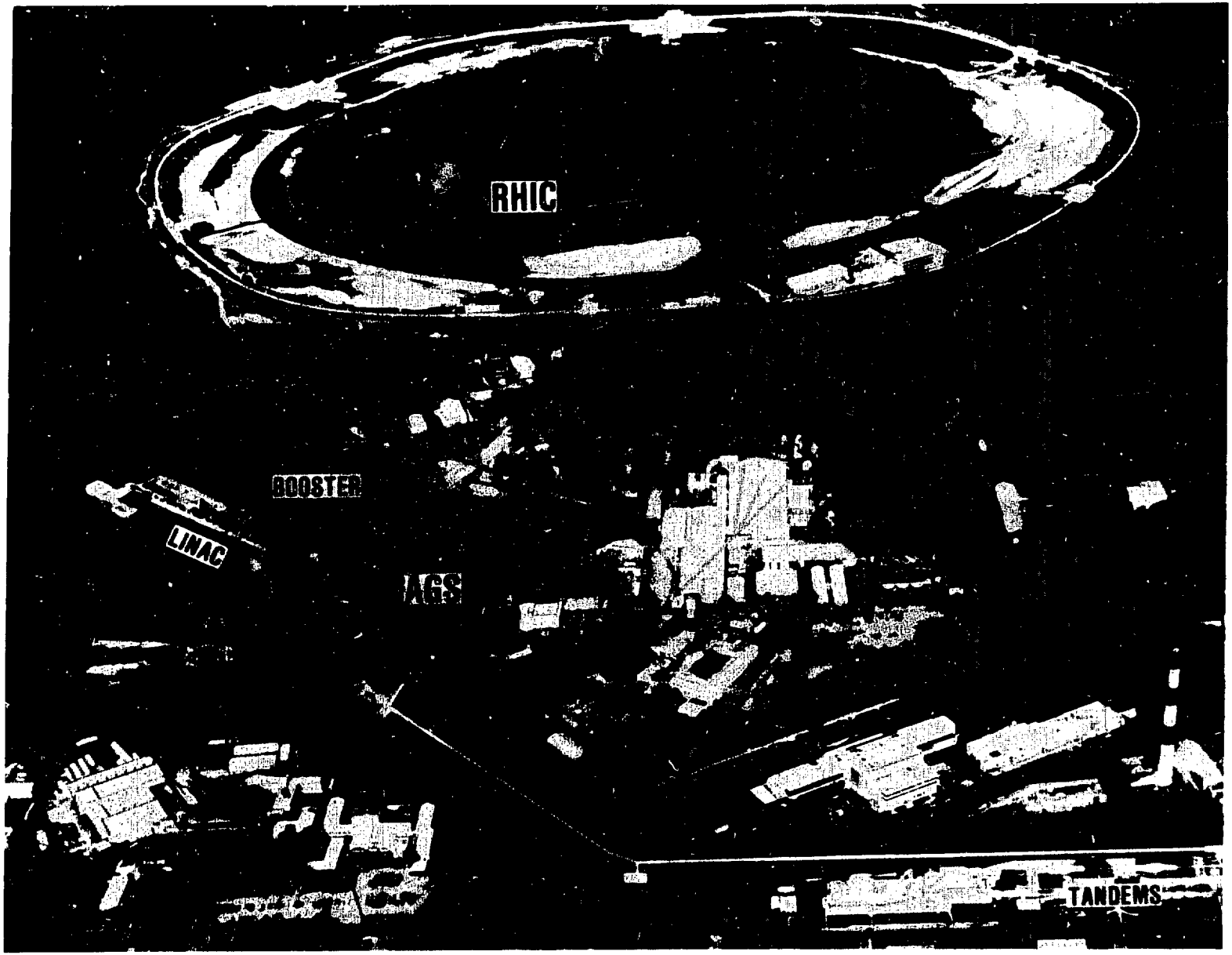
RHIC
BOOSTER
LINAC
AGS
TANDEMS

PREFACE

This report contains the Proceedings of the Second Workshop on Experiments and Detectors for a Relativistic Heavy Ion Collider. The Workshop was held at the Lawrence Berkeley Laboratory on May 25–29, 1987 and was attended by about 100 nuclear and particle physicists, mainly from the USA and Europe.

The interest in relativistic heavy ion physics has grown considerably over the last few years. The acceleration of oxygen and silicon ions at CERN and at Brookhaven in 1986 has allowed systematic studies far beyond Bevalac energies. The excitement of this was conveyed to the participants by a number of presentations of early results from the major experiments. Those presentations are not included in these proceedings since a much more complete overview of the first experimental results will be published in the proceedings of the Nordkirchen "Sixth International Conference on Ultra-Relativistic Nucleus-Nucleus Collisions" in *Zeitschrift für Physik*. These fixed target experiments are widely considered to be an important step toward a final goal—experiments at the Relativistic Heavy Ion Collider (RHIC). The great interest in the nuclear and particle physics community underlines the importance of RHIC for the vitality of the future physics program, and it is hoped that the project can be realized in a swift and timely fashion.

It was the goal of this Workshop to extend the studies done at the first Workshop. This turned out to be a very ambitious goal, given the achievements of the first Workshop. Five working groups were formed in the summer of 1986 that started to prepare for the Workshop; also, some had many meetings prior to the actual Workshop. Those meetings took place at Brookhaven and at CERN. The working groups and their hard working convenors were:

4π Calorimetry
Convenors: M. Albrow, C. Fabjan, H. Gordon, and D. Lissauer
Large Solid Angle Tracking
Convenor: S. Nagamiya
Di-Electrons
Convenors: J. Carroll, H. Specht, and M. Tannenbaum
Di-Muons
Convenors: S. Aronson, and G. Young
Fragmentation Region
Convenor: P. Braun-Munzinger

At the Workshop, the first day was devoted to introductions: the RHIC project, the new results from CERN and Brookhaven, and the working groups. During the next three days the intense work in the groups was interrupted by plenary sessions where subjects of general interest were presented. On the last day the convenors presented a summary of the work done in the groups. Some groups had rearranged and concentrated more toward a conceptual design for real RHIC experiments. The summary reports of all the working groups together with contributions that have been presented and other related contributions are published in these proceedings.

From the depth of the material presented here, it is obvious that the next step on the way toward RHIC experiments will consist of forming collaborations and writing letters of intent.

We would like to thank all the convenors, the contributors, and the participants for the tremendous amount of work that is manifested in these proceedings. We also give thanks to Ann Fitzgerald and to Colette Cadwell, the workshop secretaries; to Chris Meyer, the LBL conference coordinator; and to Wanda Smith-Burnett, Paulita Ortiz, and Linda Davis of the Nuclear Science Division, who served at the registration desk and made travel arrangements. Their devoted work made the Workshop possible.

Hans Georg Ritter and Asher Shor

TABLE OF CONTENTS

AGENDA

Monday, May 25

Welcome	D. Shirley (LBL)
Remarks on Workshop Organization	H.G. Ritter (LBL)
RHIC Project: Overview and Status	N.P.Samios (BNL)
From Fixed Target to Experiments at RHIC	H. Satz (Bielefeld) H. Gutbrod (GSI) G. Landaud (Clermont-Ferrand) S. Nagamiya (Columbia U.) A. Sandoval (GSI) J. Sunier (Los Alamos) K. Wolf (Texas A & M)
Introduction	T. Ludlam (BNL)
Presentation by Convenors	
Di-Muons	G. Young (ORNL)
Di-Electrons (West)	M. Tannenbaum (BNL)
Di-Electrons (East)	H. Specht (Heidelberg)
Fragmentation Region	P. Braun-Munzinger (Stony Brook)
Tracking, Large Solid Angle	S. Nagamiya (Columbia U.)
4-π Calorimeters	M. Albrow (CERN)
Announcement of Theory Discussions	J. Randrup (LBL)

Tuesday, May 26

Plenary Session	
Working Groups Meet	
Plenary Session: Event Generators	K. Werner (BNL) H. Boggild (Niels Bohr Inst.)

Wednesday, May 27

Plenary Session: Hydrodynamical Model	W. Greiner (Frankfurt)
Working Groups Meet	
Plenary Session: Costing Detectors	M. Marx (Stony Brook)

AGENDA
(Continued)

Thursday, May 28

Plenary Session

Working Groups Meet

Plenary Session:

Computer Requirements	S. Loken (LBL)

Friday, May 29

Convenors' Summaries

Compact Calorimeter with Leptons	M. Albrow (CERN)
Di-Muon Experiment	S. Aronson (BNL)
Electron Measurement	J. Carroll (UCLA)
4π Tracking	S. Lindenbaum (BNL)
Central Region Tracking with Calorimeter	H. Gutbrod (GSI)
Theory Perspective	L. McLerran (Fermilab)
Concluding Remarks	T. Ludlam (BNL)

LIST OF PARTICIPANTS

Name	Institution
M.G. Albrow	Rutherford Appleton Laboratory
S.H. Aronson	Brookhaven National Laboratory
T.C. Awes	Oak Ridge National Laboratory
C. Baktash	Oak Ridge National Laboratory
F.H. Berger	Universitaet Muenster
R.R. Betts	Argonne National Laboratory
R. Bock	GSI Darmstadt
H. Boggild	Niels Bohr Institute
J. Boguta	Advanced Nuclear Concepts
P. Bond	Brookhaven National Laboratory
P. Braun-Munzinger	SUNY, Stony Brook
H.C. Britt	Lawrence Livermore National Laboratory
J. Bystricky	Univ. of California, Los Angeles
A.J. Caffrey	EG&G Idaho, Inc.
J.B. Carroll	Lawrence Berkeley Laboratory
W.E. Cleland	Univ. of Pittsburgh
J.D. Cole	EG&G Idaho, Inc.
H.J. Crawford	Lawrence Berkeley Laboratory
J.M. Dairiki	Lawrence Berkeley Laboratory
C.W. Fabjan	CERN
A. Farooq	Texas A&M University
A. Franz	Lawrence Berkeley Laboratory
R. Freifelder	GSI Darmstadt
S.Y. Fung	Univ. of California, Riverside
A. Gavron	Los Alamos National Laboratory
W.M. Geist	Lawrence Berkeley Laboratory
P.M. Glassel	Univ. of Heidelberg
H.A. Gordon	Brookhaven National Laboratory
P. Gorodetzky	CRN, Strasborg
W. Greiner	Univ. of Frankfurt
E.E. Gross	Department of Energy
H.-A. Gustafsson	University of Lund
H.H. Gutbrod	GSI Darmstadt
D.W. Hahn	Lawrence Berkeley Laboratory
T.J. Hallman	Johns Hopkins University
H. Hamagaki	Brookhaven National Laboratory
J. Harris	Lawrence Berkeley Laboratory
U. Heinz	Brookhaven National Laboratory
R. Herrmann	GSI Darmstadt
B.V. Jacak	Los Alamos National Laboratory
D. Keane	Univ. of California, Riverside
D.G. Kovar	Argonne National Laboratory
M.A. Kramer	City College of New York
G. Landaud	Univ. of Clermont-Ferrand
S.Y. Lee	Brookhaven National Laboratory
S.J. Lindenbaum	Brookhaven National Laboratory
D.A. Lissauer	Brookhaven National Laboratory
H. Lohner	Universitaet Muenster

S.C. Loken	Lawrence Berkeley Laboratory
W.A. Love	Brookhaven National Laboratory
T.W. Ludlam	Brookhaven National Laboratory
L. Madansky	Johns Hopkins University
M. Maier	Michigan State University
J. Marx	Lawrence Berkeley Laboratory
H. Matis	Lawrence Berkeley Laboratory
T. Matsui	Massachusetts Institute of Technology
L.D. McLerran	Fermi National Accelerator Laboratory
W.F. Muller	Lawrence Berkeley Laboratory
M.J. Murtagh	Brookhaven National Laboratory
W.D. Myers	Lawrence Berkeley Laboratory
S. Nagamiya	Columbia University
K. Nelson	University of Wisconsin
D.L. Olson	Lawrence Berkeley Laboratory
A.M. Poskanzer	Lawrence Berkeley Laboratory
G. Rai	Lawrence Berkeley Laboratory
H G. Ritter	Lawrence Berkeley Laboratory
G.R. Roche	Lawrence Berkeley Laboratory
V.P. Ruuskanen	University of Illinois
N.P. Samios	Brookhaven National Laboratory
A. Sandoval	GSI Darmstadt
H. Satz	Universitaet Bielefeld
R. Scharenberg	Purdue University
L.S. Schroeder	Lawrence Berkeley Laboratory
P.A. Seidl	Lawrence Berkeley Laboratory
A. Shor	Brookhaven National Laboratory
W.E. Sondheim	Los Alamos National Laboratory
H.J. Specht	Univ. of Heidelberg
J. Stachel	SUNY, Stony Brook
S. Steadman	Massachusetts Institute of Technology
M. Strayer	Oak Ridge National Laboratory
J.W. Sunier	Los Alamos National Laboratory
T.J. Symons	Lawrence Berkeley Laboratory
M.J. Tannenbaum	Brookhaven National Laboratory
J. Thomas	California Institute of Technology
M.L. Tincknell	Lawrence Berkeley Laboratory
J.H. vanDijk	Brookhaven National Laboratory
H.W. VanHecke	Los Alamos National Laboratory
K. Werner	Brookhaven National Laboratory
H. Wieman	Lawrence Berkeley Laboratory
K.L. Wolf	Texas A&M University
G.R. Young	Oak Ridge National Laboratory
W.A. Zajc	Columbia University
J.A. Zingman	Lawrence Livermore National Laboratory

OVERVIEW

THE RELATIVISTIC HEAVY ION COLLIDER PROJECT: AN OVERVIEW*

T.W. Ludlam and N.P. Samios

Brookhaven National Laboratory
Associated Universities, Inc.
Upton, NY 11973

I. Origins

It has been just about a decade since widespread interest began to develop in the physics of ultra-relativistic heavy ion collisions. During this time a whole new field of scientific endeavor has grown up with its roots firmly planted in both nuclear and particle physics, establishing for the first time in recent history firm collaborative bonds between the two communities.

The central issue is the existence of quarks, their confinement in hadrons, and the realization that nuclear collisions at very high energy offer an avenue to the creation of macroscopic states of matter at high energy density in which the volume of quark confinement is much larger than the size of an elementary hadron. For nuclear physics this brings the opportunity for exploration of a new frontier in many-body hadron physics with the formation of a quark-gluon plasma; for particle physics, a means to study the theory of strong interactions (QCD) in the high density limit; and for astrophysics the chance to re-create in the laboratory the transition from quarks to nucleons which characterized the early evolution of the universe, and to study the properties of high density nuclear matter critical for the dynamics of supernovae.

We have now seen the first results[1] from experiments with high energy nuclear beams at Brookhaven and CERN. These experiments, which began about a year ago, use fixed targets at the AGS and SPS. These programs have begun with relatively light ions ($A \leq 32$ amu) to explore states of compressed nuclear matter in which high energy density is achieved in an environment of high baryon density at energies near the maximum for nuclear stopping.

---

*Work performed under the auspices of the U.S. Department of Energy.

The widespread interest and excitement which these experiments have generated is due in large part to the fact that they are providing the first glimpse of what is expected to be an entire new regime of physical phenomena, and that these experiments will be followed in the near future by measurements with much higher beam masses and much higher collision energies. This is the mission of the RHIC facility, and we are gathered at this workshop to continue the effort, begun at the April 1985 RHIC workshop[2], to prepare for a new generation of experiments which will be carried out at the collider.

Four years ago the concept of a heavy ion collider facility, reaching center-of-mass collision energies at least 10 times higher than the fixed target experiments, was identified as the highest priority need for a new facility in the Long Range Plan for basic nuclear research in the U.S.[3]. Immediately thereafter a panel was formed which included leading experimentalists and theorists from both high energy and nuclear physics representing the major interested laboratories throughout the U.S. and in Europe, to consider the basic design requirements for such a facility. This group met for three days in August of 1983 and formulated the essential design parameters for a facility which would reach energies high enough to ensure a baryon-free central region in collisions of the heaviest nuclei; incorporate the flexibility to study collisions of all nuclei, from the lightest to the heaviest; and allow experiments to be carried out over the full range of energies, from a few GeV/amu in the c.m. (AGS fixed target) up to the top collider energy, with no inaccessible gaps, and with adequate intensity for sensitive measurements[4]. The technical parameters were developed for an accelerator complex which would utilize the existing facilities already in place for the ISABELLE/CBA project at Brookhaven, with the AGS as injector, thereby saving at least a factor of two in the overall cost of such a collider.

Immediately thereafter, in 1983, these parameters and the basic physics requirements for a heavy ion collider facility were discussed among the community at large as part of the Quark Matter '83 conference at Brookhaven[5]. With this as a starting point, an intensive accelerator physics effort was undertaken at Brookhaven during 1984 to understand the problems of accelerating and storing intense, ultra relativistic beams of highly charged nuclei, and to work out a detailed design for the collider. In January 1985 the

RHIC proposal was submitted to the U.S. Department of Energy. The present Conceptual Design Report[6] is an update of that proposal.

One of the most important elements of the RHIC proposal is the design of the superconducting magnets for the accelerator rings. These magnets are the largest component of the cost of the machine, and their fabrication and installation is the major determinant of the construction schedule. The design of these magnets[7] is based on the cosine theta coil structure developed at Brookhaven for the ISABELLE/CBA magnets, which has since been adopted for the Tevatron, HERA and SSC accelerators as well. The RHIC magnets are designed to operate at a relatively low field (3.5 Tesla), and thus the coil can be wound in a single layer of superconductor. This important simplification, along with careful engineering refinement, has resulted in a magnet which is relatively straightforward to fabricate in quantity, either in the existing facilities at Brookhaven or in the facilities of commercial industrial firms. Full-size, "machine-quality" prototypes have been assembled both at Brookhaven and in industry and successfully tested.

Brookhaven has worked together with the Department of Energy to develop a detailed schedule for the project which includes R&D, construction and start-up. This comprehensive plan, which includes R&D and construction for the first round of detectors, would have the first experiments beginning five years after project authorization. This planning, the technical design on which it is based, and the scope of the research which this new facility will make possible, have been the subject of numerous scientific and technical reviews over the past two years. Each has reaffirmed the urgency for getting on with this project. The essential conclusions from two recent reviews are cited here:

- Report of the NSAC Sub-committee on Facility Construction and National Laboratories, June 1986:

  "The recent development of the field of relativistic heavy-ion physics has further strengthened the very high scientific merit for this project...RHIC will provide nuclear science in the United States with a unique world-leading facility with almost unparalleled potential for new discovery."

- Executive Summary of the Department of Energy Review Panel on Technical Design, Cost, Schedule and Management for RHIC, L.E. Temple, Chairman, May, 1987:

  "The review committee found the project ready to proceed with construction funding."

II. RHIC Design

The system of accelerators which comprise the Brookhaven heavy ion program is illustrated in Fig. 1. Ions are injected into the AGS through a long transfer line from the Tandem Van de Graaff accelerator. The commissioning of ion beams accelerated in the AGS took place during this past year, and marks the first step in a long term plan for heavy ion physics at BNL, a summary of which is given in Table I.

Table 1. Heavy Ion Facilities at BNL

1986	Begin AGS Fixed Target Experiments	
	Beam Energy:	Up to 28 $(\frac{Z}{A})$ GeV/amu
	Ion Species:	^{1}H to ^{32}S
	Flux:	$\simeq 10^{9}$ ions/pulse
	Running Time:	5-10 weeks/year
1990*	AGS Experiments with Booster Synchrotron	
	Extend ion mass to A $\simeq$ 200 (Au)	
1993*	Begin RHIC Collider Experiments	
Beam Energy:	Up to 250 $(\frac{Z}{A})$ GeV/amu per beam in collider mode	
Ion Species:	^{1}H to	^{197}Au
Total c.m. collision energy:		
	500 GeV (protons)	40,000 GeV (Au)
Luminosity:	$10^{31}cm^{-2}sec^{-1}$	$5\times10^{26}cm^{-2}sec^{-1}$

* *indicates proposed dates*

In 1986 Brookhaven received the first construction funds from the U.S. Department of Energy for the Booster Synchrotron as part of a general program to improve the AGS performance[8]. Present plans foresee completion in 1990. In addition to increased proton intensity for the high energy physics experimental program, the Booster will extend the heavy ion mass range to gold nuclei.

The basic parameters of the RHIC facility are illustrated in Fig. 2. The design calls for a top beam energy of 100 GeV/nucleon for ions of mass A=200, and the acceleration of ion masses spanning the full periodic table. The complete accelerator complex, consisting of Tandem, Booster, AGS and RHIC will provide c.m. collision energies for gold beams ranging from 1.5+1.5 GeV/nucleon to 100+100 GeV/nucleon. This energy range is covered with no inaccessible gaps, and adequate beam intensities throughout. Because operation in the collider mode at very low energy would require very large aperture (and therefore very costly) magnets--much more so than is required at the top energies--the energy range is covered in three segments: As shown in Fig. 2, the range between fixed target AGS experiments and high energy collider operation is spanned by using one of the RHIC beams striking a fixed target. For this operation an internal gas jet target would be used.

The layout of the RHIC collider is shown schematically in Fig. 3. The circumference of the collider is 3833 meters. It consists of two accelerator rings with six crossing regions (insertions) where the counter-rotating beams are brought into collisions and experiments carried out. Particle bunches accelerated in the AGS to top energy (28 GeV for protons; 11 GeV/amu for gold) are transferred to the collider by a magnet system installed in the existing transfer line tunnels. Single bunches of ions are injected 57 times into each ring in boxcar fashion. Filling time per ring will be about one minute. For gold, as an example, there will be ~ 1.1×10^{9} ions/bunch, or 6×10^{10} ions in 57 bunches in each ring. For the lightest ions, hydrogen and deuterium, approximately 10^{11} ions/bunch can be stored in the machine. Acceleration will take approximately 60 seconds. Bending and focussing of the ion beams is achieved with superconducting magnets. Given that the machine will be built in the existing CBA tunnel, a cost optimization is achieved by filling the circumference with relatively low field magnets. The maximum energy of 100 GeV/amu for gold ions (250 GeV for protons) is reached with a magnetic field of 3.4 Tesla. Maximum operational flexibility is obtained with the magnets of each ring in separate vacuum vessels, with the beams in the arcs separated by 90 cm. Figure 3 illustrates a half-cell of the arc magnet lattice, consisting of a dipole, two quadrupoles, and lumped corrector coils.

The six beam crossing regions are designed to accommodate a range of configurations to fulfill the needs of experiments. As illustrated in Fig. 4,

these include head-on collisions of beam bunches as well as a range of crossing angles. The free space available for experimental equipment in each crossing region is 9 meters on either side of the intersecting point. For head-on collisions with gold ion beams at top energy, a luminosity of 4.4×10^{26} $cm^{-2}sec^{-1}$ averaged over a 10 hour beam lifetime is expected. For protons the expected luminosity is about 8×10^{30} cm^{-2} sec^{-1}. These maximum values will be decreased by a factor of ~ 4 for a beam crossing angle of 2 mrad. Collisions of unequal species, e.g., protons in one beam and gold ions in the other will be possible as well. The Accelerator Physics Group has considered possible future upgrades of the machine performance, and these ideas are discussed elsewhere in this volume[9].

III. The Present Status

As noted above, a large fraction of the RHIC facility already exists. For the injector complex, the Tandem Van de Graaff, AGS, and heavy ion transfer line are already operational; the Booster Synchrotron is under construction. Most of the conventional construction for the collider is complete, including the ring tunnel, main service building and experimental halls for four of the six intersection regions. In addition, the liquid helium refrigerator, capable of cooling all of the superconducting magnets in the collider has been completed (as part of the CBA project) and successfully tested. The refrigerator has a capacity of 25 kilowatts at a temperature of 4.3K. The estimated heat load for RHIC is ~ 10 kilowatts at 4.6K.

The superconducting magnets for RHIC have been designed. The arc dipole magnet cross section is shown in Fig. 5. The dipole magnets are of $\cos\theta$ coil geometry with coil i.d. of 8.0 cm and yoke length 9.7 meters. As we discussed in Sec. I, the R&D work on these magnets is well along, and it is planned that a significant fraction of the magnets for the RHIC machine will be industrially fabricated. Figure 6 shows a magnet assembly, consisting of a dipole, quadrupole and corrector coils, mounted in a cryostat.

Four full-length, field-quality dipole magnets have been built during the past year, using coils wound at BNL. Three of these magnets have been assembled by the industrial firm Brown, Boveri Corp. (BBC) of Mannheim, West Germany, using tooling fixtures which are in place for the HERA project at DESY. An agreement has been reached between BNL and DESY whereby this tooling

will become available for the manufacture of RHIC magnets in exchange for BNL assistance in the superconducting and cryogenic design for HERA. The first of the full-length magnets, assembled at BNL, was successfully tested in February, 1987. Since then the remaining, industrially built magents in this series have been tested. All of these magnets reached fields of approximately 4.6 Tesla, or 35% higher than the operating field for RHIC, with virtually no training.

The magnet R&D program is continuing, with work now in progress on quadrupoles, corrector coils and the specialized magnets needed for the beam crossing reigons. A full cell of arc magnets, consisting of two dipoles, two quadrupoles and lumped corrector package, will be installed and tested prior to the production of final magnets.

The Project has been reviewed and validated by the Department of Energy, and construction could begin in fiscal year 1989 if funds are made available. A five-year construction schedule is planned. The accelerator construction cost is roughly 200 million dollars, with an additional 70 million dollars budgeted for detectors (these figures are in FY 1988 dollars).

IV. Experiments and Detectors

Of the six crossing regions built into the RHIC rings, those at the 2, 4, 6 and 8 o'clock positions have completed experimental halls, including support buildings and (except in the 4 o'clock "open area") crane coverage. The RHIC plan calls for mounting experiments initially in these four areas, leaving the remaining two unfinished until some later time.

The nature of these experiments, and specific designs for detectors have been studied by a number of groups at workshops and conferences over the past several years[2,10,11,12]. The measurement capability required for such experiments is similar to that which exists in spectrometers for high energy elementary particle experiments, but there are important differences. The most striking is the extraordinary level of particle multiplicities which experiments must deal with in high energy nucleus-nucleus collisions: Estimates for RHIC reach up to ~ 10,000 particles per event. In addition, most of the essential measurements involve soft particles, with transverse momenta and pair masses characteristic of the kinetic energies in a thermalized plasma of quarks and gluons. This is in contrast with the

elementary particle case where the focus is largely on rare processes produced in the high P_T tails of momentum distributions. In April 1985 a workshop involving about 100 nuclear and high energy physicists provided preliminary designs and cost estimates for a first-round suite of detectors for RHIC. The proceedings[2] from the workshop are available, and provide a detailed discussion of physics goals and conceptual designs for detector systems.

This Second RHIC Workshop, held at Lawrence Berkeley Laboratory, comes at a key moment in the development of the RHIC project and of the field as a whole. The earlier workshop efforts have continued, with individual working groups holding meetings at BNL, CERN and elsewhere. Major experiments have now taken data with ion beams at the AGS and SPS, and have produced many new insights into the requirements for detectors and detector development as well as sharpening the physics focus as we prepare for the higher energy regime of RHIC. The results of this workshop represent a first step in the planning for the initial round of experiments at RHIC.

References:

1. For extensive discussion see Proc. VI Int'l. Conf.on Ultra-Relativistic Nucleus-Nucleus Collisions, Aug. 1987, H. Satz and H. Specht eds. (to be published).

2. P. Haustein and C. Woody, eds., Proc. of the Workshop on Experiments and Detectors for a Relativistic Heavy Ion Collider, Brookhaven National Laboratory Report BNL 51921 (1985).

3. "A Long-Range Plan for Nuclear Science," report of DOE/NSF Nuclear Science Advisory Committee, Dec. 1983.

4. T. Ludlam and A. Schwarzschild, "Report of Task Force for Relativistic Heavy Ion Physics, Aug. 1983. (Reprinted in Proc. III Int'l Conf. on Ultra-Relativistic Nucleus-Nucleus Collisions, Nucl. Phys. A428, 657c. (1984).

5. "Report of the Round Table Discussion of Prospects for Future Experiments," D.A. Bromley, chairman; Proc. III Int'l Conf. on Ultra-Relativistic Nucleus-Nucleus Collisions, Nucl. Phys. A418, 375c (1984).

6. Conceptual Design of the Relativistic Heavy Ion Collider RHIC Brookhaven National Laboratory Report BNL 51932 (May, 1986).

7. See Ref. 6: also: E.H. Willen, "Magnets for RHIC", Workshop on Superconducting Magnets and Cryogenics, May 12-16, 1986, BNL 38966 (1986).

8. "Design and Status of the AGS Booster Accelerator, E.B. Forsyth and Y.Y. Lee, BNL 39298 (1987).

9. S.Y. Lee et al., this volume.

10. W. Willis and C. Chasman, Quark Matter '83, Proc. 3rd Int. Conf. on Ultra-Relativistic Nucleus-Nucleus Collisions, (T. Ludlam and H. Wegner, eds.), Nucl. Phys. A418, 413 (1984).

11. L. Schroeder, Ed., Proc. of the Workshop on Detectors for Relativistic Nuclear Collisions, Lawrence Berkeley Laboratory LBL-18225 (1984).

12. T. Ludlam, Quark Matter '86, Proc. Fifth Int. Conf. on Ultra-Relativistic Nucleus-Nucleus Collisions, (L. Schroeder and M. Gyulassy, eds.) p. 443 (1987). In the same volume see also: C. Fabjan, p. 371; M. Albrow, p. 417; N.DiGiacomo, p. 403; H. Gordon, p. 395, C. Gruhn, p. 375; S. Lindenbaum et al., p. 431.

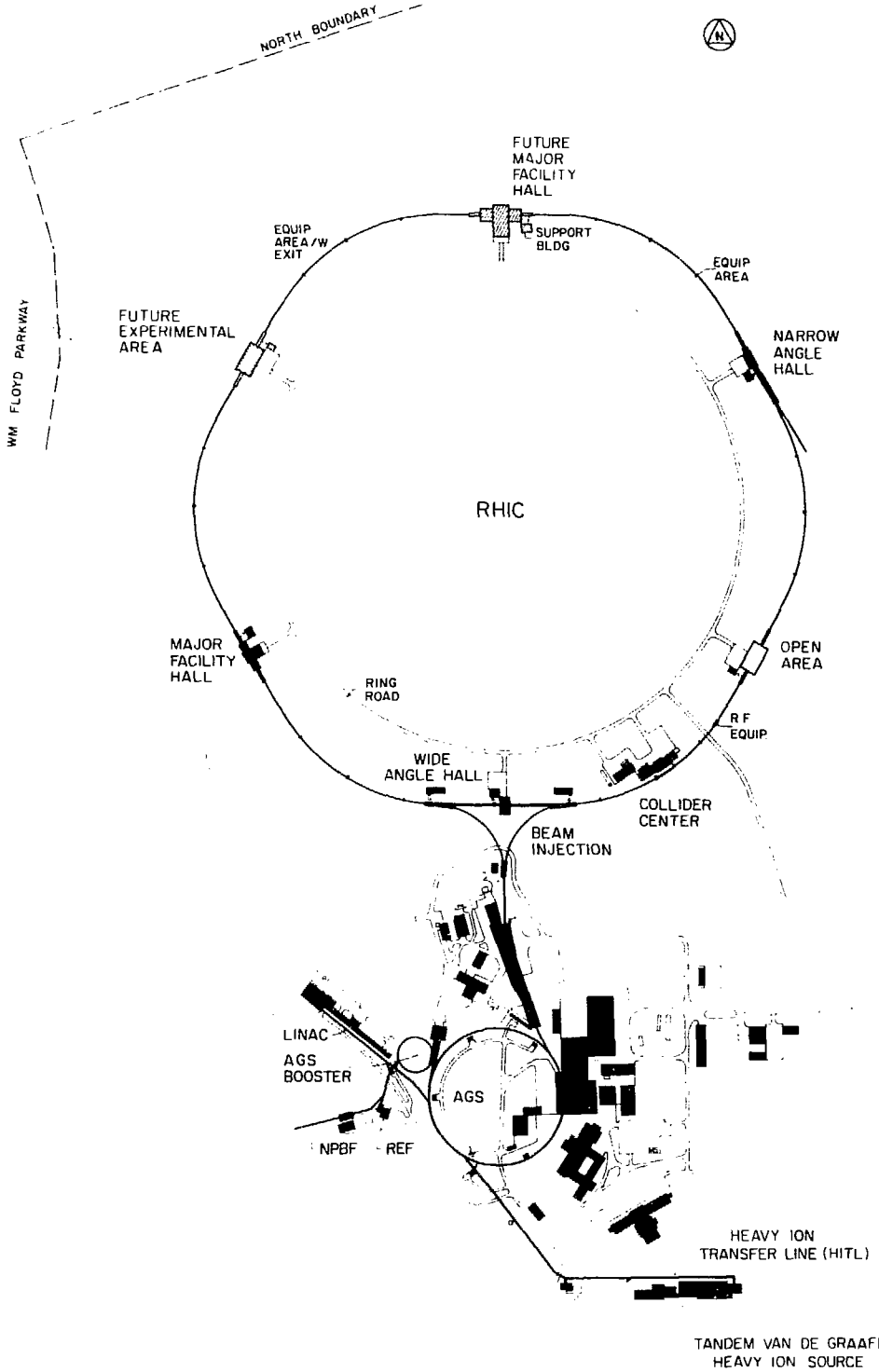

Fig. 1. Site map of present and proposed accelerators at Brookhaven. The Tandem Van de Graaff and the AGS with its linac injector are existing machines. The Booster Synchrotron for pre-injector to the AGS is currently under construction. The RHIC colliding beams accelerator to the north of the AGS complex is a proposed construction project.

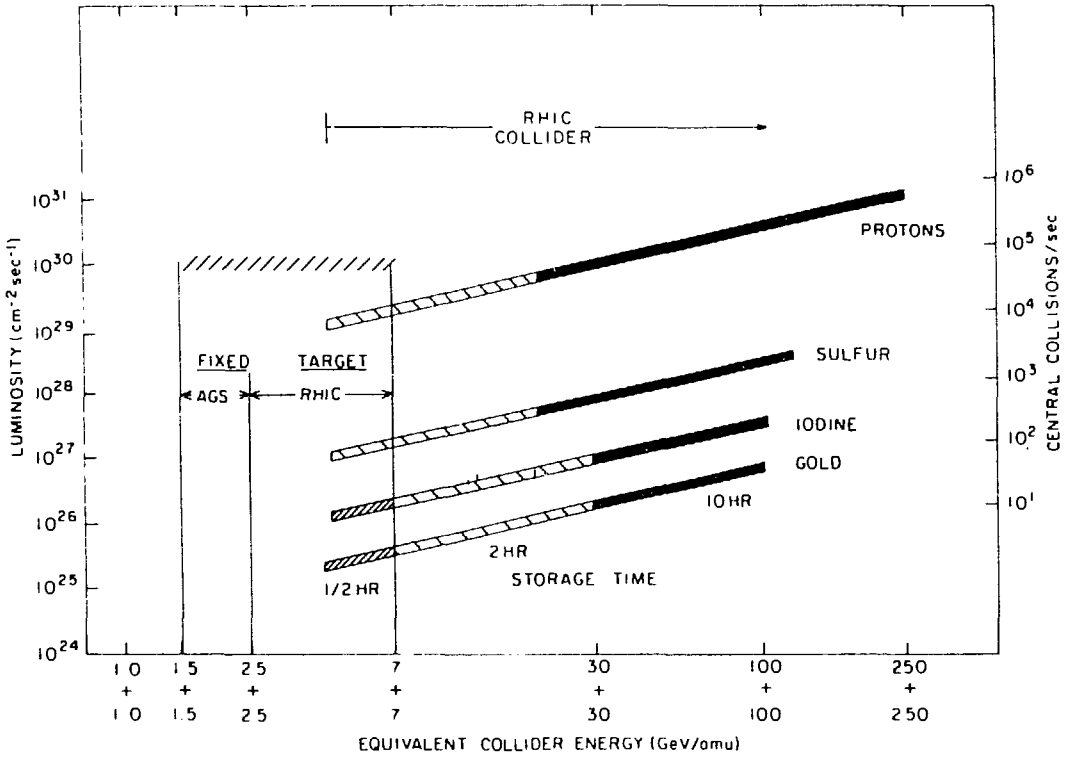

Fig. 2. The design luminosity, for various ion masses, as a function of collision energy over the full range accessible with AGS and RHIC. On the left-hand scale, central collisions correspond to impact parameter less than 1 fermi.

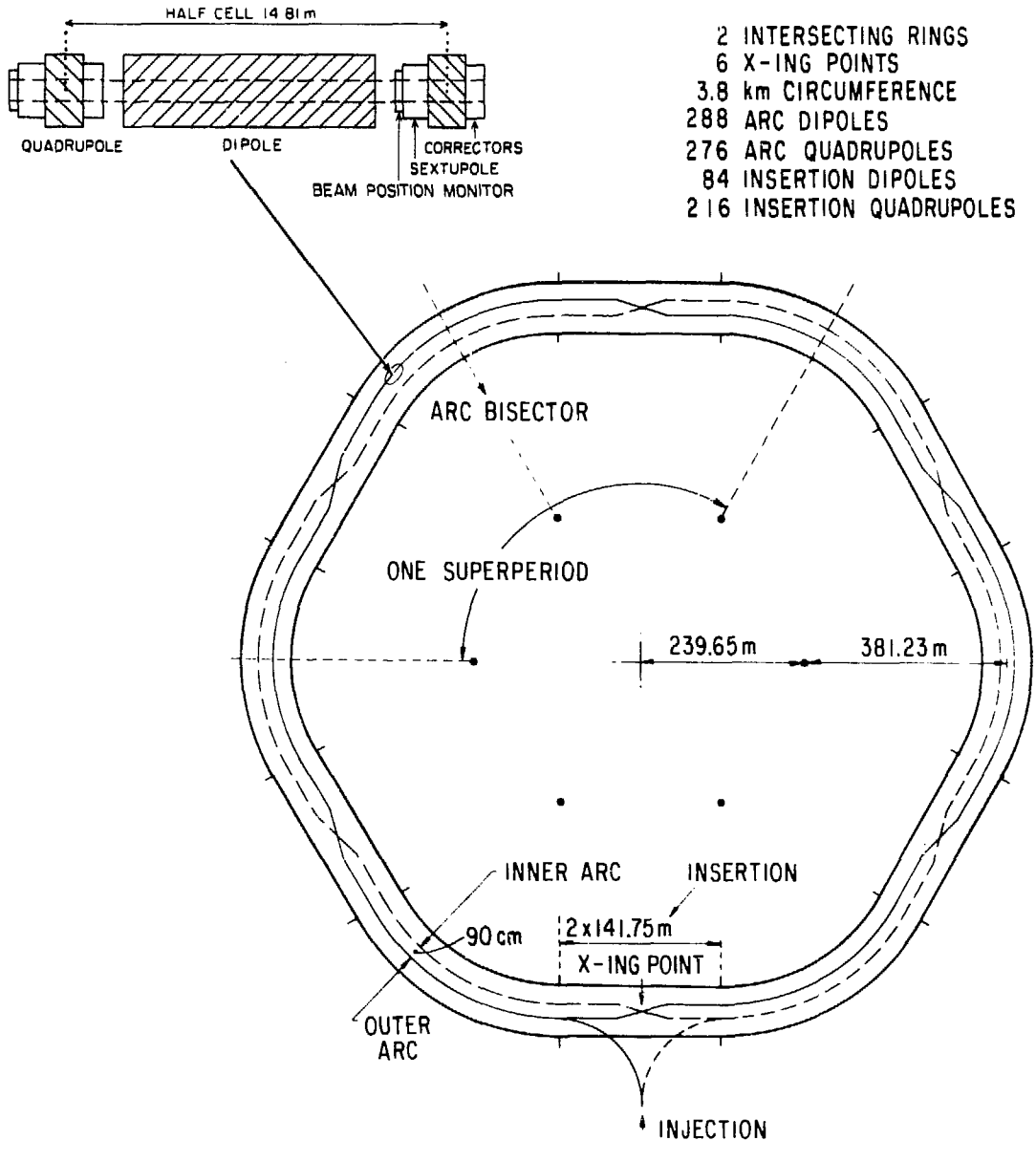

Fig. 3. Layout of the storage rings for the RHIC collider.

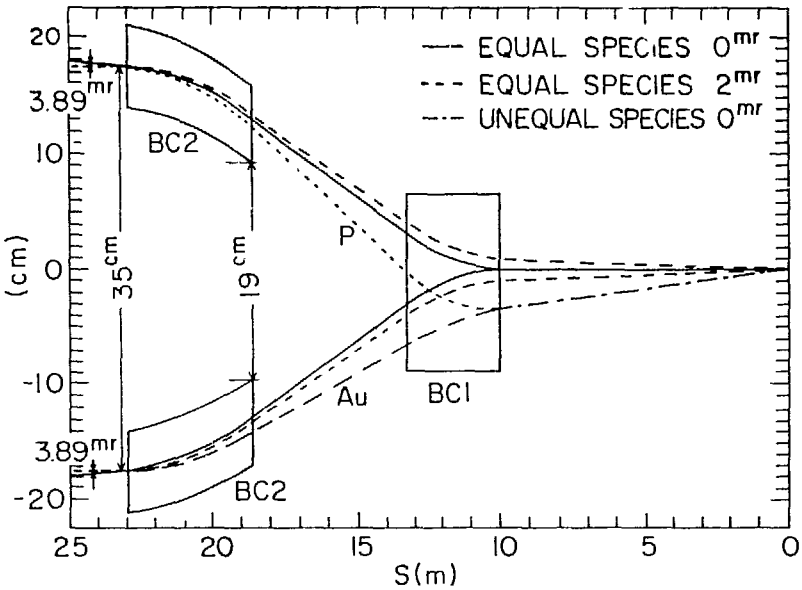

Fig. 4. Beam crossing geometry. BC1, BC2 are dipole magnets. The distance from the crossing point is denoted by S.

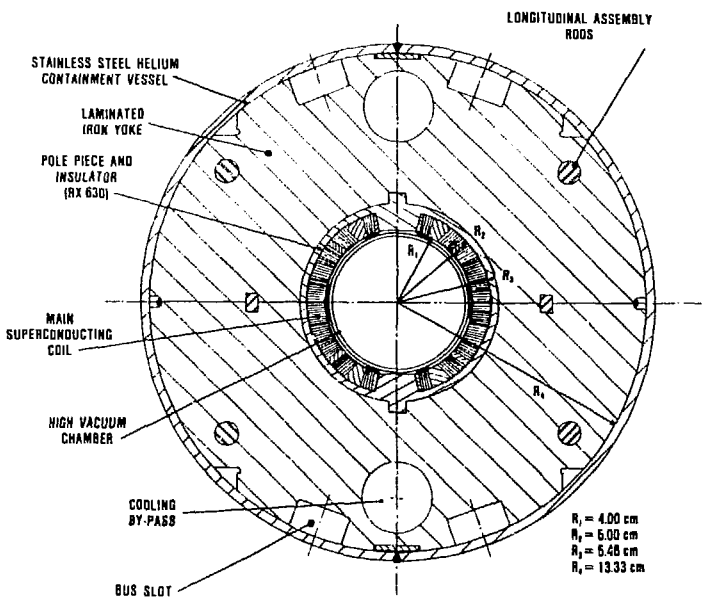

Fig. 5. Cross section of RHIC dipole magnet.

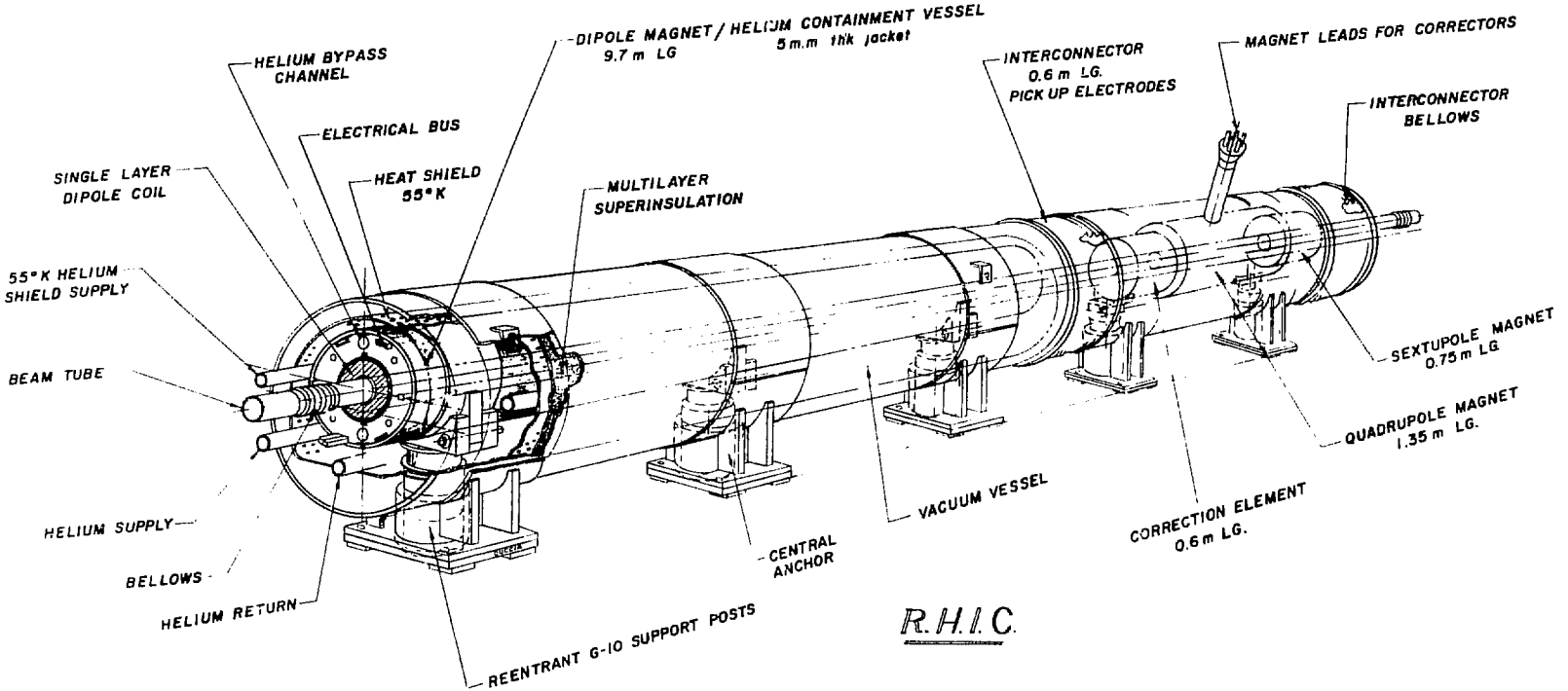

Fig. 6. RHIC magnet assembly: The drawing shows a half-cell of the arc magnet lattice, including a dipole, corrector package, quadrupole and sextupole magnets enclosed in their cryostat.

PHYSICS AT RHIC: WHAT DO WE WANT TO KNOW, AND WHAT DO WE WANT TO MEASURE?

Helmut Satz

Fakultät für Physik, Universität Bielefeld
D-4800 Bielefeld, F. R. Germany
and
Physics Department, Brookhaven National Laboratory
Upton, NY 11973, USA

This manuscript has been authored under contract number DE-AC02-76CH00016 with the U.S. Department of Energy.

PHYSICS AT RHIC

The central topic of this workshop is the planning and design of experiments for the Relativistic Heavy Ion Collider (RHIC) to be constructed at Brookhaven National Laboratory. I was asked to survey, as a short introduction, the main features of nuclear collisions which we would like to measure at RHIC. Let me therefore begin by asking: what do we want to know about the physics of high energy heavy ion collisions, and why? I shall list what to me are the main questions here. Following that, I shall indicate some possible experimental ways of addressing these questions.

1) Did the collision produce a system showing statistical or collective behavior? The most exciting aspect of nuclear collisions is the possibility to use them as a tool in the analysis of strongly interacting matter. For this, the collision should produce a "macroscopic" system, whose properties are determined by the collective action of many degrees of freedom. We thus hope that an A-A collision is more than something like a superposition of A nucleon-nucleon interactions.

2) What was the initial energy density in the different collision regions (central, fragmentation)? If we want to study strongly interacting matter at very high density, it is important to assure that nuclear collisions do indeed lead to densities higher than those found in heavy nuclei or in the neutron stars.

3) Was the produced system in thermal equilibrium? If this is the case, then we can apply the results of statistical QCD for the behavior of strongly interacting matter, and we can make use of hydrodynamic studies of the expansion and cooling of such matter. Pre-equilibrium systems appear much more difficult to analyse and understand.

4) If the system was thermal, what was its temperature? Both statistical QCD and strong interaction phenomenology suggest something like $T_H \sim 200$ MeV as a limiting (Hagedorn) temperature for hadron physics. Can we pass this to enter a new regime?

5) Was there initially a "chemical" equilibrium? With this, we want to ask if the constituents of different quantum numbers were present in the initial state according to their thermodynamical weights, or whether there still remains some "memory" of the quantum number structure of the incident beams.

Let me emphasize that all questions asked so far deal quite generally with strong interaction thermodynamics. They do not yet ask anything about color deconfinement or quark plasma formation. We now turn to these particularly exciting aspects.

6) Did the collision produce an extended system showing color deconfinement? If spatial size and lifetime of the system considerably exceed the hadronic scale of one fermi, this would mean that we have indeed created a new state of matter: the quark-gluon plasma.

7) How did this quark-gluon plasma subsequently expand and hadronize? Here we would particularly like to learn something about the nature of the transition to confinement (first order or continuous), possible hysteresis behavior (superheating, supercooling), the nature of the expansion and the formation of hadronic matter (hydrodynamic flow, deflagration/detonation, etc).

There will certainly be many further questions; nevertheless, the answers to these would give us some basis for the understanding of strongly interacting matter. What kind of experiments could provide us with these answers? I have summarized in table 1 those that have been most extensively discussed. It should be emphasized that the references listed are meant only to provide further information; they give in no way a complete coverage of the considerable amount of theoretical work on signatures. Let me now elaborate a little on each point.

1) Hanbury-Brown-Twiss type interferometry for hadronic secondaries should provide information about the spatial size of the system from which they were emitted. The photon-to-pion ratio gives an indication about collective effects, by measuring volume-to-surface emission.

2) Knowing multiplicity and energy of the hadronic secondaries allows us to reconstruct the initial energy density, if we know the longitudinal formation length; the initial transverse size is given by the nuclear radii. The formation length can be estimated on the basis of nuclear stopping experiments.

3) If the system is thermal, the dilepton spectrum should fall exponentially with the pair mass, in contrast to power-low fall-off for Drell-Yan production. Thermalization will also destroy the memory of the collision axis; thermal lepton pairs should therefore have

an isotropic angular distribution. Drell-Yan pairs, in contrast, are predicted to be aligned with the incident beam axis.

4) The initial temperature T_0 can be obtained from the thermal dilepton spectrum, if this shows a clear exponential fall-off ($\exp -M/T_0$) in the pair mass. It should be noted here that thermal dileptons can be emitted from a meson gas as well as from a quark plasma and hence do not provide evidence for plasma formation.

5) The measurement of particle ratios (such as strange to non-strange baryons) may be able to give information on the flavor distribution at the early stages of the process. It appears, however, that details do depend on the nature of the expansion process.

6) The study of the heavy quark resonance peaks in the dilepton spectra ($J/\psi, \psi', \Upsilon, \Upsilon'$) should provide a direct test of a quark deconfinement. In a deconfined medium, a $c\bar{c}$ pair cannot bind to form a J/ψ, and late production at the hadronization point is excluded because there are almost no thermal c or $\bar{c}$ quarks in the system. Hence if there is deconfinement in nuclear collisions, J/ψ production (and similarly that of ψ', Υ and Υ') should show a much suppressed signal-to-background ratio in comparison to that observed in nucleon-nucleon collisions.

7) The transverse momentum distribution of hadronic secondaries is expected to increase with multiplicity, since the latter is related to the initial energy density, and a higher energy density should result in stronger collective flow. The form of the (dN/dy) dependence of p_T may also indicate something about the nature of the transition. Moreover, both momentum distributions and energy flow behavior can be compared directly to the results of hydrodynamic calculations.

In summary: we have thus indeed some basis for the hope that high energy nuclear collisions will provide the key to the analysis of strongly interacting matter.

Table 1

Feature	**Measurement**	**Reference**
Macroscopic size and collective behavior	Interferometry; γ/π ratio	1
Energy density	Multiplicities and energies of secondaries; nuclear stopping	2
Thermal equilibrium	Spectrum and polarization of lepton pairs	3
Initial temperature	Dilepton spectrum	4
Chemical equilibrium	Particle ratio	5
Color deconfinement	$J/\psi, \psi', \Upsilon, \Upsilon'$ production	6
Plasma expansion and hadronization	Momentum distribution of secondaries; p_T vs. dN/dy	7

References

1. K. Kolehmainen, Nucl. Phys. A461 (1987) 239c;

   E. L. Feinberg, Nuovo Cim 34A (1976) 391.

2. J. D. Bjorken, Phys. Rev. D27 (1983) 140;

   L. D. McLerran, in Quark Matter 1984, K. Kajantie (Ed.), Springer Verlag (1985).

3. G. Baym, Phys. Lett. 138B (1984) 18;

   P. Hoyer, Phys. Lett. B187 (1987) 162.

4. K. Kajantie and H. I. Miettinen, Z. Phys. C9 (1981) 241;

   K. Kajantie, J. Kapusta, L. D. McLerran, and A Mekjian, Phys. Rev. D34 (1986) 2746.

5. P. Koch, B. Müller, and J. Rafelski, Phys. Rep. 142 (1986) 168;

   T. Matsui, L. D. McLerran, and B. Svetitsky, Phys. Rev. D34 (1986) 783 and 2047.

6. T. Matsui and H. Satz, Phys. Lett. B178 (1986) 416;

   F. Karsch and R. Petronzio, CERN-TH 4699/87 (April 1987).

7. L. Van Hove, Phys. Lett. 118B (1982) 138;

   M. Kataja, L. D. McLerran, V. P. Ruuskanen, and H. von Gersdorff, Phys. Rev. D34 (1986) 2755.

REPORTS FROM WORKING GROUPS

CALORIMETRY FOR A 4π-RHIC DETECTOR

Convenors:
M.G. Albrow, C.W. Fabjan, H. Gordon and D. Lissauer

A. Poskanzer
University of California, Berkeley, CA, USA

H. Gordon, D. Lissauer, T. Ludlam and L. Olsen
Brookhaven National Laboratory, Upton, NY, USA

T. Akesson, C.W. Fabjan, J. Schukraft, P. Sonderegger,
R. Wigmans and W.J. Willis
CERN, Geneva, Switzerland

S. Nagamia and W. Zajc
Columbia University, Irvington on Hudson, NY, USA

H. Gutbrod
GSI, Darmstadt, Fed. Rep. Germany

P. Glässel, U. Goerlach and H. Specht
University of Heidelberg, Fed. Rep. Germany

M. Di Giacomo, A. Gavron, J. Sunier and H. Van Hecke
Los Alamos National Laboratory, NM, USA

H. Boggild and K. Hansen
Niels Bohr Institute, Copenhagen, Denmark

W. Cleland
Pittsburg University, PA, USA

P.G. Rancoita
INFN, Milan, Italy

Y. Sirois
McGill University, Montreal, Canada

D.F. Keane
University of California, Riverside, CA, USA

M.G. Albrow
Rutherford Appleton Laboratory, United Kingdom

K. Wolf
Texas A&M University, College Station, TX, USA

P. Giubellino
INFN, Turin, Italy

ABSTRACT

Two working groups, one centered at BNL and the other at CERN, have been studying RHIC-specific calorimetry issues relevant to a large 4π-general purpose RHIC detector. Topics covered included the required energy and position resolution, low energy response and calorimeter associated background as well as instrumentation of the detectors. These considerations led to a conceptual design, which was further developed during the Workshop.

1. INTRODUCTION:

The Working Group reviewed the considerable progress on calorimetric techniques and systems achieved since the first RHIC Workshop [1]. Today, we benefit from a better understanding of the physics influencing the energy measurement [2], we have seen remarkable progress in liquid [3] and solid [4] ionization chamber readout methods and have developed new approaches to high-performance system designs [5]. We first review intrinsic performance properties, subsequently discuss those technical developments which appear of prime value to RHIC experimentation and make comments on the possible impact of the calorimetric environment on other detector components.

We then motivate and develop a specific calorimetric detector concept for RHIC, in which we attempt to combine full solid angle calorimetry with other physics, e.g. electrons and hadrons in the central region with muons at small polar angle. Finally, we conclude by identifying some areas of detector development which we identified as having the potential to influence project design.

2. PERFORMANCE BENCHMARKS

2.1 Energy Resolution and Linearity

'Compensating' Calorimeters have become a household word and the importance of 'e/h' needs no longer be explained (Fig. 1). In the most recent experimental test, compensation was measured up to particle energies as much as $\sim$ 200 GeV/c with resolution at the $\sim$2% level [6]. Based on a refined understanding of the physics of the hadronic cascade [2], Wigmans

made the important observation that compensation may also be achieved in non-Uranium calorimeters, e.g. with lead-absorbers (Fig. 2) by careful optimisation of the sampling fraction provided the readout material contains hydrogen. Thus Pb/Scintillator Calorimeters will be competitive whenever the highest densities and the best spatial resolution are not essential and where systematic effects due to the scintillator readout (R/O) can be tolerated.

While the 'compensation' mechanisms crucially affect the high-energy response of calorimeters, we still have to cope with low-energy non-linearities [7] (Fig. 3). These non-linearities could be rather serious for energy measurements in the central rapidity region at RHIC, but at present we know of no proven way to cure this disease. We may have to plan to take account of these non-linearities based on some knowledge of particle composition for the events of interest.

2.2 Spatial and Angular Resolutions

Spatial resolution in a calorimeter is closely coupled to the average absorption length in the device. Modern instruments have been evaluated to give excellent performance for multi-particle and multi-jet events (Fig. 4), while maintaining an extremely compact construction. Compared to jet physics at the TeV-scale [5], we think that RHIC physics poses less demanding requirements on angular resolution and will be well satisfied by present calorimeter technology.

3. SURVEY OF POTENTIAL READOUT TECHNIQUES

The group reviewed in detail the considerable progress in experimenting with novel readout methods. Not surprisingly, the requirements of modern precision calorimetry have prompted in particular the studies of ion-chamber techniques, which experience has shown to be well suited to adequate control of systematic measurements effects.

3.1 Room-Temperature Liquid Ion Chambers Readouts

While the suggestion to use room-temperature liquids instead of Liquid Argon for Calorimeters has been made more than ten years ago, it was only recently [3,8,9] that this concept was tested on the prototype scale. The

major efforts of the UA1-group towards a large Uranium/TMP calorimeter have promoted this concept to one of the potentially more interesting calorimeter methods meeting the requirements at diverse (e.g. RHIC and SSC) machines. We feel that it is a prime candidate for RHIC, and R&D both for UA1 and SSC could help to make it a viable alternative on the RHIC timescale.

3.2 Silicon Readout

This is an alternate 'room-temperature ion-chamber readout' with several attractive features [4]: given the typical thickness of the active Si-detectors ($\sim$ 300 μm), conceptually very compact devices may be envisaged. The charge collection is fast. Prototypes of electromagnetic calorimeters have been tested and shown to work as expected. Apart from technical problems of signal-processing (very large detector capacitances) the question of industrial procurement - i.e. price and availability for large detectors - is not answered at this moment. Our group felt that Si-R/O offers a level of performance NOT required at RHIC and does not believe that it will be a competing technique, for a large calorimeter facility. It may however be of use in specific areas where compactness is important.

3.3 Scintillator Readout

Scintillator R/O using wavelength shifters has accumulated a distinguished record of achievements over the last decade [6,7,10] and remains one of the attractive techniques for very demanding applications [11]. We do not expect that this optical R/O will result in a serious performance degradation for RHIC physics, particularly in view of the very high particle multiplicities. More recently, an interesting variation has been suggested [12,13]. It is based on the use of scintillating fibres ($\sim$ 1mm diameter), oriented in the longitudinal direction of the showers and read by light detectors at the back of calorimeters. The principal advantages appear to be:

- good control of the ratio of passive absorber to active readout: the principal requirement for compensated non-U calorimeters (e.g. Pb/Scintillator)
- good transverse uniformity and transverse segmentation
- very little 'dead-space' (no wavelength shifters needed).

Large-scale development of this technique is expected to start by the end of 1987, perhaps in time for a serious evaluation for RHIC.

The group's conclusion of this survey indicated that no new major calorimeter R&D is required to meet RHIC's performance standards.

4. RHIC SPECIFIC CALORIMETER ISSUES

Here we discuss several calorimetric issues pertinent to the RHIC experimental environment.

4.1 *Low Energy Response*

As already mentioned in Chapter 2.1, the many low-energy (below $\sim$ 2 GeV) particles in a typical RHIC collision, will require careful correction due to the non-linear response. In particular, no experimental information is available on the response for neutrons. The experimental response, which will depend critically on the composition of the calorimeter will have to be measured to provide sufficient input to our Monte Carlo simulators.

4.2 Granularity

A few physics considerations exist, from which requirements on transverse granularity may be derived:

rapidity fluctuations [14] are frequently discussed in the literature as possible quark-gluon plasma indicators. Typical domains of correlation are estimated to be approximately $\Delta y \leq 0.5$, $\Delta\phi < 0.5$ rad. Such fluctuations in particle density are adequately reflected in calorimetric cell sizes of $\Delta y = 0.1 \times \Delta\phi = 0.1$ (Fig. 5). This is a rather conventional requirement, typical for a range of hadronic processes, e.g. mini-jet and jet production, which quite plausibly may be also of interest at RHIC.

4.3 Albedo refers to the flux of particles originating from a particle cascade in a calorimeter and which escape through the front-face of the instrument. Very little is known quantitatively [15], but estimates indicate that albedo particles may not be ignored in the RHIC environment. Given the very high expected multiplicities, even a small albedo could

cause problems for track detectors or multiplicity counters. Within our Working Group two different experimental studies were carried out.

One study [16] was carried out with particles in the 2-10 GeV range. Approximately one count was detected in a 1 cm thick scintillator ($\Delta\Omega$ = 0.1 sr) per $\sim$ 50-100 incident particles. This would translate into an albedo initiated count rate comparable to the true multiplicity inside a 4π RHIC calorimeter.

A second measurement [17] was carried out at very high energies. An albedo particle flux of $\sim$ 0.3 charged and a similar number of neutral (γ or n) particles/sr per incident hadron was registered in a 0.1 cm thick counter. The flux clearly had two components: a 'prompt' charged contribution and a slow (μs scale) neutron flux. The two measurements cannot easily be compared due to the very different energies of the incident particles. If the albedo is proportional to the incident hadron energy then these results would not be worrying, but then the previous low energy study is not easy to understand. A systematic experimental study over a large energy range (< 1 GeV to > 100 GeV) with separation of prompt and slow components would be welcome.

In view of the importance of the albedo question for RHIC physics, a Monte Carlo study using the "GEISHA" hadronic shower simulation code was also carried out [18]. Representative results are given in Fig. 6 and Fig. 7.

5. A CONCEPTUAL DESIGN

5.1 Introduction

The role of full solid angle (4π) calorimetry at RHIC is, we believe, very different from that at other very high energy colliders. At e^+e^-, ep and pp or $p\bar{p}$ colliding beam machines at SLC/LEP energies and above, high resolution calorimetry [5] has become of crucial importance for measuring jets, which trace the partons in energy and direction. In contrast the physics program at RHIC, as far as we can see today, is oriented more towards large distance phenomena (confinement, phases of matter etc.). As such our main aim is to study hadronic matter at very

high temperatures and densities over extended volumina. The subset of most central, most opaque nuclear collisions which have the best chance of generating such conditions may be selected by requiring large transverse energy E_T (summed over all final state particles) in a calorimeter. While at the CERN and Fermilab $p\bar{p}$ colliders the highest E_T events (typically $E_T \sim$ 200-250 GeV) are dominated by two or three high E_T jets, at RHIC much higher E_T events with enormous multiplicity of soft particles will be relatively common. The calorimeter should have sufficient granularity to study and eventually to trigger on specific event topologies. An example would be unusual fluctuations in $dE_T/d\eta \cdot d\phi$ in rapidity η and azimuth ϕ. Cell sizes of order $\Delta\eta \times \Delta\phi \sim 0.1 \times 0.1$ (de luxe) or 0.2×0.2 (modest but possibly adequate) are considered reasonable. These sizes are also appropriate for jet measurement at RHIC when conditions allow; maintaining the possibility of jet measurement means that the calorimeter should be at least 4λ deep. At least two depth subdivisions would allow crude separation of electromagnetic (γ, π^0, η) and hadronic ($\pi^{\pm}$,K,p,n) energy flow. The combination of such a calorimeter with multiplicity detectors covering its inner surface allows one to obtain quantities like the mean E_T per particle ('temperature') - or rather the distribution of these quantities in (η,ϕ) space - on an event-by-event basis.

In contrast to some situations in the past where excellent energy resolution was mandatory (e.g. searching for high p_T jets at ISR energies and below), at RHIC we do not consider it difficult to obtain acceptable $\sigma(E)/E$. The point is that the E_T-spectrum is likely to be rather flat out to high E_T values, and if one wants to trigger on the falling edge the total energy is so high that the energy resolution on the total E_T will be very good anyway. Of course the energy in a cell will still be small, given good granularity, and the desire to measure local energy density fluctuations pushes one in the direction of good hadronic resolution.

During the process of the evaluation of 4π calorimeter concepts for a RHIC detector, we developed a conceptual design which we believe has many attractive features. One of the important guiding principles was that of flexibility, retaining the ability to explore simultaneously (or in series)

different physics avenues, and to adapt sub-systems of the detector according to acquired knowledge. The choice of an open geometry magnet (e.g. Helmholz coils or the Open Axial Field Magnet of ISR experiments R807, R808) allows the principle of 4π calorimetry to be readily adaptable to specific requirements. Fig. 8 shows a design as derived during the Workshop. The conical poles cover minimal solid angle - in the case shown from 20° to 40° in polar angle θ. This region should be 'calorimetrized', e.g. by inserting radial scintillating fibres. Forward calorimetry for $\theta < 20°$, inside the conical pole apertures could come closer to the vertex to help with muon physics ($|\eta| \geq 2$). The iron return yoke would be lumped in azimuth (Fig. 8b) and the large angle calorimetry could be constructed in such a way that (η,ϕ) windows could be opened up if space is needed, say for a special hadron identification region (the port concept retained). An innovation shown in Fig. 8 (albeit in a totally non-optimal way) is the double coil, by which we hoped to have the option of reducing the magnetic field on the interaction region itself to very small values for soft electron studies. These are discussed in more detail elsewhere. In Section 5.3 we describe briefly the results of a follow-up study by T. Taylor (CERN) of this magnet concept.

5.2 The Calorimeters

In this section we consider possible techniques for the various calorimeters, starting from $\theta \sim 90°$ and moving forward.

The central calorimeters cover angles $\theta \geq 40°$, i.e. beyond the conical pole pieces, and should be constructed in a modular way such that windows $\Delta\phi \cdot \Delta\eta$ can be opened by withdrawing elements. A "Geodesic Dome" type of geometry may be suitable. Our presently preferred readout medium is a choice between radial scintillating fibres or room-temperature organic liquid ionisation chambers (e.g. TMS, TMP). We expect radiation damage not to be a problem for scintillating fibres at large polar angles ($\theta > 20°$); they allow excellent granularity with some depth segmentation, and if embedded in lead at the right packing density we can hope for compensation and good resolution. They also have fast response. Depth segmentation can be achieved by starting fibres at different depths and taking them all to the back. In a radial scheme this can be done with approximately constant packing fraction if that is required for optimal energy resolution. Warm

liquid ionization chamber calorimetry could also be an excellent readout medium and very suitable for this region. An evaluation of the practicality of the technique should be easier a year from now when the 25 m³ Uranium TMP calorimeter being constructed by UA1 at CERN should be close to completion.

Some of the specifications for the central calorimeter are given in Table 1:

Table 1: Central Calorimeter Specifications

Depth	$\sim 4\ \lambda_{int}$ ($\sim$80cm if 15% vol. of scint.)
Depth segmentation	$5X_o$, $12X_o$, $\sim 2\lambda_{int}$, $\sim 2\lambda_{int}$
Tower size	$\Delta\phi = 0.1$, $\Delta\eta = 0.1$ for $\lvert\eta\rvert<1$; 1280 towers
Number of channels (4 depths = 5120)	
Weight	300 kg per tower, total $\sim$ 360 tons
Resolution expected	$\sigma_E/E \sim 15\%/\sqrt{E}$ (electrons), $45\%/\sqrt{E}$ (hadrons)
If scintillating fibre readout,	$\sim 2.10^6$ fibres, length $\sim$ 1m
If "TMP", sampling	$\sim$6mm Pb + 2.5 mm TMP, then 14 000 litres TMP
Total volume	40-50 m³

The magnet pole tips cover polar angles $\sim$25° to 40° and are iron. However, we must also have calorimetric measurements in this region. The technique of radial fibres following the magnetic flux lines will allow this, e.g. a 2 mm diam. fibre per cm² removes $\leq$ 4% of the iron. Three η-divisions, 64 ϕ-divisions and 3 depths gives 1150 channels (on the two poles) and we can expect $\sigma_E/E \sim 80\%/\sqrt{E}$ for hadrons. For electromagnetic energy detection, in this angular region compactness is crucial, and we envisage therefore a tungsten (X_o = 3 mm)-silicon wafer sandwich calorimeter just covering the nose of the conical poles.

The 'forward' calorimeters fill the volume between the inner edge of the pole cones and the beam pipe. In this region muon physics is emphasized, so the front face is close to the intersection ($\sim$ 50 cm

radius) to minimize π-decays. A relatively low-Z absorber to minimize multiple scattering is probably preferred here. Compared with the large angle detectors, the volume is small ($\sim$3.4 m^3) and so is the number of channels (e.g. 5 η-rings over the range $1.5 < \eta < 4$, 6 depth segments and $\sim$ 8 ϕ 'pads' on each side). This region is a prime candidate for a room-temperature liquid calorimeter because the radiation fluxes are highest, which disfavours scintillator.

In the very forward region we wish to ensure as far as possible complete calorimetric coverage, even for the spectator fragments. To this end, we would aim to (i) cover the faces of the superconducting quadrupoles (ii) install a 'neutron-calorimeter' some 30 m from the intersection, between the beam pipes where 0° neutron spectators can be stopped (iii) beyond BC1, the beam-separator bending magnet, install a 'proton-spectator' catching calorimeter (iv) investigate the possibilities of 'calorimetrizing' some of the machine magnets, e.g. BC1... perhaps by the insertion of silicon wafers.

5.3 The Magnet: An Open Axial Field Magnet with Variable Geometry

A preliminary design study has been carried out by T. Taylor (CERN) of an Axial Field Magnet with multiple independent coils, enabling one to practically cancel the field on the vertex if desired. When used in that way the gap is narrow with ±25° polar angle coverage from the interaction region centre. Fig. 9 shows one quarter of the magnet - the figure should be rotated about the z(beam) axis. The outer return yoke can then be removed over most of the azimuth, as required for an open geometry. An alternative operating configuration is with the poles retracted (Fig. 10) to enlarge the acceptance to ± 40° in θ. If the coils are then run with the same polarity, we have the standard AFM-type field. However, by choosing the relative currents in the coils one can tune the field uniformity/strength. Fig. 11 shows the axial component of the field, B_z, for these forward and back positions. Each curve is labelled by the current densities in A/mm^2 in the four coils. Fine tuning could make the field at the origin exactly zero, but one is more interested in keeping the field low over a particular region e.g. out to 10 cm radius which would be a different optimization. Fig. 9 shows, for one chosen set of coil currents, the field lines for the forward position; after 2.5 kg at 40 cm

radius the field is less than 0.5 kg beyond 80 cm. Fig. 10 shows the larger acceptance back position, with the currents chosen to give a high field integral. We believe the new degrees of freedom in field shape which result from independently powered coils is a very attractive feature for RHIC physics, at least in the early exploratory years.

5.4 Central Electrons

In the large angle region an inner sphere of radius $\sim$ 1.5 m, before the front of the calorimeter, is available for electron production studies. For the study of low p_T, low mass pairs ($m_{e^+e^-} < m_\rho$) it is necessary to have very low fields on the interaction region so the magnet would be run in the 'forward pole' configuration with the field confined between two RICH detectors. Ideally these see 'only' the electrons before and after the low field of $\sim$ 0.06 Tm, giving 7% mass resolution at m_ρ. Minimization of material for conversions ($\lesssim$ 1% X_o) before the inner RICH is crucial. Readout is via a large number of PADs ($\sim$ 200 K with pulse height information plus $\sim$ 800 K with digital information): zero suppression in readout will give $\sim$ 10 Kbytes per event.

Much more detailed studies of this problem are reported by another working group [19]. The desire to study soft electrons had considerable influence on this design. A possibly serious remaining problem is that we do not see clearly how to discriminate at the trigger level between the electron pairs of interest and the trivial background pairs (Dalitz decays and conversion). With advances in fast on-line processing a higher level trigger based on RHIC counters might be envisaged.

5.5 Direct Photons

As one example of a possible 'external detector' we considered briefly how to measure direct photons, above $\sim$ 10 MeV in a 20° x 20° window around θ = 90°. Homogeneous 2-dimensional detector arrays, like BGO crystals or Pb-glass blocks could be used. Table 2 gives a parameter list to compare these options. It may be even more advantageous to use an array of BaF_2 crystals and exploit the exceptionally fast signal of the UV-component of the scintillation light. Timing accuracy below $\sigma < 1$ ns should be achievable translating into a spatial accuracy of $\sigma \lesssim 30$ cm. Such a spatial resolution may be of fundamental importance for the

rejection of the numerous sources of background, such as neutrons or photon-skyshine from the surrounding detectors.

Table 2

Material	BGO	Pb-glass
Distance from centre	3 m	6 m
Area	1.5 m^2	6 m^2
Modules (20 X_o)	2 x 2 x 20 cm^3	3.5 x 3.5 x 40 cm^3
No. Modules	4000	5000
Resolution at 1 GeV	2.5%	6%
π^0-mass resolution	1.5%	4%
Pile-up (dN/dy = 2000)	16% charged	12% charged
	16% photons	12% photons
Weight (tons)	2.2	10

5.6 A Hadron Wedge Spectrometer

Another option we discussed for an external 'port' device was an external spectrometer with multi-hadron identification capabilities covering something like $\Delta\phi \sim \Delta\theta \sim 50°$, in the central region ($-0.45 \leq \eta \leq 0.45$). This will be covered fully in the report by Nagamiya et al.; we merely summarize some features.

The $\sim$ 2 m tracking path is followed by two-layer calorimetry, BGO or Pb-glass blocks for em showers followed by a hadronic wall of identical properties to the rest of the central calorimetry. The hadron wedge tracker comprises a jet chamber, 1.5 m^2 RICH chamber with $\sim$60,000 digital and $\sim$ 15,000 analog pads, and a time-of-flight system with some 4000 elements of 10 cm^2, each with TDC's and ADC's. As a result π, K and p are separated by at least 3 σ up to 2.5 GeV/c and pions are identified up to 4 GeV/c.

5.7 Triggering

The trigger subgroup of the 4 π calorimeter group considered ways in which the experiment could be triggered. Most of the thinking concerned the definition of the interaction and the calorimeter-based triggers. Additional triggering signals will need to be generated from the

spectrometers in the experiment, but at the present stage we consider only the structure into which they will fit.

Since the time between bunches at RHIC will be short compared to typical detector integration time or drift time, it will probably be necessary to define a collision-free window of order 1 μsec. The most rudimentary element of the trigger is the definition of these collisions. It must be a rather loose definition and include interactions outside the fiducial volume, including beam-gas collisions. For this purpose we propose two types of detectors - one, a scintillator hodoscope surrounding the beam pipe on either side of the experiment and the other a set of small calorimeters to detect neutrons and protons produced at essentially 0° in the collision. We call the latter 'spectator' calorimeters of which there are four, one placed on the beam axis between Q_3 and Q_4 on either side of the interaction region to measure neutrons and one placed between BC1 and BC2 on either side to detect the protons. Some combination of signals from the beam hodoscopes and the four calorimeters would be used to define an interaction, which may run at a rate of up to 10^6 Hz.

A pretrigger for the experiment, which activates all of the data collection electronics will be formed from the above interaction signal, in combination with another requirement such as the global E_T measured in the experiment or perhaps a signal from one of the external spectrometers. If a solution to the problem of a large diamond size is not found it would be worthwhile at this level of the trigger to make a crude definition of the vertex position using time of flight measured in the scintillator hodoscopes. A comparison of the mean time of arrival of hits in these hodoscopes with the crossing time could also be used to help eliminate double interactions. One could set the E_T threshold to a value high enough to achieve a pretrigger rate of approximately a factor of ten below the interaction rate, giving a pretrigger rate of at most 10^5 Hz.

For the remainder of the triggering system we envision a two-level scheme: a first level trigger which would operate on the time scale of about 1-2 μsecs and a second level trigger requiring perhaps 100-200 μ-secs. Each level should reduce the triggering rate by about a factor of 100, to bring the final rate to about 10 Hz. If necessary, a third

level, operating on the 10-20 ms time scale using a processor could be implemented if further rate reduction is required. The numbers have been chosen to give a 10-20% dead time for each stage of the experiment, but they are consistent with the characteristics of already operating trigger processors.

For the first level calorimeter trigger, we envision a processor which can perform the following functions:

1) Calculation of the global E_T and comparison to several thresholds. This would be done separately for electromagnetic, hadronic and total E_T sums.
2) Search for structure in the E_T deposition in a region of $(\Delta\eta,\Delta\phi)$ above some threshold. A design goal of this part of the processor would be to permit the summing intervals $\Delta\eta$ and $\Delta\phi$ to be programable in order to maintain flexibility.
3) A measurement of the dispersion in $dE_T/d\phi$ in order to define symmetric or asymmetric events at the trigger level.

The first level processor would be able to create a trigger from any combination of the above decisions or it could combine these decisions with triggering information from the spectrometer arms in the experiment.

Processors for the second level of triggering were not discussed in detail and can only properly be addressed after the spectrometer conceptual designs are complete. The working group felt that the trigger system should be constructed in a flexible way in order to permit acceptance of triggering information from the spectrometer arms on whatever time scale it is available and integration of this information with that from the calorimeter trigger processor. Another design goal would be to use the concept of parallel triggering, permitting many decisions to be made simultaneously, with appropriate downscaling of high rate triggers.

6. FUTURE DEVELOPMENTS

We summarize here for convenience a list of technical areas that we believe should be developed further, and as soon as possible, to optimize the detectors for the new RHIC environment. The list is partly random, but

these particular items came to the fore during our discussions:

(i) Scintillating fibre calorimeters, with radial fibres in lead or iron absorbers: construction techniques, hadronic energy resolution, dependence of e/h on packing fraction etc.

(ii) Room-temperature liquid ionization chamber calorimetry

(iii) General calorimetric studies of low energy (< 2 GeV) hadron response, non-linearities, albedo, etc.

(iv) Detectors that will operate in liquid Helium for calorimetrization of superconducting magnets

(v) High density and economic electronics

(vi) Ultra-violet detectors for RICHES, and studies of the environment under which they can be used (fluxes of photons, charged particles)

(vii) Very good 'time-of-flight' pads

(viii) High density tracking, or thin track-counting detectors.

Despite the length of this (incomplete!) list, we are convinced that at least in the field of calorimetry, existing technology could be used with success even at the highest envisaged luminosities.

ACKNOWLEDGEMENTS

We would like to thank the Workshop Organizers for a stimulating and enjoyable meeting. We also profited from discussions during the Workshop with C. Baktash, F.H. Berger, H. Crawford, A. Franz, A. Faroog, H.A. Gustafsson, J. Harris, H. Löhner, M. Maier and R. Scharenberg.

We thank Tom Taylor for his valuable contribution to magnet design, and Michelle Mazerand for much secretarial and administrative assistance.

REFERENCES

1. RHIC Workshop: Experiments for a Relativistic Heavy Ion Collider, BNL 51921; ed. by P.E. Haustein and C.L. Woody, Brookhaven (1985).

2. R. Wigmans: On the Energy Resolution of Uranium and Other Hadron Calorimeters, Nuclear Instrum. and Methods.

3. M. Albrow et al.: Performance of a Uranium/Tetramethylpentane Electromagnetic Calorimeter, CERN-EP/87-55; to be published in Nuclear Instrum. and Methods.

4. G. Barbiellini et al., Nucl. Instruments and Methods 235 (1985) 55.

5. T. Akesson et al., Detection of Jets with Calorimeters at Future Accelerators. Proceedings of the Workshop on Physics at Future Accelerators, la Thuile (1987), CERN-87-07, p. 174 and RHIC Note AD/RHIC-PH-24.

6. T. Akesson et al., Performance of the Uranium Plastic Scintillator Calorimeter for the HELIOS Experiment at CERN (CERN-EP/87-11) to be published into Nuclear Instrum. and Methods.

7. T. Akesson et al., Nuclear Instrum. and Methods A241 (1985) 17.

8. J. Engler et al., Nuclear Instrum. and Methods 223 (1984) 47.

9. UA1-Collaboration: Design report of a U-TMP Calorimeter for the UA1 experiment with ACOL, UA1 TN/86-112 (Nov. 1986).

10. A. Beer et al., Nuclear Instrum. and Methods 224 (1984) 360.

11. Proposal for an Experiment at HERA; the ZEUS Collaboration.

12. H. Burmeister et al., Nuclear Instrum. and Methods 225 (1984) 530.

13. P. Jenni et al., The High Resolution Spaghetti Hadron Calorimeter CERN-LAA proposal.

14. O. Miyamura and T. Tabuki, Z. Phys. C31 (1986) 71.

15. C.W. Fabjan and W.J. Willis, Proc. Calorimeter Workshop, Batavia May 1975 p.1 (Ed. M. Atac, Batavia, FNAL, Ill. USA).

16. M.G. Albrow et al., Nuclear Instrum. and Methods A256 (1987) 23.

17. P. Giubellino et al., Internal Helios Note.

18. A. Gavron, RHIC AD/RHIC-PH-23.

19. P. Glaessel and H.J. Specht, Electron Pair Spectroscopy for RHIC, these Proceedings.

FIGURE CAPTIONS

Fig. 1 The ratio of electromagnetic to hadronic energy response as a function of energy for different calorimeter systems:
(38% Cu, 62% U/Scint.: Ref. 7;
U/LAr; Fe/LAr: C.W. Fabjan et al., Nucl. Instrum Methods, 141 (1977) 61;
Cu/Scint: O. Botner et al., IEEE, Trans. Nucl. Sci. NS-28 (1981) 510;
Fe/Scint (1): H. Abramowicz et al., Nucl. Instr. Methods 180 (1981) 429;
Fe/Scint (2): A. Beer et al., Nucl. Instrum. Methods 224 (1984) 360.

Fig. 2 The signal ratio e/h for lead calorimeters employing different readout materials, as a function of the ratio of the thicknesses of the absorber and readout layers. For Si readout the horizontal scale should be read multiplied by ten (Ref. 2).

Fig. 3 The ratio of electron to hadron response in the 400 to 4000 MeV available energy range. The solid line represents a Monte Carlo calculation of the response, assuming that the particle looses energy

by ionization only up to the interaction point; for the remaining energy the asymptotic hadronic response with e/h = 1.11 is assumed (Ref. 7).

Fig. 4 Monte Carlo-based performance estimate of a calorimetric measurement of the invariant mass of a di-jet system. Different curves refer to different algorithms of associating the energy deposits with the impact points of particles (Ref. 5).

Fig. 5 Monte Carlo Evaluation of the influence of the calorimeter granularity on event structure measurements. The solid line represents the assumed transverse energy distribution, whereas the dashed distribution gives the reconstructed energy flow, after calorimeter analysis. The simulation assumed a calorimeter cell size of $\Delta\eta$ * $\Delta\phi$ = 0.12 * 0.12 with four longitudinal subdivisions. It is amply sufficient for resolving event structures at a scale plausible for RHIC-physics phenomena.

Fig. 6 Albedo neutron multiplicity as a function of projectile kinetic energy for three different projectiles (Ref. 18).

Fig. 7 Albedo neutron spectrum for 5 GeV pions. There is no significant variation between neutron spectra produced by other projectiles at other bombarding energies.

Fig. 8 Side and End Views of Open Axial Field Magnet with double coils, as envisaged at the Workshop. The position of possible large angle and forward calorimetry is indicated.

Fig. 9 One quadrant of the Open Multiple-coil Magnet, with the four coil currents adjusted (-7, 3.5, 0, -0.5) to give low field on the collision point, and the poles in the close position.

Fig 10. As Fig. 9 but with the poles retracted and the currents adjusted for high field integral (7,7,7,7).

Fig. 11 Component of field B_z (parallel to beams) for the Taylor magnet for three current settings in each of two pole positions.

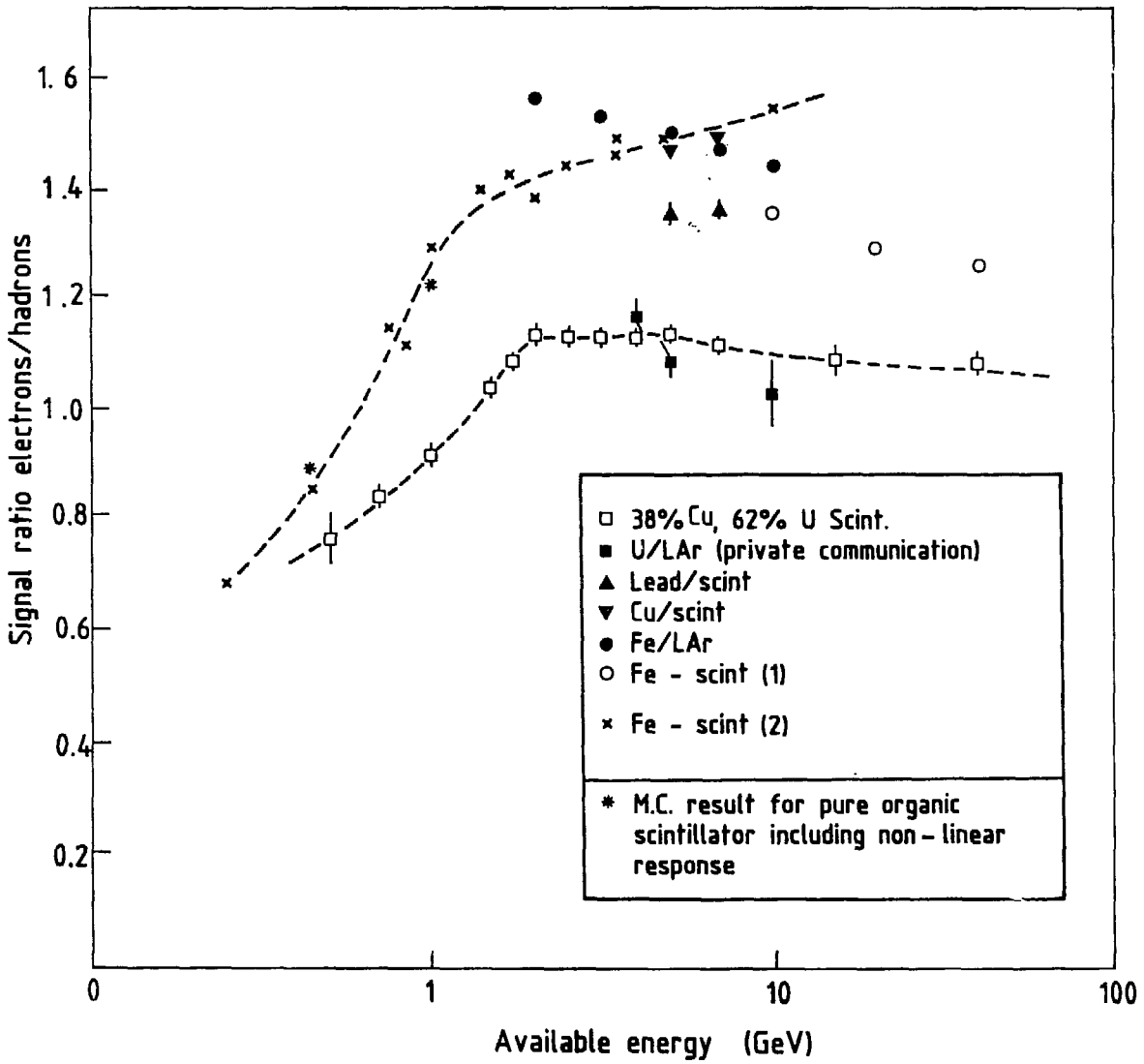
Signal ratio electrons/hadrons
1.6
1.4
1.2
1.0
0.8
0.6
0.4
0.2
0
1
10
100
Available energy (GeV)
38% Cu, 62% U Scint.
U/LAr (private communication)
Lead/scint
Cu/scint
Fe/LAr
Fe - scint (1)
Fe - scint (2)
M.C. result for pure organic scintillator including non-linear response

Fig. 1

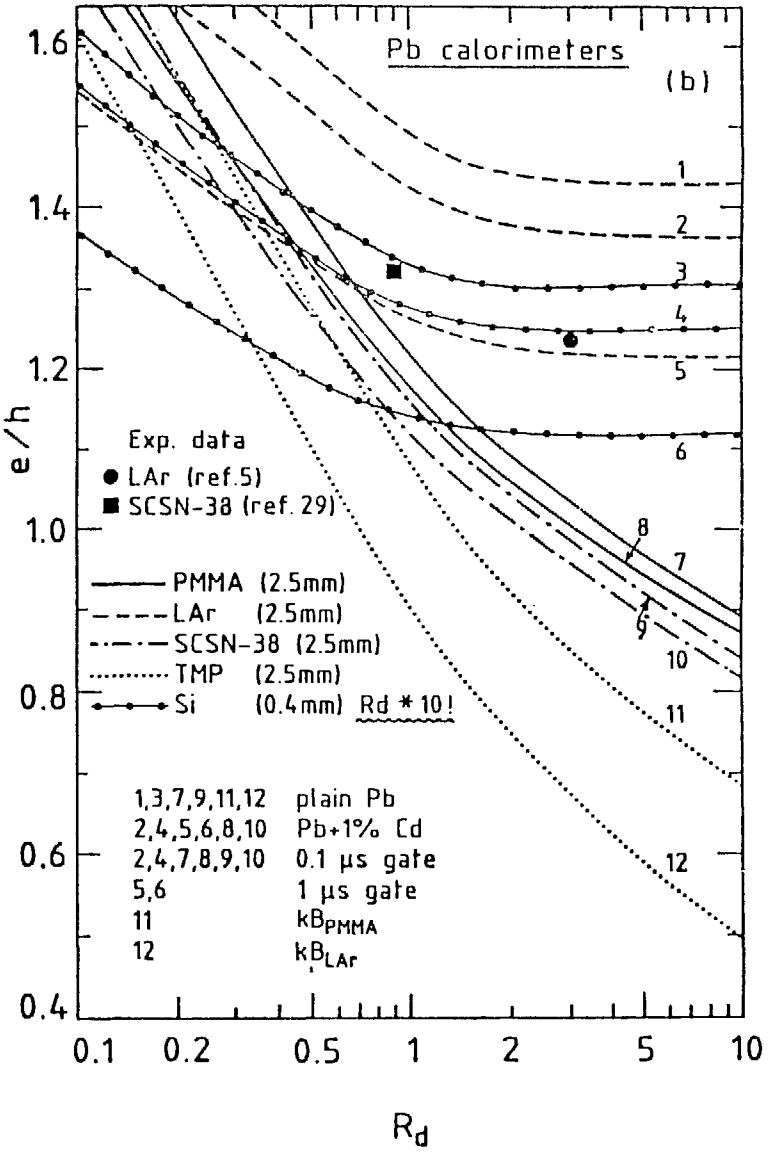
Pb calorimeters
(b)
e/h
R_d
Exp. data
LAr (ref.5)
SCSN-38 (ref. 29)
PMMA (2.5mm)
LAr (2.5mm)
SCSN-38 (2.5mm)
TMP (2.5mm)
Si (0.4mm) Rd * 10!
1,3,7,9,11,12 plain Pb
2,4,5,6,8,10 Pb+1% Cd
2,4,7,8,9,10 0.1 µs gate
5,6 1 µs gate
11 kB_{PMMA}
12 kB_{LAr}
1.6
1.4
1.2
1.0
0.8
0.6
0.4
0.1
0.2
0.5
1
2
5
10

Fig. 2

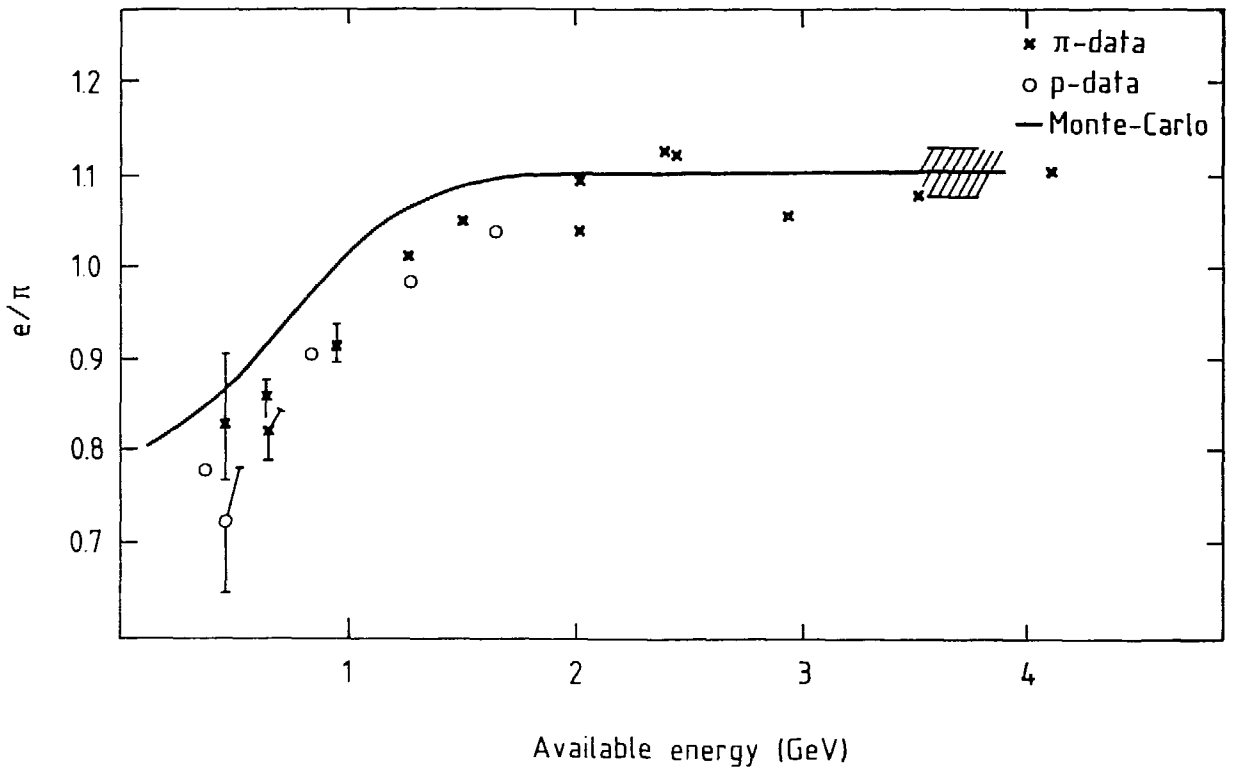
π-data
p-data
Monte-Carlo
e/π
1.2
1.1
1.0
0.9
0.8
0.7
1
2
3
4
Available energy (GeV)

Fig. 3

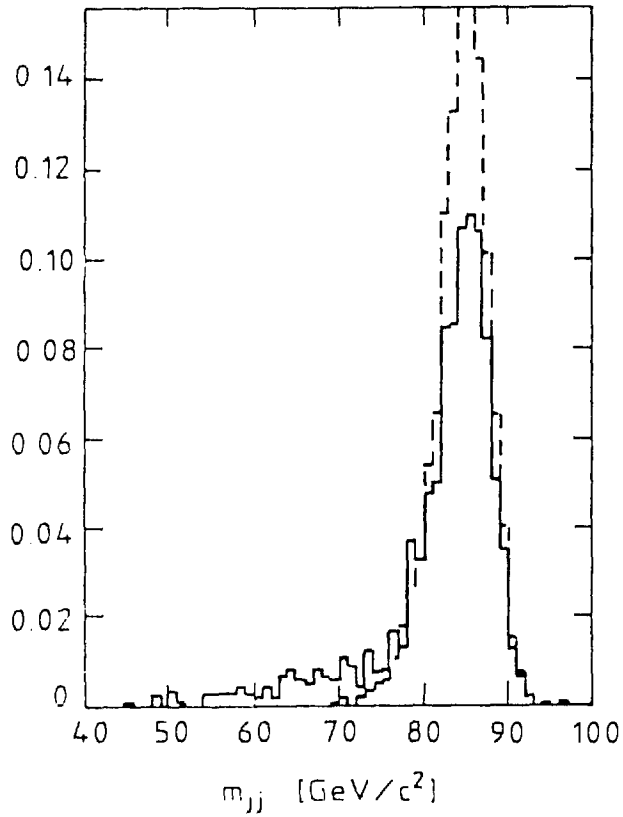
0 14
0.12
0.10
0 08
0 06
0.04
0.02
0
40
50
60
70
80
90
100
m_{jj} [GeV/c^2]

Fig. 4

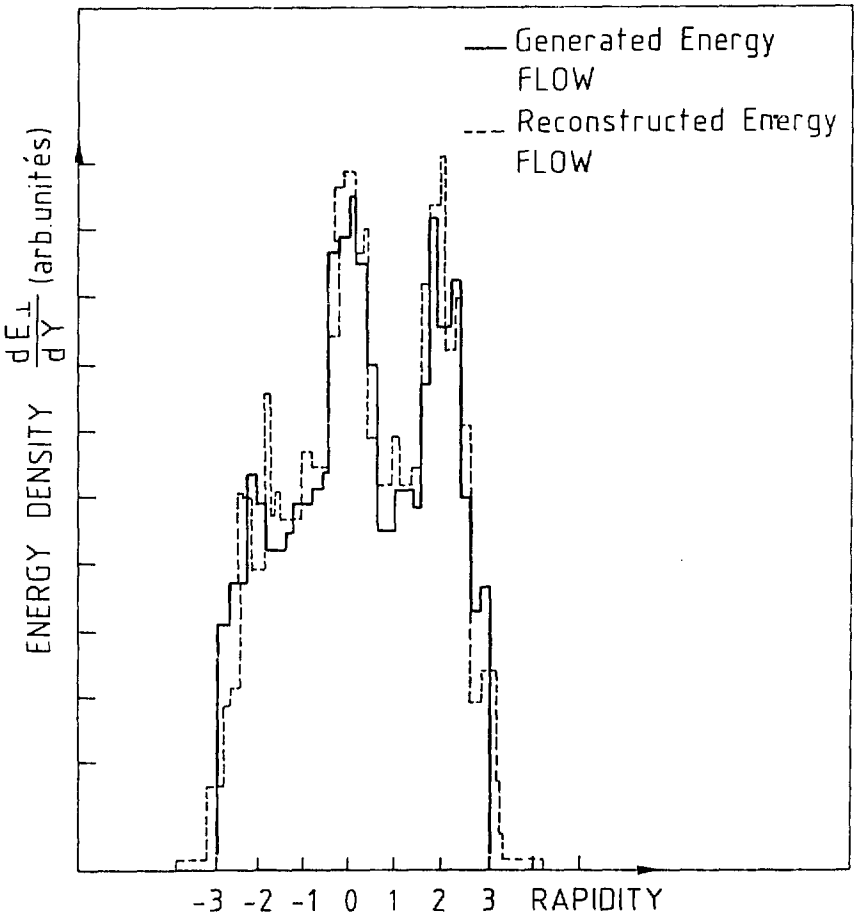
Generated Energy FLOW
Reconstructed Energy FLOW
ENERGY DENSITY $\frac{dE_\perp}{dY}$ (arb.unités)
-3 -2 -1 0 1 2 3 RAPIDITY

Fig. 5

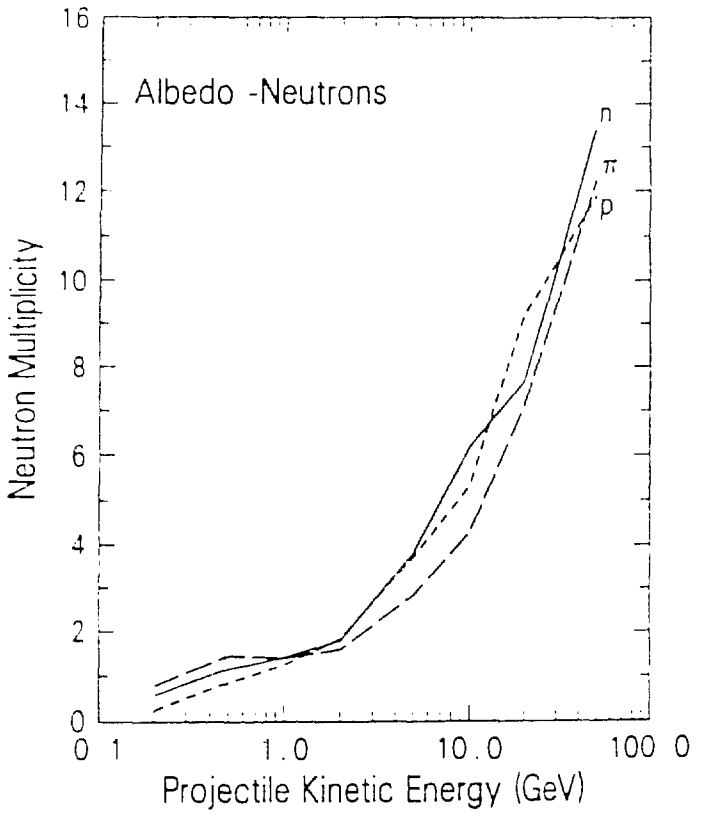
Albedo -Neutrons
Neutron Multiplicity
Projectile Kinetic Energy (GeV)
n
π
p
0
2
4
6
8
10
12
14
16
0 1
1.0
10.0
100 0

Fig. 6

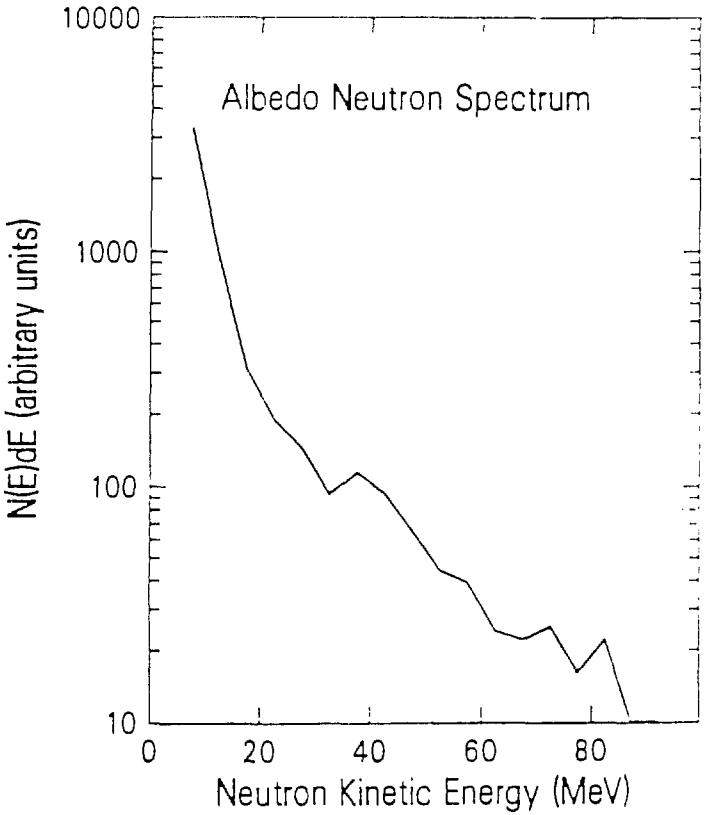
Albedo Neutron Spectrum
N(E)dE (arbitrary units)
Neutron Kinetic Energy (MeV)
10000
1000
100
10
0
20
40
60
80

Fig. 7

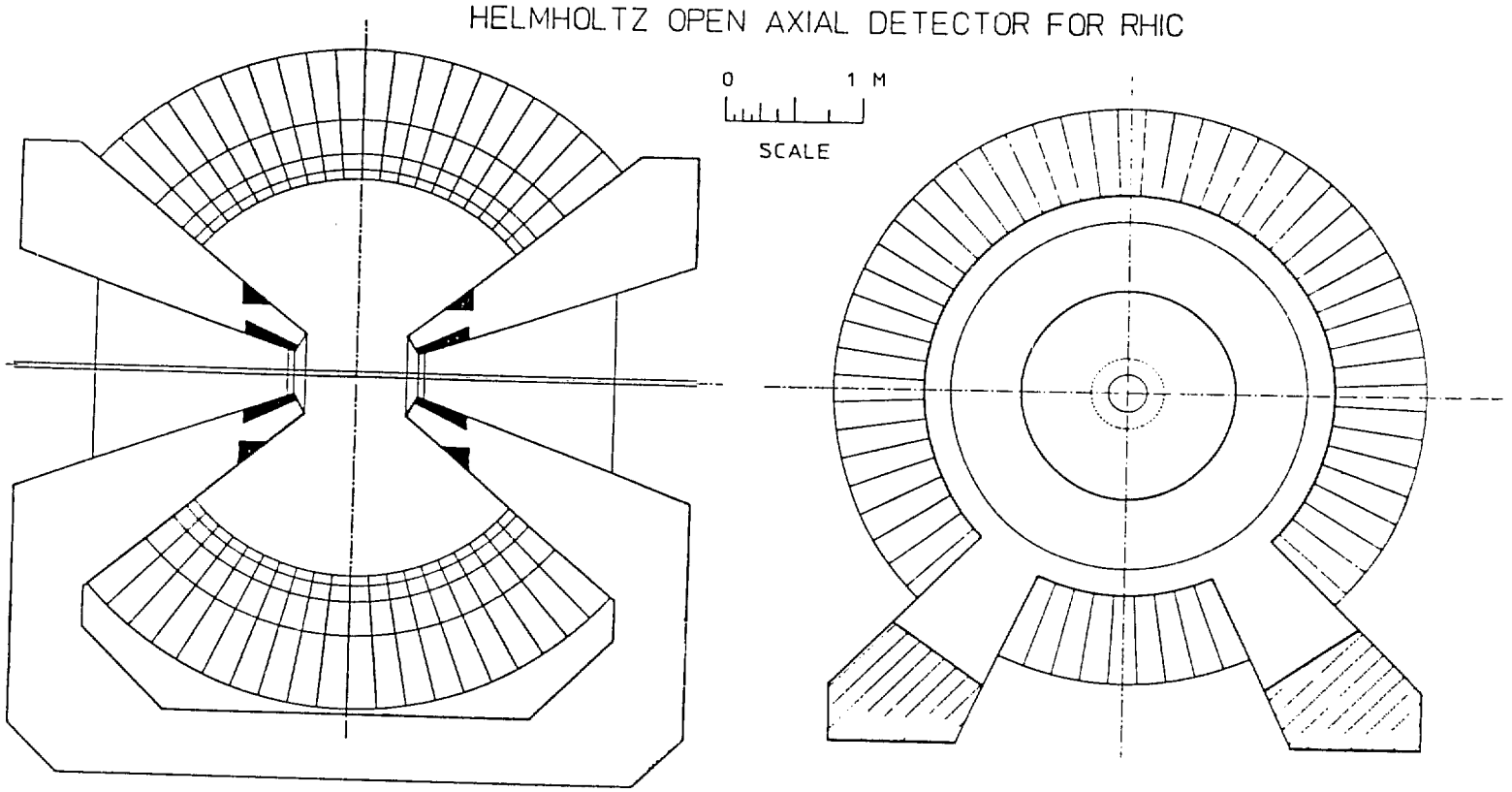

Fig. 8

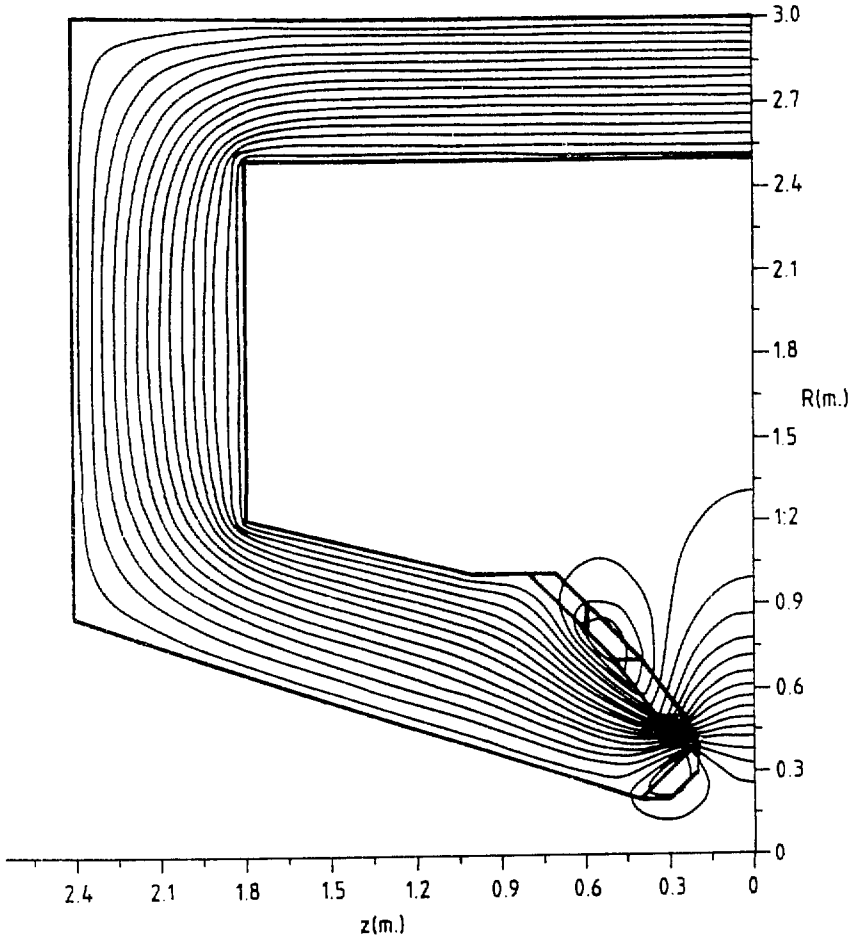
3.0
2.7
2.4
2.1
1.8
R(m.)
1.5
1.2
0.9
0.6
0.3
0
2.4
2.1
1.8
1.5
1.2
0.9
0.6
0.3
0
z(m.)

Fig. 9

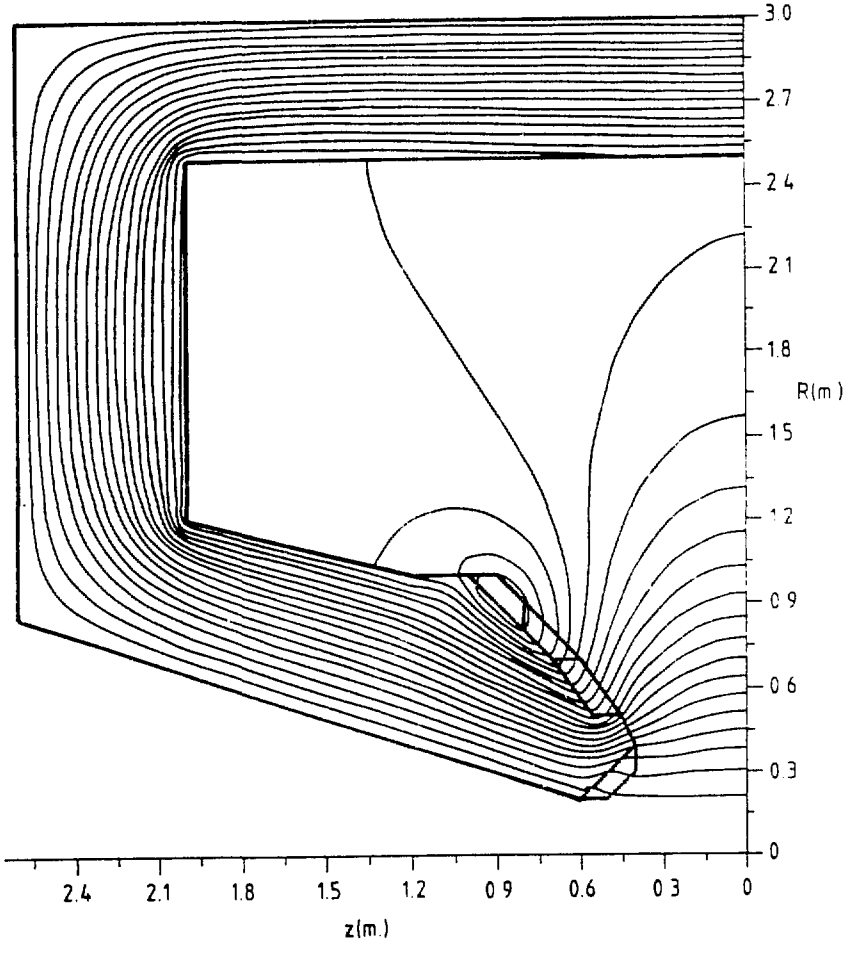
3.0
2.7
2.4
2.1
1.8
R(m.)
1.5
1.2
0.9
0.6
0.3
0
2.4
2.1
1.8
1.5
1.2
0.9
0.6
0.3
0
z(m.)

Fig. 10

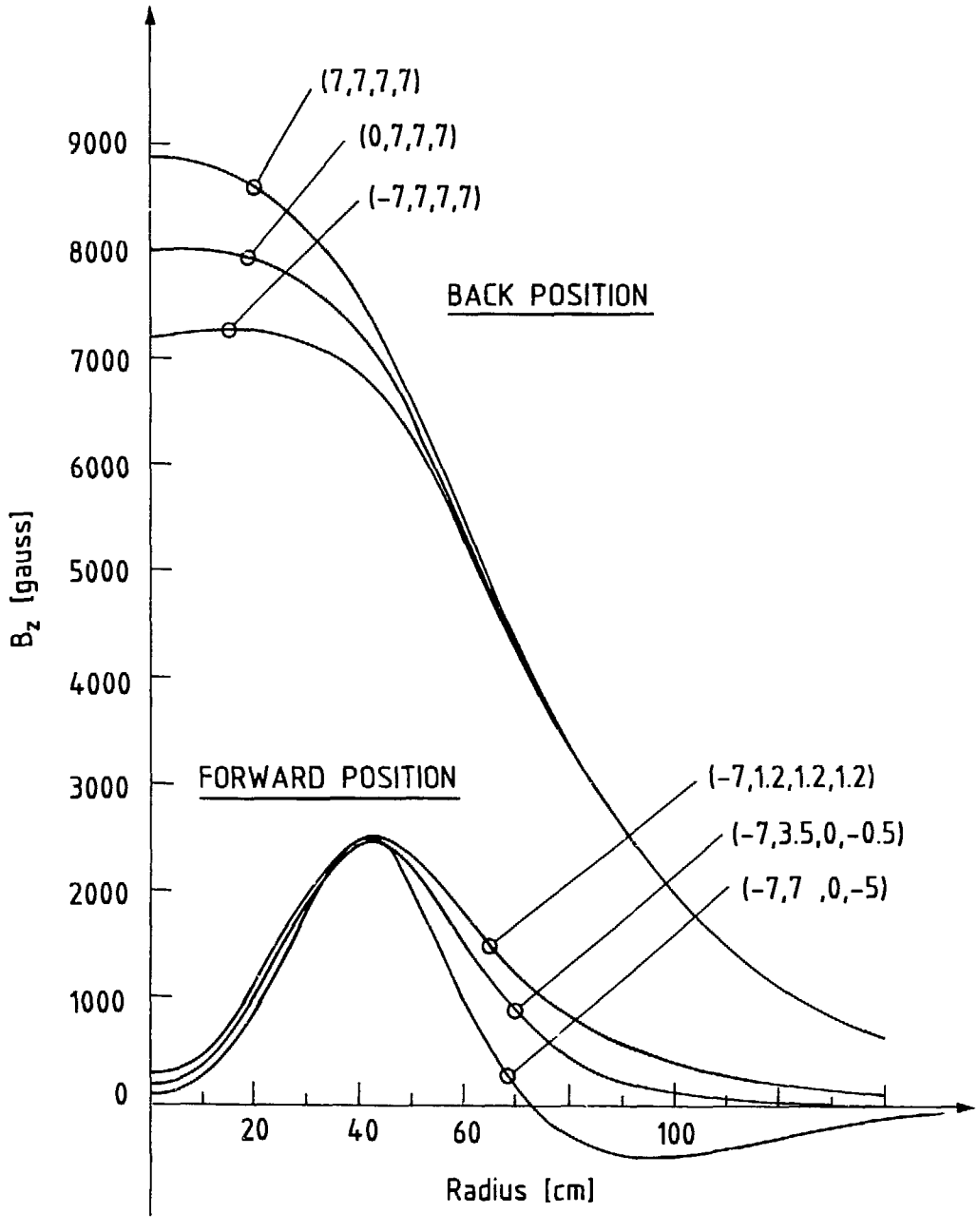
(7,7,7,7)
(0,7,7,7)
(-7,7,7,7)
BACK POSITION
FORWARD POSITION
(-7,1.2,1.2,1.2)
(-7,3.5,0,-0.5)
(-7,7 ,0,-5)
B_z [gauss]
9000
8000
7000
6000
5000
4000
3000
2000
1000
0
20
40
60
100
Radius [cm]

Fig. 11

STATUS OF THE RHIC DIMUON DETECTOR

S. Aronson* (BNL), T. Awes (ORNL),
P. Braun-Munzinger (SUNY/Stony Brook),
P. Gorodetzky (CRN Strasbourg)
E. Gross (US Dept. of Energy),
G. Landaud (Univ. Clermont-Ferrand),
T. Ludlam (BNL), M. Murtagh (BNL), A. Shor (BNL),
J. Stachel (SUNY/Stony Brook), G. Young* (ORNL)†
(* = working group co-chairmen)

1. INTRODUCTION

The Dimuon Working Group met before and during the Workshop. The goal was to build on the work reported at the 1985 RHIC Workshop [1.1] and to further develop a detector dedicated to dimuon physics at RHIC. This paper is in the nature of a status report in that the group developed more questions than answers in the course of its work. The work remaining to be done should become clear in the course of this report, and can be thought of as a job list for a serious letter of intent.

The main conclusion of the working group is that dimuon physics deserves continued serious attention; theoretical progress and new detector ideas suggest that the main goals of dimuon physics at RHIC are, if anything, more accessible than before.

In Section 2 we discuss recent theoretical input on the question of dilepton physics at RHIC. In Section 3 we present recent rate calculations in the mass regions of interest. A new estimate of physics background rates is given in Section 4, together with some thoughts on methods to deal with this background. Punch-through and decay backgrounds are reviewed in Section 5. In Section 6 we show a detector concept that is different in some respects from the one analyzed in Ref. 1.1. In Section 7 we discuss the acceptance and resolution. In Section 8 we review the interplay of the detector and machine, and present recent calculations of luminosity vs. crossing angle. Section 9 is a summary and recap of the questions that need to be addressed in detail, presumably in the course of proposing such a detector for RHIC.

---

†Work performed under auspices of US Department of Energy

2. THEORETICAL PROGRESS IN DILEPTON SIGNALS AT RHIC

We don't need to review here the role of dileptons as deep probes of relativistic nucleus-nucleus collisions. The important new thoughts on dileptons have to do with the mass spectrum of dileptons. A joint session of theorists and dilepton groups at the Workshop yielded insights which had a strong impact on our thinking about a dimuon detector:

a. The desirability of measuring dileptons in the low mass ($M < 2$ GeV) region has declined since the last Workshop. The reasons have to do with the difficulty of interpreting the data in this region. As an example, competing processes in the QGP have been identified theoretically, some of which may enhance ρ production and others of which may suppress it.

b. The mass region around the J/ψ and ψ' has become much more interesting, because the disappearance of the production of these states with the creation of the QGP looks like a very promising signal [2.1]. If this idea is right it has implications for the performance of a dilepton detector. For example, it is calculated that the suppression of the ψ' occurs before that of the J/ψ, so dilepton mass resolution sufficient to separate these states would be important. Also, onset of suppression is p_T-dependent; good dynamic range in p_T acceptance would therefore be valuable. One would like to see at least up to $p_T = 5$ GeV/c.

c. The polarization of the dilepton is a useful means of distinguishing between different dilepton production mechanisms in the mass region of interest, so good angular resolution is also a desirable feature of a RHIC dilepton detector.

The new interest in higher mass dileptons is welcome news for dimuon detectors, wherein low-momentum muons are difficult to separate from hadronic punch-through and to measure well. It should be remembered, however, that higher masses means lower rates, so the acceptance of the detector will be as important as the resolution. We can summarize the properties of the detector that is needed to do the desired dimuon physics at RHIC:

i) To have useful rate at high p_T the detector must be built for the highest foreseeable luminosities and have large solid angle coverage.

ii) To study the mass spectrum in the J/ψ region and to measure the dimuon polarization, the detector is required to have good resolution in both momentum and angle.

iii) For good acceptance over a wide range in M and p_T the detector needs coverage over a wide range in pseudorapidity; the forward angles give access to lower dimuon masses and high mass dimuons at high p_T have muons with large spread in pseudorapidity.

These considerations appear to us to point to a dedicated dimuon experiment; it is unlikely that dimuons could be done properly in a general purpose spectrometer or in combination with, say, a dielectron experiment.

3. RATE ESTIMATES FOR RESONANCE AND DRELL-YAN PRODUCTION

We estimate the production cross sections for J/ψ, ψ', and Υ resonance production as well as for Drell-Yan continuum production starting from the cross sections given in N. S. Craigie's review article [3.1] and in Matsui and Satz's discussion of J/ψ suppression [2.1]. The values we use are as follows:

a) For the J/ψ:

$$B \frac{d\sigma}{dy} = 5 \times 10^{-32} e^{-14.7M/\sqrt{s}} \text{ cm}^2 \qquad (3.1)$$

(this is a 'per nucleon' value).

b) For the ψ':

$$B \frac{d\sigma}{dy} = 1.5\% \text{ of the } J/\psi \text{ value.} \qquad (3.2)$$

c) For the Υ, we use the E288 value at $\sqrt{s}$ = 27 GeV, as quoted in Grosso-Pilcher and Shochet [3.2] of:

$$B \frac{d\sigma}{dMdy} = 7.0 \times 10^{-37} \text{ cm}^2/\text{Gev/nucleon}, \qquad (3.3)$$

where a ΔM = 1 GeV bin contains all the Υ peaks given their resolution.

We further assume that the Υ production cross section follows the same scaling with $\sqrt{s}$ as the J/ψ and Drell-Yan.

d) For Drell-Yan production, we use the value in [3.1] of

$$\frac{d\sigma}{dMdy} = 7.5 \times 10^{-32} e^{-14.7\ M/\sqrt{s}}/M^3\ \text{cm}^2/\text{GeV}. \qquad (3.4)$$

In order to scale the cross sections quoted in these references from p-p to values appropriate for nucleus-nucleus collisions, we consider two general regimes, namely impact-parameter averaged collisions and "central" collisions. We scale the cross section for production in nucleon-nucleon reactions by the following formula in order to account for impact-parameter averaging:

$$(A_1^{1/3} + A_2^{1/3})^2 \times \frac{A_1}{(1+A_1/A_2)^2} \qquad (3.5)$$

For the case of central collisions, we quote a reaction rate for central nucleus-nucleus collisions corresponding to a maximum impact parameter of b=1 fm, which is a rather restrictive definition of central collisions, as most of the nucleons in a collision are participants already at larger impact parameters.

In order to estimate the number of hard collisions in A1-A2 collisions vs those in p-p, we consider the following relations:

$$\sigma_{hard}^{A_1-A_2} = \sigma_{hard}^{p-p} \times A_1 \times A_2$$

$$\sigma_{Tot}^{A_1-A_2} = \pi \times (r_o A_1^{1/3} + r_o A_2^{1/3})^2$$

$$\sim \sigma_{Tot}^{p-p} \times (A_1^{1/3} + A_2^{1/3})^2$$

This gives as the number of hard n-n collisions in $A_1 + A_2$:

$$(\text{Mult})^{A_1 A_2}_{\text{hard}} = \frac{\sigma^{A_1 A_2}_{\text{hard}}}{\sigma^{A_1 A_2}_{\text{Tot}}} = \frac{\sigma^{p-p}_{\text{hard}} \times A_1 \times A_2}{\sigma^{p-p}_{\text{Tot}} \times (A_1^{1/3} + A_2^{1/3})^2}$$

$$= (\text{Mult})^{p-p}_{\text{hard}} \times \frac{A_1 \times A_2}{(A_1^{1/3} + A_2^{1/3})^2}$$

$$= (\text{Mult})^{p-p}_{\text{hard}} \times A^{4/3} \times \frac{1}{4} \quad (\text{for A1=A2})$$

We use this relation to scale the per nucleon cross sections quoted above to those for A1=A2 collisions.

The luminosity values are "t=2 hrs" values taken from the RHIC design report. We have decreased the values for I and Au by a factor of 1/3 and 1/9, respectively, to account for the continuing effects of intrabeam scattering in those cases and to account for the likely need to cross those beams at an angle in order to preserve a reasonably short interaction diamond length.

We quote values for runs of one "RHIC year", here taken as 3000 hours. The values quoted for resonance production are integrated over the resonance yield, while those for Drell-Yan production are for 1 GeV wide bins in pair mass. All the values quoted are for 1 unit of rapidity. Given the total rapidity gap for RHIC at top energy of around 11 units, the total yields could be one order of magnitude larger. Given improvements discussed in interaction region β^*, number of bunches in the machine, ion sources and such, it seems reasonable to expect future increases in rate by one to two more orders of magnitude.

The results are given in the following tables. Comparing the values for J/ψ and Drell-Yan production, assuming that all the J/ψ yield is within one 0.1 GeV/c^2 region in pair mass, the J/ψ yield is seen to exceed that from Drell-Yan by two orders of magnitude. It can also be seen that a study of Υ production will require the improvements to luminosity discussed above.

TABLE 3.1

A) Resonance production in "Impact-Averaged" Collisions						
Beam Species	d	C	S	Cu	I	Au
Beam mass number	2.	12.	32.	63.	127.	197.
J/ψ cross-section (cm^2)	1.3×10^{-31}	2.5×10^{-30}	1.3×10^{-29}	4.0×10^{-29}	1.3×10^{-28}	2.7×10^{-28}
Events produced/ RHIC yr/unit η						
J/ψ	1.3×10^{7}	1.2×10^{7}	5.4×10^{6}	7.7×10^{6}	1.5×10^{6}	2.9×10^{5}
ψ'	2.0×10^{5}	1.9×10^{5}	8.1×10^{4}	1.2×10^{5}	2.3×10^{4}	4.4×10^{3}
Υ	2.5×10^{4}	2.4×10^{4}	1.9×10^{4}	1.5×10^{4}	2.9×10^{3}	5.7×10^{2}

TABLE 3.1 (cont'd.)

B) Resonance production in "Central" Collisions						
Beam Species	d	C	S	Cu	I	Au
A_{beam}	2	12	32	63	127	197
J/ψ cross-section (cm^2)	1.6×10^{-31}	5.7×10^{-30}	4.1×10^{-29}	1.6×10^{-28}	6.4×10^{-28}	1.6×10^{-27}
Events produced/ RHIC yr/unit η						
J/ψ	2.6×10^{6}	1.4×10^{6}	4.3×10^{5}	4.9×10^{5}	7.6×10^{4}	1.3×10^{4}
ψ'	3.9×10^{4}	2.0×10^{4}	6.4×10^{3}	7.3×10^{3}	1.1×10^{3}	1.9×10^{2}
Υ	5×10^{3}	2.6×10^{3}	8.3×10^{2}	9.4×10^{2}	1.4×10^{2}	2.4×10^{1}

TABLE 3.1 (cont'd.)

C) Drell-Yan production in "Central" Collisions						
Beam Species	d	C	S	Cu	I	Au
A_{beam}	2	12	32	63	127	197
Events produced/ RHIC yr/unit η/ GeV in mass						
M_{D-Y}(GeV)						
2	8.4×10^{5}	4.4×10^{5}	1.4×10^{5}	1.6×10^{5}	2.5×10^{4}	4100
3	2.3×10^{5}	1.2×10^{5}	3.8×10^{4}	4.3×10^{4}	6700	1100
4	9.0×10^{4}	4.8×10^{4}	1.5×10^{4}	1.7×10^{4}	2600	440
5	4.3×10^{4}	2.3×10^{4}	7100	8100	1300	210
6	2.3×10^{4}	1.2×10^{4}	3800	4300	680	110
7	1.4×10^{4}	7100	2200	2500	400	70
8	8400	4400	1400	1600	250	40
9	5500	2900	910	1000	160	30
10	3700	2000	610	700	110	20

4. BACKGROUND IN THE DIMUON CHANNEL FROM KNOWN PHYSICS PROCESSES

We identify the main source of background in the dimuon signal coming from real muons to be from the decay of charmed hadrons produced in the collision. This was studied for Au + Au collisions at 200 GeV/A. A calcu-

lation was performed incorporating HIJET for the systematics of nucleus-nucleus collisons, ISAJET for computing the cross-section and hadron spectrum for charm production, and a Monte Carlo code combining these results and generating dimuon pairs from the charmed hadron decay products. The details of the calculation are presented elsewhere in these Proceedings [4.1] and are merely summarized here.

One finds a multiplicity distribution of charmed hadrons which has an approximately Poisson shape with a mean of 3.3 charmed hadrons per central Au + Au collision at top RHIC energies. One muon or more, resulting from the decay of charmed particles, are present in 25% of collisions; 5% have two or more muons. The dimuon mass distribution resulting from random combinations of these muons is shown in Fig. 4.1, together with theoretical calculations of various sources of dimuons.

It is clear that this is a potent source of background in the interesting region $M_{\mu\mu} > 2$ GeV. However there are several handles on this source and further analysis will no doubt improve our ability to discriminate against this background: On an event-by-event basis a cut on the polarization of the lepton pair is a powerful cut, since the high-mass part of the background comes from pairs of uncorrelated muons in opposite hemispheres $|\cos\theta| \sim 1$ while the signal is isotropic. On a statistical basis the subtraction of like-sign muon pairs is also a powerful cut.

5. BACKGROUND FROM HADRONIC DECAY AND PUNCH-THROUGH

A simple Monte Carlo program for following muons from pion and kaon decay and punch-through was described in Ref. 1.1. We have carried this study a few steps further, as follows. In Ref. 1.1 the probability that a hadron of given production angle and momentum would survive as at least one charged track at the back of the absorber was calculated with the Monte Carlo program. This probability was combined with the HIJET-calculated [5.1] spectrum of charged hadrons in central heavy ion collisions. The result was a crude estimate of the raw fake-muon rate.

Here we have used the Monte Carlo with about 17,000 HIJET pions and kaons on a track-by-track basis; each is followed through the absorber, the

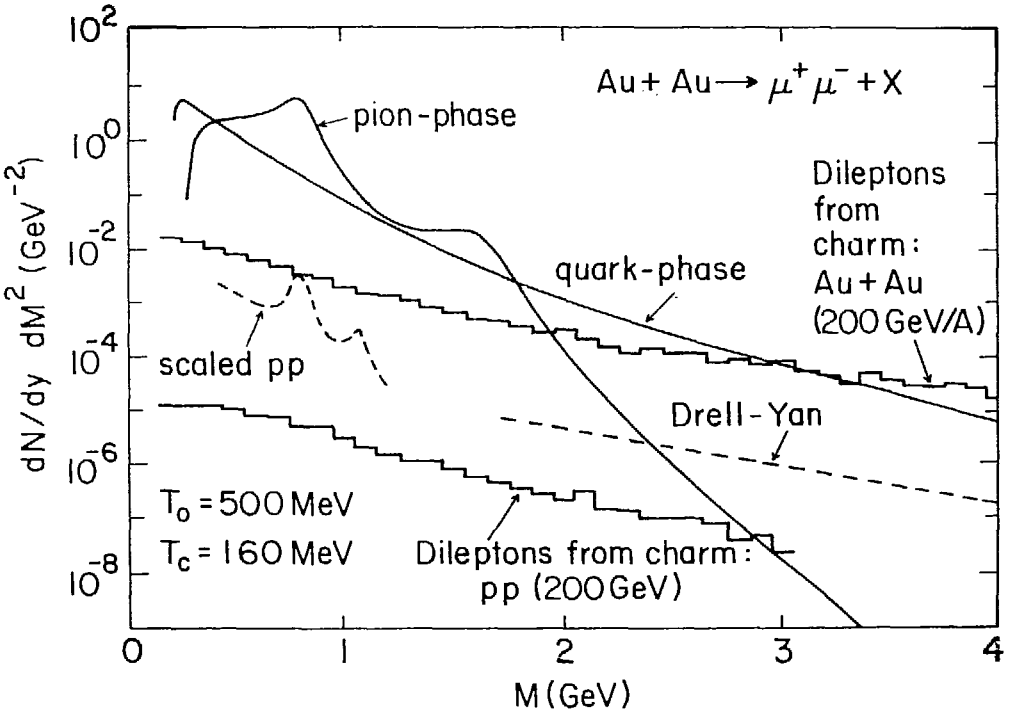

Fig. 4.1 Dimuon mass spectra from various sources, including the background arising from random pairs of muons from charm decay.

dimensio · of which are shown in Fig.5.1. The resulting raw fake-muon rates are displayed in Table 5.1 as a function of pseudo-rapidity. It is seen that for the 5-7 interaction-length absorber the dominant source of fake-muons is from interacting punch-throughs and that these in turn are concentrated forward.

TABLE 5.1. Probabilities for hadrons to contribute to the raw fake-muon rate. "Detected" = survived to the back of the calorimeter/absorber.

Pseudo-rapidity Interval	$0< \eta <1$	$1< \eta <2$	$2< \eta <3$	$3< \eta <4$
Fraction Ranged Out	0.421	0.187	0.049	0.010
Muon decays	0.022	0.021	0.015	0.010
"Detected " Muon Decays	0.000	0.000	0.001	0.003
Interacting Hadrons	0.557	0.792	0.935	0.980
"Detected" Interacting Hadrons	0.002	0.002	0.011	0.066
"Detected" Non-interacting Hadr.	0.000	0.000	0.000	0.001
All "Detected"	0.002	0.002	0.012	0.070

The next step is to take these fake-muon counts and determine what fraction appear to come from the vertex. The vertex can be seen with real muons to the limit of multiple scattering in the absorber, while charged tracks from a hadronic interaction straggling out of the absorber can be expected to have a much broader angular distribution. We have begun to study the tails of such showers with GEANT. Comparing 10 GeV pions and muons passing through 7 absorption lengths we find that a 10 cm cut on vertex reconstruction loses about 1% of muons while reducing the muon candidates from

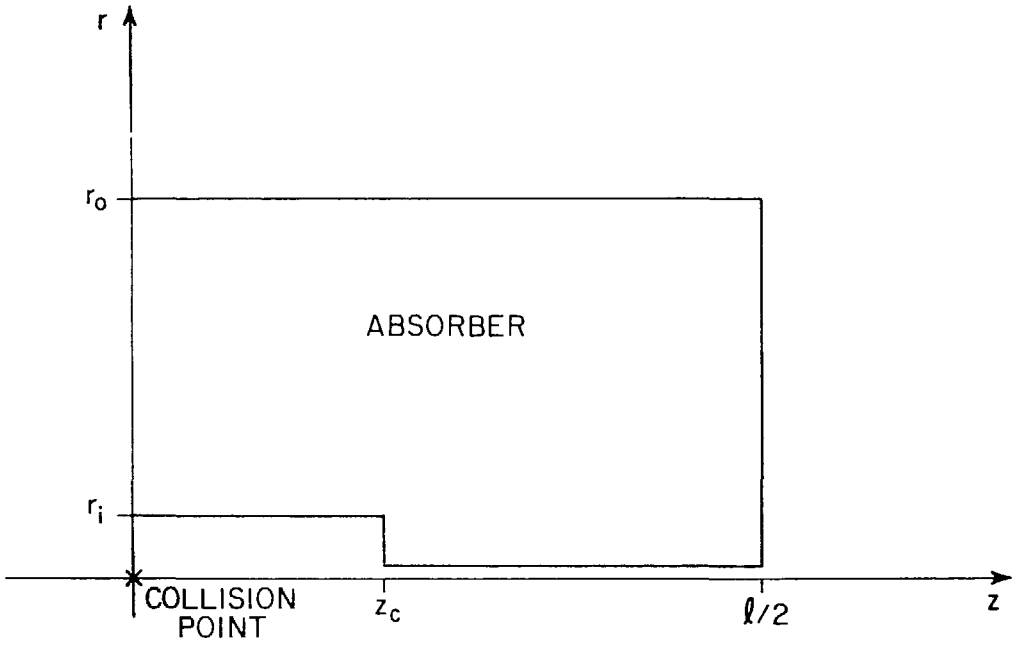

Fig. 5.1 Schematic cross-section of the absorber geometry used in the calculation of muon background from hadronic punch-through and decay.

punch-through by a factor 12. Applying this factor to punch-throughs with $\eta > 2$ in the Table we find that these are reduced to the same level as the decays. Applying the vertex cut to all punch-throughs, summing all sources of fake-muons, and multiplying by a typical charged hadron multiplicity for central Au + Au HIJET events at $\sqrt{s}$ = 200 Gev yields:

TABLE 5.2

Pseudo-rapidity Interval	Muon candidates/event
0 - 1.	< 0.3
1.- 2.	< 0.3
2.- 3.	3
3.- 4.	9

The entries in Table 5.2 represent an upper limit on the number of fake-muon candidates per event, since no cuts have been applied other than pointing back to the vertex with punch-throughs. That cut would also reduce somewhat the decay muons, which are about half the candidates in Table 5.2. Other cuts on event toplogy (e.g. accompanying soft tracks from the tail of the shower for punch-throughs) would reduce the background candidates further. There is clearly much more to be done with the output of GEANT; we are at the same stage with GEANT output that the 1985 working group was with HIJET and Monte Carlo output.

A preliminary look at the dimuon mass spectrum due to the fakes is encouraging from the point of view of our region of physics interest. Since most of the fakes are forward, the mass of random pairs of fakes is either quite low (< 1 GeV) for pairs in the same hemisphere or very high (> 5 GeV) for pairs in opposite directions. We have not looked at enough statistics to see a measurable background in the 2 - 4 GeV mass range.

6. THE RHIC DIMUON DETECTOR CONCEPT

A side view of one quarter of our current design concept is shown in Fig. 6.1. Fig. 6.2 shows the detector end-on at the beam crossing point. The features of this design are discussed briefly below; some aspects are presented in more detail in the Appendices.

A. First-Level Trigger System: Scintillation counters at small angles forward and backward signal a beam-beam interaction which is likely to be a central collision. Appendix A discusses the segmentation, rates and efficiency of this trigger system.

B. The Vertex Detector: Surrounding the interaction region is a small chamber system whose functions are to measure the charged multiplicity of events and to locate the vertex precisely. The vertex detector is composed of two layers of MWPC chambers with pad readout [6.1] to give two-dimensional information on tracks. The details are provided in Appendix B.

C. Calorimeter/Absorber: Behind the vertex detector is an active absorber whose function is to absorb and measure the energy distribution of particles other than muons and neutrinos. The design shown is 5 absorption lengths deep at $\eta = 0$, increasing to over 7 absorption lengths in the forward/backward directions. Its inner surface is 20 cm from the interaction point at $\eta = 0$, increasing to 80 cm at the ends. These distances represent a compromise between reduction of decays in flight and the space requirements of the vertex detector. It is known from studies for LHC and RHIC calorimeter experiments [6.2] that quite good calorimetry can be done with such a compact arrangement. It remains to be seen how much segmentation is required for dimuon physics. Just as with multiplicity distributions, energy flow distributions are presumed to be important signals of new physics and this detector needs to be able to see these distributions in conjuction with dimuons. The calorimeter/absorber described in the 1985 Workshop had about 4,000 channels read out. It might be prudent to design the device with a higher degree of segmentation and to instrument it electronically only in stages.

The forward region has a lower-Z absorber, as in Ref. 1.1, to reduce multiple scattering of the muons. The version sketched in Fig. 6.1 assumes

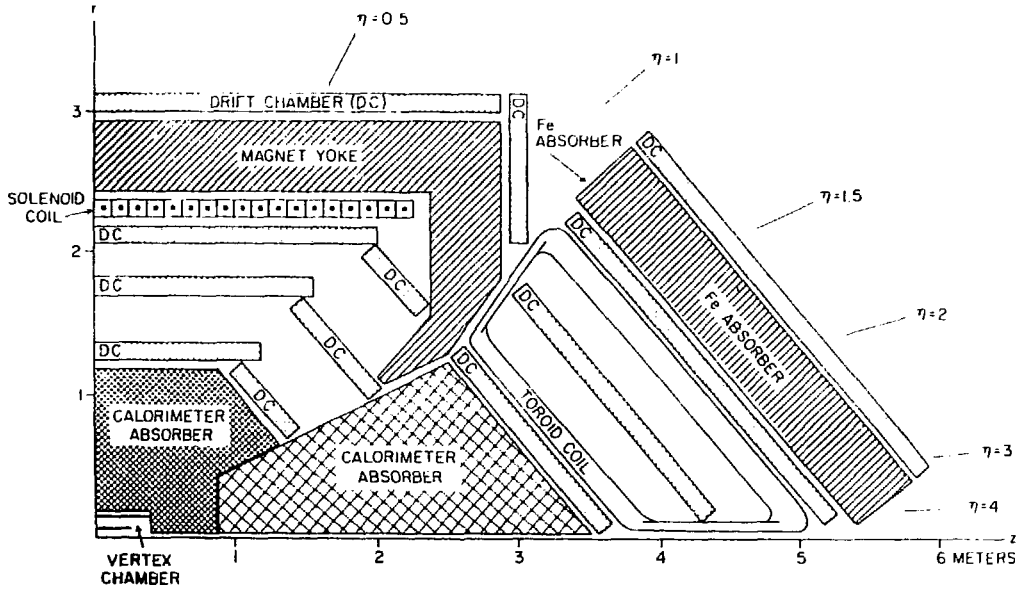

Fig. 6.1 Cross-sectional view of one quarter of the conceptual design of the dimuon spectrometer.

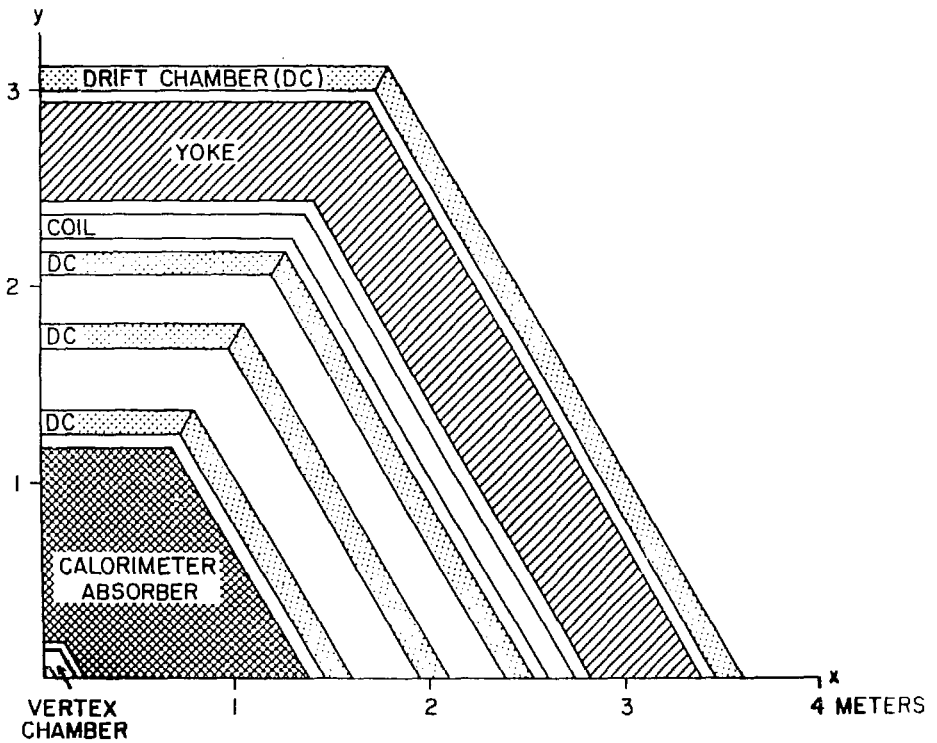

Fig. 6.2 "Beam's-eye view" of the conceptual design of the dimuon spectrometer.

that the forward absorber has 50 cm/int. length, compared with 20 cm in the central region. However the first 2.5 interaction lengths are made using the denser central absorber to reduce decays in flight, as is done in fixed-target dimuon detectors [6.3]. The ratio of central and forward absorption lengths, the amount of dense absorber in the front of the forward calorimeter/absorber, etc. are parameters which eventually need to be optimized more carefully than was done here.

D. Muon Chamber System: The biggest departure of the present concept with respect to that presented in Ref. 1.1 is the use of a solenoidal field with tracking in air (rather than iron toroids) in the central region. The intent is to achieve better muon momentum (and dimuon mass) resolution. The design sketched in Fig. 6.1 has a tracking volume with $BL^2 = 0.5$ T-m^2 and a transverse momentum resolution

$$\frac{\delta p_T}{p_T} = 1.6\times10^{-5} p_T$$

where p_T is in MeV/c. This assumes the sagitta of tracks is measured to a precision of 300 microns. For $p_T = 1500$ MeV/c, $\delta p_T/p_T = 2.4\%$; this is to be compared with about 18% in the iron toroid case, where momentum resolution is multiple-scattering limited.

The calorimeter/absorber is also immersed in the 0.5 T field; charged tracks with $p_T < 100$ MeV/c remain in the absorber until they either interact or range out. The return yoke of the solenoid acts as a final "muon filter;" additional tracking behind it serves as another signature for muon candidates. It can be used to suppress further the hadron punch-through background, at the expense of raising the muon p_T threshhold by another 600 MeV/c or so. (The 5 absorption length calorimeter/absorber ranges out muons below about 1 GeV/c.)

In the forward direction ($\eta > 1.5$) we retained the "lampshade" aircore toroid spectrometer of the 1985 version. There is iron behind it and more tracking to serve as a muon tag as with the central yoke.

The mass resolution with the present system is discussed in Section 7 below.

7. DETECTOR RESOLUTION AND ACCEPTANCE

The results presented in this section on dimuon acceptance and mass resolution are derived from a Monte Carlo study using the event generator described in Appendix C.

A. Mass Resolution Estimates

We have estimated the mass resolution for the proposed spectrometer for muon pairs of invariant mass between 250 MeV/c^2 and 10 GeV/c^2. The calculations were extended to much larger masses than previously, due to the new interest in the behavior of the massive vector mesons, particularly the J/ψ, ψ' and the Υ resonances. In order to focus the presentation here, we present results for pairs with no transverse momentum and for the case where the pair decays into two muons traveling at 90° to the beam axis. This will give the resolution trends for much of the decay phase space. It is helpful in identifying specific problem areas in spectrometer response, such as:

1) cutoff near $\eta = 0$ rapidity due to ranging out of the muons in the absorber, which was a deficiency in the 1985 design for the case of the J/ψ;

2) multiple scattering contributions at forward angles, which dominate the resolution at, e.g., $\eta = 3$ up to $M_{\mu\mu} = 4$ GeV/c^2;

3) momentum resolution at forward angles for large mass pairs, where there will be a premium on chamber resolution due to the modest BL^2 obtained with the air-core toroid magnet.

We have assumed that the central absorber is cylindrical for these calculations, with a radius of 5 absorption lengths and a half-height of 10 absorption lengths. The absorber is taken to be made of copper with liquid-argon readout. The solenoidal region at mid-rapidity is taken to have a magnetic field of 0.5 Tesla and an open region extending 1 meter radially. The forward air-core toroid is taken to have a magnetic field of $B(r) = 0.25$ Tesla/r, where r is in meters, and to extend for 2 meters along the beam axis. By replacing the downstream parts of the forward absorber with lower Z material, as suggested above, the effects due to multiple scattering can be lessened at forward angles.

The mass resolution is shown as a function of rapidity of the pair in Fig. 7.1. Three curves are given, corresponding to the ρ, J/ψ and Υ masses. The decay muons from the ρ are ranged out in the central region. A break appears in the resolution at the transition from the solenoidal to the toroidal spectrometers. This is largely due to the change in absorber thickness and the resulting jump in multiple scattering. The curves in Fig. 7.1 assume chambers with a position resolution of 300 microns. Because the resolution for the Υ is dominated by the momentum resolution, a similar curve as that in Fig. 7.1 is shown in Fig. 7.2, but this time for chambers having a resolution of 150 microns. This is seen to give similar results for the J/ψ and Υ resonances. In both cases, the ρ resolution is dominated by the severe effects of multiple scattering. The resolution for the J/ψ and Υ is quite encouraging, indicating that the higher mass members of the families can be seen, if counting statistics permit.

The general trend of the mass resolution with pair mass can be seen in Fig. 7.3, plotted for pair masses from 0.5 GeV/c^2 to 10 GeV/c^2. Lower mass pairs result in muons that range out everywhere. Curves are given for pair rapidities of 1,2, and 3. For a rapidity of one, only pairs with mass above 2 GeV/c^2 are seen. Due to effects of multiple scattering, the resolution is somewhat worse for pairs of rapidity 2 than for those with rapidity 3 up to around the J/ψ resonance. Above that point, the situation is slightly worse for larger rapidity due to the increasing fractional contribution of the momentum resolution.

The contribution to the resolution from the momentum and angular resolution terms can be seen in Figs. 7.4 and 7.5. The percent contributions to the total resolution are given as a function of pair rapidity for the ρ, J/ψ and Υ resonances in Fig. 7.4. Fig. 7.5 is a plot of the percent contributions as a function of pair mass for pairs with rapidity 3. It can be seen there that the momentum term begins to dominate at pair masses of 4.3 GeV/c^2 and above. For larger rapidities, the momentum term dominates for lower pair masses, and vice versa.

The values presented here must be understood as being lower limits to the resolution. We have not included contributions due to chamber misalignment, magnetic field inhomogeneity, crossing diamond size (and therefore production

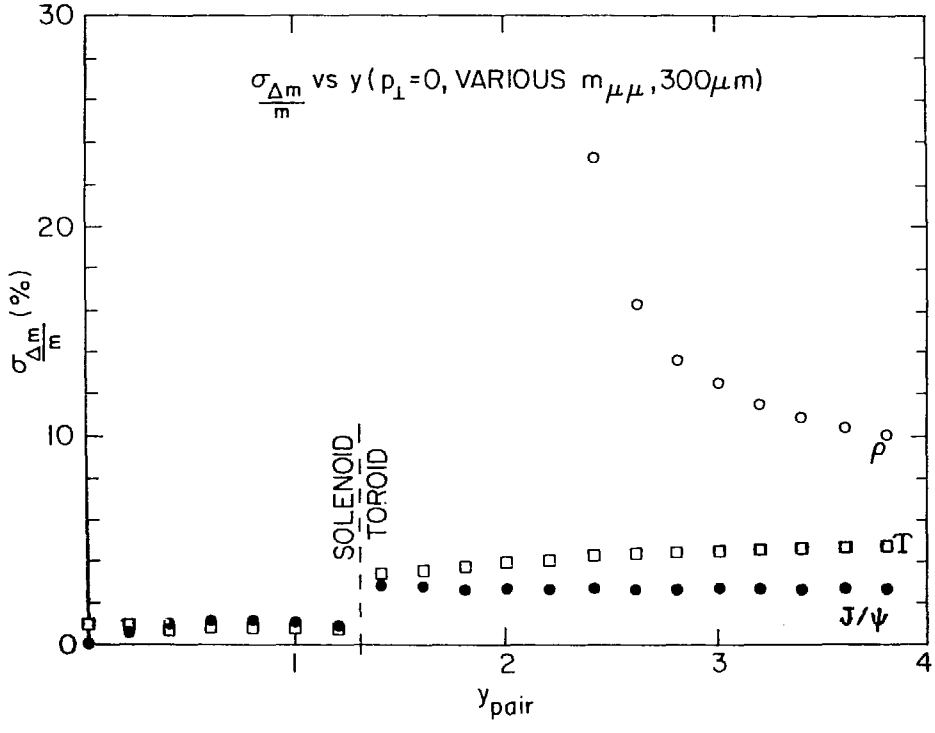

Fig. 7.1 Dimuon mass resolution as a function of the rapidity of the pair.

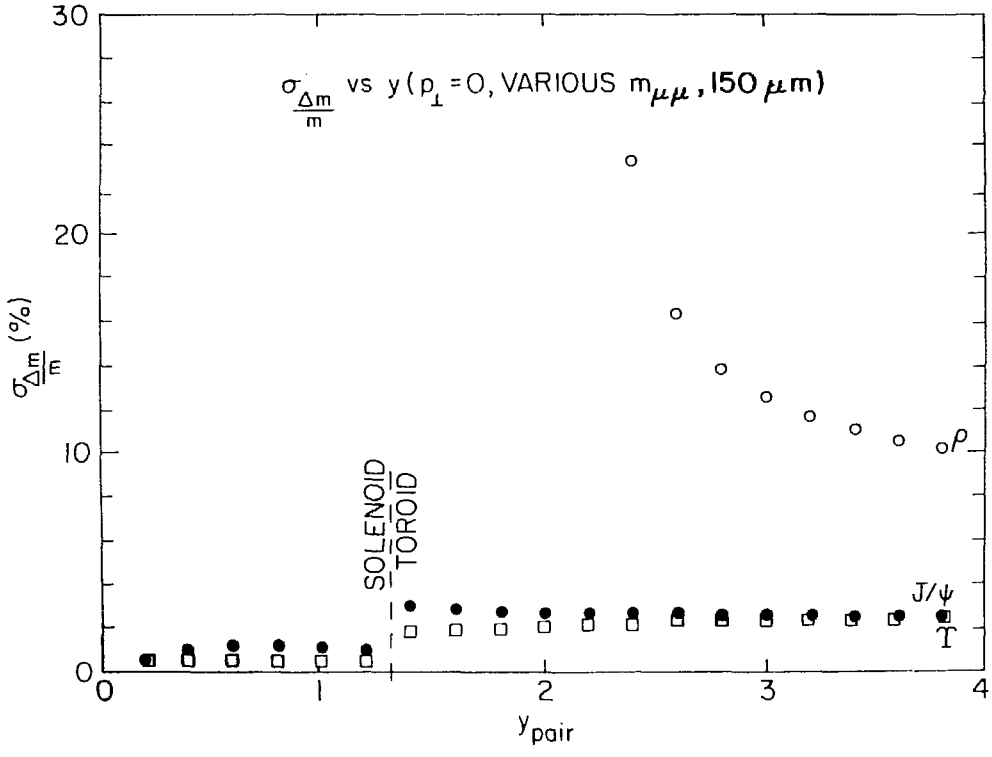

Fig. 7.2 Dimuon mass resolution as a function of the rapidity of the pair, with improved chamber position resolution.

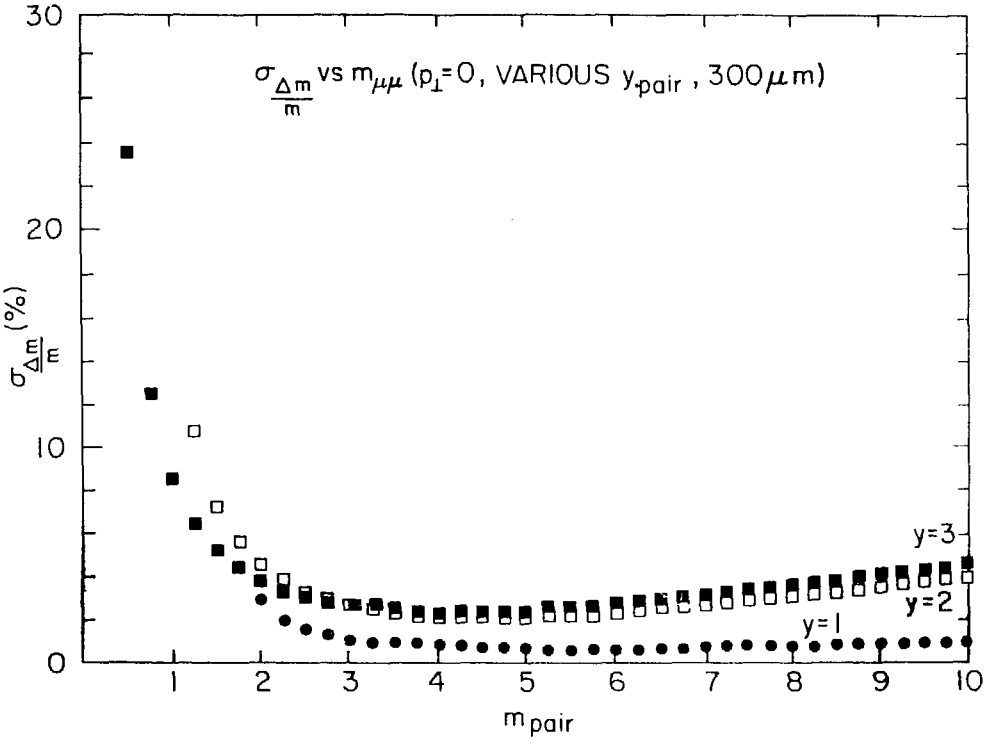

Fig. 7.3 Dimuon mass resolution as a function of the invariant mass of the pair.

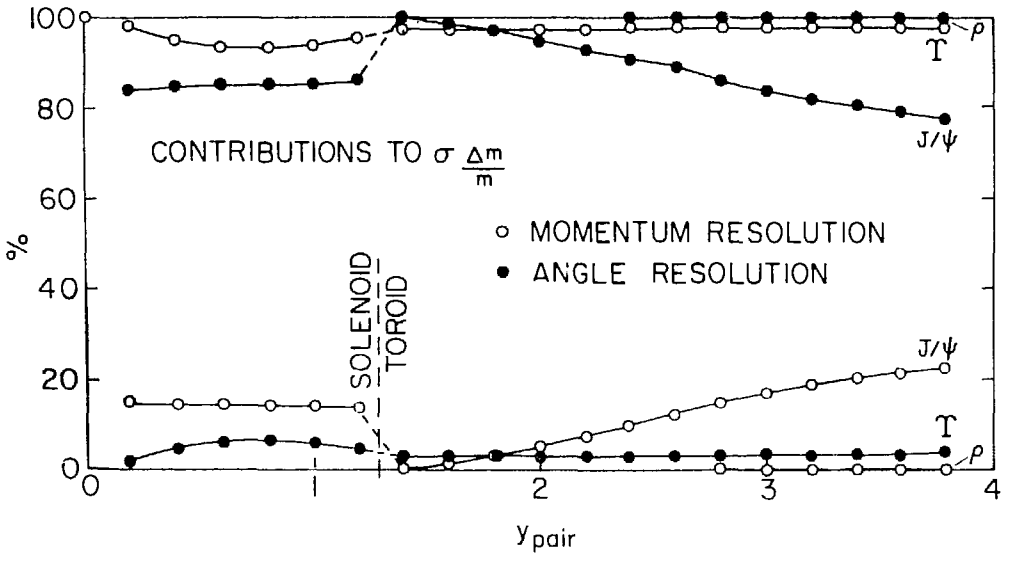

Fig. 7.4 Contributions to the mass resolution at the resonances as a function of the rapidity of the pair.

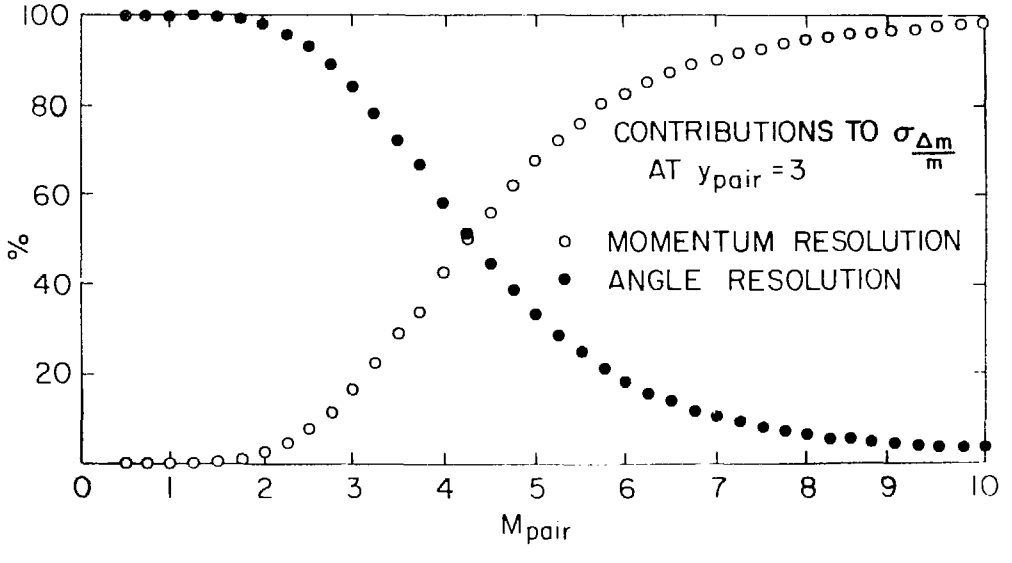

Fig. 7.5 Contributions to the mass resolution at high rapidity as a function of the invariant mass of the pair.

angle uncertainty), or energy-loss straggling. These contributions all worsen the resolution, though rough estimates indicate their effects should not be severe. The next obvious step is a full simulation of these effects as well as inclusion of the full kinematic decay phase space.

B. Diumon Acceptance of the Detector

Some preliminary studies of the acceptance of the spectrometer have been made. The spectrometer studied for acceptance had the following geometry.

One air-core toroid was located upstream and one was located downstream of the interaction diamond. They covered polar angles (using the beams to define the z-axis) from 2 to 30 degrees and 150 to 178°.

Coil windings and beam pipe were assumed to cover the region of $\theta < 2^\circ$ and $\theta > 178^\circ$. The coils for the toroids had hexagonal symmetry. The coils subtended 8°out of the 60°in ϕ in each sextant. The return yoke for the central solenoid was taken to cover the polar range from 30-33° and 147-150°. Particles striking any part of the coils or yoke were assumed to be lost. The central absorber was taken as a right-circular cylinder with its long axis along the z-axis. Its radius was taken to be 5 interaction lengths and its half length was taken to be 8.66 interaction lengths, giving a polar angle for the 'corner' of 30°. It was assumed to be made of copper with liquid argon/G-10 circuit board for readout.

Muons resulting from the decay of virtual photons were allowed to lose energy in the central absorber and were then tagged by where they entered the magnetic field region. Losses due to particles leaving the magnetic field region are not yet included. The muons were required to exit the central absorber with at least 200 MeV kinetic energy, so that they could penetrate a further absorber of one interaction length of iron before striking the trigger hodoscopes. A number of short studies of the acceptance were made by following the paths taken by the muons resulting from decay of virtual photons with given invariant mass, transverse momentum and rapidity. A calculation was also made of the observed spectrum of muon pairs for an input spectrum

calculated following the prescription of Kajantie, et. al. [7.1], using the event generator described in Appendix C.

Results of a study of the overall losses due to geometric constraints (coil locations, etc.) are given in Table 7.1a, which shows the number of accepted pairs, per thousand incident, as a function of rapidity and transverse momentum, for a pair mass of 3 GeV/c^2. Rapidities of $-5 < y < 5$ and transverse momenta $p_T < 6$ GeV/c were considered. At this stage, the energy loss in the central absorber is ignored. That the acceptance is zero for rapidities of 4.5 and 5 is expected given the inner coil edge at a polar angle of 2° ($y = 4$).

In general, the forward and rear coils cause a loss of 12-24% of the pairs at $1.5 \leq y \leq 3.5$ and all p_T, the solenoid yokes cause a loss of around 10% at $1 \leq y \leq 1.5$. A few percent of the pairs are lost by each member hitting a different obstruction. The inner holes cause the most loss (>50%) for $y > 5$. As expected, the solid angle lost due to the toroid coil leads to the largest acceptance loss. Optimization of the coil geometry is clearly required in a final design.

The effect of removing the 'back' toroid is seen in Table 7.1b, and the effect of also removing the part of the solenoid corresponding to $\theta > 90^\circ$ is shown in Table 7.1c. These two tables give the same values as 7.1a, with the aforementioned change in geometry.

The effect of including the energy loss in the central absorber is given in Tables 7.2a thru 7.2c. In these tables the number of accepted pairs per thousand incident is given as a function of y and p_T, now only for $y \geq 0.0$ and for $0 \leq p_T \leq 6.0$, on a somewhat finer grid than before. Results are given for a pair invariant mass of 1,3, and 10 GeV/c^2 in Tables 7.2a, b, and c, respectively. The region at low y and p_T where all pairs have at least one member range out is clearly seen.

The above results are shown in a different form in Tables 7.3a through 7.3c. In that case the rapidity of the pair is held fixed at $y = 0$, 1 and 3 respectively, and the number of accepted pairs per thousand incident is given as a function of pair invariant mass and p_T, for $0.5 \leq M \leq 10$ GeV/c^2 and $0 \leq p_T \leq 6.0$ GeV/c.

Table 7.1a

M = 3.0 GeV/c^2, FULL geometry

(Number of hits per thousand incident)

6.0	0	0	51	603	694	742	715	723	796	966	971	944	777	657	727	738	708	562	50	0	0
5.5	0	0	81	613	691	755	760	669	796	953	973	949	794	717	758	732	715	570	84	0	0
5.0	0	0	36	556	678	732	746	735	792	942	971	949	811	727	744	749	713	581	31	0	0
4.5	0	0	62	522	679	711	737	711	781	929	961	917	785	686	731	727	673	533	67	0	0
4.0	0	0	47	519	684	714	710	727	811	917	965	919	812	687	728	690	648	512	56	0	0
3.5	0	0	35	505	670	701	726	720	808	923	956	910	818	729	706	735	647	511	27	0	0
3.0	0	0	30	461	649	723	703	727	777	895	940	902	800	737	735	691	635	480	32	0	0
2.5	0	0	52	470	621	696	715	715	800	920	940	913	801	743	712	700	657	423	40	0	0
2.0	0	0	44	411	641	702	713	725	792	905	924	911	790	718	728	689	644	423	43	0	0
1.5	0	0	33	405	601	690	726	767	799	878	927	899	806	730	726	681	588	394	37	0	0
1.0	0	0	32	385	593	684	731	735	815	877	928	890	806	756	711	675	610	378	31	0	0
0.5	0	0	36	362	581	683	689	772	825	874	918	882	805	753	718	664	578	395	45	0	0
0.0	0	0	42	426	664	758	758	765	801	893	947	884	800	747	785	753	677	399	40	0	0
PPERP	-5.0	-4.5	-4.0	-3.5	-3.0	-2.5	-2.0	-1.5	-1.0	-0.5	0.0	0.5	1.0	1.5	2.0	2.5	3.0	3.5	4.0	4.5	5.0

R A P I D I T Y

Table 7.1b

M = 3.0 GeV/c^2, Rear toroid not present

(Number of hits per thousand incident)

6.0	0	0	0	0	0	0	0	0	456	881	948	938	774	655	727	738	708	562	50	0	0
5.5	0	0	0	0	0	0	0	0	421	845	937	938	793	716	758	732	715	570	84	0	0
5.0	0	0	0	0	0	0	0	0	377	824	936	938	804	726	744	749	713	581	31	0	0
4.5	0	0	0	0	0	0	0	0	350	810	931	902	781	685	730	727	673	533	67	0	0
4.0	0	0	0	0	0	0	0	0	356	757	913	901	811	685	727	690	648	512	56	0	0
3.5	0	0	0	0	0	0	0	0	322	739	915	898	817	722	705	735	647	511	27	0	0
3.0	0	0	0	0	0	0	0	0	291	701	877	883	796	733	735	691	635	480	32	0	0
2.5	0	0	0	0	0	0	0	0	271	714	865	891	796	742	712	700	657	423	40	0	0
2.0	0	0	0	0	0	0	0	0	215	672	853	884	776	714	727	688	644	423	43	0	0
1.5	0	0	0	0	0	0	0	0	236	629	851	873	791	726	724	680	588	394	37	0	0
1.0	0	0	0	0	0	0	0	0	230	621	831	862	791	754	710	674	610	378	31	0	0
0.5	0	0	0	0	0	0	0	0	219	621	829	845	795	751	718	664	578	395	45	0	0
0.0	0	0	0	0	0	0	0	0	203	644	836	831	788	747	785	753	677	399	40	0	0
PPERP	-5.0	-4.5	-4.0	-3.5	-3.0	-2.5	-2.0	-1.5	-1.0	-0.5	0.0	0.5	1.0	1.5	2.0	2.5	3.0	3.5	4.0	4.5	5.0

R A P I D I T Y

Table 7.1c

M = 3.0 GeV/c^2, Rear toroid and rear half of solenoid not present

(Number of hits per thousand incident)

6.0	0	0	0	0	0	0	0	0	0	0	0	721	721	634	723	738	708	562	50	0	0
5.5	0	0	0	0	0	0	0	0	0	0	0	702	738	648	735	731	715	570	84	0	0
5.0	0	0	0	0	0	0	0	0	0	0	0	659	755	711	736	748	713	581	31	0	0
4.5	0	0	0	0	0	0	0	0	0	0	0	602	735	661	722	726	673	533	67	0	
4.0	0	0	0	0	0	0	0	0	0	0	0	595	733	658	721	690	646	512	56	0	0
3.5	0	0	0	0	0	0	0	0	0	0	0	591	747	694	694	733	647	511	27	0	0
3.0	0	0	0	0	0	0	0	0	0	0	0	547	699	699	716	689	635	480	32	0	0
2.5	0	0	0	0	0	0	0	0	0	0	0	540	705	686	694	694	657	423	40	0	0
2.0	0	0	0	0	0	0	0	0	0	0	0	501	619	651	717	682	644	423	43	0	0
1.5	0	0	0	0	0	0	0	0	0	0	0	474	645	679	703	677	587	394	37	0	0
1.0	0	0	0	0	0	0	0	0	0	0	0	443	612	692	687	671	610	378	31	0	0
0.5	0	0	0	0	0	0	0	0	0	0	0	468	639	700	702	663	578	395	45	0	0
0.0	0	0	0	0	0	0	0	0	0	0	0	454	587	674	785	753	677	399	40	0	0
PPERP	-5.0	-4.5	-4.0	-3.5	-3.0	-2.5	-2.0	-1.5	-1.0	-0.5	0.0	0.5	1.0	1.5	2.0	2.5	3.0	3.5	4.0	4.5	5.0

R A P I D I T Y

Table 7.2a

Pair Invariant Mass = 1.00 GeV/c^2

(Number of hits per thousand incident)

PPERP	0.00	0.25	0.50	0.75	1.00	1.25	1.50	1.75	2.00	2.25	2.50	2.75	3.00	3.25	3.50	3.75	4.00	4.25	4.50	4.75	5.00
6.0	652	664	675	679	613	467	448	595	642	673	676	722	725	735	707	649	176	0	0	0	0
5.8	643	646	658	682	607	423	472	614	628	676	694	679	730	710	685	657	173	0	0	0	0
5.5	620	605	632	634	593	425	466	612	638	655	691	697	703	702	701	658	167	0	0	0	0
5.3	625	624	628	646	547	456	460	587	610	670	668	699	693	710	689	638	177	0	0	0	0
5.0	618	607	636	627	556	409	433	578	604	648	687	713	726	726	698	651	176	0	0	0	0
4.8	597	577	569	582	507	426	460	582	621	669	676	698	707	697	677	611	140	0	0	0	0
4.5	549	550	555	560	483	436	435	542	630	629	677	675	696	708	698	598	171	0	0	0	0
4.3	546	528	560	521	473	409	410	544	580	648	649	692	713	695	659	582	149	0	0	0	0
4.0	478	475	508	514	431	395	392	514	586	612	646	671	713	661	666	591	143	0	0	0	0
3.8	467	450	450	467	403	407	357	540	584	622	651	652	694	676	648	541	138	0	0	0	0
3.5	411	428	435	438	339	411	355	529	566	591	660	660	646	702	661	551	156	0	0	0	0
3.3	382	386	375	376	299	350	362	476	563	588	651	666	678	677	661	489	145	0	0	0	0
3.0	327	329	315	336	280	342	285	471	533	578	604	658	671	629	623	513	51	0	0	0	0
2.8	272	247	273	273	206	337	283	440	493	552	613	643	655	643	599	466	73	0	0	0	0
2.5	189	204	206	236	198	266	210	410	494	555	597	657	647	608	598	469	63	0	0	0	0
2.3	110	123	115	133	148	233	213	386	451	519	567	622	632	623	576	380	81	0	0	0	0
2.0	15	19	34	34	82	203	162	342	449	496	574	605	610	600	529	376	47	0	0	0	0
1.8	0	0	0	0	4	121	150	294	417	464	549	572	580	591	535	326	91	0	0	0	0
1.5	0	0	0	0	0	33	98	241	340	450	504	557	563	501	437	314	45	0	0	0	0
1.3	0	0	0	0	0	0	40	163	302	397	472	473	504	508	412	298	51	0	0	0	0
1.0	0	0	0	0	0	0	0	84	227	346	411	459	465	438	369	273	20	0	0	0	0
0.8	0	0	0	0	0	0	0	21	197	289	359	443	448	397	362	247	31	0	0	0	0
0.5	0	0	0	0	0	0	0	0	117	250	379	459	445	422	385	231	30	0	0	0	0
0.3	0	0	0	0	0	0	0	0	67	213	334	448	448	492	338	223	22	0	0	0	0
0.0	0	0	0	0	0	0	0	0	45	218	380	490	554	569	406	223	20	0	0	0	0

RAPIDITY

Table 7.2b

Pair Invariant Mass = 3.00 GeV/c^2

(Number of hits per thousand incident)

6.0	695	659	679	646	610	612	536	597	635	617	643	694	658	634	566	416	50	0	0	0	0
5.8	680	647	667	658	565	581	552	578	636	670	648	662	675	670	552	375	72	0	0	0	0
5.5	698	669	641	646	547	606	552	592	648	628	676	682	662	613	572	392	85	0	0	0	0
5.3	633	640	640	626	538	602	561	610	620	650	689	676	673	633	562	386	93	0	0	0	0
5.0	647	607	641	615	590	621	556	569	645	649	672	660	655	612	561	411	29	0	0	0	0
4.8	642	612	602	618	581	605	531	581	613	661	669	649	649	597	561	346	39	0	0	0	0
4.5	650	576	569	569	573	603	542	572	602	640	686	666	648	628	493	358	62	0	0	0	0
4.3	592	575	604	583	569	583	521	561	602	629	622	650	634	621	494	376	78	0	0	0	0
4.0	572	560	599	540	561	607	504	548	599	650	670	646	606	617	498	318	40	0	0	0	0
3.8	600	515	572	529	571	573	509	561	562	620	637	616	618	547	496	310	57	0	0	0	0
3.5	543	515	547	568	546	547	500	542	585	591	632	648	594	575	491	285	27	0	0	0	0
3.3	557	509	517	539	542	559	512	541	543	601	605	616	583	552	462	286	50	0	0	0	0
3.0	533	491	523	527	537	566	487	535	563	577	611	618	581	535	439	301	27	0	0	0	0
2.8	495	458	483	526	526	557	498	576	534	584	596	607	577	539	437	278	46	0	0	0	0
2.5	469	492	478	521	527	548	488	527	553	575	593	611	592	503	419	278	53	0	0	0	0
2.3	494	468	496	508	486	548	496	530	523	557	591	594	576	516	388	292	30	0	0	0	0
2.0	461	427	473	509	523	525	489	536	524	557	565	554	522	497	409	258	31	0	0	0	0
1.8	476	443	480	487	489	546	482	505	552	576	591	575	576	488	421	254	40	0	0	0	0
1.5	457	411	491	507	496	494	483	488	531	576	555	565	549	511	425	249	45	0	0	0	0
1.3	472	439	480	534	538	501	486	473	484	546	573	589	562	472	379	259	41	0	0	0	0
1.0	573	526	589	595	579	560	512	492	513	540	587	569	572	465	383	234	37	0	0	0	0
0.8	616	608	642	633	585	559	533	513	496	530	596	569	578	518	381	205	35	0	0	0	0
0.5	651	682	678	605	546	556	534	497	517	568	608	614	595	503	365	204	44	0	0	0	0
0.3	706	743	650	625	582	556	525	539	550	585	627	622	608	527	402	226	39	0	0	0	0
0.0	738	816	638	607	551	577	544	568	586	643	687	731	661	547	432	236	43	0	0	0	0

PPERP	0.00	0.25	0.50	0.75	1.00	1.25	1.50	1.75	2.00	2.25	2.50	2.75	3.00	3.25	3.50	3.75	4.00	4.25	4.50	4.75	5.00

RAPIDITY

Table 7.2c

Pair Invariant Mass = 0.00 GeV/c^2

(Number of hits per thousand incident)

6.0	931	916	892	855	812	761	712	713	729	710	653	653	600	524	431	256	36	0	0	0	0
5.8	932	934	888	837	802	784	729	721	718	719	683	650	588	522	441	226	39	0	0	0	0
5.5	934	933	913	854	788	796	740	728	676	684	676	650	623	532	420	258	54	0	0	0	0
5.3	918	911	895	851	807	791	722	697	715	689	688	641	644	493	410	256	46	0	0	0	0
5.0	914	933	896	855	811	773	749	700	707	698	684	662	596	529	395	249	42	0	0	0	0
4.8	919	916	885	850	785	763	700	690	701	699	650	640	572	499	418	250	42	0	0	0	0
4.5	927	923	899	868	811	811	743	705	710	686	644	645	578	500	408	231	37	0	0	0	0
4.3	925	930	881	852	812	802	722	712	734	702	673	664	575	533	408	230	38	0	0	0	0
4.0	939	910	892	848	808	793	718	693	677	668	665	627	573	506	376	266	26	0	0	0	0
3.8	925	912	915	853	805	794	741	727	684	677	686	627	579	490	388	219	41	0	0	0	0
3.5	928	908	873	849	810	776	732	694	684	675	656	639	557	492	395	217	21	0	0	0	0
3.3	906	919	891	844	799	774	739	736	696	695	672	617	613	498	374	229	33	0	0	0	0
3.0	924	898	895	840	788	799	727	697	710	683	680	647	598	521	370	238	36	0	0	0	0
2.8	924	931	865	833	794	801	721	699	684	665	693	626	584	509	378	225	29	0	0	0	0
2.5	910	915	879	839	792	791	716	702	676	682	675	657	611	508	375	245	43	0	0	0	0
2.3	901	912	885	845	820	761	726	712	703	708	663	627	572	493	363	204	44	0	0	0	0
2.0	921	903	872	870	786	784	747	731	725	714	677	652	575	482	377	185	39	0	0	0	0
1.8	922	912	875	835	812	800	743	727	714	680	683	651	576	491	378	202	36	0	0	0	0
1.5	929	898	869	814	768	772	745	721	708	679	675	633	575	499	383	240	35	0	0	0	0
1.3	918	895	875	848	785	786	746	726	713	673	692	678	590	510	388	218	32	0	0	0	0
1.0	917	901	896	845	808	792	733	725	709	720	697	635	580	515	345	190	40	0	0	0	0
0.8	906	918	877	838	813	803	753	747	727	693	688	645	629	516	400	238	46	0	0	0	0
0.5	908	899	859	860	801	790	764	746	740	716	712	704	638	522	392	220	35	0	0	0	0
0.3	911	895	869	852	816	804	767	766	783	774	720	744	656	545	427	202	43	0	0	0	0
0.0	952	911	891	860	809	792	769	796	787	789	777	743	671	541	406	229	35	0	0	0	0
PPERP	0.00	0.25	0.50	0.75	1.00	1.25	1.50	1.75	2.00	2.25	2.50	2.75	3.00	3.25	3.50	3.75	4.00	4.25	4.50	4.75	5.00

R A P I D I T Y

Table 7.3a

Number Accepted Per Thousand Incident

Pair Rapidity = 0.00

PPERP	0.50	1.00	1.50	2.00	2.50	3.00	3.50	4.00	4.50	5.00	5.50	6.00	6.50	7.00	7.50	8.00	8.50	9.00	9.50	10.00
6.00	693	670	666	673	694	716	708	740	782	821	880	917	943	932	928	951	931	941	936	947
5.75	689	648	649	683	675	685	703	736	754	812	882	921	940	920	928	929	937	939	924	918
5.50	661	599	629	623	660	671	725	740	776	800	885	936	939	947	935	932	932	931	931	943
5.25	665	621	621	642	633	673	707	736	744	801	901	936	946	937	939	925	941	927	914	912
5.00	661	604	622	611	638	623	683	701	767	850	901	938	939	945	912	940	935	913	924	925
4.75	625	585	566	570	585	616	704	732	774	849	913	927	923	954	932	918	920	933	926	936
4.50	578	551	563	586	581	601	685	711	778	868	903	934	947	932	932	910	930	918	926	917
4.25	567	527	560	527	600	618	653	699	785	890	941	938	944	922	915	927	915	925	920	933
4.00	510	470	492	516	557	593	668	738	785	883	920	933	939	929	916	935	927	925	928	921
3.75	493	438	459	486	543	584	656	714	801	892	930	915	914	923	938	918	927	921	937	936
3.50	436	424	437	463	496	582	628	732	813	886	939	920	923	909	930	905	931	918	920	931
3.25	390	377	379	414	473	542	643	694	852	897	919	920	940	919	932	933	925	919	924	899
3.00	332	327	334	381	468	534	626	714	849	920	923	934	923	924	916	915	914	919	920	922
2.75	266	256	292	302	402	541	639	762	881	924	910	927	914	923	911	914	916	909	918	932
2.50	180	204	236	302	368	488	592	774	890	917	921	901	914	934	925	918	914	921	925	929
2.25	76	123	168	234	347	475	599	808	893	918	929	913	914	910	925	918	911	906	925	941
2.00	0	15	83	159	311	469	638	839	906	920	912	926	917	930	913	913	911	906	922	928
1.75	0	0	41	124	276	479	678	847	912	922	922	920	922	939	921	911	924	914	919	911
1.50	0	0	0	79	264	472	712	879	906	904	919	930	902	909	912	915	927	905	913	915
1.25	0	0	0	45	241	461	732	888	917	909	906	931	896	932	922	926	911	906	910	928
1.00	0	0	0	16	245	568	761	888	917	926	919	940	922	910	911	924	912	919	918	920
0.75	0	0	0	1	209	582	777	894	930	934	928	923	915	926	908	922	909	919	904	926
0.50	0	0	0	0	269	653	776	908	920	935	920	912	897	920	924	916	924	924	917	922
0.25	0	0	0	0	423	695	817	921	908	916	922	923	921	919	920	933	914	921	938	920
0.00	0	0	0	0	559	738	852	960	948	955	955	944	958	956	962	959	959	959	946	961

INVARIANT MASS

Table 7.3b

Number Accepted Per Thousand Incident

Pair Rapidity = 1.00

6.00	745	627	555	555	544	610	598	649	706	698	739	753	753	786	777	783	761	786	788	811
5.75	697	578	539	558	563	565	630	657	671	737	745	754	750	782	763	795	790	792	775	801
5.50	698	581	530	512	550	547	622	677	668	707	719	769	758	770	784	797	788	802	776	810
5.25	683	543	504	504	549	538	619	657	688	743	737	749	783	762	791	795	805	796	807	795
5.00	657	543	472	513	556	590	614	671	699	717	758	748	762	773	789	779	764	794	795	786
4.75	650	512	476	487	558	581	621	643	693	739	784	752	774	805	790	785	818	813	803	807
4.50	624	485	460	469	535	573	628	644	680	753	752	767	758	781	799	772	800	802	806	799
4.25	595	432	420	469	528	569	619	636	690	704	750	743	756	782	761	815	802	805	793	825
4.00	549	413	405	473	507	561	618	630	697	707	755	766	758	780	795	771	788	792	806	806
3.75	516	390	378	477	482	571	599	648	696	717	740	754	767	785	791	811	791	792	787	818
3.50	470	339	362	437	514	546	601	650	708	711	759	765	749	779	778	802	809	784	810	800
3.25	398	308	345	440	501	542	592	656	724	727	752	747	787	790	818	783	802	791	806	794
3.00	342	254	355	445	496	537	590	666	735	741	754	760	760	783	806	810	803	787	826	795
2.75	313	217	314	390	477	526	606	686	721	719	735	766	779	776	776	796	795	809	778	808
2.50	236	200	347	374	458	527	613	666	701	709	758	737	766	774	808	758	785	800	806	794
2.25	142	156	262	357	435	486	598	686	701	715	740	751	775	772	795	778	801	798	814	817
2.00	13	71	206	335	416	523	604	688	701	724	743	780	777	787	778	798	796	808	794	813
1.75	0	4	158	280	416	489	644	667	699	753	702	782	807	809	764	791	790	814	800	804
1.50	0	0	70	240	378	496	585	664	708	749	759	777	782	791	775	802	794	790	798	809
1.25	0	0	18	199	378	538	613	683	722	714	735	765	777	831	810	802	795	803	817	827
1.00	0	0	0	157	364	579	609	694	711	747	758	770	762	801	804	782	806	770	791	795
0.75	0	0	0	105	342	585	614	703	724	733	768	770	776	807	809	825	809	813	803	795
0.50	0	0	0	45	396	546	627	684	714	720	748	780	788	785	812	797	796	781	790	806
0.25	0	0	0	1	438	582	635	674	688	707	754	790	777	816	796	799	773	797	802	815
0.00	0	0	0	0	405	551	642	672	715	742	738	752	773	790	789	797	792	787	801	798

PPERP	0.50	1.00	1.50	2.00	2.50	3.00	3.50	4.00	4.50	5.00	5.50	6.00	6.50	7.00	7.50	8.00	8.50	9.00	9.50	10.00

INVARIANT MASS

Table 7.3c

Number Accepted Per Thousand Incident

Pair Rapidity = 3.00

PPERP	0.50	1.00	1.50	2.00	2.50	3.00	3.50	4.00	4.50	5.00	5.50	6.00	6.50	7.00	7.50	8.00	8.50	9.00	9.50	10.00
6.00	792	727	693	680	654	696	640	620	655	626	631	635	640	587	615	637	621	596	612	622
5.75	773	701	711	690	675	669	675	637	616	632	629	634	620	604	631	618	588	600	597	643
5.50	781	720	690	684	689	678	645	650	637	634	603	619	585	638	598	597	595	615	613	612
5.25	774	718	673	650	653	681	656	655	617	592	620	612	638	622	607	608	604	608	604	608
5.00	762	683	700	671	673	637	652	615	612	618	609	570	573	607	625	646	607	597	593	582
4.75	786	702	693	678	658	666	635	611	625	628	609	608	580	590	606	615	628	591	585	584
4.50	778	693	681	651	631	654	622	588	619	600	600	597	616	595	603	614	610	578	592	591
4.25	771	701	685	658	656	640	635	607	596	579	620	608	585	598	601	593	590	560	596	609
4.00	742	694	662	677	655	595	624	626	614	594	582	589	603	599	583	580	558	600	580	583
3.75	768	684	649	663	628	619	596	578	571	548	599	610	620	606	612	587	560	576	567	575
3.50	753	693	640	661	613	584	613	594	588	549	572	575	574	572	596	610	589	600	582	607
3.25	736	645	664	644	612	618	559	586	566	561	598	565	576	583	578	582	587	553	555	595
3.00	740	651	645	608	593	621	572	565	564	603	562	583	576	586	569	585	571	598	594	582
2.75	718	632	606	634	575	577	569	571	576	567	581	576	589	553	555	560	580	568	578	586
2.50	733	651	600	595	575	613	564	573	587	588	593	549	599	574	605	583	602	595	610	566
2.25	699	615	610	575	556	567	549	596	566	558	580	581	590	587	587	573	588	599	606	558
2.00	674	589	592	569	588	544	572	603	562	566	587	586	572	590	559	608	606	565	574	583
1.75	692	600	571	525	541	572	543	571	584	576	575	586	584	567	560	579	564	571	579	580
1.50	644	545	523	528	544	554	574	548	576	579	602	574	557	553	597	582	597	613	613	606
1.25	586	508	525	510	525	547	552	556	577	581	601	582	600	567	602	584	579	594	616	579
1.00	547	4[illegible]	500	525	574	557	553	560	574	563	595	574	578	578	589	592	605	561	596	599
0.75	470	401	493	515	529	571	602	589	587	601	589	592	596	578	613	617	600	611	623	585
0.50	309	432	522	518	555	588	586	590	599	614	573	596	612	641	627	601	623	601	632	621
0.25	270	465	514	572	580	597	591	619	620	619	605	611	624	654	661	663	643	677	625	629
0.00	293	545	665	695	655	672	686	667	667	661	670	668	656	666	674	665	668	661	684	669

INVARIANT MASS

In Figures 7.6a, b and c we show the acceptance as a function of rapidity for invariant masses of 1,3, and 10 GeV/c^2. In each figure we give the acceptance for p_T = 0, p_T = M/2 and p_T = M. For the 1 and 3 GeV/c^2 cases, the acceptance rises with increasing rapidity due to the diminishing effects of energy loss, whereas for 10 GeV/c^2 the acceptance drops at forward rapidity due to the geometrical losses in the toroid coils.

In Figures 7.7a, b and c we show the acceptance for pairs with the mass of a J/ψ, for rapidities of 0, 1, and 3, and for p_T values of 0 and 1.5 GeV/c, as a function of the polar angle that the muons make with respect to the pair direction, in the pair rest frame. For p_T = 0, the acceptance is sharply delineated by the cutoffs due to energy loss in the absorber. The loss occurs for polar angles near 0 and 180°, as that corresponds to emission along the beam axis in the coordinates used. The plateau for y = 1 and 3 is less than 100% due to the forward and backward coils. It only corresponds to a 13% loss of acceptance however, because for p_T = 0 the muons are sharply correlated in ϕ, so the geometrical loss enters linearly instead of quadratically. For p_T = 1.5 GeV/c the acceptance rolls off more gradually with polar angle approaching 0 and 180°, though for the same basic reason, namely ranging out of muons. Dips due to the solenoid yoke return can be seen.

In Figures 7.8 through 7.10 we show the spectrum given by the parametrization of Ref. 7.1 as a function of invariant mass and for rapidities of 0, 1, and 3. The two curves show the input spectrum, given by the event generator described in Appendix C, and the same spectrum after the acceptance is folded in. The results have been summed over p_T in these figures, using the p_T distribution from the event generator. The J/ψ appears as a single-channel spike because the mass resolution was deliberately left out of the present calculation. As expected, the spectrum is quite suppressed at small masses for small rapidities due to ranging out in the absorber of soft muons. However, for y = 3, the acceptance is 20-50% for masses near 1 GeV/c^2.

It does appear possible to construct a dimuon spectrometer with 50% or better acceptance over a large kinematic range for RHIC.

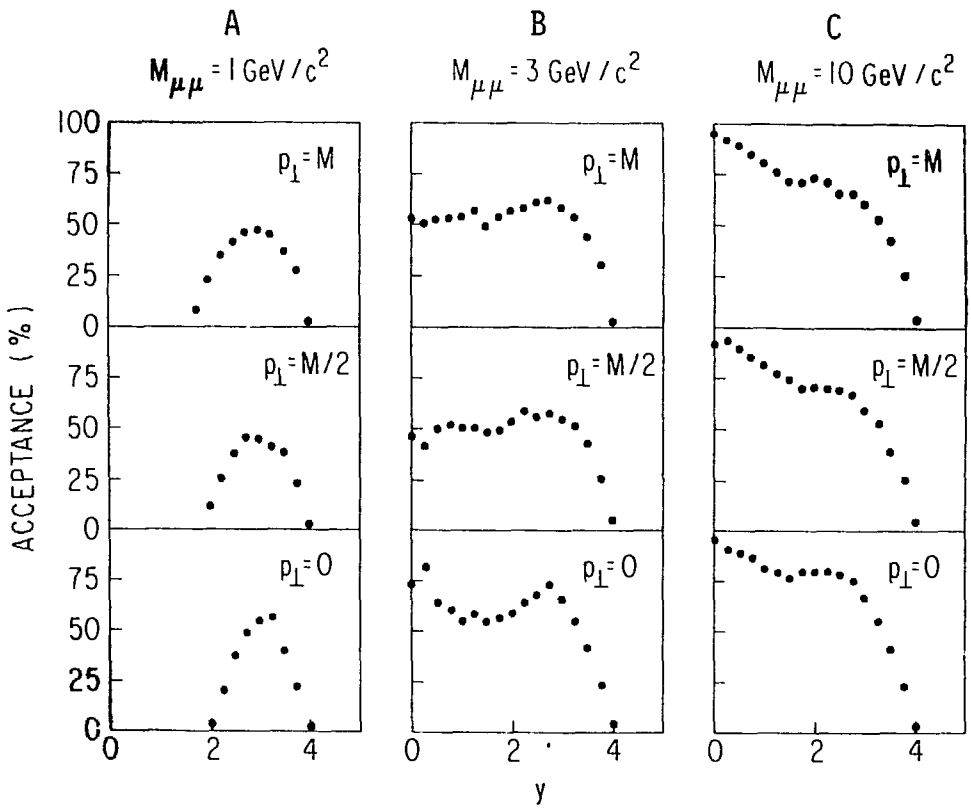

Fig. 7.6 Dimuon acceptance as a function of the rapidity of the pair, for several values of the invariant mass and transverse momentum of the pair.

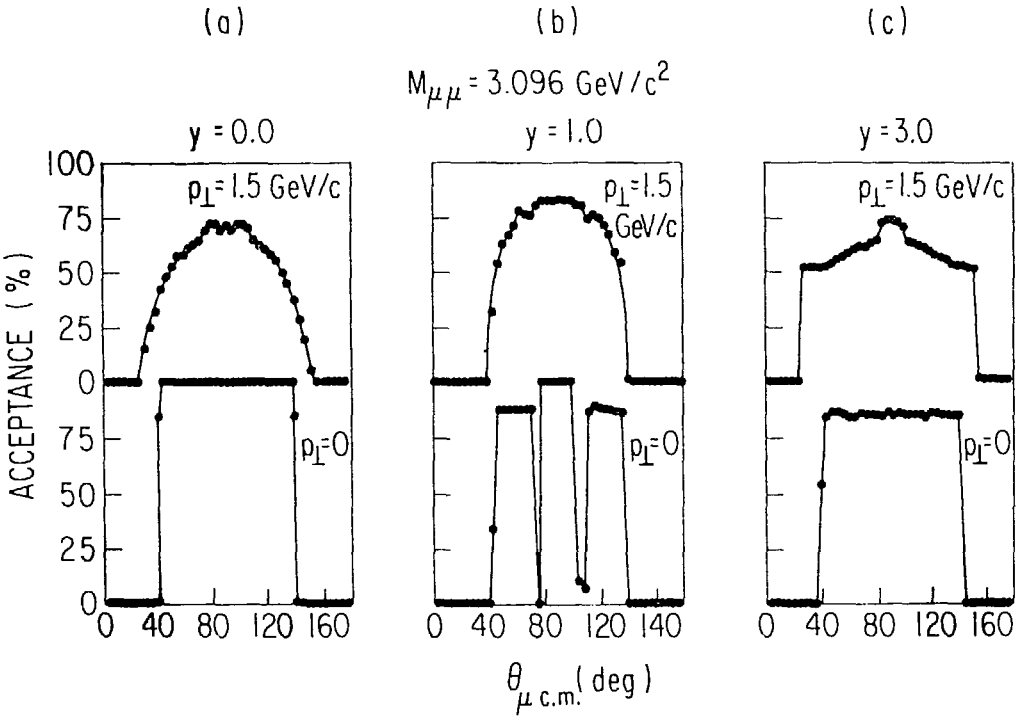

Fig. 7.7 Dimuon acceptance at the J/ψ mass as a function of the decay angle in the pair rest frame, for different values of the transverse momentum.

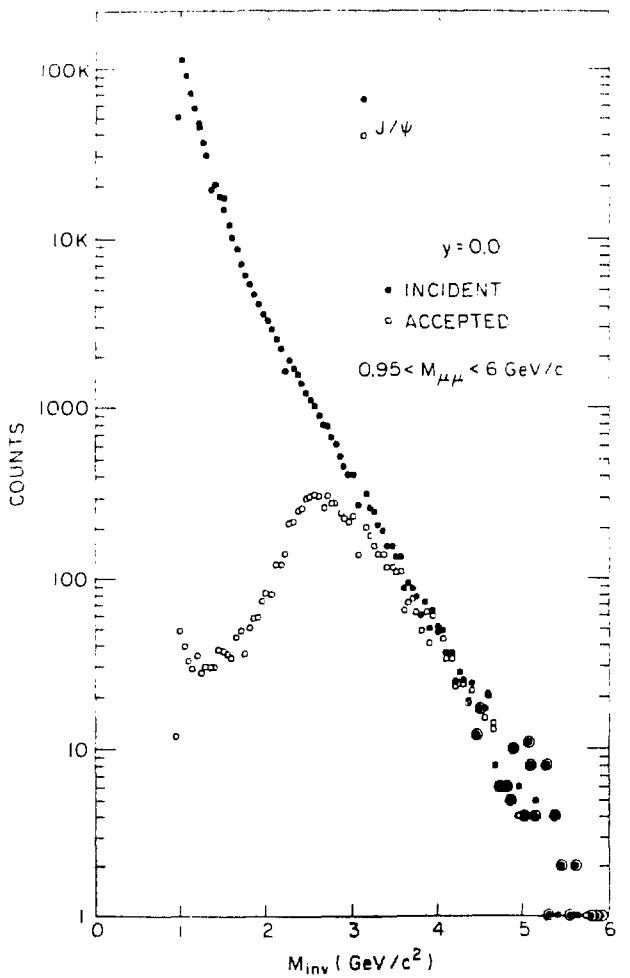

Fig. 7.8 Generated and accepted pair invariant mass spectra at y = 0.

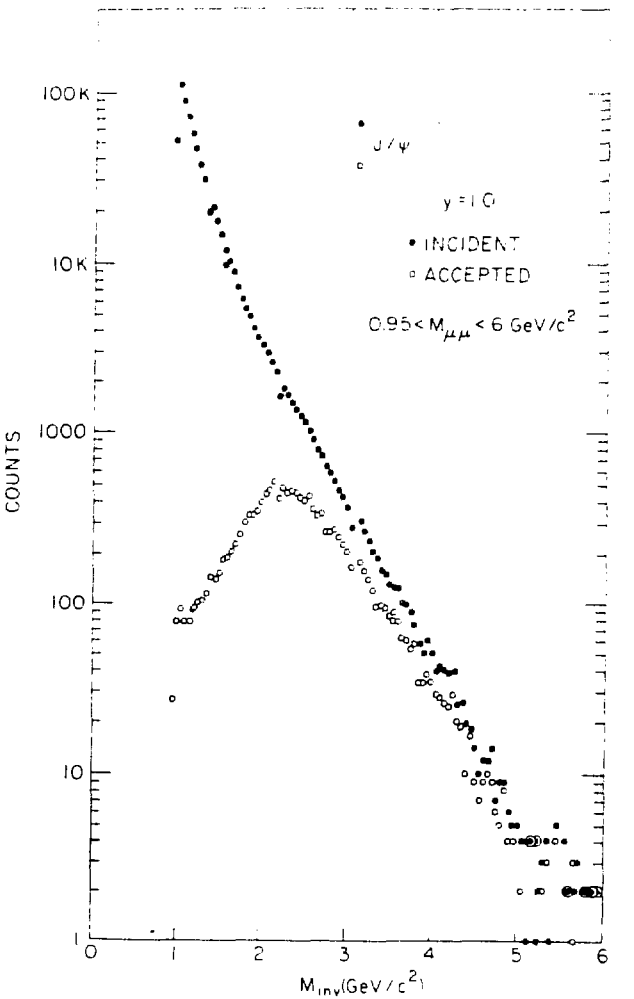

Fig. 7.9 Generated and accepted pair invariant mass spectra at y = 1.

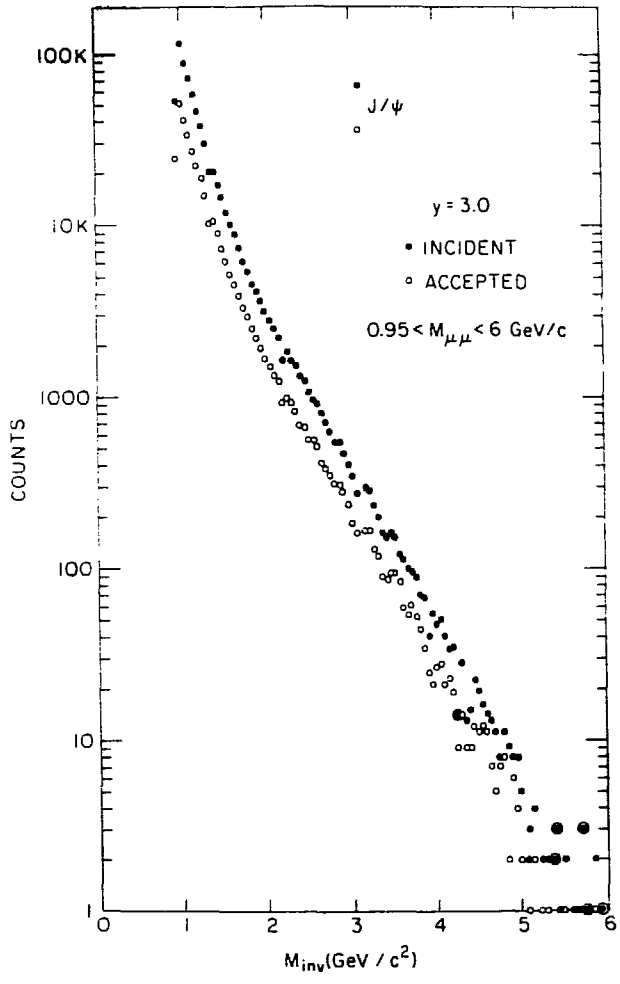

Fig. 7.10 Generated and accepted pair invariant mass spectra at y = 3.

8. RELATIONSHIP BETWEEN THE DIMUON DETECTOR AND RHIC INSERTION PARAMETERS

For the heavier beams at RHIC, the beam bunch length grows quite a bit during a long store due to the coupling of transverse and longitudinal motion within a bunch arising from intrabeam scattering. To avoid running with a diamond length that can have $\sigma \gtrsim 1$m after several hours, we have considered running with a small crossing angle. It is our opinion that the loss in luminosity is more than compensated by the improved definition of the interaction vertex, as the latter renders the whole apparatus more compact as well as ensuring that events arise from vertices within the acceptance of the device.

In order to compensate for the loss in luminosity we further consider running with a lower β^* than the value for the standard RHIC lattice. Values of $\beta^* = 2$ meters in both planes seem quite reasonable, given that the design of the spectrometer has been made so as to permit mounting extra, low-β quadrupoles inside of the RC1 merging magnets. Another considerable gain in bunch length would be had by doubling the RF frequency in RHIC so as to halve the basic length of a bunch. It is assumed here that the deleterious effects of intrabeam scattering will not be worsened by such a change.

The following table presents 1σ values for the bunch length and interaction region length and for the resulting luminosity, as a function of various crossing angles. All values are for Au + Au collisions at 100 GeV/nucleon/beam. The normalized transverse emittances used are the same as quoted in Ref. 3.2 but for a 26 MHz RF system there, while this table assumes a frequency of 53 MHz. A value of $\beta^* = 2$ meters in x and y is also assumed.

TABLE 8.1. Bunch length interaction, diamond length and luminosity as functions of crossing angle. (All lengths are in units of centimeters. All luminosities are in units of $cm^{-2}sec^{-1}$. An RF frequency of 53 MHz and a β^* of 2 meters are assumed.)

		Crossing angle (milliradians)			
		0	2	5	8
T = 0 hours	σ_ℓ	24	24	24	24
$\varepsilon_n = 10\pi$	σ_{IR}	12	7.1	3.4	2.2
	$\mathcal{L}$	2.7×10^{27}	1.6×10^{27}	7.6×10^{26}	4.9×10^{26}
T = 2 hours	σ_ℓ	55	55	55	55
$\varepsilon_n = 18\pi$	σ_{IR}	28	10.9	4.8	3.1
	$\mathcal{L}$	1.9×10^{27}	7.4×10^{26}	3.2×10^{26}	2.1×10^{26}
T = 10 hours	σ_ℓ	74	74	74	74
$\varepsilon_n = 28\pi$	σ_{IR}	37	13.7	5.9	3.7
	$\mathcal{L}$	1.3×10^{27}	4.8×10^{26}	2.1×10^{26}	1.3×10^{26}

9. SUMMARY: OPEN QUESTIONS

Although a large amount of work has gone into the preparation of the present report, there are some gaps and inconsistencies which need work before a Letter of Intent can be prepared. The more important of these are listed below.

A. Backgrounds: As pointed out above, a more complete and coherent treatment of dimuon backgrounds is needed. For example, we have not done a full transport of hadrons and muons through a properly simulated absorber. As a result we cannot apply realistic cuts to background muon candidates. GEANT or equivalent needs to be applied on a particle-by-particle basis. We have considered background dimuons from charm separately from hadron punch-through and decay; this ignores dimuons composed of one muon candidate from each of

these separate sources. We also don't have a good feel for the effect of several potential cuts applied in series. This requires more statistics and more complete simulation. In sum, while it appears likely that there is sufficient power in the detector to suppress back-grounds adequately, this has not been conclusively demonstrated.

B. Resolution and acceptance: A very good start has been made on this problem but work remains here as well. Some (presumably minor) contributions to the resolution function have not yet been included in the calculation. The trade-offs between resolution and background (e.g., in optimizing the absorber material and thickness) have not been faced yet. The muon chamber performance is somewhat idealized; inefficiencies, spurious hits, misalignments, delta-rays, etc. would be included in a full-blown calculation.

C. Triggers: Only the lowest level triggering has been considered in detail. The calorimeter/absorber is a rich source of triggering (and physics) information which has not yet been tapped. Similarly, muon triggers have not been developed beyond the statement (supported by preliminary GEANT studies) that pointing back to a vertex will strongly suppress punch-through backgrounds.

D. Hardware: Figs. 6.1 and 6.2 represent a concept only; nothing has been fully optimized yet. Magnet designs; calorimeter/absorber technology, segmentation and readout; chamber designs; trigger hardware; data acquisition: all these need to be addressed (and costed!). It is not demonstrated that the design concept presented can take the highest luminosities and cover the required mass and transverse momentum space to do the dimuon physics suggested in Section 2.

This list is not intended to convey a sense of pessimism on the part of the working group. All indications are that we can "get there from here" so to speak; the present design concept is a direct descendent of the spectrometer proposed at the 1985 Workshop. We are reasonably confident that it can be further developed (with a few man-years of hard work) into a viable dimuon experiment for RHIC.

APPENDIX A. FIRST-LEVEL TRIGGER SYSTEM

This is a preliminary study of possible low-level triggers for a dedicated muon experiment at RHIC. No attempt has been made to look at a muon trigger. Rather the focus has been on the initial trigger levels which serve to define the presence of an interaction, to select candidate central collisions and to act as a luminosity monitor. The study is based on, and essentially limited by, small samples of minimum-bias HIJET events (Table A.1) and a sample of pp collisions for comparison. It is worth noting (Table A.2) that, apart from the pp case, the maximum real event rate expected for the heavy ion collisions is modest, ranging from ~$6X10^4$/sec for light ions down to ~$5X10^3$/sec for Au on Au. Consequently even modest (~10-100) rejections in the preliminary trigger levels should produce rates low enough to allow quite sophisticated muon triggers.

TABLE A.1. HIJET event samples for study

INTERACTION	NO. EVENTS	IMPACT PARAMETER(B)	BMAX(fm)
Si,Si	500	Averaged	6.7
Au,Au	50	Averaged	12.8
Au,Au	50	Central	12.8
p,p	5000	-	-

TABLE A.2. Maximum interaction rates at RHIC

INTERACTION	σ_{tot} (barns)	$\mathcal{L}_{MAX}$ ($cm^{-2}sec^{-1}$)	Event Rate = $\ell\ \sigma$ (sec^{-1})
Si,Si	1.37	3.9×10^{28}	6×10^4
Au,Au	5.13	9.2×10^{26}	5×10^4
p, p	.15	9.5×10^{30}	1.5×10^6

The triggers considered here are based either on particle multiplicity or calorimeter E_T sums. Since this is a muon detector it is essentially all

absorber and it is not possible to use particle counts in a precise way. However the track multiplicities are high enough that particle counting seems satisfactory for defining the presence of a real collision and rejecting interactions originating outside the crossing diamond. The detector is a good calorimeter so once the initial trigger is satisfied central collision candidates can be isolated using either a global E_T trigger or a trigger based on E_T in a restricted pseudorapidity range.

The average particle multiplicities (all, π/K only) are shown in Fig. A.1a for Au on Au and in Fig A.1b for Si on Si. In these plots all particles with $\eta < 5$ are included. The corresponding average multiplicity for pp is only 16 particles so it will be very difficult to work with pp interactions in this detector. For an explicit level-0 trigger consider 2 counter arrays 150 cm from the nominal crossing point and with inner radius 5 cm and outer radius 45 cm. These arrays cover the approximate pseudorapidity range $2 < \eta < 4.5$. The timing precision of these arrays allows a definition of the event vertex. For example, if the relative timing of the 2 arrays is ~.25 nsec then the vertex can be localized to ~7 cm. Clearly these counters can be used to reject spurious events from outside the interaction diamond and can provide an initial vertex location for the E_T trigger and final muon trigger.

The average charged particle (π/K only) multiplicities in each counter array as a function of impact parameter in the absence of any absorber is shown in Fig A.2. If one assumes that 10% of the particles reach the counters without interacting in the absorber then the trigger will be very efficient for Au on Au collisions with $B < 10$ and Si on Si collisions with $B < 4$. The average multiplicity for lower impact parameters is at least 5 so there will essentially always be at least one good hit in each array. This is actually a worse case estimate since some of the charged particles which scatter will produce secondaries which reach the counters and some of the neutrals which shower will also contribute to the signal. Clearly the counter arrays defined above will provide an excellent level-0 trigger for heavy ion collisions. They can be used to reject collisions not originating in the interaction diamond. They will give an in-time coincidence for valid collisions with high efficiency for almost all impact parameters even for light ion collisions.

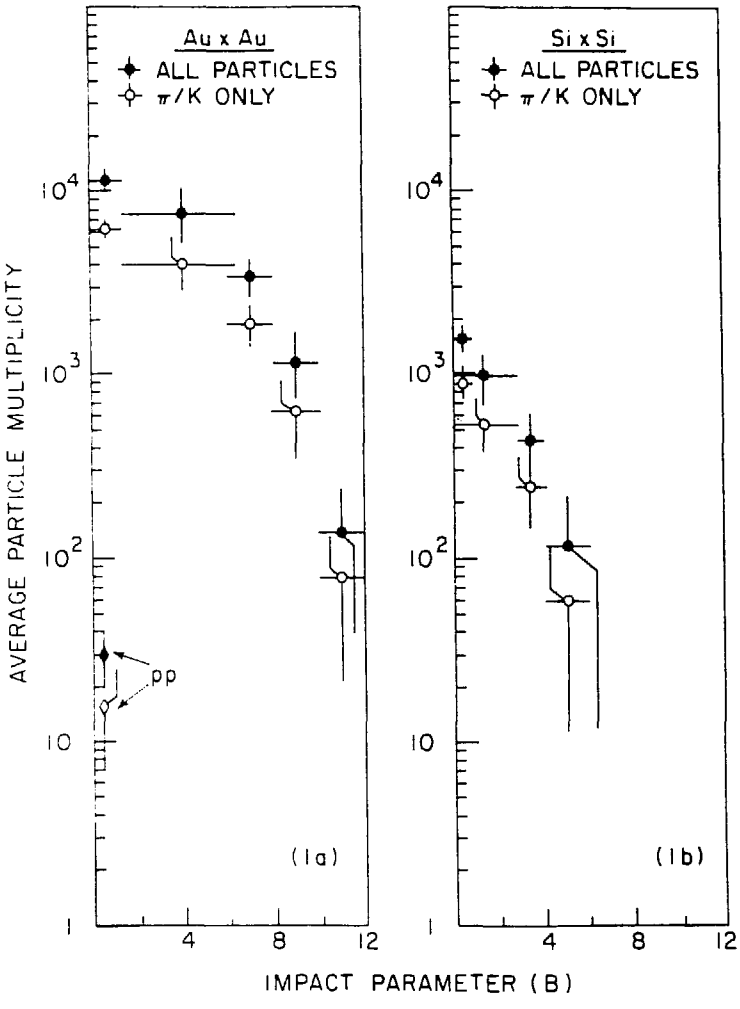

Fig. A.1 Average particle multiplicities for a) Au + Au and b) Si + Si interactions.

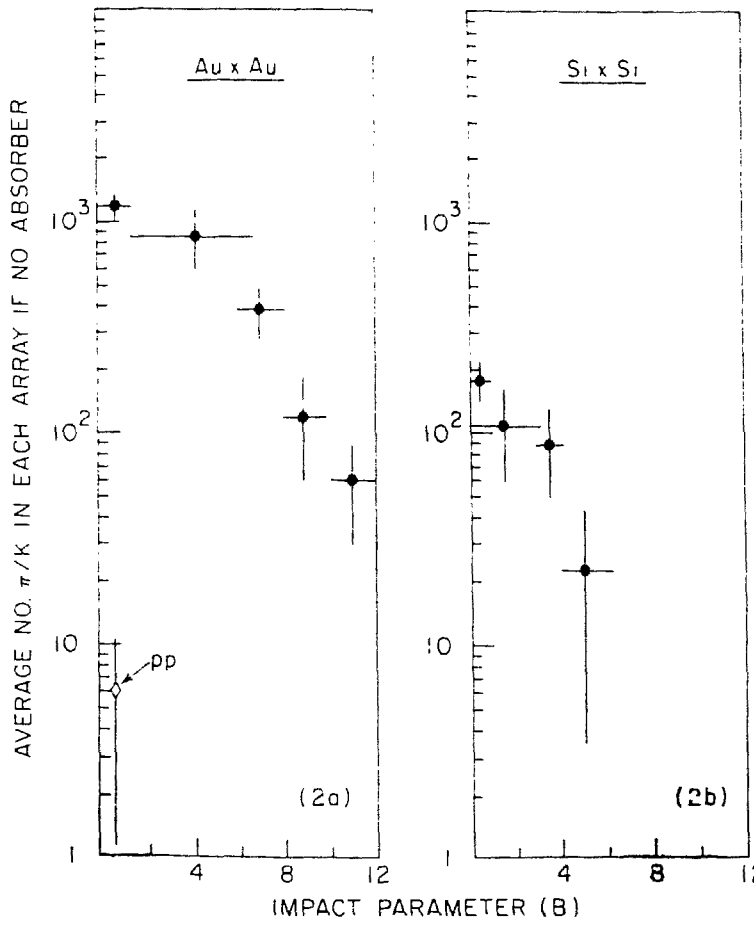

Fig. A.2 Average charged particle multiplicities in each trigger counter as a function of impact parameter.

And with adequate timing resolution they can give a fast definition of the event vertex which can be used by the higher-level triggers.

The counters have two real drawbacks. First, because of the absorber in front the actual particle counts are not reliable so they can not be used as a trigger say for central collisions. Second, since the multiplicity in the counters for pp collisions with no absorber is only 1.5 on average, the efficiency will be very low for pp collisions. One possible solution to the pp problem would be to put equivalent counter arrays at +-40 cm, before the absorber begins. These arrays could also be useful for peripheral light ion collisions where the multiplicities are not much greater than for pp.

Once an event candidate has been identified it is necessary to consider a level-1 trigger to select central collisions. Since particle multiplicities can not be used the logical choice would appear to be an E_T-trigger based either on the full calorimeter or on a selected region, for example $\eta < 1$. The average E_T as a function of impact parameter for Au on Au and Si on Si is shown in Fig A.3 and the overall E_T distribution for all impact parameters is shown in Fig. A.4. The calorimeter is assumed to cover the range $\eta < 4$. As expected there is a sharp decrease in $\langle E_T \rangle$ with impact parameter. Requiring $E_T > 2500$ GeV for Au on Au ($E_T > 300$ GeV for Si on Si) retains only 6% (10%) of events and the selected events all have very small impact parameter (B < .1 BMAX). The number of events available at present is inadequate for further study on the E_T distribution. However increasing the cut to $E_T > 3500$ GeV for Au on Au ($E_T > 350$ GeV for Si on Si) will eliminate all the present events. All these numbers have been generated assuming a fixed interaction point and perfect resolution. Given the rapidly falling E_T spectrum as a function of impact parameter, more detailed study is required to ensure an adequate E_T-trigger for selecting central collisions. However it does appear reasonable that a straightforward E_T-trigger can be used to select central collisions or to reduce the initial trigger rate by a factor of ~10-100. This should be an adequate reduction to provide time for implementing the actual muon trigger for the experiment.

The following then appears to be a reasonable triggering strategy for a dimuon experiment at RHIC:

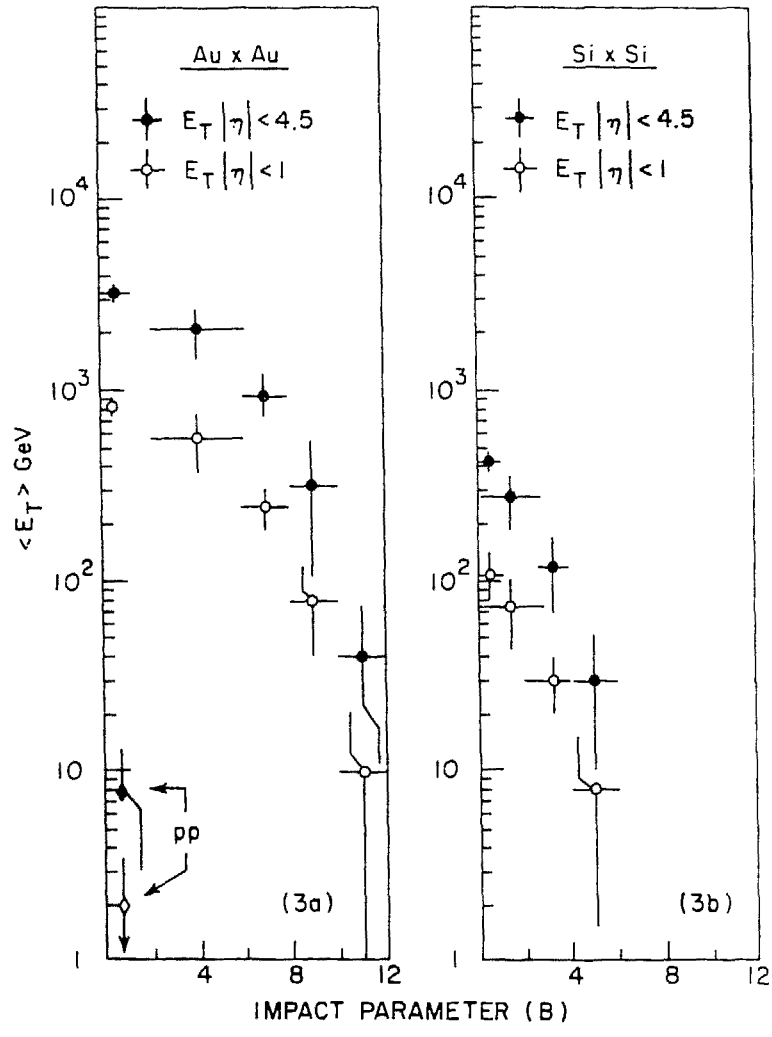

Fig. A.3 Average transverse energy as a function of impact parameter, for Au + Au and Si + Si interactions.

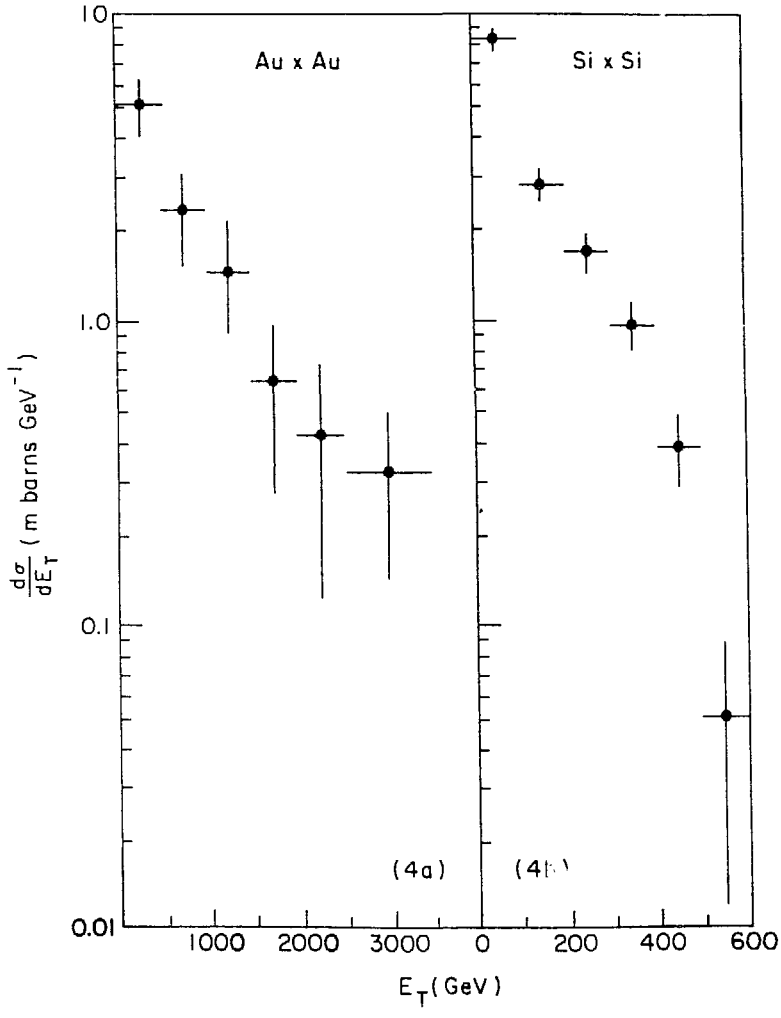

Fig. A.4 Transverse energy summed over impact parameter.

LEVEL-0 Trigger. Two arrays of scintillation counters, inner radius 5 cm, outer radius 45 cm, located +-150 cm from the nominal interaction point. If the arrays are ~1.5 interaction lengths into the calorimeter then any real interaction with a reasonable impact parameter should yield an in-time coincidence between the two arrays with a threshold of a few times minimum ionizing. If the density of the absorber is greater than that assumed here then equivalent arrays closer to the interaction point would suffice. For pp collisions or large impact parameter collisions for light ions it will probably be necessary to augment these arrays with equivalent arrays at the end of the interaction region and before any absorber. The relative timing between the arrays can be used to discriminate real interactions from spurious processes and can also be used to provide a crude vertex definition for the later triggers.

LEVEL-1 TRIGGER. A reasonable level-1 trigger to select central collisions could be based either on global E_T, or E_T in a restricted pseudorapidity range. A simple cut on global E_T can reduce the trigger rate at least a factor of 10 and it will retain all the central collision candidates. Increasing the E_T cut will further reduce the trigger rate but the statistics used in the present study were not adaquate to evaluate the significance of the additional cuts

At present it is not clear how adequate these triggers will be under more realistic detector simulations. More important, it is not obvious what effect they will have on more interesting event categories than the minimum-bias events in the present HIJET study. And there is little indication of their relevance to the study of significant heavy ion phenomena such as the presence of a quark-gluon plasma. However they do appear to be relatively simple triggers and should provide time for the implementation of sophisticated muon triggers without significantly impacting potentially important physics processes.

APPENDIX B. VERTEX DETECTOR

At the core of the spectrometer, inside the central active absorber, is a small cavity surrounding the beam crossing region where the first layers of detectors look directly at all of the secondary particles produced near central rapidity in the collision. Inside this cavity, which must be kept reasonably small, lies a highly segmented, position sensitive charged particle detector whose purposes are:

i.) To provide an accurate reconstruction of the interaction vertex position.

ii.) To provide a measure of the multiplicity and angular distribution of charged particles (in the central rapidity region) for use off-line in conjunction with the calorimeter measurements to determine such event characteristics as impact parameter and degree of thermal excitation in the collision.

In specifying this detector we assume that the luminous interaction region has a total length of not more than 40 cm. along the beam axis [B.1], and that the detector covers a rapidity interval of at least ±1.5 units for any interaction point along this length. We further assume that the closest detector to the beam will be 5 cm. from the beam axis. We propose a device in which each track crosses two planes of detector, providing a precise measurement of track angles and a degree of redundancy sufficient for an accurate multiplicity measurement [B.2]. The proposed geometry is shown in Fig. B.1. It consists of twelve detector planes forming two concentric hexagonal tubes around the beam pipe.

We expect this detector to be more or less uniformly populated by charged tracks. For the most extreme (and most interesting) cases we expect the number of charged particles traversing this detector to be of the order of 1000. With this in mind, and without benefit of detailed simulation, we require that the effective segmentation of the device be approximately 10^4 pixels. The detector layers should be as thin as possible to minimize the number of photon conversions. We aim for a thickness less than 1% radiation

Pad Chamber Vertex Detector

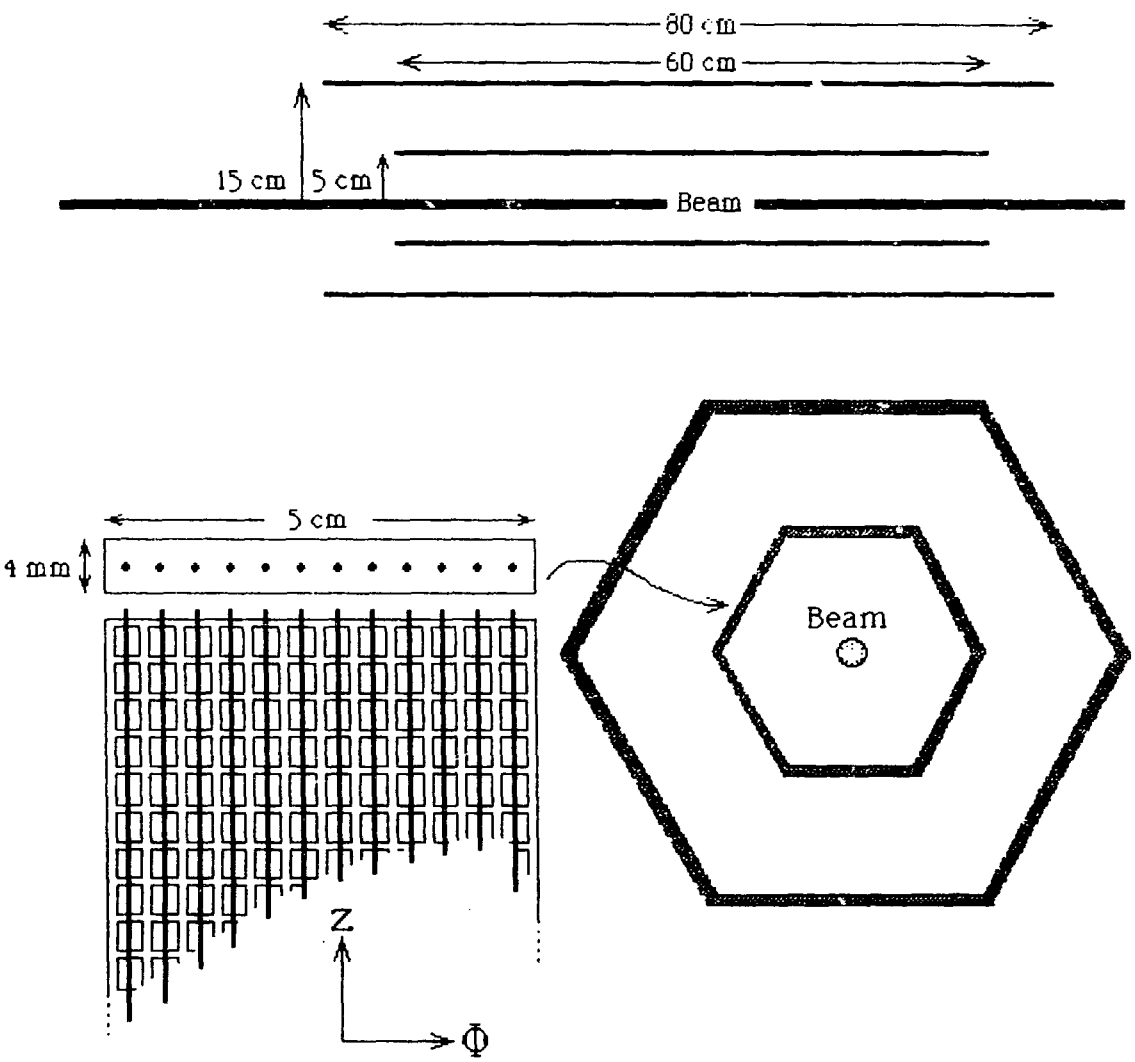

12 Pad Rows, 60 Outputs/Row

approximately 15,000 total output channels
(multiplexed read-out)

Fig. B.1 Schematic of a pad chamber vertex detector as described in the text.

length. The detector must be capable of sustaining event rates up to 10^6 sec^{-1}.

As an example of a detector type which shows promise for satisfying these requirements, we sketch here the design of a high multiplicity proportional detector with segmented cathode readout [6.1] (sometimes referred to as a "pad chamber"). The design is illustrated in Fig. B.2 which shows one plane of the inner detector hexagon. There is a single plane of wires, with a segmented cathode strip (pad row) running beneath each anode wire. Field wires between anodes and guard strips between pad rows form a square drift cell. The basic cell structure is shown in Fig. B.3, again for the inner detector. The outer detector is similar, but with a basic cell size of 3 mm.

Each track, incident normal to the detector plane, produces an avalanche charge localized to within a small fraction of a millimeter along the length of an anode wire, inducing a charge on the underlying pad row. The induced charge distribution on the cathode pads spreads out a few millimeters along the wire length. Some charge is also induced on the neighboring pad rows (about 5%). A centroid-finding readout system is distributed along each pad row [B.3]. As illustrated, the row of pads is resistively coupled (via a thin resistive film) and low-noise, charge-sensitive preamplifiers are spaced at intervals along the pad row. This readout spacing determines the accuracy of position measurement along the wire direction, and also determines the degree of segmentation of the device (number of output channels for a given detector area). The chamber affords precise position measurement along one coordinate (the centroid-finding direction), and coarser measurement determined by the wire spacing in the other coordinate. With the basic cell size of 2 mm, as illustrated here, and outputs spaced at 10 mm intervals along each pad row, the position accuracy is:

$$\sigma_z \leq 0.2 \text{ mm}$$
$$\sigma_\phi \simeq 1 \text{ mm}$$

The anode wires are not read out, and there is no drift time measurement. Each wire (pad row) can handle many tracks. The total occupation time per event (charge collection plus pulse shaping) is $\lesssim$ 300 μs, so that RHIC event rates are easily accommodated.

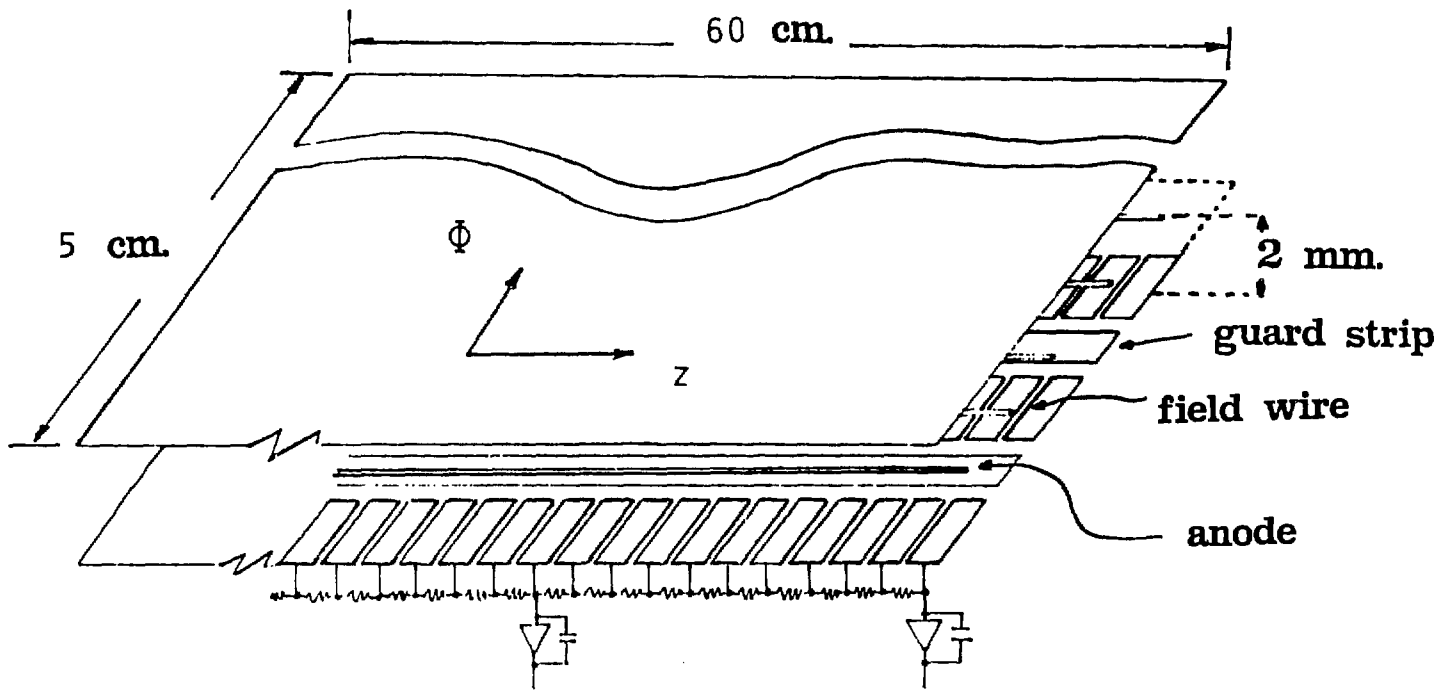

Fig. B.2 Exploded view of a pad chamber detector module (inner plane).

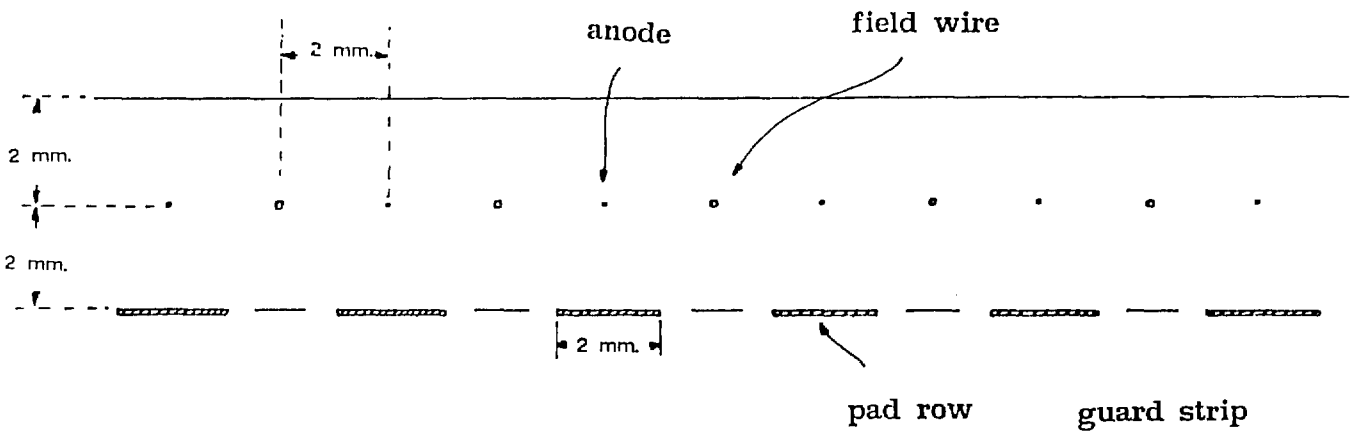

Fig. B.3 Basic cell geometry of the vertex detector.

Prototypes of such detectors are currently being prepared for study by the E802 and E814 groups at BNL and HELIOS group at CERN [B.4]. By constructing the segmented cathode plane on thin layers of dielectric (such as Kapton), with foam stiffener for flatness, the total thickness of such a detector plane can be kept to less than 1% of a radiation length. These prototypes involve 500 to 1000 readout channels over active areas of 200-300 cm^2. Printed leads on the multi-layer cathode circuit are utilized to bring the pad signals to the edge of the detector, where the preamplifiers are mounted and connections are made to cables carrying the signals to pulse-shaping amplifiers and ADC units. The area occupied by these components on the periphery of the chamber typically exceeds the active area of the detector. The vertex detector described here has a total active area of approximately 9000 cm^2, and ~ 15,000 readout channels. Placed in its small cavity, this detector presents obvious difficulty in getting the signals out without introducing large additional "dead" volumes at the core of the muon spectrometer. The solution which we see as making this problem tractable is the further development of integrated "Microplex" circuits of the type which have been tested by the CERN-Stanford-Hawaii group [B.5]. Ideally, this would take the form of a small, monolithic chip which could be mounted directly on the cathode plane with each chip providing amplification, analog memory and multiplexed output for a few hundred pad channels. The development of such circuits, capable of continuous operation at high rates, and at low cost, is a subject receiving considerable attention for many applications [B.6], and clearly stands high on the list of R&D priorities for RHIC.

APPENDIX C. MUON PAIR EVENT GENERATOR

To study detector acceptance and resolution under somewhat realistic conditions we have developed a Monte Carlo event generator for dimuon production. The basic ideas are outlined below.

As a starting point, dimuons are generated following the theoretical work of Kajantie et.al.[7.1]. To be specific, we assume collisions of Au + Au at 100 GeV/nucleon energy in each beam and focus on dimuon production as predicted from a quark-gluon plasma formed at T = 250 MeV with a critical temperature T_c = 160 MeV (see, e.g., Fig. 3b of Ref. 7.1). Dimuon production from a mixed phase, a pion gas or from other (background) sources such as Drell-Yan could easily be incorporated should the need arise. In the dimuon mass range 0.5 < M < 6 GeV the dimuon spectrum is simply parameterized as

$$\frac{dN}{dy\ dM\ dE_T} = 2\ M\gamma e^{-\gamma E_T}(\alpha_1 e^{-\alpha_2 M} + \beta_1 e^{-\beta_2 M}) \qquad (C.1)$$

Typical parameters, following Ref. 7.1, are γ = 4.7 GeV^{-1}, α_1 = 30 GeV^{-2}, α_2 = 6 GeV^{-1}, β_1 = 0.13 GeV^{-2} and β_2 = 2.4 GeV^{-1}. This parameterization implicitly assumes a rapidity plateau and scaling (y-independence) of the mass and E_T distributions. The rapidity range is an input parameter of the program and most calculations were performed with dN/dy = const. for -4 < y < 4. Since the dimuon decay angular distribution may contain information about whether the dimuons were thermally produced or result from (direct) Drell-Yan production, we have incorporated the possibility of an angular anisotropy of the form

$$\frac{ds}{dcosj} = 1 + \lambda\ cos2j \qquad (C.2)$$

The anisotropy parameter λ can vary in the range $1 > \lambda > -1$. Recent studies of Drell Yan production deduce [7.1] λ = +1 for the continuum. For J/ψ production one expects λ = 0 except for values of (Feynman) X_F near 1, where recently [7.1] λ = -0.8 has been observed. Of course, one expects λ = 0 for production following quark-gluon plasma formation.

Since present interest in dimuon production focusses on the question whether or not resonances such as J/ψ are suppressed in the plasma

environment, we have also included in the event generator the possibility of resonant production.

To illustrate the kinematical conditions a dimuon detector at RHIC has to deal with, we present, in the next few figures, some of the results from this event generator. In Fig. C.1 is shown the muon energy in the laboratory system as a function of dimuon rapidity. Muon energies ranging from a few GeV to nearly 100 GeV are typical and indicate the broad dynamic range to be covered by such a detector. Relevant for acceptance studies is the correlation in angle between the two muons as shown in Fig. C.2 for a muon rapidity interval $3 < y_{lab} < 4$ corresponding to an angular range $2.1 < j < 5.7^{\circ}$. From this figure one can see that small opening angles among the muon pairs dominate but one also observes a rather sizeable tail out to larger opening angles. Note also that this distribution in angles depends on the angular anisotropy of the decay of the dimuon pair: compare, e.g., Figs. C.2a and C.2b.

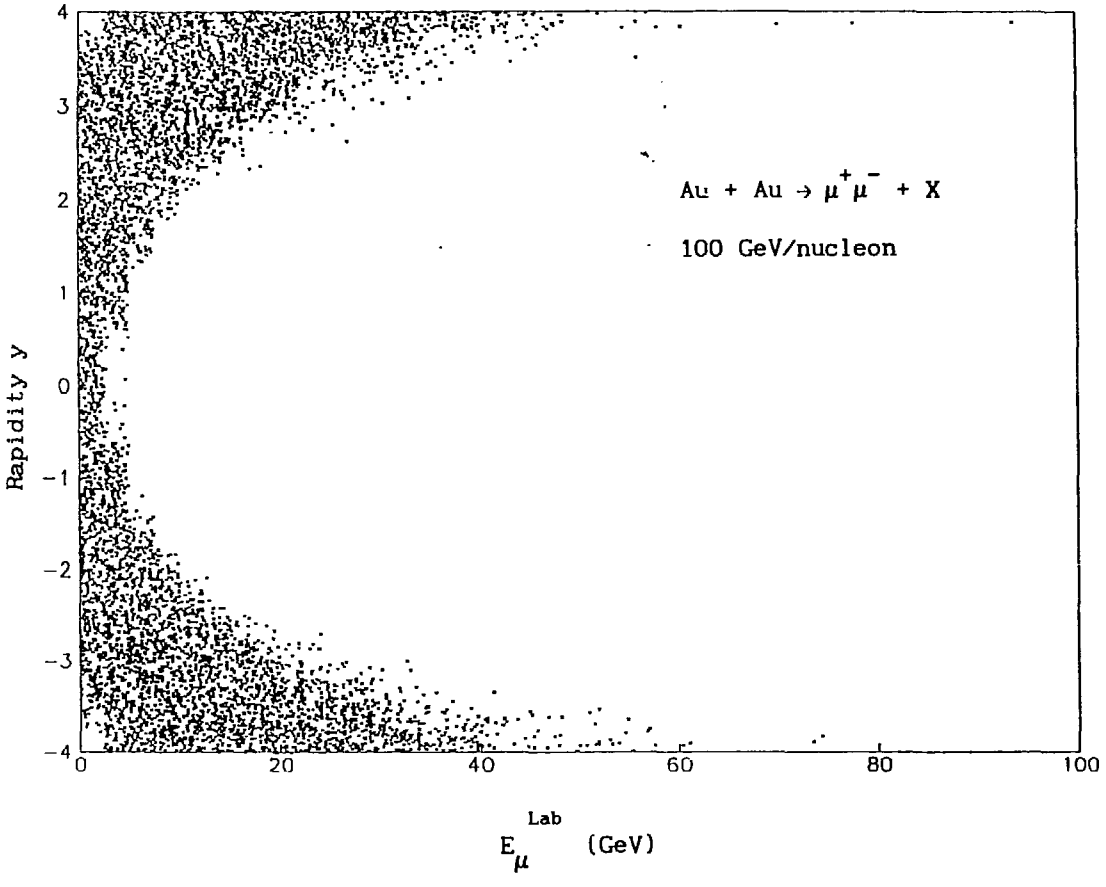

Fig. C.1 Muon laboratory energy as a function of the rapidity of the pair.

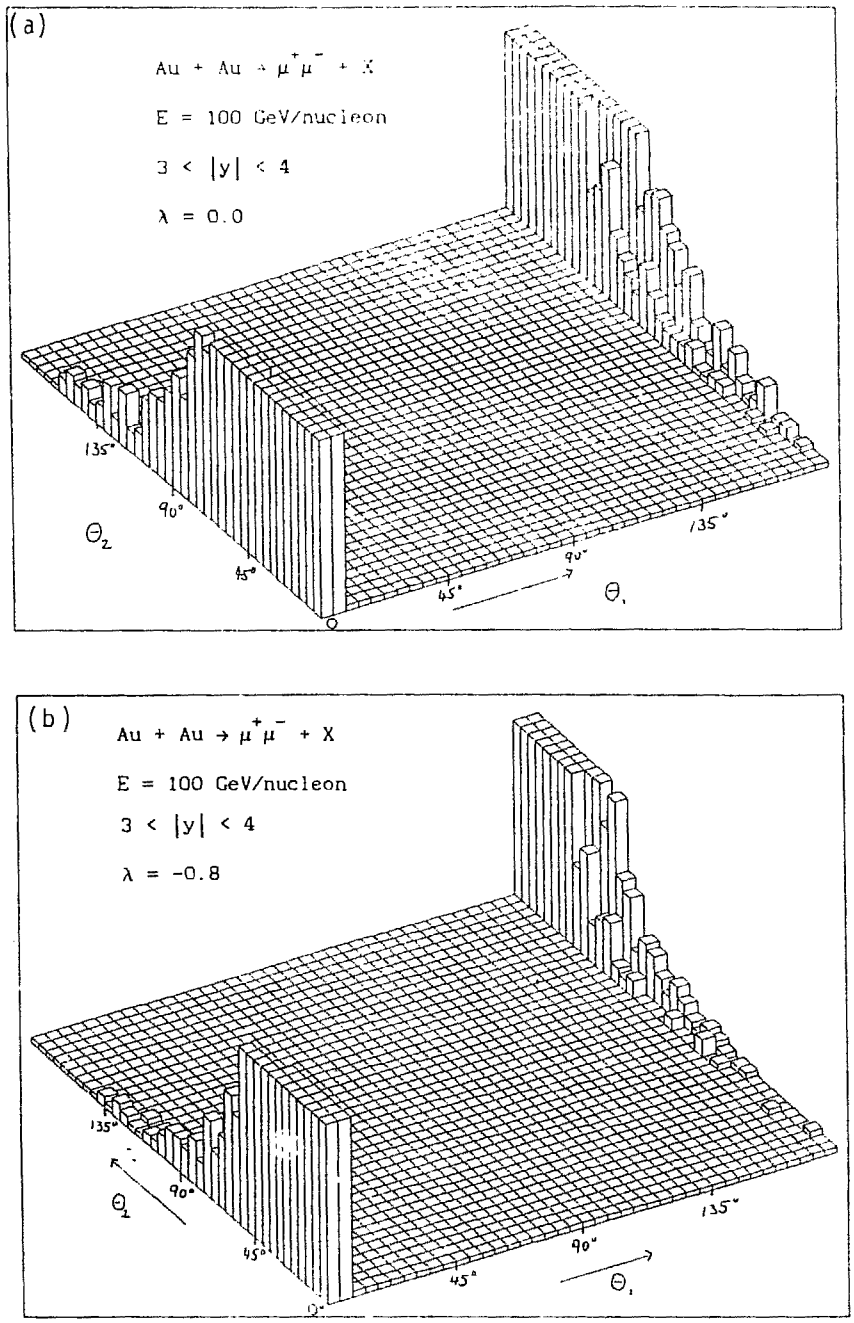

Fig. C.2 Angular correlation between the muons of a pair at high rapidity.
(a) $\lambda = 0$, i.e., isotropic production
(b) $\lambda = -0.8$, typical of Drell-Yan production.

REFERENCES

1.1 S. Aronson, G. Igo, B. Pope, A. Shor, and G. Young, Proc. RHIC Workshop: Experiments for a Relativistic Heavy Ion Collider, BNL 51921 (referred to below as "RHIC85"), p.171 (1985).

2.1 T. Matsui and H. Satz, Phys. Lett. B178, 416 (1986).

3.1 N. S. Craigie, Physics Reports 47, 1 (1978).

3.2 C. Grosso-Pilcher and M. J. Shochet, Annual Review of Nuclear and Particle Science 36, 1-28 (1986).

4.1 A.Shor, these Proceedings.

5.1 T. Ludlam, A. Pfoh, and A. Shor, RHIC85, p.373.

6.1 T. Ludlam, et al., E802 note, October 1985, (unpublished).

6.2 M. Albrow, et al., these Proceedings.

6.3 A. Baldit, et al., "Study of High-Energy Nucleus-Nucleus Interactions with the Enlarged NA10 Dimuon Spectrometer," Proposal 211 to the CERN SPSC, SPSC/P211 (March 1985) and SPSC/P211/Add 1 (July 1985).

7.1 K. Kajantie, J. Kapusta, L. McLerran, and A. Mekjian, "Dilepton Emission and the QCD Phase Transition in Ultrarelativistic Nuclear Collisions," RHIC-PH-11 (June 1986).

B.1 For gold beams at full luminosity the r.m.s. length of the luminous interaction region, as given by the RHIC Conceptual Design Report (May 1986), is 24 cm. at injection time and grows to 74 cm after 10 hours of operation. This length can be reduced by operating with a non-zero beam crossing angle, but the luminosity is then reduced. See Section 8 above. The general problem of the interaction region size and possible enhancements of performance are discussed elsewhere in this volume by Hahn, Lee and Ruggiero.

B.2 We have not considered in detail the question of noise due to backscattering from the calorimeter/absorber (albedo). The calculations of A. Gavron (RHIC Physics note RHIC-PH-23) indicate that this will be a few percent offset, which will not be a serious distortion for our purposes.

B.3 V. Radeka et al., Nucl. Instrum. & Methods 178, 543 (1980).

B.4 T. Ludlam, W. Willis, private communication.

B.5 C. Adolphsen et al., Nucl. Instrum. & Methods A253, 444 (1987).

B.6 V. Radeka, Introduction to the 1986 Munich Symposium on Semi-conductor Detectors and Readout Electronics, Nucl. Instrum. & Methods A253, 309 (1987).

LEPTON PAIR SPECTROSCOPY FOR RHIC *

P. Glässel and H. J. Specht
Universität Heidelberg, Federal Republic of Germany

1. Introduction

Continuum lepton pairs are among the most interesting signals to be studied in the search for a quark-gluon plasma in relativistic heavy ion collisions. In this paper we discuss the possibilities for electron pair spectroscopy at RHIC, based on the insights gained in Monte Carlo simulations and design studies for an electron pair spectrometer for the CERN HELIOS experiment.

In the first section, we shortly review the main results of our Monte Carlo studies[1 – 3] on the principal feasibility of electron pair spectroscopy below masses of 1 GeV/c^2 in the presence of the unavoidable combinatorial pair background from π-Dalitz decays and γ-conversions. These studies have been performed both for the fixed target situation at the SPS[1,2] and with special attention to RHIC[3].

In the next sections, we present additional Monte Carlo results on the combinatorial backgound using purely geometrical cuts for the low mass pair rejection, on the background situation at masses above 1 GeV/c^2, and on the evaluation of inclusive electrons. Acceptances for geometries with partial azimuthal coverage, which could be of interest for general-purpose detector systems at RHIC, are also discussed.

The following section contains the hardware concept of the HELIOS electron pair spectrometer and the line of reasoning which led to the choice of "hadron blind tracking" with two Ring Image Cherenkov (RICH) detectors. Some prototype results for these detectors are also given[4]. In the final section, we propose a direct adaptation of this concept to RHIC, including some considerations on possible magnet configurations and overall performance limits.

2. Basic Monte Carlo results

Extensive Monte Carlo calculations have been reported in refs. 1 - 3; they will be only shortly summarized here. As a signal, the "anomalous" pair continuum in the mass range $0.2 \leq m_{ee} \leq 1$ GeV/c^2 known from p-nucleon collisions[5] was chosen; the signal was scaled to AA collisions by keeping the ratio e^+e^-/π° constant. The background was defined as the combinatorial background of residual higher-mass pairs after low-mass pair rejection. As shown in Fig. 1, the resulting signal-to-background ratio S/B depends on the local charged

* supported by BMFT under contract no. 06HD983I/0

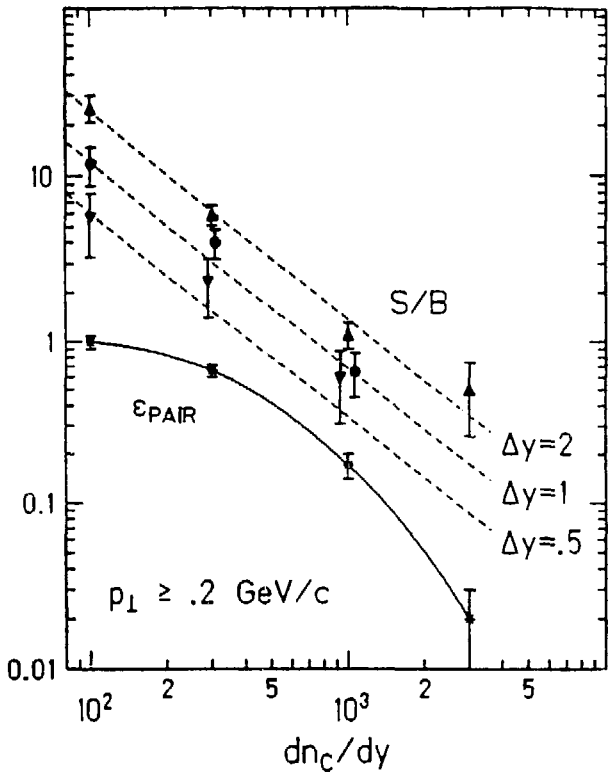

Fig. 1: Signal/combinatorial background for varying rapidity coverage (upper curves) and pair finding efficiency ε_{pair} (bottom curve) as a function of charged rapidity density. The cut $p_\perp \geq 200$ MeV/c is employed. (From ref. 3)

rapidity density dn_c/dy and the rapidity acceptance Δy, scaling roughly as

$$\frac{S}{B} \propto \Delta y \cdot \left(\frac{dn_c}{dy}\right)^{-1}$$

for azimuthally complete geometries with $\Delta y \lesssim 2$. For example, considering an ideal detector with $\Delta y = 1$ at $dn_c/dy = 200$ – an uppermost value for ^{32}S on a heavy target –, the ratio is $S/B = 5$. For a more realistic case with 1% conversions, 95% track efficiency and a lower threshold at $p_\perp = 10$ MeV/c, the S/B ratio reduces to ~ 1.

Recent results on the E_T-dependence of lepton pairs in pp collisions at ISR energies[6] exhibit a production rate $N_{e^+e^-} \propto N_\pi^2 \propto E_T^2$. If we assume a production of pairs proportional

to a volume $R_\perp^2 \cdot \tau_0$ with τ_0 constant, then

$$N_{e^+e^-} \propto N_\pi^2 \cdot A^{-\frac{1}{3}}$$

might provide a more appropriate scaling to AA collisions[7]. Such a dependence would improve the S/B ratio by factors, but in order to stay conservative, we have thus far ignored it in the estimates.

3. Geometrical low mass pair rejection

The crucial role of high detection efficiency, low threshold and a veto area larger than the fiducial area for the rejection of trivial low mass pairs have been discussed previously[1 – 3]. In the Monte Carlo simulations reported above, full 4-momentum knowledge was assumed for all electrons (in the following, the term electrons will be used for electrons and positrons). In a practical design, the simultaneous fulfilment of all these requirements will be extremely difficult, since low momentum threshold and good resolution at large momenta are hard to reconcile using magnetic field tracking.

The way to circumvent this problem is to do low mass pair rejection using purely geometrical information, i. e., using the undeflected direction of the electron tracks without knowing their momenta or charges. In such a scheme, one needs a highly efficient first electron-identifying detector close to the target *before* any magnetic field opens soft pairs. The efficiency and threshold of the second tracking device after the field, used to measure the particle momenta and charges of the interesting electrons surviving the low mass pair rejection, is then less critical.

The pair filtering algorithm used in this modified simulation contains the following steps:

1. Remove *all* electrons that have a pair angle with *any* other electron less than Θ_1. Θ_1 depends on rapidity; 6 to 10° is a reasonable value at $y_{lab} = 0$. This cut removes all conversions and a good fraction of the Dalitz pairs.
2. Remove pairs in the order of increasing pair angle up to Θ_2, with $\Theta_2 \approx 2\Theta_1$. This cut removes most of the more open Dalitz pairs.
3. For the remaining electrons a cut $p_\perp \geq .2$ GeV/c is applied. (The same cut was used in refs. 1 - 3 in order to improve the signal-to-background ratio). The pair mass is reconstructed assuming knowledge of charge and 4-momentum.

With this procedure, the combinatorial background increases by a factor of ~ 2 compared to the results in refs. 1 - 3.

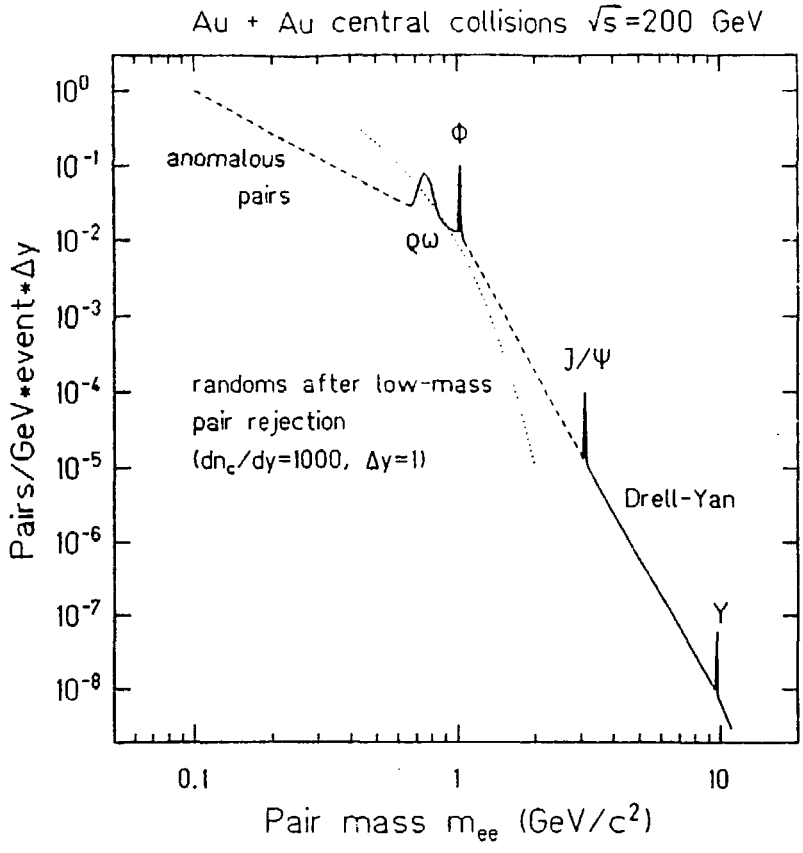

Fig. 2: Signal and background for Au + Au at $\sqrt{s_{pp}} = 200$ GeV/c^2 central collisions (schematic), assuming $dn_c/dy = 1000$ and an acceptance of $\Delta y = 1$. The signal contains the known sources including the anomalous lepton pair source scaled from pp as in refs. 1 - 3.

4. Combinatorial background for $m_{ee} > 1$ GeV/c^2

The Monte Carlo evaluation of the combinatorial backgound at higher masses was done using the following method to circumvent the problem of low statistics at high pair mass. It was found that the spectral shape of the combinatorial mass spectrum (above $\sim$ .2 GeV/c^2) is unaffected by the low-mass pair rejection. The spectral shape was thus determined with good statistics up to $\sim$ 2 GeV/c^2 by doing all possible random combinations of electrons *before* low-mass pair rejection. The absolute scale was normalized to the combinatorial background below 1 GeV/c^2 obtained from the full pair rejection algorithm. The result is shown in Fig. 2 for the case of central Au + Au collisions assuming $dn_c/dy = 1000$. Below

the ρ/ω-resonance, the signal-to-background is ~ 0.2, at the ρ it is ~ 2, above 1 GeV the background falls much steeper than the signal.

5. Inclusive electrons

A measurement of inclusive electrons might be interesting from two points of view: (i) the electron pair signal due to new physics could be so strong that random combinatorial background produced by the signal itself would preclude a pair reconstruction; (ii) one could consider a small detector geometry suitable for singles only.

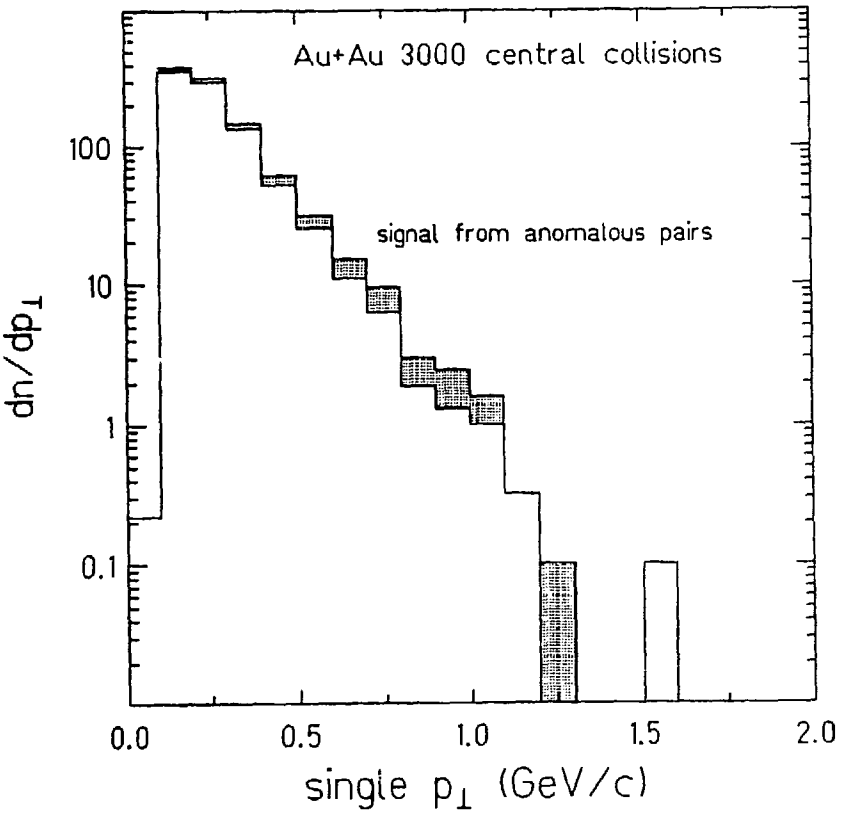

Fig. 3: Singles background remaining after low-mass pair rejection for central Au + Au collisions. The signal are singles from the anomalous pair source (hatched). A tracking efficiency of 95% and 1% conversions were assumed for the detector recognizing close pairs. Note that other hadronic sources like charm decays are not included in this simulation: the region above ~ 0.7 GeV/c is therefore not very realistic.

In the evaluation of non-trivial inclusive electrons, one would of course go through the same low-mass pair rejection algorithm. In that sense a strategy using a veto area larger than the fiducial for rejection is still needed, resulting in some minimal useful acceptance of a singles spectrometer. Monte Carlo simulations of the singles background using the same low-mass pair rejection algorithm as above led to the following general conclusions:

1. The signal-to-background ratio is independent of the fiducial acceptance, given sufficient additional veto acceptance.
2. The signal-to-background ratio depends only very weakly on dn_c/dy, in contrast to the situation for pairs, where the signal-to-background decreases approximately as $(dn_c/dy)^{-1}$.

Fig. 3 shows a comparison of the singles background due to Dalitz and conversion pairs – remaining after the low-mass pair rejection – and the singles from the anomalous pair source, demonstrating a reasonable signal-to-background ratio $\gtrsim 1$ for $p_\perp \gtrsim 0.5$ GeV/c. Note that the inclusive electrons have a clear advantage over direct photons in this range, since the trivial background from π°-originating pairs (which are always close) can be rejected to $\sim 90\%$, while in the photon case the background from $\pi^\circ \to 2\gamma$ (where the γ's have much larger opening angles) cannot be rejected at all in a high multiplicity environment.

6. Acceptances for geometries with partial azimuthal coverage

In the discussions about a practical design for an electron pair spectrometer, the conflicts with other components of the experiment and cost considerations may make it desirable to consider geometries with only partial azimuthal acceptance.

The most crucial feature of geometries with only partial azimuthal coverage is the problem of an inhomogeneous pair acceptance in the m_{ee} vs. $p_\perp$ (or $m_\perp$) plane. Fig. 4 shows acceptance maps for various geometries with the same total fiducial solid angle. Geometries with one about quadratic sector (b) are blind to large m_{ee}, geometries with two back-to-back sectors are blind to large $p_\perp$. Clearly, at least 3 or more sectors in φ are needed for an adequate coverage without essential information losses.

Fig. 5 shows a compilation of pair acceptances of various geometries vs. their total solid angles, calculated for the anomalous pair source for $m_{ee} > 0.2$ GeV/c^2 with the usual cut $p_{\perp single} \geq 0.2$ GeV/c. The acceptances roughly follow $\varepsilon \propto \Delta\Omega^2 = \Delta\theta \cdot \Delta\varphi$ (dashed line in Fig. 5), independent of the shape of the geometry. The combinatorial background scales approximately as $\Delta\Omega$, resulting in $S/B \sim \Delta\Omega$. Since, due to the integration over the whole mass spectrum down to 0.2 GeV/c^2, the inhomogeneities of the individual acceptances in the m_{ee} vs. $p_\perp$ plane are rather washed out in Fig. 5, proper judgement of a particular geometry can only be made with the additional information from Fig. 4. For a mass cut much higher

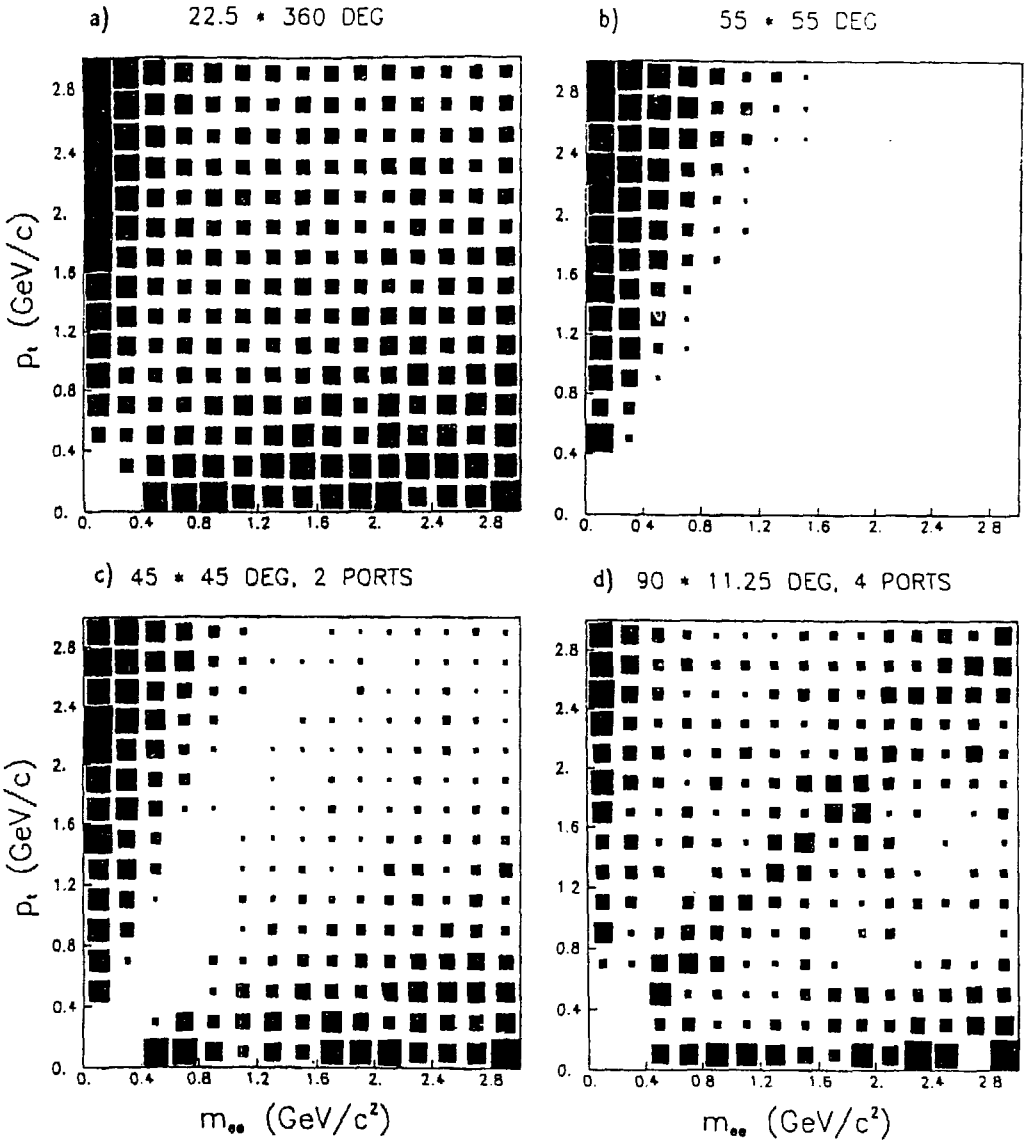

Fig. 4: Acceptance maps in $p_\perp$ vs. m_{ee} for the following geometries:
(a) full azimuthal coverage, $\Delta\Theta = 22.5°$ or $\Delta y = 0.25$
(b) One port with $\Delta\Theta = 55°$, $\Delta\varphi = 55°$.
(c) Two ports back-to-back with $\Delta\Theta = 45°$, $\Delta\varphi = 45°$each.
(d) Four ports at 90°, $\Delta\Theta = 90°$, $\Delta\varphi = 11.25°$

The total solid angle is the same for a, c, and d, for b it is 25% smaller. The acceptances correspond to the area of the boxes drawn, normalized to the case of full azimuthal coverage and $\Delta y = 1$. The full scales are 30, 15, 20, and 8.3% for a - d, respectively.

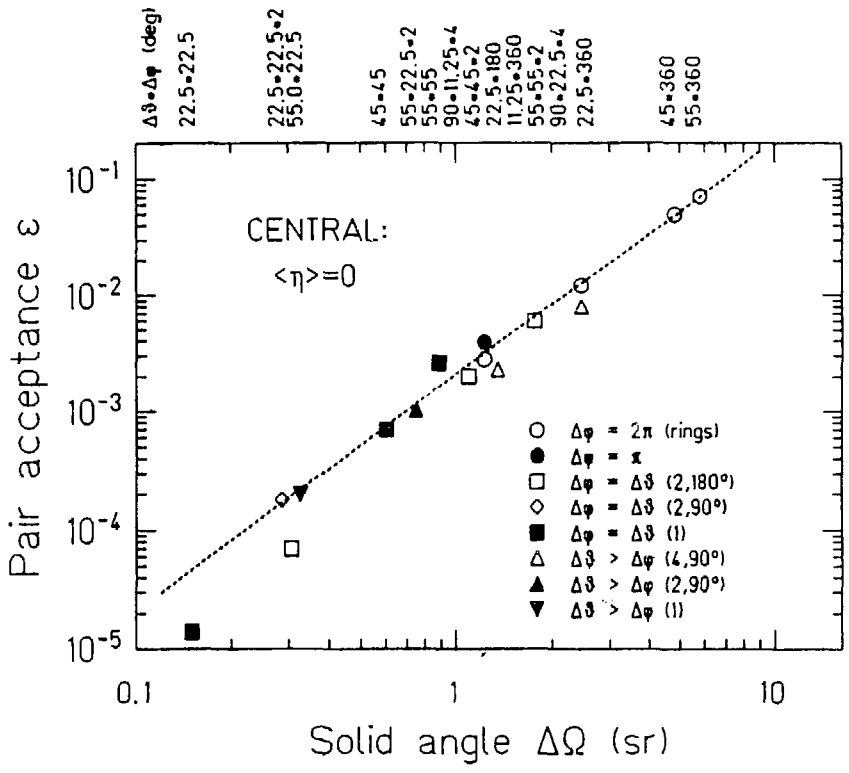

Fig. 5: Acceptance for anomalous pairs ($m_{ee} > 0.2$ GeV/c^2) vs. solid angle for various geometries. The sizes are listed above the figure. For the geometries consisting of more than one port, the number of ports and the angular separation of their centers in φ are noted for each symbol. Normalization: all pairs created in $\eta = \pm 1/2$.

than 0.2 GeV/c^2, Fig. 5 would indeed not show such a universal scaling.

7. The HELIOS electron pair spectrometer

The extremely difficult problem of how to actually measure the electron pair continuum in the high-multiplicity environment of a nuclear collision has been under study within HELIOS for several years. As usual, conceptual ideas on hardware arrangements and Monte Carlo studies have influenced each other, and the Monte Carlo results presented above reflect somewhat the final convergence.

The original concept contained in the NA34/2 proposal[8,9] consisted of a Ring Image Cherenkov (RICH) detector for electron identification, a ring of BGO crystals for energy-momentum determination, and a weak-field dipole magnet together with a Si-detector before, and a pad detector after the magnet for charge determination. Azimuthal symmetry of the

acceptance was already obeyed. In the second stage of the evolution[1,2], the BGO matrix was dropped because of the prohibitive background from π^0-decay photons for beams heavier than ^{16}O. Energy-momentum determination by calorimetry was replaced by tracking, enforcing a higher field; the dipole was therefore replaced by an axial field arrangement to keep soft pairs in the acceptance. However, very severe problems now occurred in the matching of low-momentum tracks between the two tracking detectors, due to their sensitivity to the total charged multiplicity. In the third stage of the evolution[10], the concept of "hadron-blind tracking" on the basis of RICH detectors alone was introduced, discarding all conventional tracking chambers. This was made possible by the recognition (i) that sufficient angular resolution and π-rejection could be obtained in RICH's using radiator gases with unusually low chromatic aberrations together with read-out techniques consistent with such physics limits, and (ii) that low-mass pairs could be sufficiently well rejected *before* the magnet with angular cuts alone (in a detector sensitive to electrons *only*), making it unnecessary altogether to track low-momentum electrons through the magnet and thereby completely eliminating the matching problem (which persists, on some level, even among electrons alone in extreme high-multiplicity events).

The lay-out of the double-RICH spectrometer is shown in Fig. 6. The angular acceptance, still 2π in azimuth, covers polar angles of 13 - 16° (veto) for the first RICH and 15 - 22° (fiducial) for the second RICH. Both RICH's have spherical mirrors centered on the beam axis, with a focal length larger than the target-mirror distance, resulting in positions of the UV-photon detectors at backward angles in a region of low particle density. Fortuitously, the focal surface is practically flat for this arrangement.

The magnet system consists of two short superconducting coils and an outer warm correction coil. The (opposite) currents of the two cold coils are chosen such that the fringe fields towards the target side cancel to first order. The particle tracks in the radiator of the first RICH are thus not deflected, a necessary condition for sharp ring images. The total flux of the two coils exits to the right and is shaped by the correction coil to be parallel to the particle tracks, which therefore are again not deflected (to first order) in the radiator of RICH 2. (The second-order deflection towards the beam axis is negligible for the momenta of interest in RICH 2). The deflection in the φ-direction is thus concentrated in this arrangement to the narrow space between the two RICH's, resulting in a simple momentum measurement from the observed azimuthal angle difference $\Delta\varphi$.

The overall momentum resolution of the system is determined by the intrinsic physics limits, i. e., chromatic aberrations and multiple scattering. With overall ring center resolutions of order $\delta\Theta \sim 0.5$ mrad and realistic field integrals, a relative mass resolution of $\delta m/m \sim 5\%$ at the ρ-mass may be achievable.

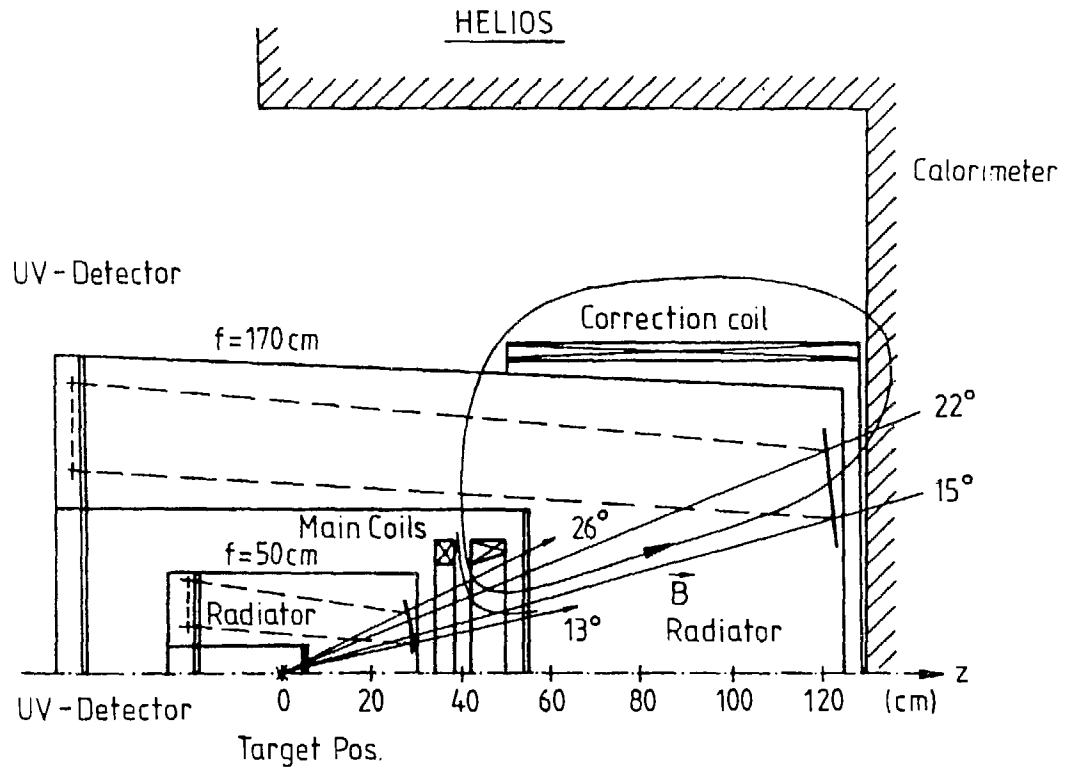

Fig. 6: Setup of the HELIOS electron spectrometer. The arrangement is axially symmetric about the beam.

A vigorous development program on the appropriate RICH UV-detectors has been pursued over the last two years in collaboration with the Weizmann Institute. Excellent results have been obtained with low-pressure gas detectors (as pioneered by Breskin), operated with C_2H_6 and TMAE as the photosensitive agent, and using two-step amplification together with additional gate electrodes[4]. Several advantages make this superior to any other choice: low dE/dx and thus low sensitivity to the residual (backward) flux of charged particles, further reduction of sensitivity to background (e. g., low-energy γ-rays, electrons, etc.) through the gated mode of operation, high gas gains, minimization of the photon feedback problem. Three read-out schemes have been successfully tested[4]:

- An xy(u)-coordinate read-out of crossed anode and cathode planes (using FADC's during the test stage)
- An optical read-out of the visible light emitted from the final stage avalanche via a system of lens, image intensifier and CCD (using a commercial video scan in the tests)

- A true two-dimensional electronical read-out with anode pads (2.54 × 2.45 mm) based on a 128-channel preamplifier chip with analog storage on the chip and serial read-out.

The Cherenkov rings seen with all three methods from a several GeV electron test beam are unusually clean, containing extra hits outside the ring on a level of < 0.05/ring area, a feature rather vital for pattern recognition. The optical and the pad read-out are superior to the xy-method in terms of signal-to-noise ratio and multihit capability; both have actually been demonstrated, in the realistic environment of a high radiation level test zone, to have single electron detection efficiencies of $> 90\%$. In terms of simplicity, performance and cost, the two are competitive.

8. A possible RHIC electron pair spectrometer

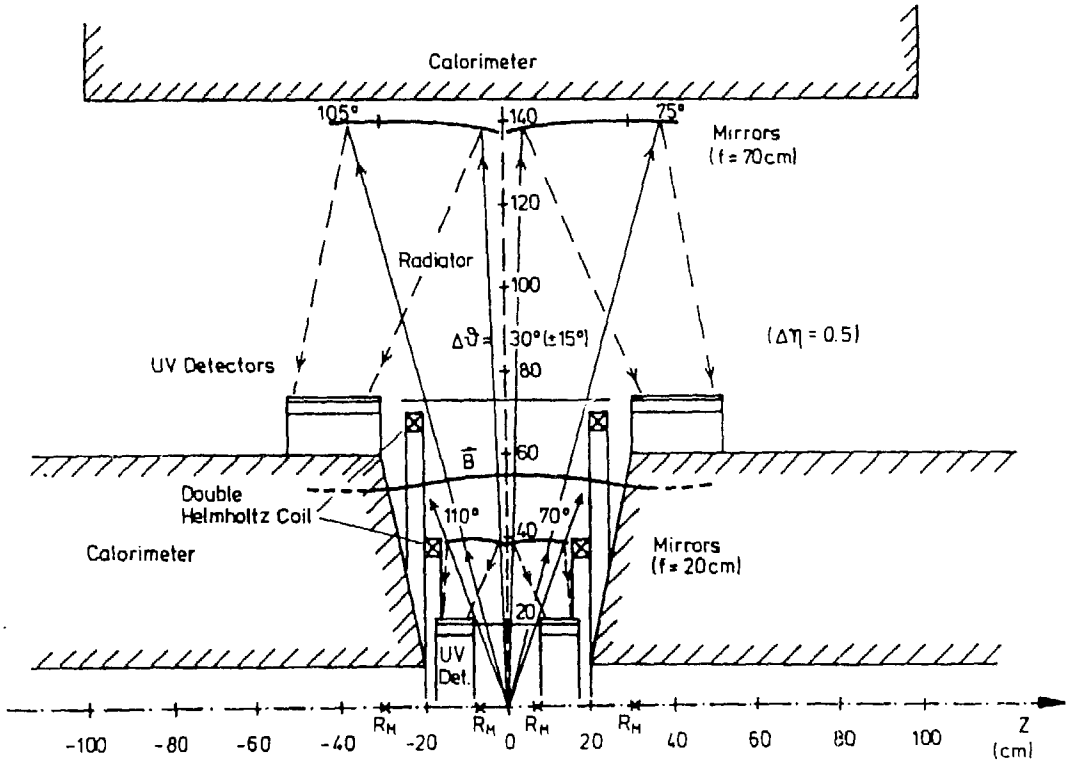

Fig. 7: A possible arrangement for an electron spectrometer for RHIC centered at $y_{cm} = 0$ with an acceptance of $\Delta\eta = 0.5$, rotationally symmetric around the beam axis.

A direct transfer of the double-RICH concept to a collider geometry, centered around 90° relative to the beams and covering again 2π in azimuth, is shown in Fig. 7. With the rapidity coverage of $\Delta\eta = 0.5$ ($\Delta\Theta = \pm 15°$) as drawn, the acceptance for the anomalous pair mass range $0.2 < m_{ee} < 1$ GeV/c^2 would be about 0.02. This is a factor of ~ 2 smaller than for the system of Fig. 6 (although the physical detector arrangement is much larger), reflecting the great advantage of "kinematical focussing" in a forward geometry.

The mirrors are parts of spherical surfaces such that the centers of the spheres lie on the beam axis, but are symmetrically displaced from $z = 0$ along the axis. This assures unsplit ring images (except at 90°), and allows to retract the UV-detectors out of the electron paths to minimize the problems of multiple scattering and pair production down to the limits dictated by windows and radiator gases. A slight further displacement of the sphere centers together with some widening of the UV-detectors in the z-direction would allow to accommodate an extended diamond region of ±5 cm without any acceptance losses, decreasing by a factor of > 2 towards ±10 cm. Rough estimates show the geometrical aberrations of the arrangement to be within the physics limits of chromatic aberrations and multiple scattering. The UV-detectors, forming short cylinder-like rings, are unavoidably exposed to the dense particle flux, but the low-pressure technique should still be adequate (although the outer detectors, situated behind a calorimeter of very few interaction lengths, do need some closer consideration). Pad read-out as mentioned above appears to be the preferred choice in such a non-planar geometry.

The length of the radiators (20 and 60 cm, resp.) together with the appropriate UV-windows (CaF_2 and quartz for the short and long RICH, resp.) should be sufficient to assure a realistic number of photoelectrons > 10 with heavy freons as radiator gases.
Two basic magnetic field configurations were considered.

(i) Two concentric pairs of Helmholtz coils with different coil radii R_{small} and R_{large}, centered on the beam axis, as shown in Fig. 7, allow to concentrate the field and thus the track bend in the region $R_{small} < r < R_{large}$. The field of the inner pair is adjusted to compensate the field of the outer pair for $r < R_{small}$. The field outside the large coil pair is rather small, it may be made even smaller by providing an appropriate flux return yoke. This Helmholtz coil solution has the advantage of keeping all shower-producing material outside the acceptance of the RICH's and is thus especially suited for geometries with large (or complete) azimuthal coverage. Due to the bulging of the field lines between the coils, the polar opening angle $\Delta\Theta$ is limited to $\sim 45°$, if the deflection is to be concentrated in a region with $R_{max}/R_{min} \lesssim 2$. An example of such a field for a polar opening angle of $\sim 45°$ is shown in Fig. 8 (without a return yoke), including the bending of 0.1 GeV/c tracks in this field.

(ii) For geometries split in several ports in azimuth, toroidal coils are possible. For free acceptance angles $\Delta\varphi \gtrsim 45°$, the same problem of bulging flux arises. The advantage is that the flux path is enclosed in the toroid.

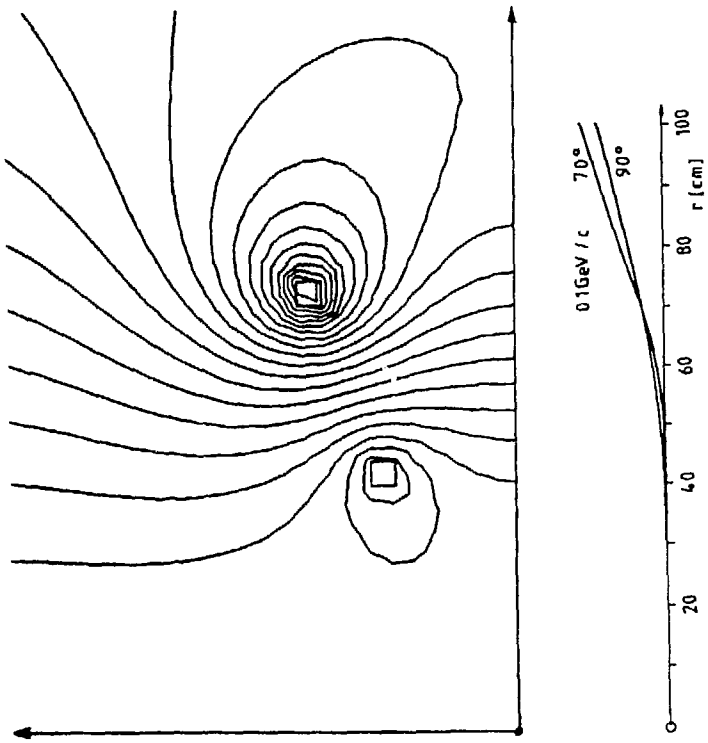

Fig. 8: Field of two coaxial Helmholtz coil pairs. The figure is axially symmetric about the lower boundary and reflection symmetric about the right boundary. V. Neumann boundary conditions were applied for the outer boundaries. The coils have 4×4 cm^2 cross section, centered at $r, z = 42, \pm 22$ and $72, \pm 34$ cm, resulting in a usable acceptance $\Delta\Theta \lesssim 45°$. The azimuthal deflection for $p = 0.1$ GeV/c tracks at $\Theta = 90$ and 70° is shown to the right. The currents are -106 kA and 160 kA for the inner and outer coils (requiring superconducting coils). For 1 GeV/c, the deflections $\Delta\varphi$ are 23 mrad at $\Theta = 90°$ and 31 mrad at $\Theta = 70°$.

Due to the lack of any Lorentz boost, the overall momentum resolution of the system is now more limited by multiple scattering than anything else, at least for masses < 1 GeV/c^2. With a field integral of 0.09 Tm as obtained in the sample case (Fig. 8), a relative mass resolution of $\delta m/m \sim 4\%$ at the ρ-mass can be expected.

9. Conclusions

A measurement of continuum electron pairs at RHIC appears to be difficult, but feasible. The basic ingredients have been discussed in the report. It is clear that a major additional effort is needed to elaborate the concept and incorporate it in a large, more general experiment.

Acknowledgement

We have benefitted from discussions with B. Willis and the RHIC Calorimeter (East) Group.

References

1. The internal electron spectrometer for NA34/2, HELIOS note 135, March 1986, unpublished
2. P. Glässel: Event simulation for the HELIOS electron pair spectrometer; Proc. 5th Int. Conf. on Ultra-Relativistic Nucleus-Nucleus Collisions, Asilomar 1986, Nucl. Phys. A461 (1987) 453c
3. P. Glässel, H.J. Specht, Proc. Workshop on Experiments for a Relativistic Heavy-Ion Collider, Brookhaven National Lab., Upton N.Y. (1985) p. 149
4. A. Drees, P. Fischer, P. Glässel, G. Lamade, H. Ries, E. Schmoetten, H.J. Specht, A. Breskin, R. Chechik, Z. Fraenkel, I. Tserruya, accepted by Nucl. Instr. Meth. A

   A. Breskin, R. Chechik, Z. Fraenkel, D. Sauvage, V. Steiner, I. Tserruya, G. Charpak, W. Dominik, J. P. Fabre, J. Gaudean, F. Sauli, M. Suzuki, P. Fischer, P. Glässel, H. Ries, A. Schön, H. J. Specht, Proc. Int. Conf. on Position-Sensitive Detectors, London 1987, to be published in Nucl. Instr. and Meth. A

   A. Breskin, R. Chechik, A. Drees, P. Fischer, Z. Fraenkel, P. Glässel, G. Lamade, H. Ries, D. Sauvage, A. Schön, E. Schmoetten, H. J. Specht, V. Steiner, I. Tserruya, 1987 IEEE Symp. Nucl. Science, to be published in IEEE-NS

   P. Fischer et al., 1987 IEEE Symp. Nucl. Science, to be published in IEEE-NS
5. K.J. Anderson et al., Phys. Rev. Lett. 36 (1976) 237

   S. Mikamo et al., Phys. Lett. 106B (1981) 428

   D. Blockus et al., Nucl. Phys. B201 (1982) 205

   M.R. Adams et al., Phys. Rev. D27 (1983) 1977
6. T. Åkesson et al., Phys. Lett. 192B (1987) 463
7. R.C. Hwa, K. Kajantie, Phys. Rev. D32 (1985) 1109

   M.I. Gorenstein, O.P. Pavlenko, Phys. Lett. 192B (1987) 198
8. H. Gordon et al., Proposal P189 to the SPSC, CERN-SPSC/83-51 (1983)
   H. Gordon et al., Proposal P203 to the SPSC, CERN-SPSC/84-43 (1984)
   accepted as NA34 and NA34/2 (HELIOS)
9. H.J. Specht, in Quark Matter 84, Helsinki, ed. K. Kajantie, Lecture Notes in Physics 221 (1987) 221, Springer, Heidelberg
10. An Electron Pair Spectrometer for Nuclear Collisions, Heidelberg-Weizmann, HELIOS note, 1987, in preparation

Tracking for Limited Solid Angles and the Mid-Rapidity Hadron Spectrometer

Shoji Nagamiya

Department of Physics, Columbia University
New York, NY 10027, U. S. A.

1. Introduction

About a year ago a working group called "tracking" was formed to study multi-particle tracking at RHIC (Convenors: C. Gruhn and S. Nagamiya). The group met a few times at BNL before the real Workshop was held in May. In these meetings two different approaches were proposed in the group; one to try to track all the particles over 4π solid angles by sacrificing particle identification, and the other to track a few hundred particles in the limited solid angles with full capability of particle identification. Let's call the former the "4π group" and the latter the "limited solid-angle group".

During the one-week Workshop period in May, new working groups were created based on the physics needs. The 4π group mentioned above was absorbed by a new group convened by S. Lindenbaum. On the other hand, the limited solid-angle group was absorbed mainly by the 2π tracking group convened by H. Gutbrod but also partly by the calorimeter group convened by C. Fabjian and M. Albrow. Although the major items which were discussed in the original "tracking" group were covered in these three new working groups, some items were not picked up by any of these three groups. The reason for writing this article is that I thought it appropriate to describe those items not covered by any of the three reports. This article is therefore a supplemental note to these reports. Contributors to this note are P. Bond (BNL), B. Knapp (Columbia), D. Kovar (ANL), Y. Miake (BNL), D. Shapira (ORNL), B. Shivakumar (Yale), J. Thomas (Caltech), and Koos van Dijk (BNL).

Tracking of charged particles, in particular multi-particle tracking, is not a trivial task. At RHIC the total multiplicity of charged particles in an event is expected to be on the order of 4000-8000[1] in the central Au + Au collision. On the other hand, the tracking of particles by electronic devices was, so far, successful up to multiplicity 10-20 but not more than

that. Considering this fact, the tracking of a few hundred particles is already a very challenging task.

Fig. 1 shows (a) the expected charged-particle distribution in rapidity (dM_{ch}/dy) and (b) the corresponding distribution of charged-particle density ($dM_{ch}/d\Omega$). It is clear from the figure that the tracking is the easiest at $y_{c.m.} \sim 0$ (that is, the angle of 90 degrees). As a first choice, therefore, we focus on the design of a spectrometer to cover the mid-rapidity region. This region is also interesting from the physics point of view, because rich physics related to quark-gluon plasma would mainly be expected there. Furthermore, we focus on the hadron detection, not only because this has been the main concern of our working group but also because it is in fact a very important element at RHIC.

Designing the "event trigger" is important for the entire game. According to recent data from CERN and BNL,[2] it seems that the total transverse

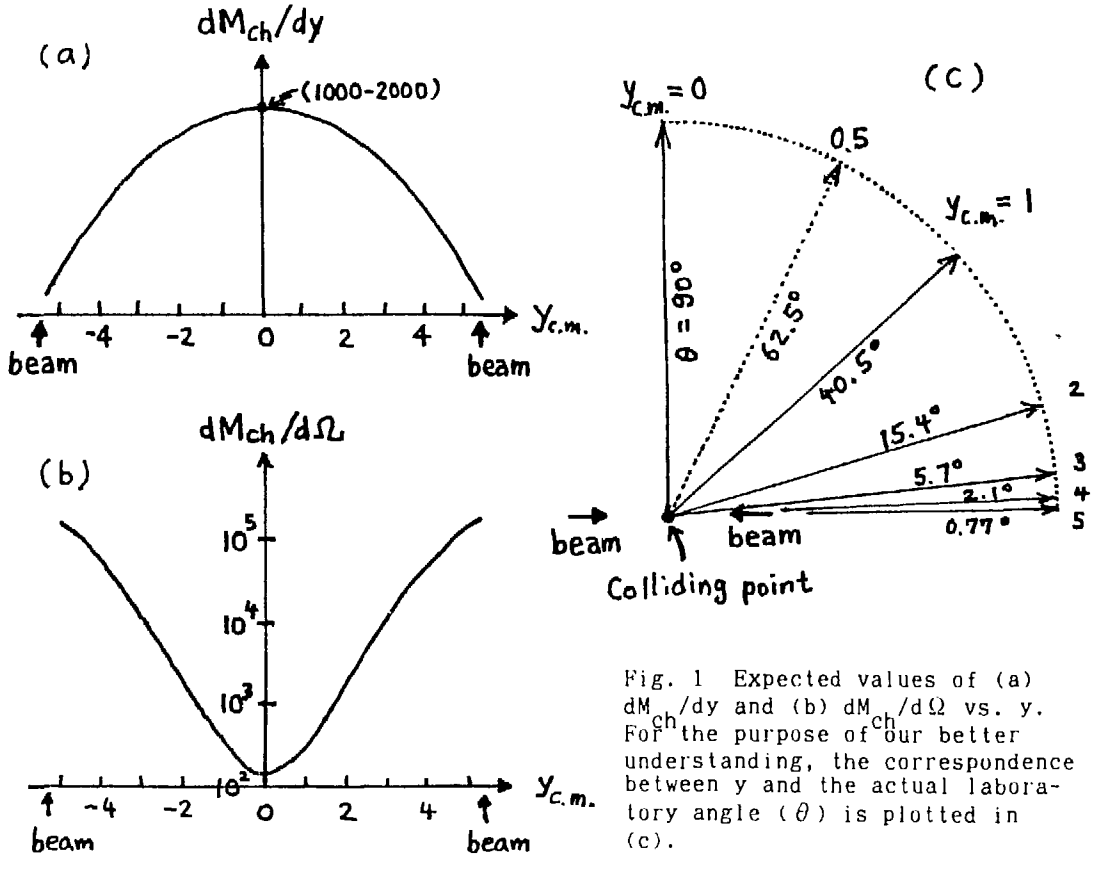

Fig. 1 Expected values of (a) dM_{ch}/dy and (b) $dM_{ch}/d\Omega$ vs. y. For the purpose of our better understanding, the correspondence between y and the actual laboratory angle (θ) is plotted in (c).

energy (E_T) is approximately proportional to the event multiplicity of charged particles (M_{ch}). Since it is expected that high event multiplicities correspond to central collisions, the event trigger for "high multiplicity" or "high transverse energy" would be crucially important to select a "central" collision. In other words, a preparation of either calorimeter to measure E_T or multiplicity array to measure M_{ch} is important for any type of research at RHIC. We assume that such a device will be prepared in addition to the hadron spectrometer discussed in this article.

When one studies each individual event, a fluctuation in E_T (or M_{ch}) as a function rapidity (y) might be expected. A reasonably well-segmented calorimeter is needed to detect this fluctuation. Furthermore, the detection of "jets" with the calorimeter would also be interesting. It requires a much finer segmentation of the calorimeter. This subject is discussed in detail in the report of Albrow and Fabjan, and will not be repeated here.

In Sec. 2 the physics goals of hadron spectroscopy are reviewed. In particular, various constraints to the detector design from physics requirements are discussed in this section. Then, an overview of the proposed system is presented in Sec. 3. The particle identification device is a very important element in the present system and it is discussed in Sec. 4. Preliminary thoughts about tracking are mentioned in Sec. 5. Finally in Sec. 6 the homework problems that we must study in the immediate future are listed.

2. Physics Goals and Their Constraints to Detectors

a) Spectra of Standard Particles

Measurements of energy spectra of $\pi^{\pm}$, $K^{\pm}$, $p^{\pm}$, $d^{\pm}$, etc. are always important when one starts to study nuclear collisions at new beam energies and new projectiles. In addition, the measurement of $\langle p_T \rangle$ for each particle species as a function of dE_T/dy (or dM_{ch}/dy) would be important, since it would provide one of the key signals for the formation of quark-gluon plasma.[3] In these measurements the following two points should be noted:

1) The behavior of $\langle p_T \rangle$ vs. dE_T/dy could be different from particle to particle. As the mean free path of K^+ in nuclear matter is the longest among others, it is likely that K^+ probes the earlier and thus hot stage of

the collision whereas particles like $\pi^{\pm}$ probe only the later expanded cold stage of it.[4] Measurements of $\langle p_T \rangle$ vs. dE_T/dy for K^+ would, therefore, be particularly interesting.

② If one accumulates a large number of events, the distribution of dE_T/dy would be a smooth function of y, as shown in Fig. 2a). However, in each event a significant fluctuation, as shown in Fig. 2b) or 1c), might be expected due to possible formation of local hot spots (or, they are called "quark nuggets"). In this case it is extremely interesting to study particle spectra or yields by gating the region of high dE_T/dy [Fig. 2b)] and the region of low dE_T/dy [Fig. 2c)], and to compare them to each other.

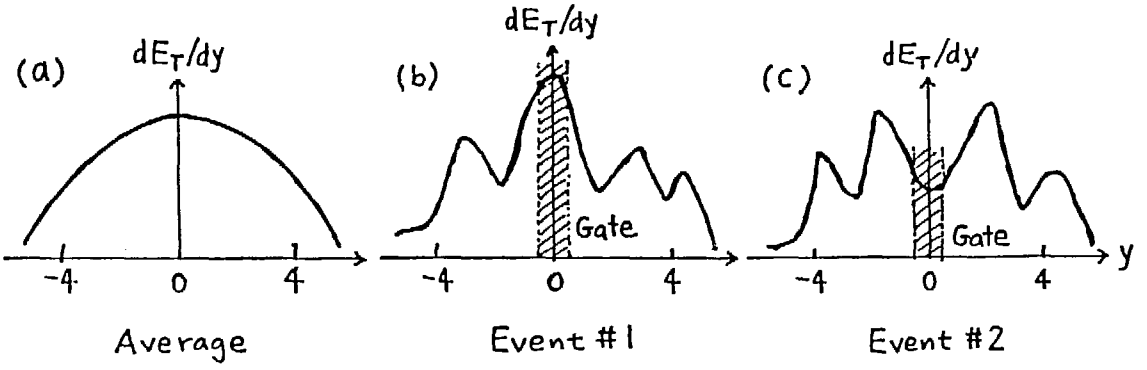

Fig. 2 Expected distributions of dE_T/dy for (a) the event average, and for (b)-(c) various individual events.

For these measurements the solid angle of the spectrometer need not be large. The spectrometer with $\Omega \cong$ 1-10 msr would be sufficient.

Fig. 3 shows an expected momentum distribution for pions.[5] We notice that most of the particles are clustered in the region of $p < 1.5$ GeV/c. This point is important for the evaluation of needed segmentation of a particle identification device, as described in Sec. 4.

b) Spectra of Specific Particles

It is believed that the yield of strange particles also provide a signal of the formation of quark-gluon plasma.[6] In particular, particles that contain $\bar{s}$-quarks, such as $\phi(s\bar{s})$ or $\bar{\Lambda}(\bar{u}\bar{d}\bar{s})$, are important.

Fig. 4 shows the decay kinematics of ϕ-mesons into K^+K^-, where it is assumed that ϕ's are emitted at $y_{c.m.} \cong 0$. Clearly, the coverage of $\delta y >$

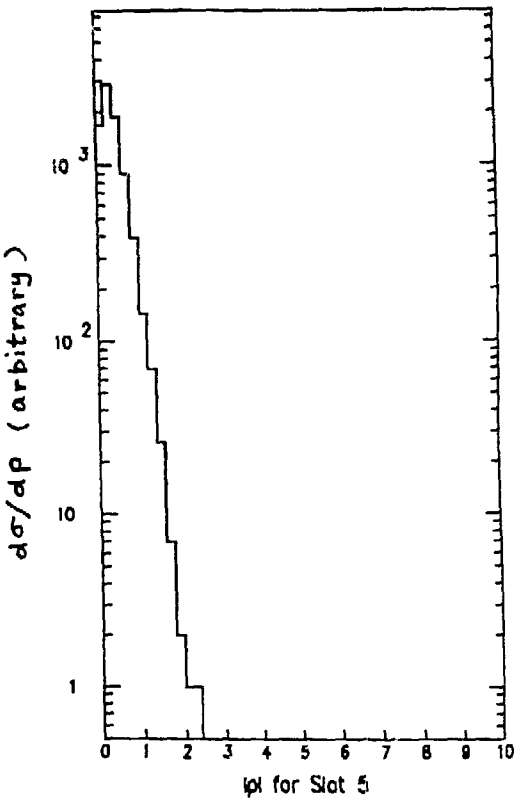

Fig. 3 (left) The expected momentum distribution of pions emitted at y ~ 0.

Fig. 4 (below) Decay kinematics of positive and negative kaons from ϕ mesons that are emitted at y = 0.

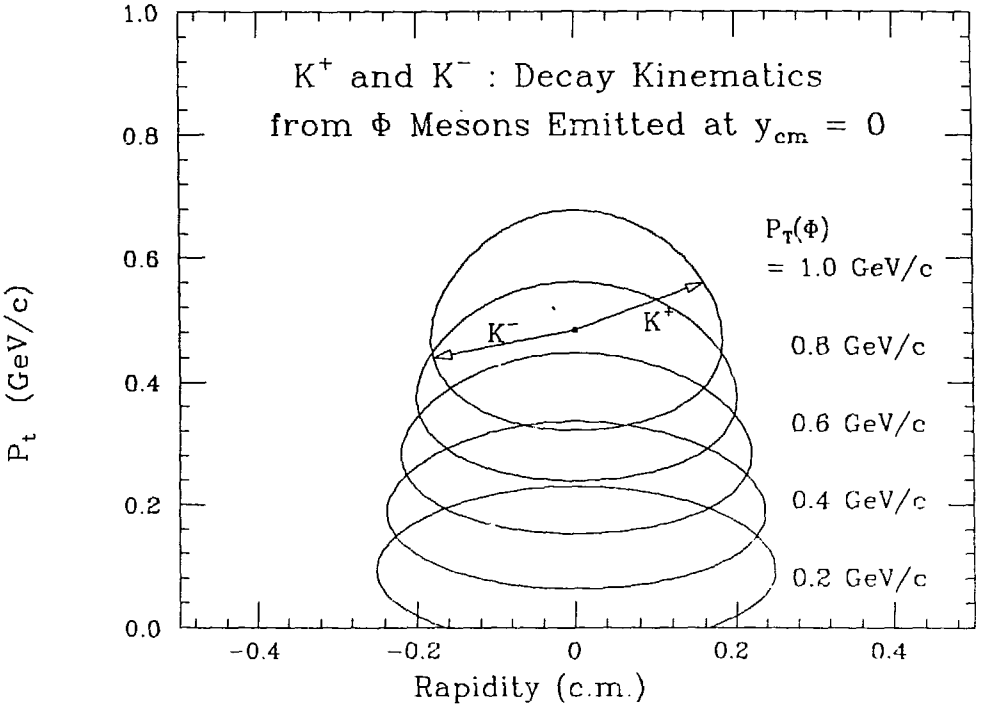

0.5 is required. In the space of azimuthal angle the coverage of $\delta\phi > 0.5$ is required as well. To attain a uniform acceptance over the kinematical domain of interest, it is reasonable to prepare a spectrometer to cover angles of $\Delta\theta \sim \Delta\phi \sim 1$, which corresponds to the spectrometer solid angle of $\Omega \sim 1$ sr. Note that $\Delta y \cong \Delta\theta$ in the region of $y_{c.m.} \cong 0$. A similar argument can be extended to the detection of $\bar{\Lambda}$.

A calculation is needed to test if the ratio of signal (of ϕ or $\bar{\Lambda}$) to noise (K^+-K^- random combinatorial background for the case of ϕ) is large enough so that it is practically possible to detect these strange particles. This point has not yet been studied but will be studied soon. An intuitive guess is that these resonances can be detected reasonably well because of small resonance widths.

c) Hanbury-Brown/Twiss Correlations

Hanbury-Brown/Twiss (HBT) correlations provide information on the size and shape of the reaction region. In a collider experiment it is expected that a majority of particles in the mid-rapidity region are from the baryon-free central region. This region would have a cylindrical shape elongated along the beam direction. In this case, however, the shape observed by the HBT correlations would not show a longitudinally elongated shape due to the fact of longitudinal growth (any pairs with small relative momenta are emitted with space-time separation of the order of 1 fm).[7]. Nevertheless, the HBT correlation measurements would be important for the study of space-time evolution of the system and possibly for the study of the coherence effect in heavy-ion collisions. In particular, two-kaon interferometry would be interesting, because the mass of the kaon is large so that the "space" and "time" separation can be attained more easily for KK than for $\pi\pi$.[7]

Since the width of the HBT correlations is on the order of 100 MeV/c, the measurement has to be done with momentum resolution of $\Delta q \cong 10$ MeV/c over the range of 300 MeV/c in q, where q is the relative momentum between two particles. It converts to momentum and angular resolution of $\Delta p/p \cong \Delta\theta/\theta \cong \Delta\phi/\phi \cong 1$ % and solid angle of $\Omega \sim 1$ sr.

d) Shape of High p_T Component and High-p_T Associated Correlations

In pp collisions the production of a high-p_T particle is often associated

with $q\bar{q}$ opposite-side jets. In quark-gluon plasma the temperature of the system can well exceed the Hagedorn limiting value of 140 MeV and, as a result, the production of high-p_T particles would be possible also from the chaotic source of quark-gluon plasma. It is interesting to study the spectrum shape in the high-p_T region at p_T up to 10 GeV/c. In addition, it would be interesting to study if azimuthal correlations remain for particles that are associated with the high-p_T particle production.

e) New Particles

RHIC would offer for the first time in history a collider of the total energy of 40 TeV in the center-of-mass frame in laboratory. That may lead to an observation of a new particle that has not been seen in the past. This interesting possibility should not a priori be excluded.

3. Zeroth-Order Idea of the System

Shown in Fig. 5 is the zeroth-order idea of the spectrometer system to attain the scientific goals described in the previous section. For the purpose of attaining goals b) and c) it is appropriate to prepare a spectrometer with solid angle of

$$\Omega \cong 1 \text{ sr}$$

which subtends angles of $\Delta\theta \cong \Delta\phi \cong 60$ degrees. This solid angle is also enough to attain goal a). The magnetic field of

$$\int B \cdot dl \sim 0.5 \text{ T} \cdot \text{m}$$

is reasonable for the momentum analysis, because, with this field combined with tracking detectors of a few 100 μm resolution, the momentum resolution of $\Delta p/p \sim 1$ % can be achieved.

In the region of $y_{c.m.} \cong 0$ the value of dM_{ch}/dy, where M_{ch} is mainly from pions, is about 1000-2000 (see also Fig. 1). This is equivalent to $n_c \cong (1000\text{-}2000)/2\pi \cong (150\text{-}300)/\text{sr}$. Note that $\Delta y \cong \Delta\theta$ in the region of $y_{c.m.} \cong 0$. We adopt the number of $n_c = 300/\text{sr}$ for a design criterion of the present spectrometer. These 300 charges are clustered in the region of $p <$ 1.5 GeV/c, as seen in Fig. 3, whereas in the region of $p >$ 1.5 GeV/c the

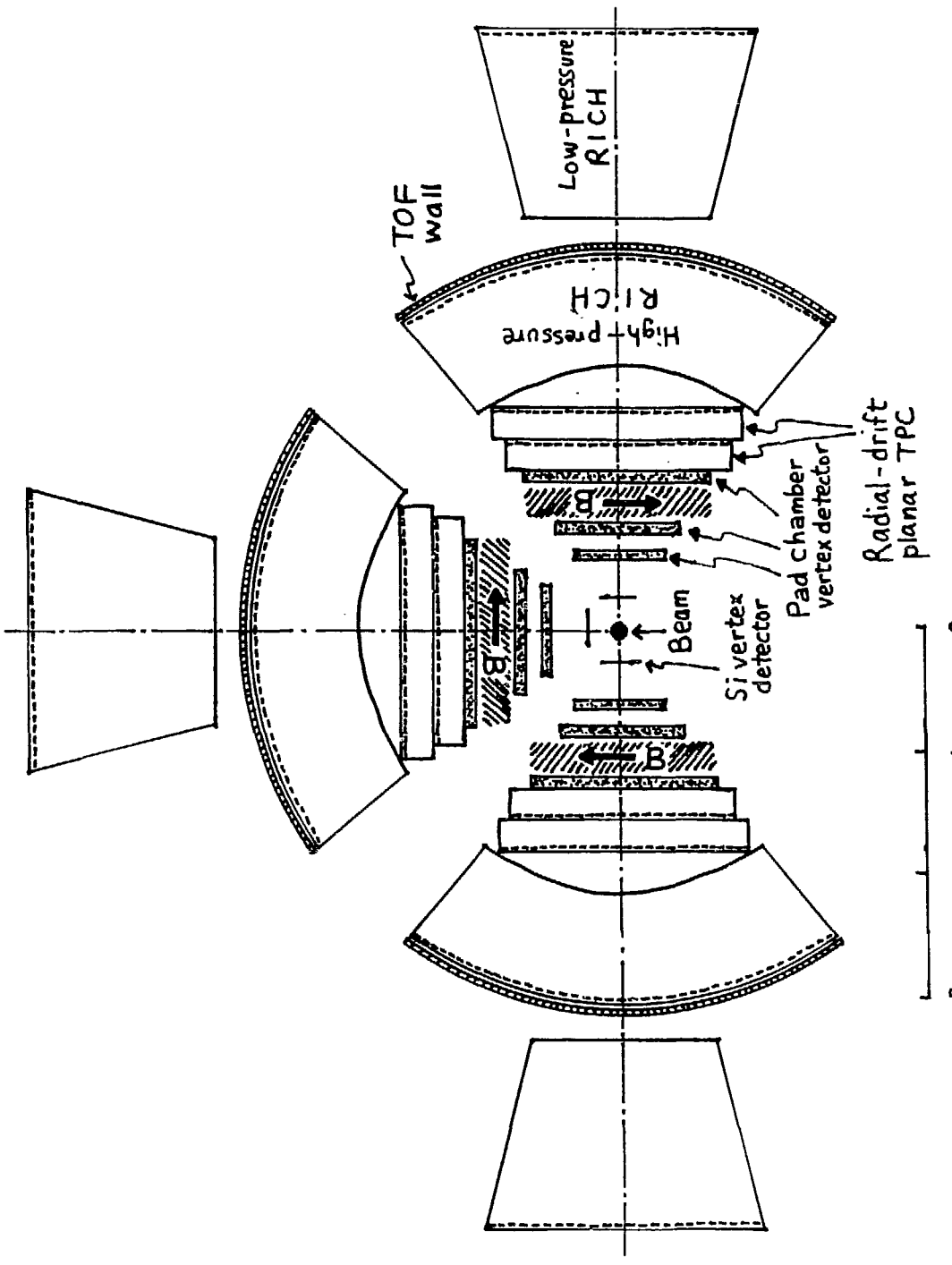

Fig. 5 Zeroth-order idea of the proposed system.

average multiplicity is less than 1.

In addition, for the purpose of attaining goal d), additional elements for particle identification up to 10 GeV/c would be needed. Furthermore, a three-arm spectrometer system would be reasonable with which to measure "in-plane" and "out-of-plane" particle correlations. Our final goal is set to prepare the three-arm spectrometer. For the purpose of e), additional particle identification devices such as those to detect high-p_T lepton pairs would be needed.

Evidently, the key questions here are (a) tracking and (b) particle identification. These are discussed in what follows.

4. Particle Identification

a) TOF Wall

Fig. 6 illustrates the capability of particle identification by the TOF wall that is installed at 3 m distance from the colliding point. If the TOF

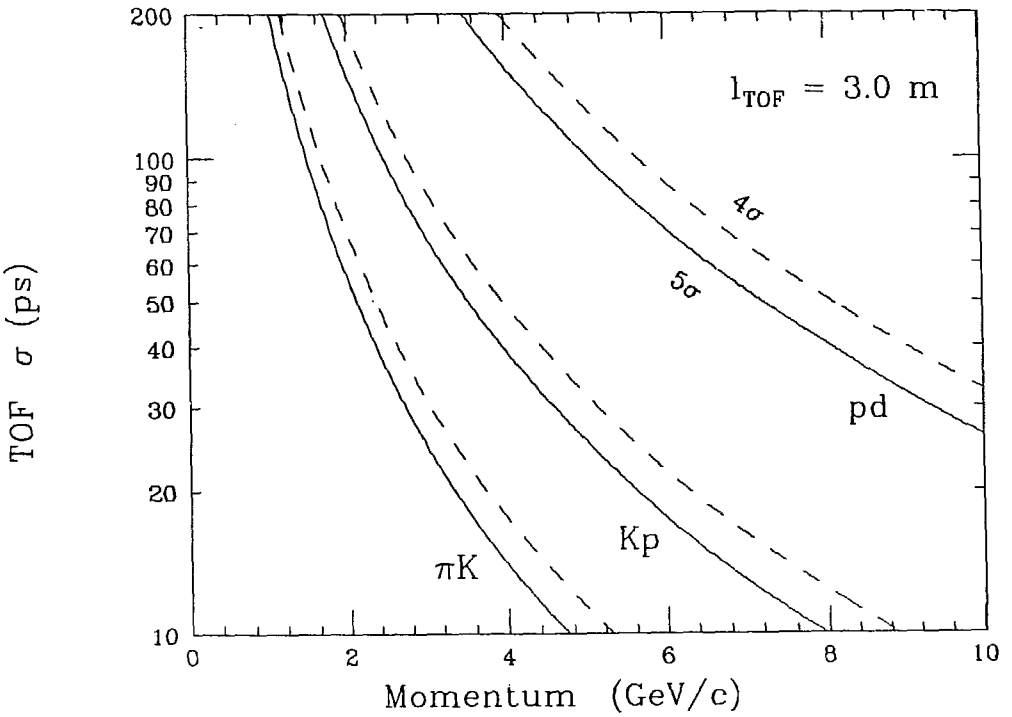

Fig. 6 Particle lν capability for TOF wall plotted in the plane of time resolution and momentum.

resolution is σ = 100 ps, which seems not unreasonable,[7] the 4σ separation requirement will allow π-K separation up to 1.6 GeV/c, K-p separation up to 2.8 GeV/c and p-d up to 5.7 GeV/c. As most of these particles are clustered in the momentum region below 1.6 GeV/c, a highly segmented TOF wall would be a first choice for particle identification.

The segmentation of this TOF wall is determined by two factors. One is by the resolution required for the HBT correlation measurement, which requires $\Delta\theta \simeq \Delta\phi \simeq$ 1 %. At the 3 m position, this is equivalent to the area of each counter of 3 cm x 3 cm $\sim$ 10 cm^2. The other comes from the multiplicity. In order to identify 300 charged particles at less than 0.5 % confusion probability, the needed segmentation would be about 6000. This converts in the area of each counter to be 300x300/6000 $\sim$ 15 cm^2. We therefore consider here 4 cm x 4 cm (1.5 inch by 1.5 inch) as a starting value for the design of each TOF segment.

Engineering ingenuity is required for the actual construction of this wall. If we use a standard TOF technique with a 3 m long scintillator with phototubes at both ends, each scintillator can have the width (and thickness) of only 0.5 mm to attain the required segmentation, which, of course, is not practical. Therefore, the most realistic way would be that shown in Fig. 7.

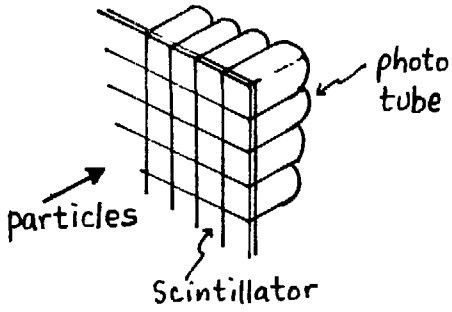

Fig. 7 Scheme of TOF wall.

Problems in this case are that

a) no particle identification instruments after the TOF wall may be installed due to electromagnetic multiple collisions of a particle with a phototube, and

b) Cerenkov light from the window of the phototube, which is superposed on the scintillation light, may distort the time resolution.

A preliminary test concerning the second point b) was performed at the BNL-AGS when we designed TOF counters for E802. This test result showed that even with the existence of the Cerenkov light from the phototube window the time resolution of σ = 120 ps was obtained. We should emphasize, however,

that more consistent and careful R&D work is needed concerning this point.

The first problem a) will be less serious than the second point b). However, in order to avoid this difficulty a possible scheme might be that a slab-type wall be installed for a limited portion of the entire wall.

b) Particle Identification for High-p_T Particles

As mentioned at the beginning, the multiplicity of particles whose momenta are larger than 1.5 GeV/c is less than 1. Therefore, the particle identification for high-p_T particles (p_T > 1.5 GeV/c) does not require any segmentation. RICH counter as sketched in Fig. 5 or a standard gas Cerenkov counter is an option for this purpose. In this proposal two types of RICH counters are proposed, one at high pressure to cover the momentum region above that which can be resolved by the TOF wall and the other at low pressure to cover high p_T region above 10 GeV/c. Details of the design, however, have to be done in the future.

c) How Many Arms?

We aim at constructing three arms to cover azimuthal angles of $(0 \pm 30)^0$, $(90 \pm 30)^0$, and $(180 \pm 30)^0$. Ideally, the three arms should be the identical ones, as shown in Fig. 5. However, for the practical purpose, one may also consider the option that the first arm is like what is described in this article but the second and third arms are much simpler ones such as highly segmented calorimeters.

5. Tracking

We have discussed various options for tracking. The following are possible candidates. Of course, before constructing actual detectors extensive R&D work is definitely needed. The AGS would be an ideal place to make a peformance test of prototype detectors, as the charged-particle multiplicity is (400-800)/sr at 5^0 in the central Si + Au collisions at 14.5 GeV/c per nucleon.

a) Radial-Drift Planar TPC

As discussed in the report by H. Gutbrod, this chamber has various merits. We do not repeat the discussion here, but the important point is that the conventional design of TPC in which the drift direction of electrons is

parallel to the beam direction is not appropriate at RHIC because of the long drift time (20-40 μs for 2 m), whereas the radial-drift planar-type chamber allows us to reduce this drift time by a factor of 10. Note that our design criterion for the counting rate is about 10^4/sec.

b) Pad Chamber Vertex Detector

We have also discussed the possibility of a pad chamber vertex detector. Details of this detector are described in the article by T. W. Ludlam of this Proceeding. Prototypes of this detector are currently under construction at both BNL and CERN. At BNL both E814 and E802 groups are constructing prototypes. Our E802 is planning to use it as a chamber located at about 1 m from the target. About 500 pads over the area of 10 cm x 20 cm are currently being constructed, and over this area the multiplicity up to 20 would be expected.

c) Si Vertex Detector

The solid-state vertex detector has recently started to be used in collider experiments. The advantage of this is it can handle a very high particle density per unit area. On the other hand, a shortcoming is that it is difficult to make a detector of large dimension. As a supplemental detector in the inner region close to the interaction point, this detector might be useful.

d) Multi-Layer Drift Chambers

B. Knapp[8] has recently succeeded at BNL to track events of multiplicity 10-15 including V-particles with conventional drift chambers (Experiment E766). A great achievement of this group is that multi-particle tracks of this type were analyzed with a special processor within a short time on the order of 2 μs. It means that this quick analysis can be used as an event trigger in their experiment.

We have studied if this projective geometry can be used for the tracking of 300 charged particles. Work is still going on, but no definite conclusions have been obtained. Since the analysis time increases sharply as the particle density per cm^2 increases, it would be wise to use this type of chamber in the outer region far from the interaction point.

6. Homework Problems

Definitely more work is needed. Listed below are the homework problems that are going to be performed during the coming years. We plan to continue our work even after the Workshop.

a) Physics Goals

Deeper thoughts about physics goals are still needed.

b) Monte-Carlo Calculations

Using the most updated Monte-Carlo code, the following calculations have to be done:

1. The ratio of signals of ϕ, $\bar{\Lambda}$, etc. to combinatorial backgrounds.
2. Capability of tracking, especially the hit pattern recognition, momentum resolution, V-particle identification, etc.
3. Most appropriate layout of the actual counters, including the appropriate solid angle.
4. Evaluation of data analysis time.

c) Tracking Chambers

1. Prototype construction. In particular, the pad chamber, the planar TPC, the Si vertex counter are interesting. For TPC the study of the most appropriate gas would also be important.
2. Development of readout electronics. Design and construction of fast micro-processors is important.
3. Concerning the projective geometry, the Monte-Calro calculations for needed numbers of planes as well as a possibility of a fast processor would be important.

d) Particle Identification

1. Prototype construction of TOF wall, in particular, a systematic study of the effect of Cerenkov light from the phototube window on the time resolution would be important. The goal of the time resolution is σ = 50 ps with a perfect Gaussian fall-off over four decades.
2. More thoughts about the particle identification in the region of $p > 1.5$ GeV/c.
3. Design studies of RICH have to be done in the immediate future. In addition, the prototype construction of RICH should be started soon.

e) Others

1. Design of the magnet.
2. Compatibility with other experimental devices, in particular, with the calorimeter and multiplicity array.
3. Cost estimate.

References

1) T. Ludlam, A. Pfoh, and A. Shor, Proceeding of the 1985 RHIC Workshop, BNL-51921, p. 373 (1985); see also contributions to the present Workshop.

2) Preliminary data presented on the first day at this Workshop.

3) L. Van Hove, Phys. Lett. **107B**, 320 (1981)

4) S. Nagamiya, Phys. Rev. Lett. **49**, 1383 (1982).

5) W. A. Zajc, Proceeding of the 1985 RHIC Workshop, BNL-51921, p. 83, (1985).

6) P. Koch, B. Muller, and J. Rafelski, Phys. Rep. **142**, 167 (1986).

7) W. A. Zajc, "Bose-Einstein Correlations: From Statistics to Dynamics" (review article) and references therein. Preprint may be available from him at Nevis Laboratories, P.O. Box 137, Irvington, NY 10533.

8) B. Knapp, private communication; see also Ph.D Thesis by M. Church (1987), Nevis Publication 260, Columbia University.

Hadron Spectroscopy Group

Convenor :	Hans Gutbrod GSI Darmstadt and CERN	
Participants :	R.Freifelder	GSI
	Y.Karant	LBL
	D.Kovar	Argonne
	W.Mueller	LBL
	S.Nagamiya	Columbia
	D.Olson	LBL
	W.Geist	LBL
	W.Sondheim	LANL
	J.W.Sunier	LANL
	J.Thomas	Caltech
	K.vanDijk	BNL
	H.vanHecke	LANL

Introduction

In nuclear collisions at RHIC energies the formation of the quark-gluon plasma (QGP)is considered by some theorists to be the dominant reaction mechanism. Others do expect, however, the QGP to show up only in fluctuations. One has to prepare an experiment which can look for observables associated with the plasma. As known from nuclear collisions at Bevalac energies, it is necessary to investigate in a globally well characterized event :

i) particle ratios per event on an event by event basis;

ii) momentum distributions of well identified particles as a function of the mass involved in the reaction;

iii) multiparticle correlations, e.g., looking for azimuthal asymmetries of the events in order to see possible underlying collective phenomena;

iv) etc.

The following experimental concept was put forward to this group for study :

a) Full particle identification in $|y| < 1$ for γ, $e\pm$, $\mu\pm$, p, $\bar{p}$ based on tracking in a magnetic field with additional detectors for particle identification.

b) Full calorimetry – EM, as well as Hadronic – in $|y| > 1$ with the capability of detecting and somehow measuring jets in the reaction.

Tracking of approximately 2000 particles and more represents the major problem and is considered to be not trivial. A feasibility study is necessary and will be worked on by S. Nagamiya first in a finite solid angle of 1 sr containing approximately 300 particles. A new, radial drift chamber concept will be discussed here in this report and should be considered as a first try inviting full criticism.

The calorimeter measurements at $|y| > 1$ are following closely the plans detailed in the 4 π calorimeter group East (convenor : M. Albrow, Ch. Fabjan) and only a short discussion is dedicated to that part of the experiment.

The following topics of the detector concept, shown in fig.1, are discussed :

a) Magnet;

b) Tracking at $|y| < 1$

c) particle identification;

d) Calorimeters at midrapidity and in the Fragmentation region;

e) Multiplicity of charged particle measurement : $|y| > 1$

1) **Magnetic Field**

Three magnetic field configurations have been discussed. All have in common the axial symmetry, which is considered essential in studying multiparticle correlations (fig.2)
The solenoidal field was rejected because :

a) many low rigidity particles are circling (spiraling) in the field for a long time;

b) the coil and the return iron freezes the geometry of detectors. Once built, the distance of a detector to the vertex can only be shortened but not be lengthened;

c) the photomultipliers of an additional TOF system behind the tracking would have to be in the magnetic field;

These three points were considered to outweigh the positive aspects of a solenoid, as there are :

a) a uniform magnetic field;

b) existing designs ready to be taken over;

c) an iron free left-right region for calorimeters;

d) the iron yoke could be used as absorber in a possible muon detection scheme. Only if a superthin coil structure is sufficient, then the solenoid could be reconsidered;

From the Axial-Field Spectrometer (AFS) the magnet design was considered – – despite lack of existing designs (besides the AFS itself) – – to be the appropriate one. It allows good access to the magnetic field region, it has versatility due to the open geometry and there will be few spiraling tracks for tracking in a low magnetic inhomogeneous field. There is less iron necessary due to the smaller magnetic volume, and the PM's of the TOF are in the low field region.

The geometrical concept most appealing is that developed by the 4 π calorimeter group (convenors, Albrow/Fabjan). There, however, the magnetic field is for low momentum electrons and it must therefore be modified to provide a bending power of 0.5 to 1 Tm. Furthermore, our accepted diamond length of 20 cm is somewhat larger than the requirements for electron spectroscopy, and thus requires a widening of the polecap by 20 cm. These conditions require a total polegap of approximately 130 cm and a pole face diameter of approximately 110 cm. A field of nearly 10 kilogauss over that area should give enough bending power for soft components in the particle spectra (fig.3).
Several open questions have to be answered :

a) How much more complicated is tracking in an inhomogeneous field?

b) How should the field be shaped ?

c) Where should the tracking start, inside the magnetic field or as far outside as possible?

d) How much more computing is required than in a solenoid?

2) **Tracking at $|y| < 1$**

As a typical event, we use the same one as described in BNL 51921 based on HIJET calculations. How to track approximately 2000 particles in the $|y| < 1$ region, and where to start tracking? A simple illustration should help to see the problem. Given a cylinder of radius R and distributing all 2000 particles uniformly over the cylindrical surface (excluding the end caps), one obtains the following picture :

R(cm)	Surface of cylinder	Size of Patch containing one particle on the average
20	5,000 cm^2	2.5 × 2.5 cm^2 = 6.25 cm^2
50	34,000 cm^2	4 × 4 cm^2 = 16 cm^2
100	125,000 cm^2	8 × 8 cm^2 = 64 cm^2

This leads immediately to the concept that the particle tracking should be started as far away from the vertex as possible in a reduced particle density region.

As possible candidates for tracking the OPAL-JET Chamber, the TPC, and the Radial Drift Chamber are discussed :

a) The OPAL-JET Chamber consists of 24 sectors in a solenoid magnet, each containing 160 sense wires parallel to the beams. The electrons drift perpendicular to the magnetic field lines with a minimum drift of 8 cm and a distance of 40 cm form the vertex to 24cm at 200 cm distance.
This chamber has a two-track resolution of 2 mm but a confusion length equal to the total wirelength. A simple argument rules out this chamber as a candidate for tracking 2000 particles : e.g. at a radius of 100 cm there are 2000 tracks crossing the cylindrical surface. With a 2 particle separation of 2 mm, in azimuth, but no resolution for double hits along the wire, there are about 3150 cells of 2 mm x 4 m, i.e., nearly all of the cells contain 1 of the 2000 particles. The confusion due to this large probability of double hits limits this chamber design to much smaller total multiplicities.
From a different viewpoint, the OPAL Driftchamber would have to be modified to incorporate a gated" ion trap" to avoid large positive ion build-up by ions coming from the multiplication wires.

b) As an alternative, the standard TPC was discussed. The inherent long drift time is a disadvantage, especially since increased luminosity of RHIC has to be anticipated. With a total length of 4m and a drift time of 10microsec/m one is faced with at least 20 microsec drift time when reading out on both sides.

A positive ion build up in the detector volume can be neglected according to D. Nygren. The gas multiplication at the cylinder ends, however, is gated which avoids ions drifting back into the detector volume. The TPC would go best together with a solenoid magnet, although an application in a inhomogeneous axial field seems also to be possible, requiring probably a more sophisticated analysis.

c) A very promising scenario seems to be a chamber where electrons are drifting radially outwards (fig.3) until they reach on the outer chamber surface the multiplication wires which are read out by pads (Radial Drift Chamber : RDC). The gated gas-multiplication wires and read-out modules are forming mechanically the outer surface of the cylinder. The inner tube (scattering chamber, beampipe or entrance window for the chamber) is on high voltage and the electrical field is shaped on the edge via field-wires. Calibration is done via laser light ionizing the gas and producing straight tracks.

Most of the tracks end on the electronics and readout pads. With very fast microprocessors there could be the possibility of "on-line track vectoring" that could be a tremendous help in data reduction. A surface area of 500,000 cm^2 in total or 250 cm^2 per particle in a 2000 particle event is available as real estate for electronics and gas amplification mechanics with easy access. The electronics would be the same as presently under development for several TPCs. Microelectronics with a large number of channels per chip are promised for the near future. A typical optimal pad size of 5mm x 5mm is leading to a total number of 2 x 10^6 pads. Every chain of 40 pads could form a cell with a right and left readout. Thus, 100 000 channels of electronics are to be constructed and financed. The expected position resolution is about ~500 μm with this pad read-out scheme. With approximately 2000 particles in an event distributed over 50 000 cells (in the rapidity region of $|y| < 1$) the problem of double hits is considered small.
The radial drift chamber (RDC) with approximately 75 cm drift and an outer radius of 2 m would be a decent detector with an eigentime of ca.7.5 microsec. This allows rates of about 10,000 interactions per second, probably even up to 5x10^4, because the detector sees dominantly tracks from the central region.

3) Particle Identification

Fig.4 shows the dE/dx vs. momentum plot of e, μ, π, k, p, d, ...as measured by the time projection chamber of PEP4 at Stanford *at high pressure*. We deduce from that the possibility of separating π, K, p with DE dx and $B-\rho$ measurement in a non-pressurized drift chamber up to momenta of 0.5 GeV/c (or event a little bit higher).

A high pressure chamber is ruled out because all walls would have to be quite thick for mechanical reasons. This in turn would increase the photoconversion to a non-tolerable level.

A particle identification up to 1.5 GeV/c is possible if TOF is added to the system. There one needs about 3m flight path and a time resolution of 100-200 psec (FWHM). Since 2000 particles are to be measured, 20,000 modules or cells would be needed to work with approximately 10% double bit probability. These could be, in a convential way, photomultipliers with scintillator pads in front, or in a more elegant way, parallel plate avalanche detectors at atmospheric pressure with pad-readout. [For highly ionizing particles low pressure counters have been built with time resolution close to 140 picosec(FWHM)].The efficiency of such detectors needs to be established first.
If the conventional way of photomultipliers is chosen, then a combination of time of flight measurement with EM-calorimeter measurements invites itself as it could be done with a scintillator/Pb glass module. Another possibility of fast timing and calorimetric measurement is with Pb-scintillation fiber compounds (P. Sonderegger) and should be pursued. Both options would differentiate and measure γ and $e\pm$.

Possible RICH detectors between the tracking chamber and the TOF array have been discussed and, due to the open geometry, can be implemented if a particle identification is needed much beyond momenta of 2 GeV/c.

Work has to be done to find out if there are any benefits of tracking without a dE/dx measurement in the radial drift chamber (RDC).

4) **Calorimeter at midrapidity and in the Fragmentation Region**

The concept of this experiment is to have full calorimetric energy measurements in the region not covered by tracking. At $|y| < 1$ calorimeters are considered of interest only if they can add to the particle identification. Since most of the particles are of low momentum, a sampling calorimeter is not a good tool with the best resolutions of only $15\%/\sqrt{E}$ in EM and $40\%/\sqrt{E}$ in hadronic section.

However, a full non-sampling EM-calorimeter coverage (e.g. Pb.-Glass) might be of great interest in studying photon energy spectra in mid-rapidity which showed non-trivial signals in α-α collisions at the ISR and in ^{16}O + Au collisions at the SPS CERN.

We would like to see a highly segmented calorimeter at $|y| > 1$ with a resolution good enough to identify and measure jets in the reaction. This requires a position not too close to the reaction diamond .

The most important unresolved issue in a combination of calorimeters and tracking chambers is the possible particle flux out of the calorimeter (called "albedo" for backward scattered particles and leakage for particles coming out of the side and the back of the calorimeter). With the beams anticipated we are dealing with energies of several tens of TeVs deposited in the calorimeters. In particular any opening in the calorimeter is sending out this background next to the particles of interest. Protruing iron yokes, e.g., will be sources of such background.

Expecting a strong albedo problem, we suggest moving the calorimeters as far away from the vertex as possible. This allows the use of steel or lead as material instead of Uranium with adequate fine segmented tower geometry for resolving jets and measuring precisely Et.
The calorimeter readout must be optimized for radiation hardness. Besides the approximately 2 x 20 TeV hitting the calorimeter there are unknown halo problems to be expected from beam − beam interactions at the previous intersection points as well as particles hitting the calorimeters during beam preparations.
Et will reflect in first order the number of participants in a reaction, and should be measured with high precision. Only then can fluctuations in Et be measured with significance.

We propose measuring the total energy in the reaction by carefully catching all spectators or projectile fragments going down the beampipe. This must be done in a sophisticated beamline calorimeter behind BC1 and partly behind BC2 (see Fig. IV.3 in RHIC proposal).

The spectators in Au + Au collisions will be of different rigidity than the Au beam and can therefore be measured after a magnetic analysis. This is not possible for N/Z = 1 nuclear beams like ^{40}OCa where most of the fragments have the same N/Z = 1 and go therefore right down the beamtransport system until the small difference in mass excess separates them from the beam.

5) Multiplicity of charged particle measurement at |y| > 1

Since we intent to have full particle identification at |y| < 1, due to a successful tracking in a magnetic field the multiplicity of charged particles and their distribution is measured simultaneously. At rapidities larger than one, particle densities as well as the total number of particles are high. Two scenarios are discussed in the first RHIC-Detector workshop (BNL-51921) and are still relevant options. From the first experiments at CERN with 3.2 TeV oxygen beams it became clear that albedo effects have to be considered to be serious. Therefore one should try to avoid detectors which are sensitive to the particles in the albedo, like e.g. slow neutrons. Gas detectors should be used which do not use gases containing a lot of hydrogen. A recent study showed that streamertubes can be operated with carbon-dioxide.

Also silicon detectors are now being used as multiplicity detectors (NA34 and NA35 at CERN). A micro pad Silicon detector wall with a hole for the beams could serve as a multiplicity detector very closely positioned to the interaction vertex. Experience with a silicon wall in the experiment UA2 at the CERN SppS should be carefully followed to learn more about the reliability of these detectors. Furthermore, developments of high density electronics on the silicon waiver are under way and could solve the problem of the huge cable load close to the detector.

Conclusion :

This group has started during the conference to design a 4 π experiment, which aims at a fully global eventcharacterization in combination with a full particle identification in a limited region of rapidity ($|y| < 1$). Drawing on a lot of the work done in the previous workshops ,of the various other working groups and especially of the high energy studies of the SSC and the LHC detector groups,there is a promising outlook for a positive outcome of a feasability study for such a 4 π experiment for RHIC.

PHOTON & HADRON SPECTROMETER FOR RHIC

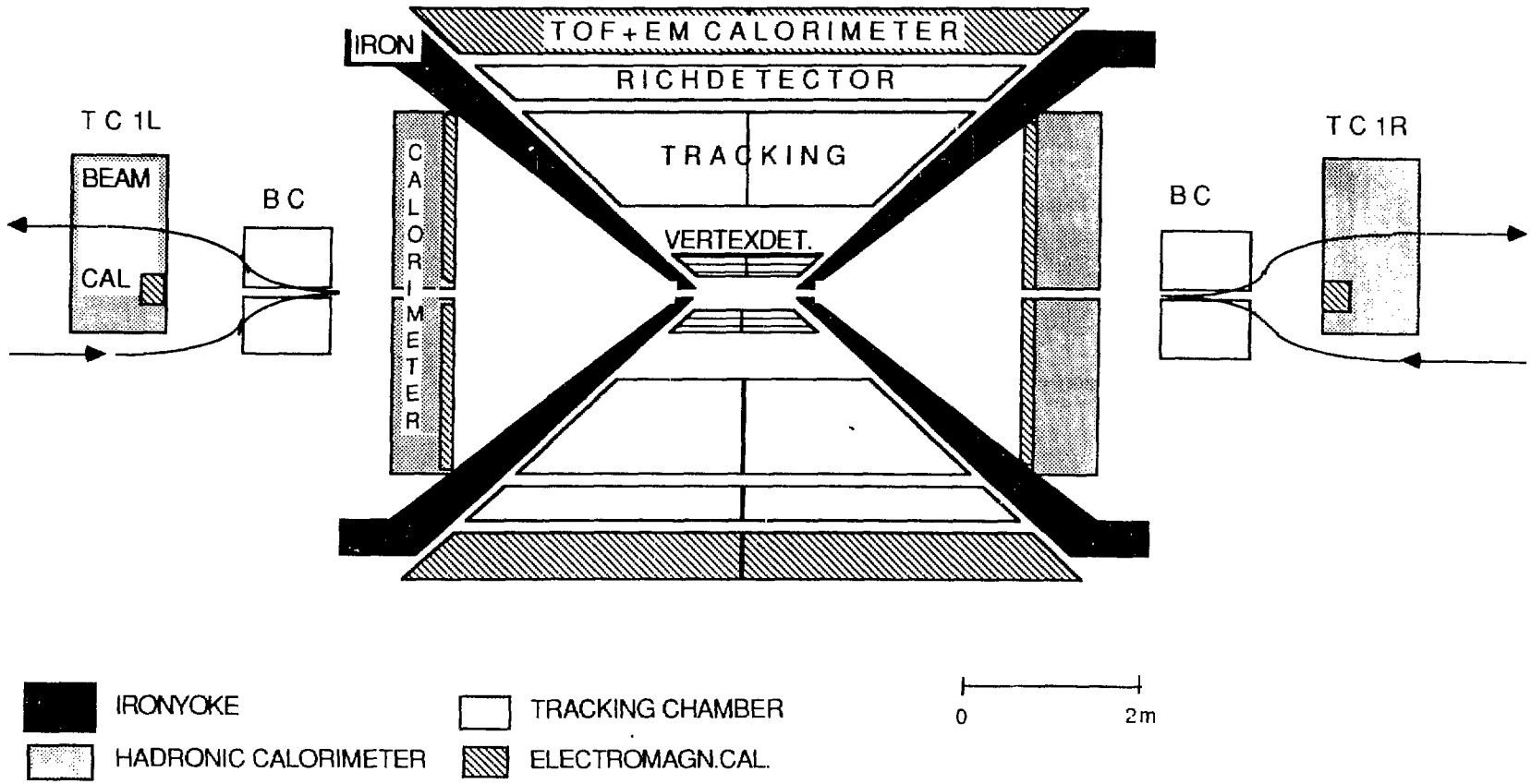

Fig. 1.

MAGNETIC FIELDS

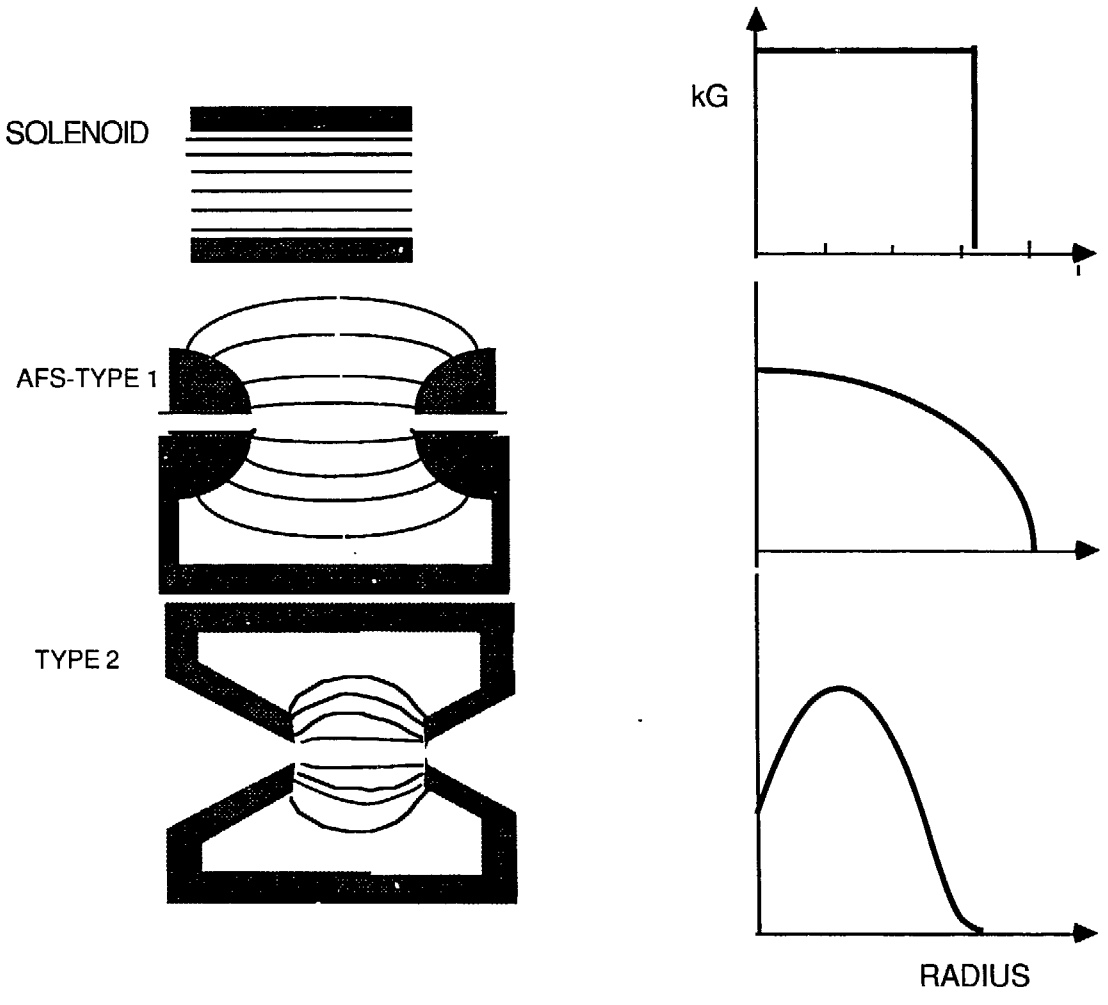

Fig. 2.

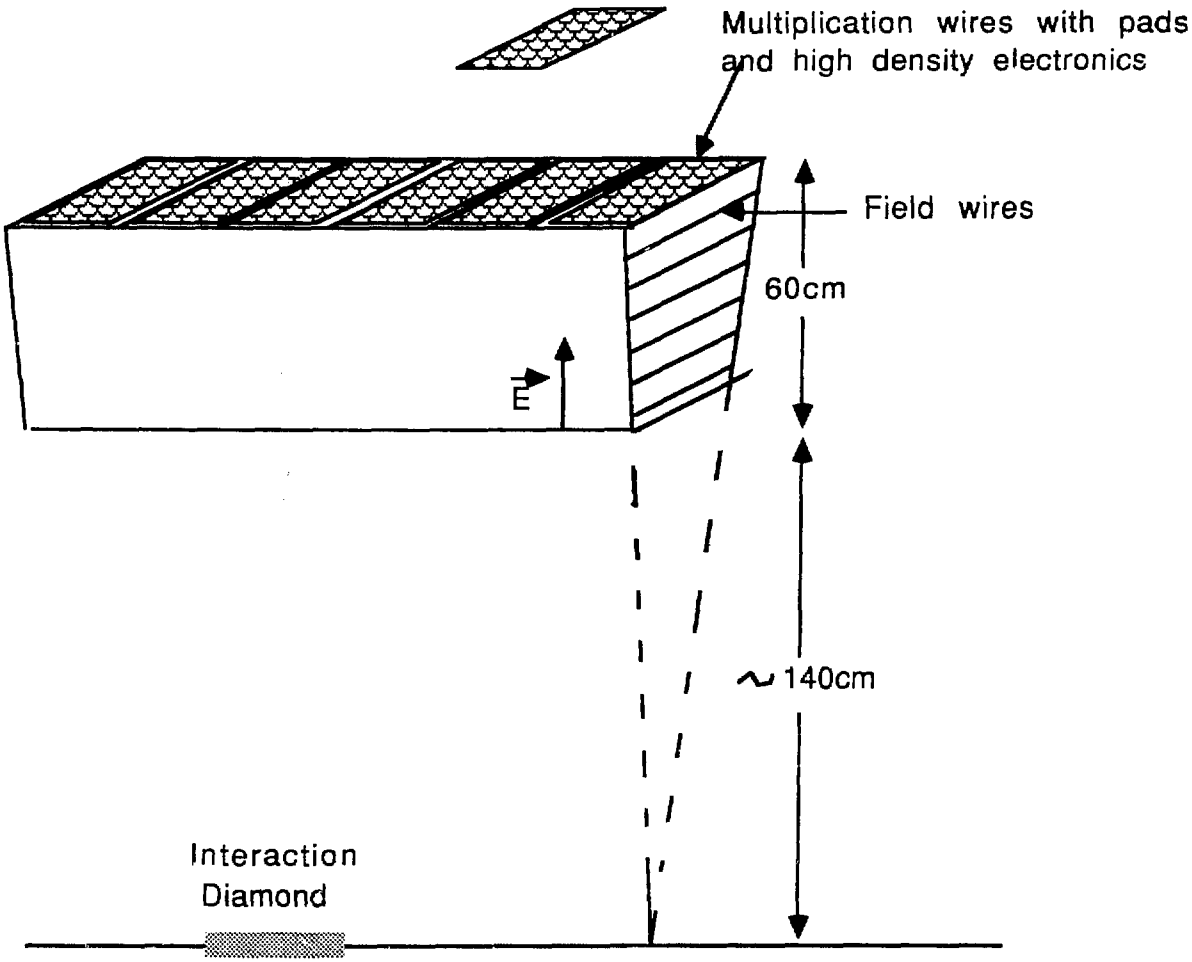
Multiplication wires with pads
and high density electronics
Field wires
60cm
E
~140cm
Interaction
Diamond

Fig. 3.

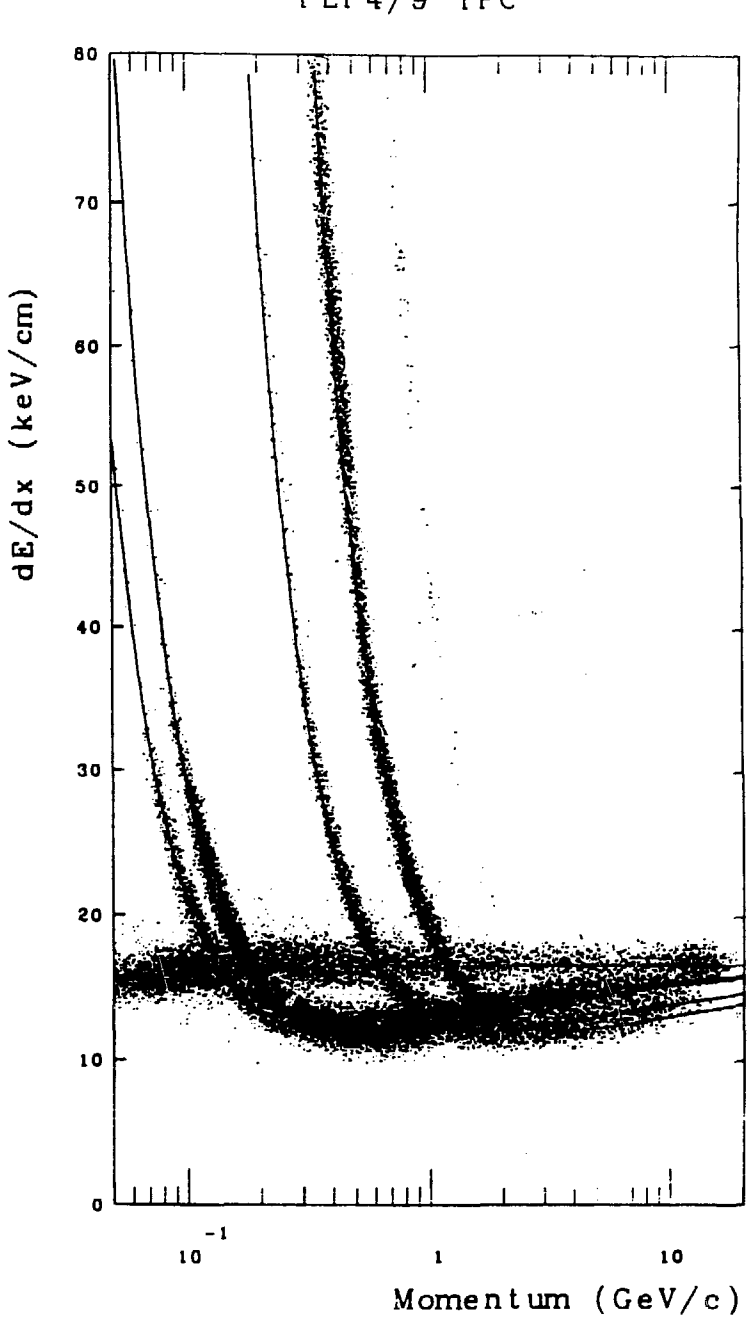
PEP4/9 TPC
dE/dx (keV/cm)
80
70
60
50
40
30
20
10
0
10^-1
1
10
Momentum (GeV/c)

Fig. 4.

An Approximately 4π Tracking Magnetic Spectrometer for RHIC *

Report of the 4π Tracking Group of the Berkeley RHIC Workshop -- May 1987

by S. J. Lindenbaum -- Convenor
Brookhaven National Laboratory and City University of New York

Membership of the Group

Major contributions were made to this effort and report by the following:

Members of the working group attending the Berkeley Workshop were A. Faroog (Texas A&M), S. A. Kleinfelder (LBL), M. A. Kramer (CCNY), S. J. Lindenbaum (BNL/CCNY), W. A. Love (BNL), M. Maier (MSU-NSCL), D. R. Nygren (LBL), E. D. Platner (BNL), G. Rai (LBL), and H. H. Wieman (LBL).

Other members of the group substantially contributing before and after the Workshop were C.S. Chan (CCNY), G. T. Danby (BNL), A. Etkin (BNL), K. J. Foley (BNL), R. W. Hackenburg (BNL), R. S. Longacre (BNL), J. N. Marx (LBL), T. W. Morris (BNL), and A. C. Saulys (BNL).

Abstract

A tracking magnetic spectrometer based on large Time Projection Chambers (TPC) is proposed to measure the momentum of charged particles emerging from the RHIC beam pipe at angles larger than four degrees and to identify the particle type for those beyond fifteen degrees with momenta up to 700 Mev/c, which is a large fraction of the final charged particles emitted by a low rapidity quark-gluon plasma. This work is a variation of a device proposed at the first RHIC Workshop.[1]

Physics Motivation

There has been considerable theoretical speculation[2,4-8] about the production of a Quark-Gluon Plasma (QGP) and the possibility of other new phenomena in heavy ion collisions.

---

* Research carried out under the auspices of the U.S. Department of Energy under Contract Nos. DE-AC02-76CH00016 (BNL), and DE-AC02-83ER40107 (CCNY).

Most calculations conclude that baryon densities ($\gtrsim$ 5 times the nuclear density) or high enough temperatures ($T \gtrsim 200$ Mev) or a combination of both will result in such phenomena for central collisions of heavy ions.

Thermalization of Large Regions

Many calculations assume that central collisions of heavy ions can be described by employing local thermal equilibrium which adjusts adiabatically as the collision zone develops in space and time.

One can have serious reservations that complete transition into the new phase (even if energy densities and/or temperatures are sufficiently high) can in reality be achieved except in a small fraction of central collisions. Therefore, it is prudent for planning purposes to assume that even in the case of central collisions ($\lesssim$ 1% of the heavy ion collisions) only a small fraction of these collisions may be expected to lead to the QGP effects.

Thus the experimental capability of studying these interactions in detail on an event-by-event basis is an essential ingredient for our experimental investigation at RHIC if one is to extract the desired signals from the background.

Non-Equilibrium Conditions

A second approach has been to recognize that it is unlikely that thermalized conditions can describe the whole collision dynamics, in particular the phase transition itself. Thus these new phenomena (QGP, etc.) occur under inherently non-equilibrium conditions. This scenario has been suggested and strongly emphasized by Van Hove.[2,6-7]

The non-equilibrium scenario would produce formation of local droplets of quark gluon plasma. As the droplets expand, each droplet could separate into several smaller droplets. These QGP droplets could hadronize by deflagration,[2,6-8] since this appears to be the more likely of the two possible explosive phenomena, being favored by entropy considerations.

These non-equilibrium treatments have assumed the chemical potential is zero (i.e. baryon No. B ≈ 0) and thus are directly applicable to the central region.[2,6-8]

If plasma droplets (possibly after breaking up) hadronize by deflagration, the resulting rapidity distribution of hadrons should show maxima at the rapidities of the droplets. The expected width of the maxima would be ≈ 1 rapidity unit. Hadrons from the plasma should have $P_\perp$ larger

than normal and have angular distributions characteristic of a deflagration occurring in plasma droplets. The generally expected plasma signals such as enhanced strangeness, lepton pair production, etc. would occur in these events within similar rapidity intervals and thus detailed studies on an event-by-event basis are necessary to observe these.

Using the existing theoretical work only as a guide, if there are QGP or other new effects produced in heavy ion collisions at RHIC they may be rare phenomena compared to the central collision rate and may indeed be quite localized* within an event.

Therefore it is desirable that an experimental program to search for such phenomena should have the ability to survey as much as practical of the characteristics of each event considered, and the ability to observe unusual phenomena occurring locally in a small part of the event. The observations of as many characteristics of the event as possible on an event-by-event basis is necessary so that the rare unusual occurrences can be observed under reasonable signal to background ratios. Even if new phenomena are unexpectedly abundant rather than rare, one will certainly not lose by designing an experimental program which can detect and identify rare phenomena. Because even in the fortunate case where some new phenomena are relatively abundant, with history as our guide, we can expect other new phenomena which are rare. The certainty with which one can draw conclusions will be dramatically dependent on the signal to background ratio.

Variations of the A and A' (including protons) used in the collisions will be required in order to decide whether observed phenomena are evidence for new phenomena. Furthermore, to test observed or specific theoretically predicted new phenomena, the experimental data will have to be compared to Monte Carlo calculations with and without these new phenomena. The Monte Carlo events, of course, have to be cut and treated in the same way as the data.

The Large Magnetic Spectrometer Method

We have previously proposed[1] a large magnetic spectrometer to track and momentum analyze a very large fraction of the particles emitted in a heavy

---

* There may be more than one localized QGP region per event.

ion collision. This will allow us to determine pseudorapidities (and rapidities when particles are identified), to reconstruct neutral Vee's if $P_\perp$ is high enough, and have momentum information on both positive and negative particles in the same event. We plan to handle gold on gold events at 100 GeV/nucleon in RHIC. The negative particles will be predominantly pions.* In the present proposal we have added dE/dx information for low momentum particle identification in the central region where the quark-gluon plasma effects are expected to most often occur. We have also extended the rapidity region.

In addition, highly segmented Cherenkov hodoscopes, as well as time-of-flight information can additionally be used to identify some of the particles, as the program progresses and more funding becomes available.

By utilizing charged particle tracking we will miss neutral particles such as neutrons, π^0's, and photons. It is important to realize that from HIJET generated events we expect that charged multiplicities of central 100 GeV Au on 100 GeV Au collisions will be $\gtrsim$ 4,000. With such high statistics the charged particles should give a rather adequate picture of the characteristics of each event.

One important capability we will have, is the ability to look on an event-by-event basis for unusual events not expected from known processes. These events, could be characterized by:

1. Excessive local fluctuations (up or down) in pseudorapidity density (i.e., pseudorapidity bumps). In the case of negative particles which are momentum analyzed we can assume they are pions (or alternatively kaons) and look for rapidity bumps. Low momentum central region particles will be identified by dE/dx measurements and we can look for rapidity bumps for each particle.
2. Excessive fluctuations in multiplicity.
3. Excessive local or global enhancement of strangeness.
4. Anomalous behavior in $P_\perp$ ($E_\perp$), or energy flow patterns.
5. Hanbury-Brown and Twiss effects, and Speckle Interferometry.
6. Evidence for deflagrations (or detonations).

---

* In particles coming from the plasma droplets themselves, this may not be true.

7. Something else which catches our eye.

8. Most important - the correlations between these -- For example we might find that pseudorapidity (or rapidity) bump(s) or other anomalous behavior are associated with one or more of the above and may have similar pseudorapidity (or rapidity).

The above illustrations are to be taken only as a guide. The important point is that we are planning to see a great deal of the multitudinous characteristics of each event on an event-by-event basis and therefore we shall see what if anything is anomalous, in a most favorable signal to background environment.

Since the theory of the formation, expansion, and hadronization of the Quark-Gluon Plasma, the principal motivation for the RHIC project, is not yet at the stage of unique reliable detailed predictions.[2] The best quantities to measure may not be learned until RHIC is in operation. Helmut Satz provided a theorist's list of desireable measurements in the opening session of the Workshop. Among the quantities on that list that can be measured by this device are identical particle interferometry to determine the system size, multiplicity per unit rapidity, energy distributions, particle ratios and momentum distributions, especially $p_\perp$ versus dN/dy. It is of utmost importance to be able to measure many of these quantities simultaneously on an event-by-event basis, since the effects may be rare, and a correlation of several of these and other effects may provide an ensemble of selected events which give the clearest signal of new phenomena.

Selection of the Detector

Since the effects of plasma formation are expected to be clearest in the region of central rapidity and to result in a large number of relatively low momentum particles (perhaps as many as one thousand or more per unit of rapidity) the detector should provide good information about this signal. Calorimeters are capable of measuring some characteristics of large numbers of particles with rapid response times. However, the accuracy of energy measurement for particles below 1 GeV/c^2 is poor. Charged particle tracking devices with even modest position resolution and relatively low magnetic fields can achieve very good momentum resolution in this region and also measure the particles individually. Measurement of particle mass by combining ionization measurements with momentum measurements is also most successful at

these low momenta. The large numbers of tracks to be measured requires a device with very good two track separation. These considerations led to the selection of the Time Projection Chamber (TPC) as the best detector for the central rapidity and non fragmentation regions. The three dimensional nature of the track element measurements, the straightforward incorporation of ionization measurements, and the low mass of the detector volume are cardinal virtues of the TPC for this application. One drawback is a relatively long drift time which limits the event rate (and thus the usable luminosity). This is not expected to be a limitation at the RHIC design luminosity for gold-gold collisions. To maximize the position measurement accuracy, the magnetic field over the TPC should be as parallel to the drift electric field and as uniform as practical. Two possible magnetic field configurations were considered, the solenoid (possibly flanked by dipoles for small angle tracks) and the dipole. The dipole was selected for study in this workshop since it offers lower cost and easier pattern recognition for a system with effective magnetic field for small angle tracks.

Detector Characteristics

1. RHIC Interface

This detector would benefit from the smallest possible length of interaction diamond such as that available in a special intersection region where the BC1 dipoles are not installed.

2. The Magnet

A version of the proposed device is shown in Figure 1. Momentum measurement is made possible by a large dipole magnet, M1, centered over the crossing point. The general characteristics of the magnet are based on various design options provided by Gordon Danby. The magnet aperture is 2.8 meters high by 5 meters wide by 5 meters long. The design magnetic field is 5 kGauss. The requirement of cancellation of the effect of the dipole field on the circulating beam means that two compensating dipoles are needed whose fields are ramped with that of the central dipole.

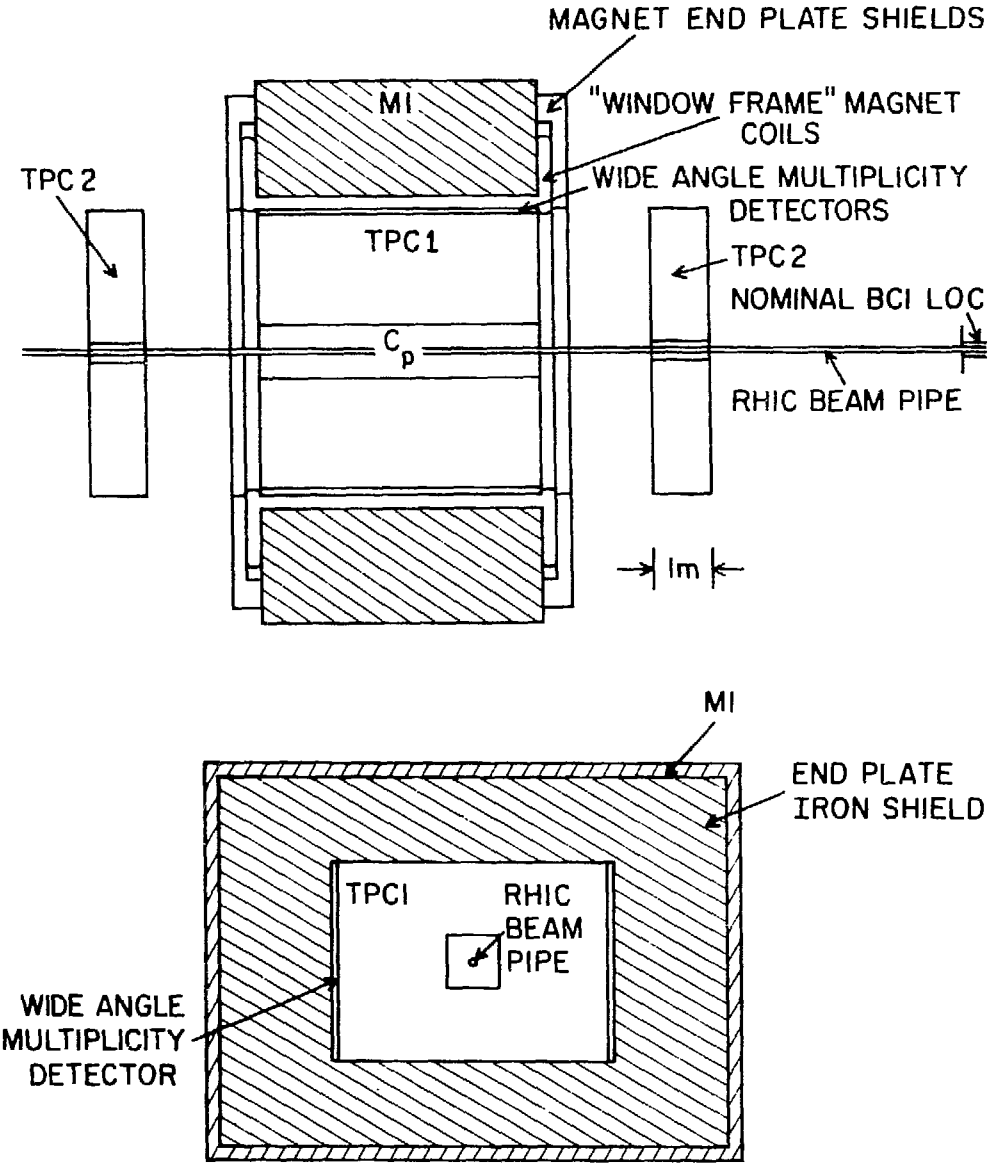

Fig. 1. Plan (above) and elevation (below) views of the proposed device.

3. The TPC's

The magnet is filled with TPC modules at atmospheric pressure, occupying the entire volume except for a region 80 cm wide by 80 cm high centered around the beam pipe. This TPC (TPC1) is read out by a conventional anode wire and cathode pad system like that used for the original PEP-4 TPC. In this case, however, the readout is located over the two pole faces of the dipole. A full

meter of track is measured for polar angles greater than 15° from the beam axis. The pseudorapidity interval covered is $-2 < \eta < 2$. For most of the volume at least 100 energy loss samples will be made for each track. For tracks at small angles to the field lines momentum is not well measured.

Two other TPC's (TPC2) are located outside the magnet at each end to measure the small angle tracks. They cover the angular range from about 4° to the beam out to 24° (pseudorapidity from 1.5 to 3.5 and -1.5 to -3.5). These detectors use the short anode wire readout scheme developed for AGS experiment 810, which gives better two-track separation but yields no usable dE/dx information. Anode wire spacing of 2.5 mm is used arranged in rows 5 cm apart. The angle and position measurements in TPC2 will enable the reconstruction of the momentum and assignment to the primary vertex of these tracks.

4. TPC Readout Electronics

TPC1 has a 50 m^2 readout area (read out top and bottom for speed) covered with closely spaced anode wires and cathode pads underneath arranged in rows locally roughly perpendicular to the average track direction with 0.4 cm pads on 0.5 cm centers. TPC1 requires about a half million channels of readout electronics each capable of recording multiple sets of measurements of time and pulse height (up to 16 segments of 8 amplitude samples each). The device should separate hits in the time dimension which are 0.5 cm apart so the bin size should correspond to ≈ 1 mm. This requires 10 or 11 bits of time resolution. The result is to divide the volume of the TPC into about a billion cells and to present each track with the equivalent of 150 detector planes each with pixels 0.5 cm × 1.5 cm (assuming 3 pads corresponds to the pixel length). Since the track density at 90 cm from the pipe should be less than 0.05 cm^{-2}, the frequency of two tracks hitting the same pixel is small.

In order to implement such a large fast sampling analog and time measuring system, work is under way to develop large scale integration electronics utilizing the concept of the segmentable analog memory. With the addition of recent developments in fast analog IC technology it will be possible, with only two integrated circuits, to construct 8 channels of low noise amplifier, waveform shaping and desparsified analog and time digitizing circuitry. This will allow sufficient miniaturization to attach the full half million channels of electronics directly to the cathode pad readout planes of the TPC. Thus only highly compacted data containing useful tracking and dE/dx

information ever leaves the immediate perimeter of the TPC. This very high degree of channel number and signal processing compaction has the additional benefit of reducing estimated electronics costs to less than $10.00 per channel.

The two modules of TPC2 each have 5 m × 1 m area readout on top and bottom for a total of 20 m^2. Since no dE/dx measurement is contemplated in TPC2, 20 rows each with elements on 2.5 mm spacing should suffice (equivalent pixel figured at 5 × 7.5 mm). This requires an additional 160,000 channels of electronics which needs to record only the drift time.

5. Data Acquisition from the TPC

Organizing and compressing time and amplitude sampling information from a half million pads raises some challenging issues. The raw uncompacted data from TPC1 produces > 10^9 bytes of information, > 99% of which are samples empty of relevant information. Therefore the first strategy is to record, even temporarily, as little of the empty samples as possible at the front end of the electronics chain. It is proposed at this level, to reduce the empty samples by a factor of 100-200 using the concept of the segmentable analog memory. This will leave analog data encompassing the time samples that have been triggered by an analog threshold detection.

The next level of compaction is to fit the analog samples in time yielding another factor of two or three. These two levels of compaction can be accomplished with electronics mounted on the TPC, reducing the event size to 2 - 5 MB for further processing. Higher levels of organization would be done remotely from the TPC. Electronic systems for these first two levels of compaction would be organized in 1000-2000 serial links to this external processing system.

6. The Triggering System and Other Detectors

A small calorimeter surrounding the beam pipe and subtending a pseudorapidity range from 4 to 5 will measure an energy that depends strongly on the impact parameter of the collision. A large plane device located just behind the central TPC which measures multiplicity will give a more direct measurement of the interest of the event as far as TPC response is concerned. Note that the region 80cm wide by 80cm high immediately around the interaction region is available for insertion of a special device capable of dealing with

the very large track densities. Such a device would have to have very low mass, of course, to avoid compromising the TPC.

Detector Performance

1. Monte Carlo Event Simulation

Events have been generated by a variant of the HIJET code which allows for simulation of Quark-Gluon Plasma formation and the CERN GEANT program used to investigate the detector response to these events.

The modified HIJET Monte Carlo uses a simple model for plasma formation based on a geometrically tagged region of each nucleus-nucleus collision. The energy and momentum of the cascading particles in this tagged region are transfered to a spherical plasma bubble (a Van Hove type) at critical temperature with chemical potential and volume that conserves baryon number and energy. We have written a program that models a plasma breakup based on work of P. Koch, M. Muller and J. Rafelski. From this model we determine the particle production probablities which depend on the critical temperature and the gluon fragmentation function. We then produce particles according to these probablities with a momentum distribution of that of the critical temperature. We have interfaced this program with HIJET and conserve energy and momentum by the tagging procedure. Tagged particles either lose energy or go completely into making plasma. These plasma bubbles spread over about one unit of rapidity (thus leading to a rapidity bump) with rapidity near zero. When the plasma tagged energy is 7% of total Au-Au RHIC energy, kaon production in the middle two units of rapidity increases by a factor eight and the proton and antiproton production increases by a factor seven, whereas pion production increases by about a factor of two. At all other values of rapidity one sees the ordinary HIJET physics. Two data files of tracks from 100 Gev Au on 100 Gev Au central collisions were produced for this study. The first file called "CENTRAL" contained ordinary events; the second, "PLASMA," events with plasma bubbles described above. Figure 2 is the rapidity distribution from those events.

2. TPC Acceptance

The GEANT program tracked all charged particles through the detector shown in Figure 1. Hits were recorded as the tracks passed over pad rows. If a particle decayed, no further hits were recorded. Figure 3 is a GEANT plot

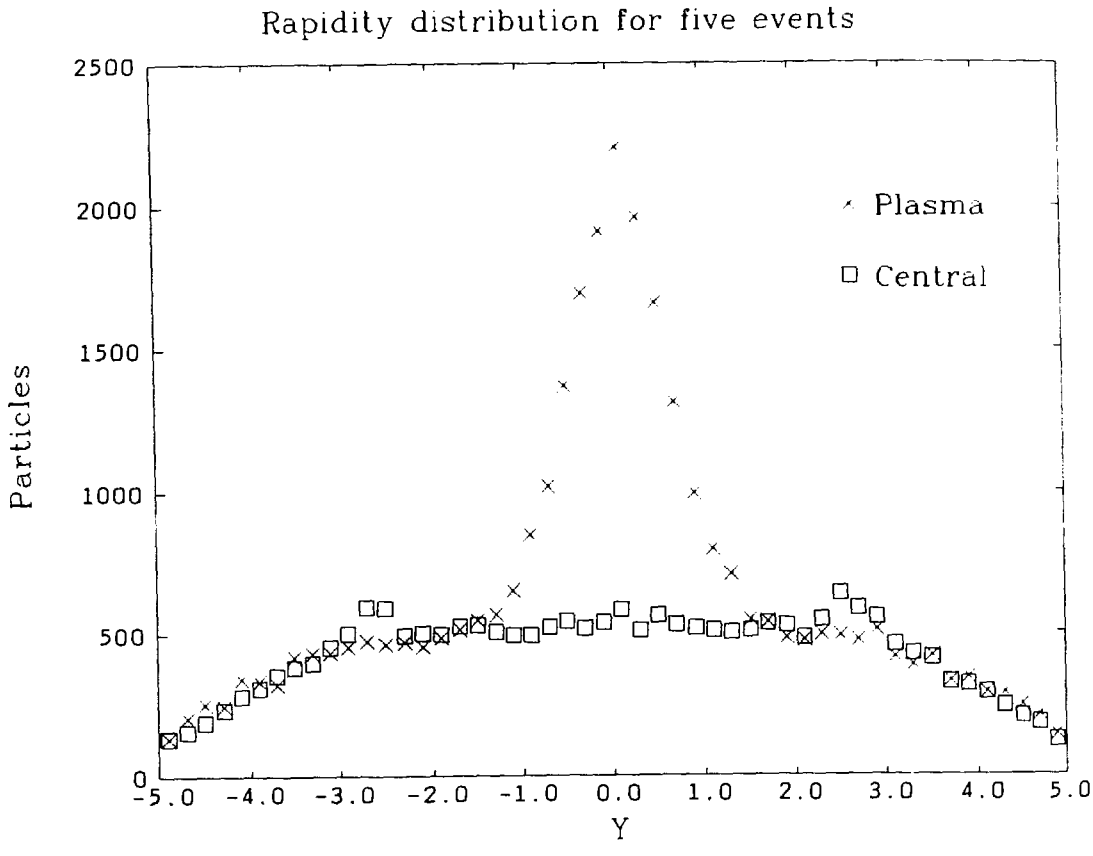

Fig. 2. **Rapidity distribution of all particles from five "central" events (squares) and five "plasma" events (crosses)**

of the hits from a small fraction (≈ 2%) of the tracks from one central event in the proposed TPC. Because of the larger number of tracks involved it is difficult to produce a presentable figure of a full RHIC event. The pattern recognition results are based on complete events, of course. The track was defined as "accepted" for momentum measurement if there were 10 separate hits recorded.The particle was "accepted" for particle identification if there were 80 cm or more of track samples recorded. The resultant acceptance is indicated in the following table.

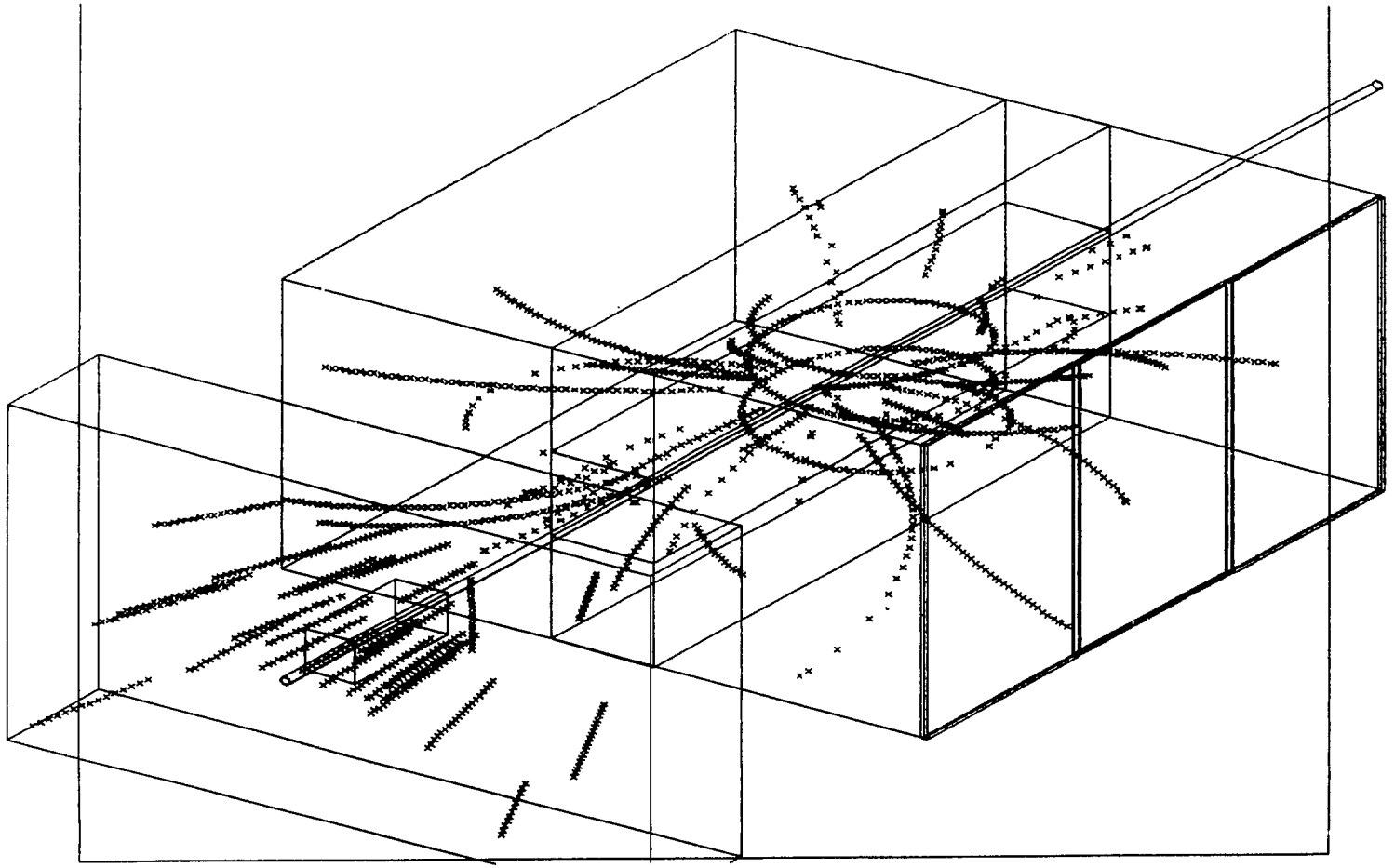

Fig. 3. **Plot of the detector with hits from about 2% of the charged tracks of one central event. Only one of the TPC2 modules is shown.**

Central Event Acceptances

$\|Y\|$ Range	Tracks	TPC1 > 10 hits	TPC1 Particle I.D.	TPC2 > 10 hits
0 to 1	445	95.0%	81.8%	3.9%
1 to 2	513	88.3	81.7	33.7
2 to 3	497	35.8	19.7	84.1
3 to 4	384	0	0	70.6
above 4	266	0	0	16.9

Plasma Event Acceptances

0 to 1	1284	88.6	74.1	4.3
1 to 2	556	86.4	80.1	29.4
2 to 3	433	35.9	20.6	85.9
3 to 4	335	0	0	72.0
above 4	279	0	0	16.1

As expected, the close correspondence between rapidity and polar angle causes TPC1 to be quite efficient for $|Y| < 2$ and TPC2 complements the acceptance for larger Y where it is quite efficient.

TPC Pattern Recognition

Track reconstruction efficiency for the proposed RHIC TPC was estimated by analysing the plasma events using an existing TPC reconstruction program[3]. GEANT was used to convert the HIJET events into hits in the TPC padrows. Each hit was then converted into a simulated TPC readout taking into account Landau fluctuations, ion drift time and diffusion, and readout electronics characteristics. Background noise was added, and a randomly distributed 5% of the readout channels were assumed dead. A readout signal was generated based on the expected amplifier characteristics. The resulting detection efficiency for individual hits was ≈ 90%.

The simulated readouts were then analysed by the track reconstruction program developed for AGS Exp 810. The E810 TPC is rectangular with parallel readout pad rows. The proposed RHIC TPC1 will have padrows oriented in different directions to optimize the two-track resolution.

In order to investigate the pattern recognition efficiency using the program developed for E810 the proposed RHIC TPC was simulated by analysing events with three different TPC configurations.

90 deg Chamber: 100 cm by 140 cm by 200 cm TPC centered at (X,Y,Z) = 90, 70, 0 cm relative to the beam intersection point; readout plane normal to X (beam along Z).

0 deg Chamber: 100 by 140 by 200 at 90, 70, 150 cm; readout plane normal to Z.

30 deg Chamber: similar to 0 deg chamber, but with readout planes rotated 30 degrees

Efficiencies were computed for correctly reconstructing tracks which spanned ten or more padrows. Overall efficencies achieved in the 0, 30, and 90 degree chambers were, respectively, 94%, 98%, and 95% for positive tracks; 97%, 81%, and 90% for negative tracks.

By choosing the configuration which gave the highest efficiency for a given rapidity to simulate local optimization of the padrow configuration we determined that the efficiency for tracks with at least ten hits was greater than 95% in the pseudorapidity range $|\eta| < 2$.

4. Momentum Resolution

The momentum resolution in the TPC1 detector will be dominated by multiple scattering and can be estimated by comparing the momentum of the reconstructed track with the generated momentum. For this comparison only tracks that spanned 25 or more padrows were used. The fraction of tracks with $\Delta P/P < 5\%$ was 74%, 83%, and 85% for the 0, 30, and 90 degree chambers, respectively. The fraction with $\Delta P/P < 10\%$ was 87%, 95%, and 94%.

Due to the generally higher momentum of the tracks the momentum resolution of TPC2 will be dominated by measurement accuracy. An estimated position resolution of 1 mm leads to an angle resolution in TPC2 of about 3 mrad and a momentum resolution $\Delta p/p^2 = .01$.

5. Particle Identification

Particle identification is of particular importance for the aforementioned physics goals. In Figure 4 is plotted the momentum spectrum for π's, K's and protons in the central rapidity region. As has been demonstrated by PEP4, the TPC is particularly effective in separating

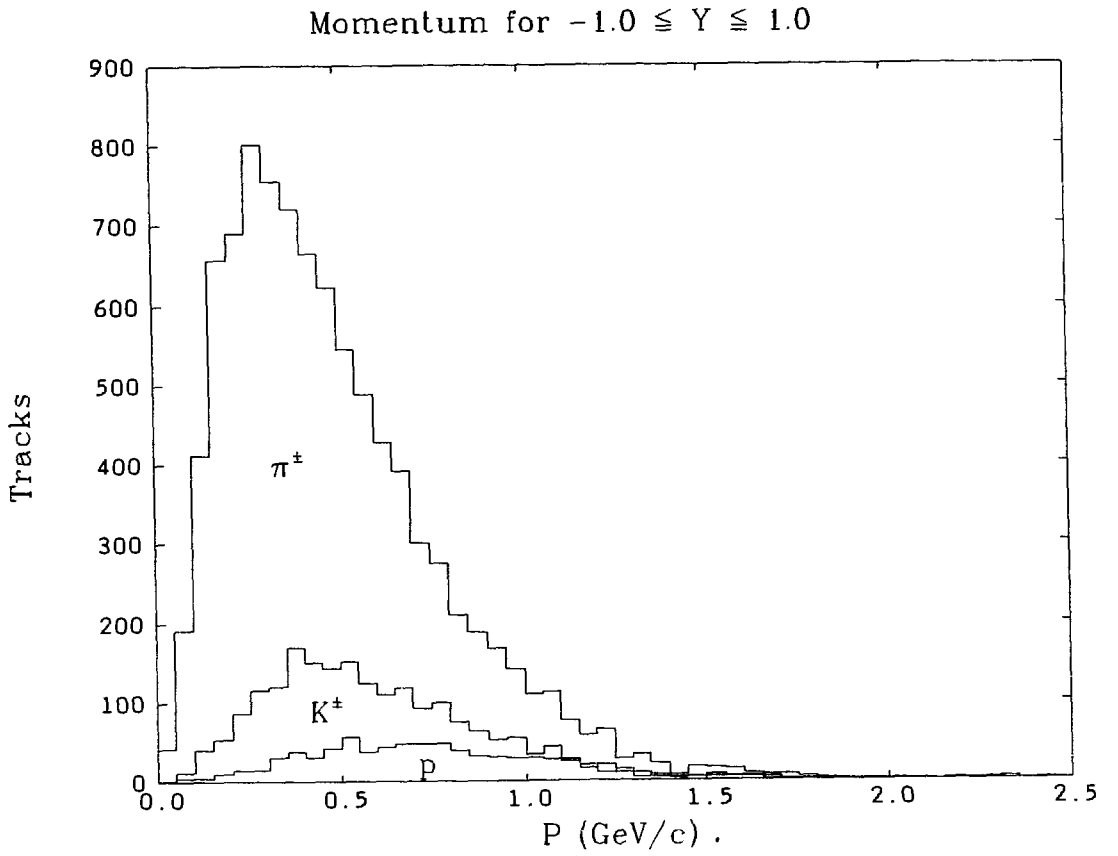

Fig. 4. **Momentum spectrum of charged pions, charged kaons and protons in the central rapidity region**

particles by ionization loss in the region between 100 and 700-1500 MeV/c depending on the particle species; see Fig. 5. It should be noted that clear π/μ separation is possible below 100 MeV/c (a unique feature of this method). $\pi/K/p$ separation is obtained between 100 MeV/c and 700 MeV/c. K/p to > 1000 MeV/c and deuterons to 1500 MeV/c. All of this with narrow bands of electron contamination. Extending $\pi/K/p$ separation to as low a momentum as possible imposes difficult requirements on electronics dynamic range; see Fig. 6 . It is seen that a dynamic range of 50:1 is required to distinguish K's from p's down to 100 MeV/c although π/K separation should work to 50 MeV/c. With a

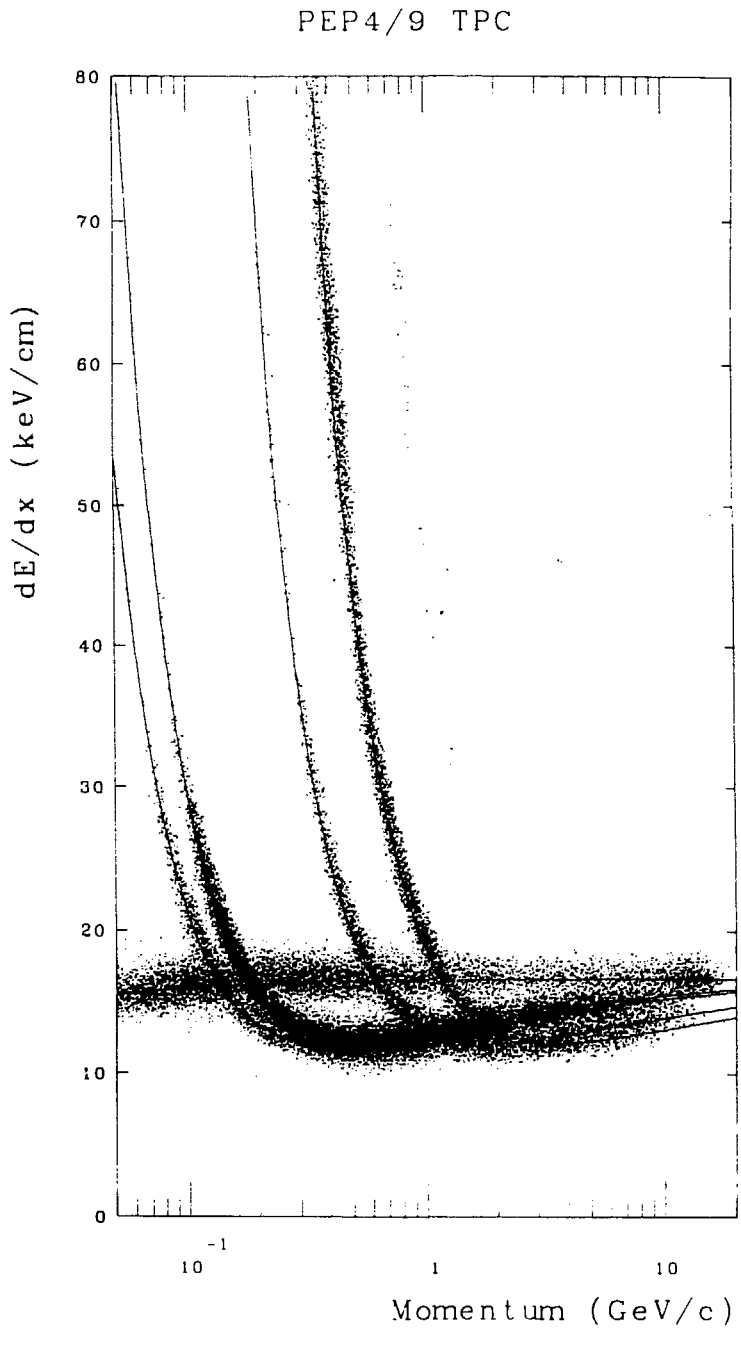

Fig. 5. **Energy loss spectrum of tracks measured in the PEP-4 TPC**

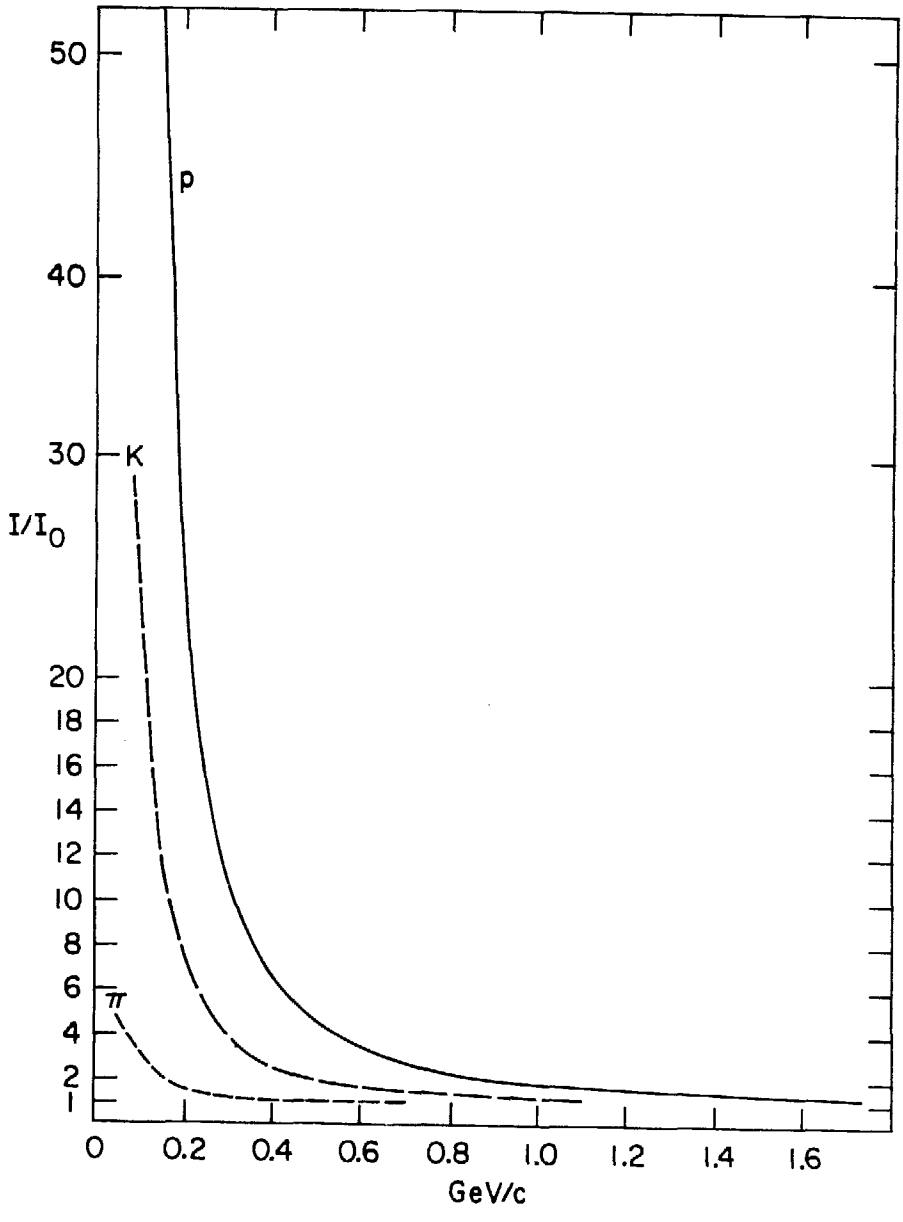

Fig. 6. Calculated ionization of pions, kaons, and protons as a ratio to the minimum ionization level.

nominal 100 cm of sampled track (100 cm of gas) the sigma of truncated mean samples at minimum ionization is 5-6%. In order that the sampling granularity does not materially reduce this resolution, minimum ionization should be more than 5 times the least significant bit of the digitizer. Thus to cover 50 times minimum, 8 bits of dynamic range is essential (10 bits would be more comfortable). The effort in progress mentioned in "readout electronics" has as goal a dynamic range of 10 bits.

Estimated Detector Costs

1. The Magnet

The cost of constructing the magnet has been estimated by Gordon Danby at about five million dollars.

2. The TPC

Even though we have increased the number of chambers, increased the number of channels, and added analogue dE/dx information for the central TPC, the estimated cost of the electronics remains about the same as the previous $6.5M. This is because of the technological improvements which have occurred during the past two years and are expected to occur in the near future which we are taking advantage of in our design.

The estimated cost of the TPC chambers and associated equipment is approximately 2 million dollars.

3. Computers

The interaction rate for Gold on Gold at a small diamond luminosity of $\sim 10^{25}$ is $\sim$ 100 per second. Triggers selecting central collisions are expected to reduce this to one readout per second or less. Early triggers may achieve only a further factor of ten improvement on this to make an analysis load of about 50,000 events per week. The largest computer load is generated by the track finding (pattern recognition) task which is about 0.1 seconds per track on a VAX 780, approximately linear in the track number[3]. Thus the pattern recognition load corresponds to approximately 500 × VAX 780 speed (roughly a kiloVAX) assuming data reduction is to keep up with data generation.

Currently the Fermilab ACP project is operating event computing power in amounts corresponding to 200 VAX780 equivalents acquired from a commercial

source at a cost of about $2000 per 780. Thus a kiloVAX is currently available for around two million dollars. ACP plans include a replacement of the CPU by one ten times faster at a target price of $2500 per unit. This would mean a kiloVAX would cost under a half million dollars very soon (hardware cost only).

Nevertheless if one were to plan on a dedicated computer facility to do all the various jobs required for this project we do not wish for planning purposes to depart from our prior estimate of 3-4.0 million dollars made in Ref. 1.

All the above costs do not include the usual EDIA and contingency nor the salaries of the collaboration working on the project.

Summary of Estimated Approximate Costs

The basic TPC electronics has been estimated to cost	$6.5 M	These two items should be considered together as a package
The TPC chamber and associated equipment is estimated to cost	2.0 M	
Trigger calorimeters, etc.	$ 1.5 M	
The Magnet is estimated to cost	5.0 M	
Dedicated Required Computer Facilities	3.5 M	
TOTAL COST	$18.5 M	

All the above costs do not include the usual EDIA and contingency nor the salaries of the collaboration working on the project.

These cost estimates are very close to those estimated two years ago in Ref. 1 except that the loss of the free SREL magnet has increased the magnet cost by ≈ 4 M and trigger calorimeter costs have been added. This is in spite of the increased electronics capability due to dE/dx measurements, increased number of channels, etc., and addition of 2 TPC chambers.

References

1. Lindenbaum, S.J. and Schroeder, L. Large Magnetic Spectrometer. RHIC Workshop: Experiments for a Relativistic Heavy Ion Collider, April 15-19, 1985, P.E. Haustein and C.L. Woody, Editors, pp. 211-252 (Brookhaven National Laboratory, Upton, New York, 1985).

2. Proc. of the 5th Intern. Conf. on Ultra-Relativistic Nucleus-Nucleus Collisions (Quark Matter '86), Asilomar, California, April 13-17, 1986, L.S. Schroeder and M. Gyulassy, Editors. Nucl. Phys. A461 (1987).

3. Lindenbaum, S.J., Etkin, A., Foley, K.J., Hackenburg, R.W., Longacre, R.S., Love, W.A., Morris, T.W., Platner, E.D., Saulys, A.C., Asoka-Kumar, P.P.V., Chan, C.S., Kramer, M.A. Large Solid Angle Tracking of Monte Carlo Events of Heavy Ion Collisions in TPC Magnetic Spectrometers. Proc. of the 5th Intern. Conf. on Ultra-Relativistic Nucleus-Nucleus Collisions (Quark Matter '86), Asilomar, California, April 13-17, 1986, L.S. Schroeder and M. Gyulassy, Editors. Nucl. Phys. A461, pp. 431c-442c (1987).

4. Proceedings of the Bielefeld Workshop, May 1982, Quark Matter Formation in Heavy Ion Collisions, Eds. M. Jacob and H. Satz (World Scientific, Singapore).

5. Proceedings of the Third Int. Conf. on Ultra Relativistic Nucleus-Nucleus Collisions, Brookhaven National Laboratory, September 1983, Nucl. Physics A418, (1984).

6 L. Van Hove, Z. Phys. C, Particles and Fields 21, 93-98 (1983).

7. L. Van Hove, Hadronization Model for Quark-Gluon Plasma in Ultra-Relativistic Collisions. CERN-TH.3924, June 1984.

8. M. Gyulassy, K. Kajantie, H. Kurki-Suunio and L. McLerran, Nucl. Phys. B237 (1984) 477.

SOME THOUGHTS ABOUT EXPERIMENTS IN THE FRAGMENTATION REGION

P. Braun-Munzinger and J. Stachel
Physics Department, SUNY, Stony Brook

We present the results of some discussions about possible experiments in the fragmentation region. At RHIC energies one expects the baryon-rich regions to be within, say, 3 units of the beam rapidity, so that the fragmentation region is defined as $|y|>3$ or $\theta<5.7°$. In the previous RHIC workshop [1] an experiment was designed to study the decay of one of the two hot, baryon-rich fireballs presumably formed in a central collision of two heavy ions at RHIC energies. Due to the very large rapidity densities expected in this angular region the detector considered in [1] consisted of a very large magnetic spectrometer to spread out in space the produced charged particles. The main physics motivation for this detector is to study properties of the quark gluon plasma (hopefully) formed in the baryon-rich fragmentation region. Meanwhile the first results from experiments at the AGS and CERN have provided evidence [2] that energy densities predicted to be necessary for plasma formation are already reached in fixed target experiments at energies where there is still substantial stopping. In such experiments the central region is baryon-rich and studies of it should yield information similar to what can be obtained from the fragmentation region at RHIC.

In view of this new development we have tried to reassess the physics goals of an experiment covering the fragmentation region at RHIC. Some of the findings are listed below:

(i) Quark gluon plasma formation in the fragmentation region should be strongly correlated with plasma formation in the

central region. In particular we expect large rapidity shifts of the fragment fireballs and high temperatures for events producing a high energy density in the central region. Plasma investigations in the fragmentation region should therefore be coupled to experimental set-ups covering the central region.

(ii) There are observables for plasma formation in the RHIC fragmentation region which might yield information different from that obtained by studies of the baryon-rich central region at CERN or AGS energies. For example, we do not expect a strong Drell-Yan contribution to dilepton production for rapidities $y>3$. Any sizeable cross section for dilepton pairs in this rapidity region will indicate a strong thermal component and may be used as a thermometer of the hadronic or quark-gluon fireball formed in the fragments. On the other hand, thermally produced dimuon pairs will be very rare in the high mass range ($m \geq 3$ GeV) unless the temperature is very high. At temperatures around $T = 500$ MeV, however, the quark phase, if it exists, will be the dominant source of high mass dimuon pairs [3].

(iii) There is clearly an interest in dedicated smaller set-ups to study specific observables in the fragmentation region. A small hadronic calorimeter fitting in between the beampipes of the two rings can be used to study the energy or rapidity distribution of forward going neutrons in an effort to gain information on the stopping mechanism. Similar but complementary information may be obtained by studying soft, low p_T photons produced in the deceleration process. Both set-ups would be of medium complexity and could be combined with one of the big experiments covering the central region. More ambitious would be a project to search for objects with unusual charge to mass ratio as this would require a forward spectrometer carefully worked into the machine lattice.

Some of these considerations have led to changes in the planned design of experiments in the central region. The study of dileptons in the fragmentation region can, e.g. be incorporated into the dimuon detector (see the discussion there). In general, it is our conclusion that a large experiment in the fragmentation region will be a second generation experiment at RHIC unless some exciting new physics idea comes around.

References:

[1] M. Faessler et al. in Proceedings of the RHIC Workshop 1985, ed. by P.E. Haustein and C.L.Woody, BNL51921, p.269.

[2] W.J. Willis, rapporteur's talk at the International Conference on High Energy Physics, Uppsala, Sweden, July 1987;
see also: Proceedings of the Quarkmatter 1987 Conference, Nordkirchen, Germany, August 1987, to be published in Z.Physik C.

[3] K. Kajantie et al., Phys. Rev. D34(1987)2746.

CONTRIBUTIONS

GHEISHA Simulation Calculations of Albedo

Avigdor Gavron

Los Alamos National Laboratory

Introduction

The pupose of this note is to present some results of albedo calculations using the code GHEISHA version 6, of H. Fesefeldt, Aachen, FRG. Until confronted with experimental results, these results should be used to obtain order of magnitude of albedo effects only. Their purpose is to enable designers of detectors for RHIC and other facilities to estimate the effect of albedo from a Uranium/Scintillator calorimeter on other detectors. The calorimeter used in the simulation is comprised of alternating Uranium plates (3 mm. thick) and scintillator plates (also 3 mm. thick). The total depth of the calorimeter is 6.4λ. The plates were cirular with a radius of 1 meter. The beams (p,n,π-s) impinged perpendicular to the plates at the center of the circle.

Results

We have performed calculations for beam kinetic energies of 0.2, 0.5, 2, 5, 20 and 50 GeV. For each of these energies we present detailed results for $dE/d\Omega$ and $dN/d\Omega$ (the total kinetic energy and particle multiplicity per unit solid angle) for albedo neutrons. There is a threshold of 5MeV, below which albedo neutrons are discarded. (This is due to lack of disk space for the albedo file generated by GHEISHA but should not affect the conclusions). For albedo pions and protons, the albedo results are less accurate due to the very limited statistics of the Monte-Carlo simulation. The results were obtained using 2 weeks of CPU-time on a microvax II computer(!), so it was not

feasible to obtain significantly better statistics. Thus, I can only summarize the average albedo-pion kinetic energy:~100MeV; the albedo-pion multiplicity is presented in Fig. 9. The proton-albedo multiplicity is somewhat lower and consequently - the statistics too poor to present any meaningful result. The few proton events seem to indicate that the proton kinetic energy is of the order of 50-200 MeV.

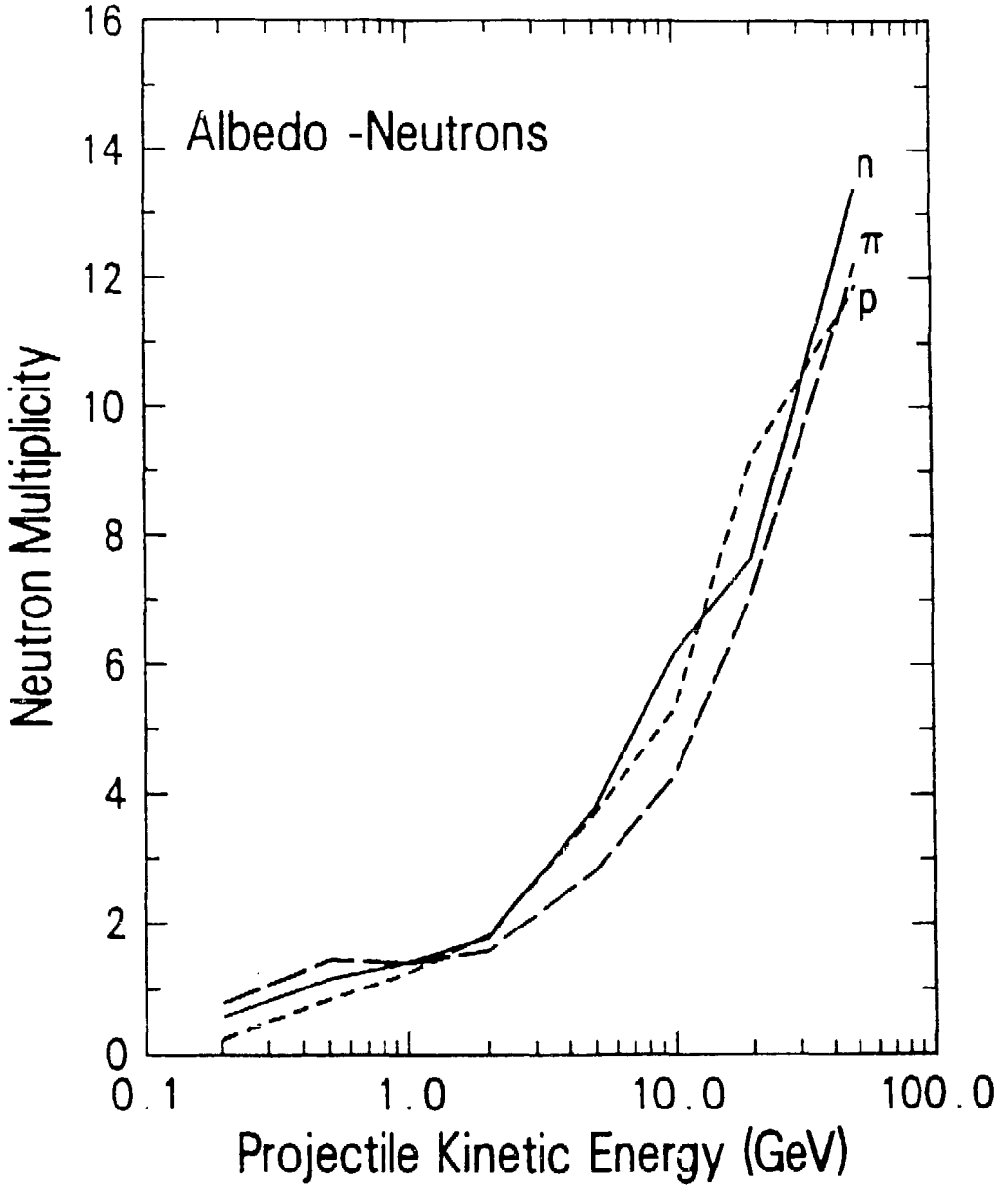

Fig. 1: Albedo neutron multiplicity as function of projectile kinetic energy. The curves are labelled by the projectile.

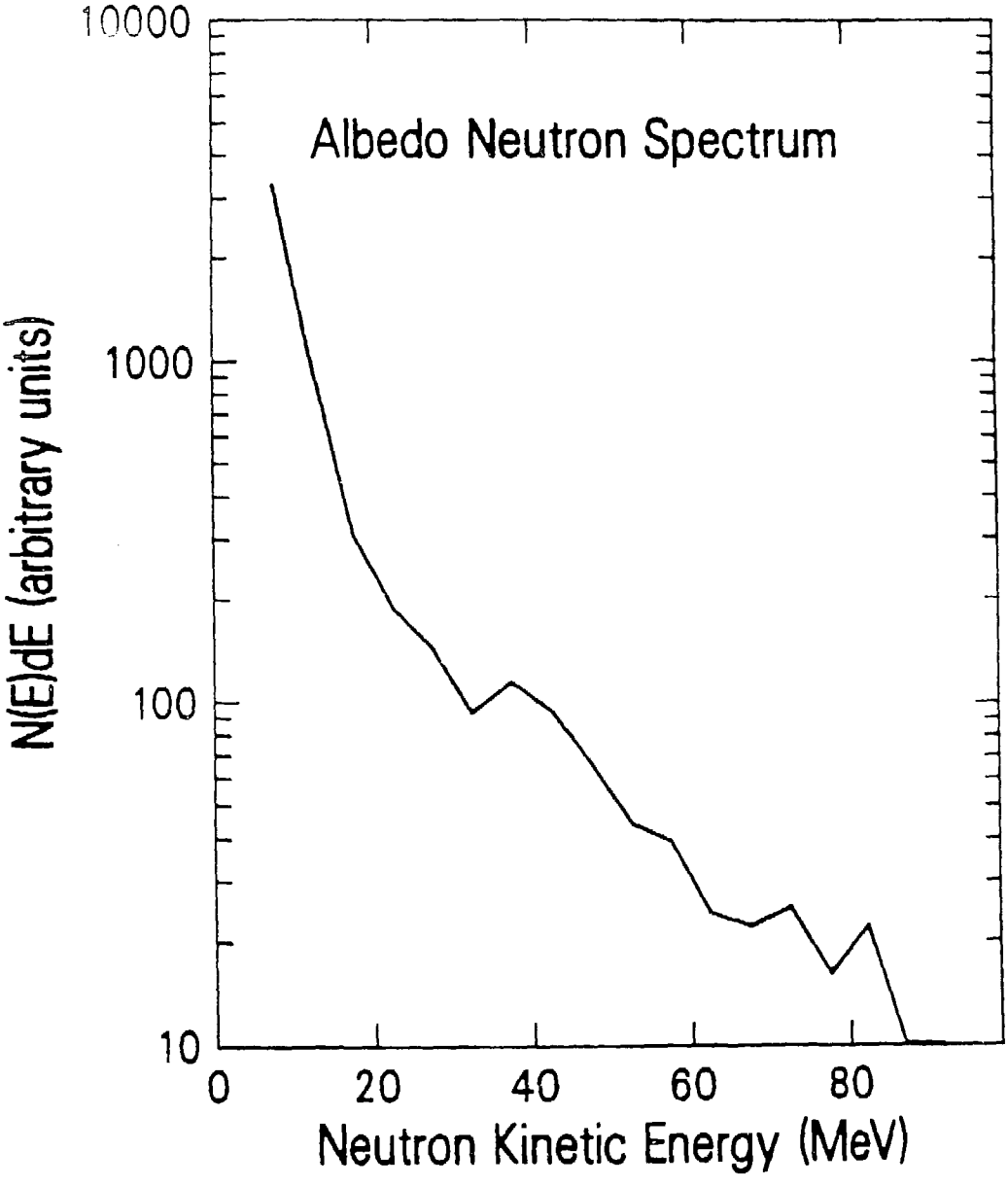

Fig. 2: Albedo neutron spectrum for 5 GeV pions. There is no significant variation between neutron spectra produced by other projectiles at other bombarding energies.

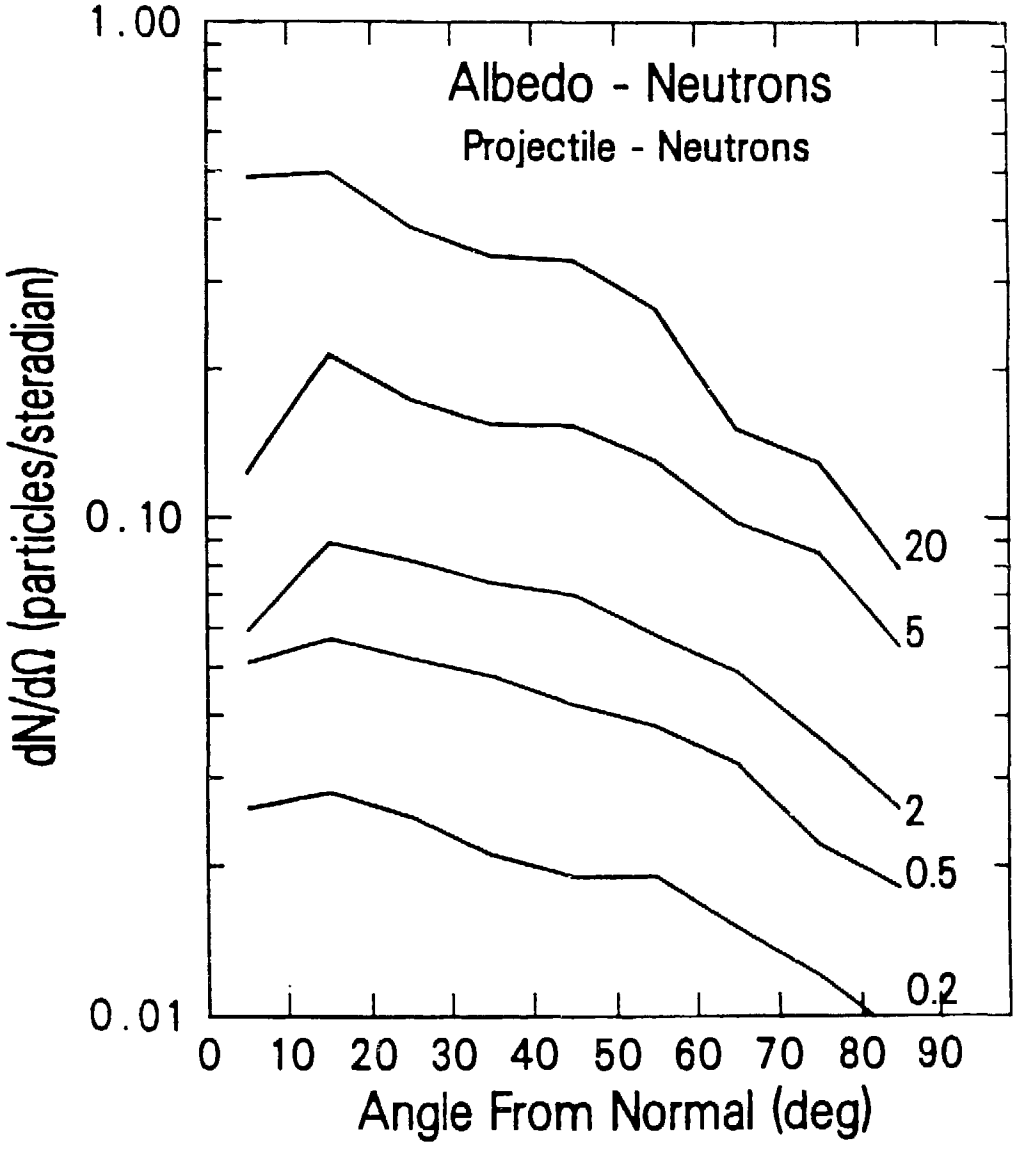

Fig. 3: Albedo neutron angular distribution. Projectile - neutrons. Curves are labelled by the projectile kinetic energy.

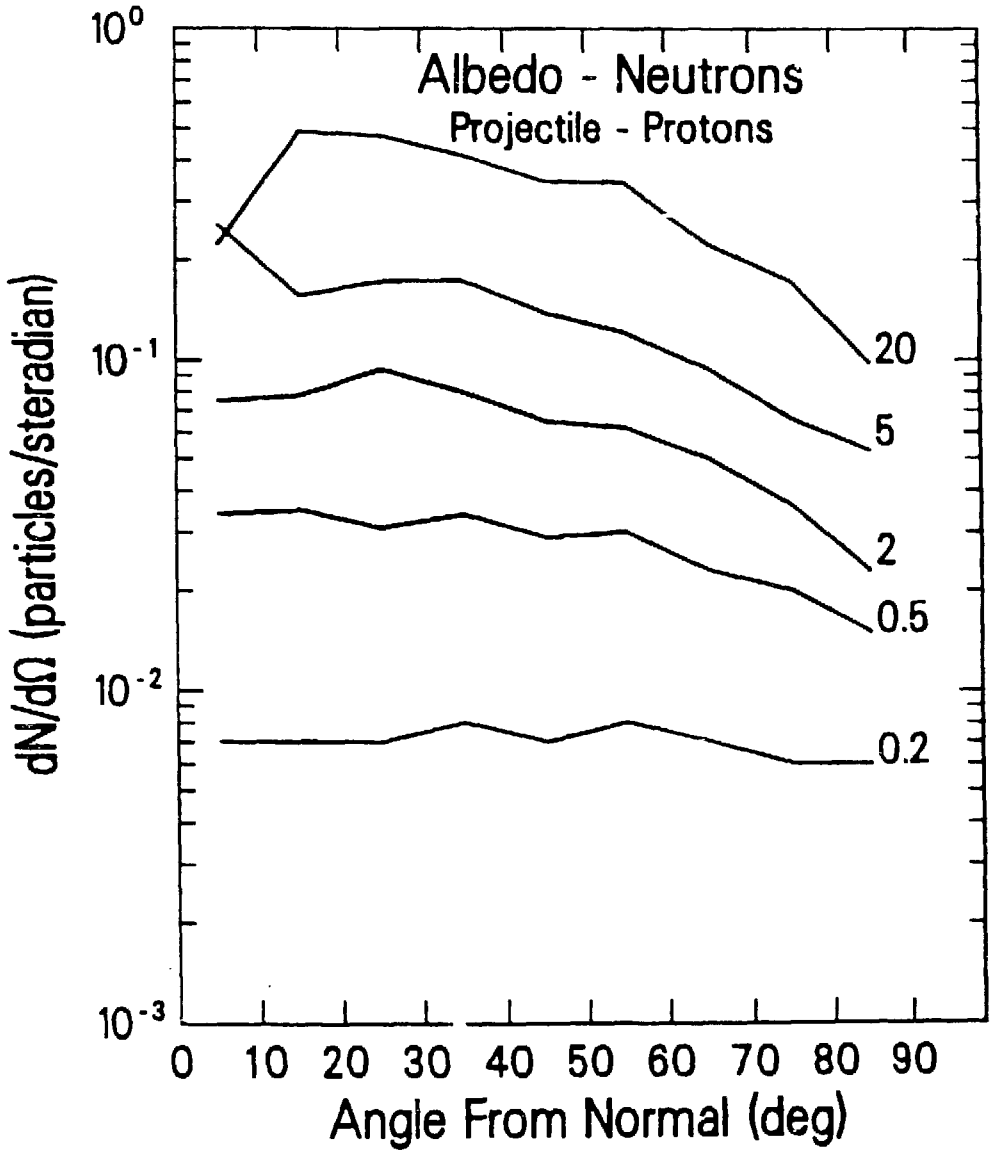

Fig. 4: Albedo neutron angular distribution. Projectile - protons. Curves are labelled by the projectile kinetic energy.

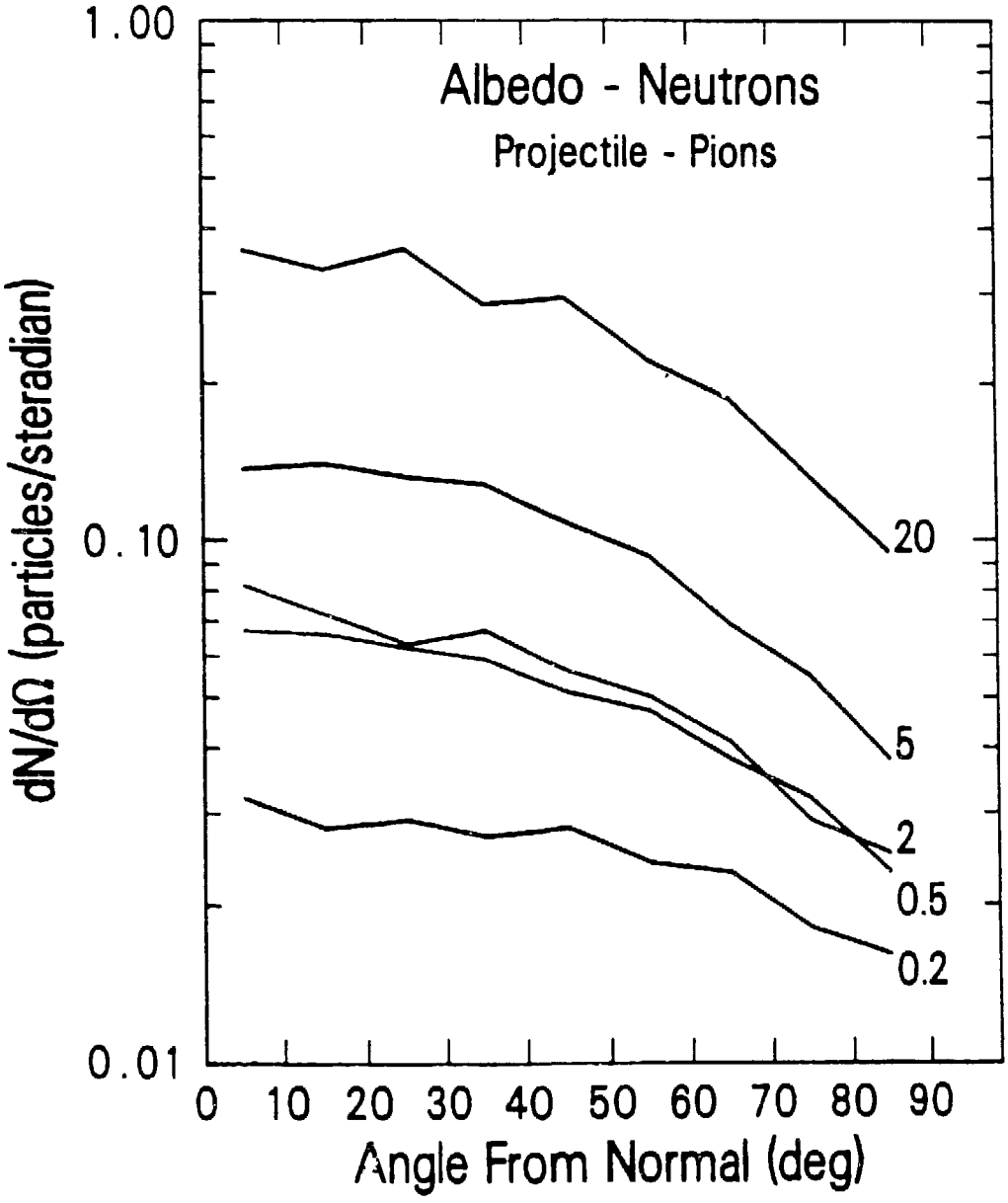

Fig. 5: Albedo neutron angular distribution. Projectile - pions. Curves are labelled by the projectile kinetic energy.

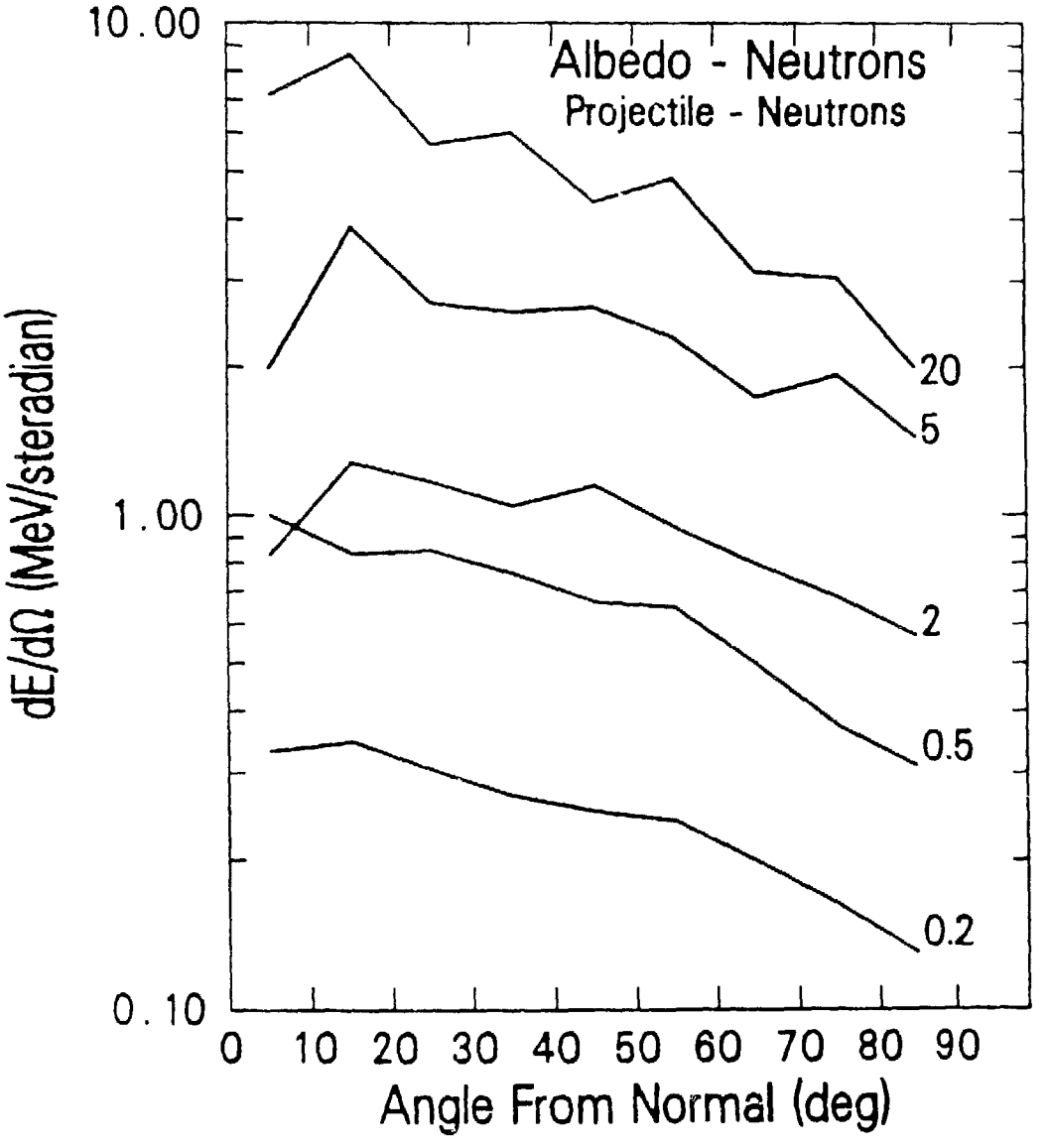

Fig. 6: Albedo neutron energy per unit solid angle. Projectile - neutrons. Curves are labelled by the projectile kinetic energy.

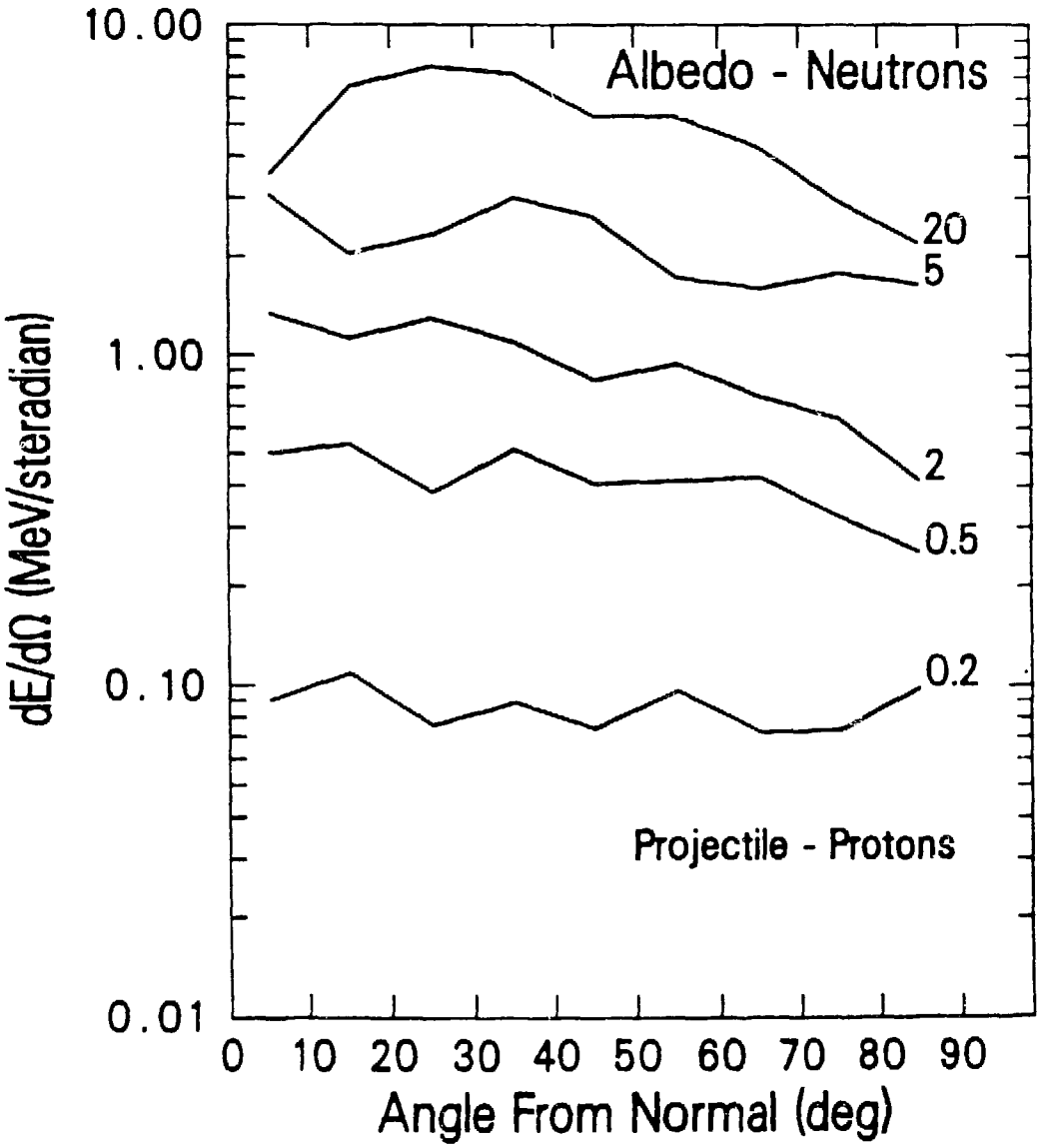

Fig. 7: Albedo neutron energy per unit solid angle. Projectile - protons. Curves are labelled by the projectile kinetic energy.

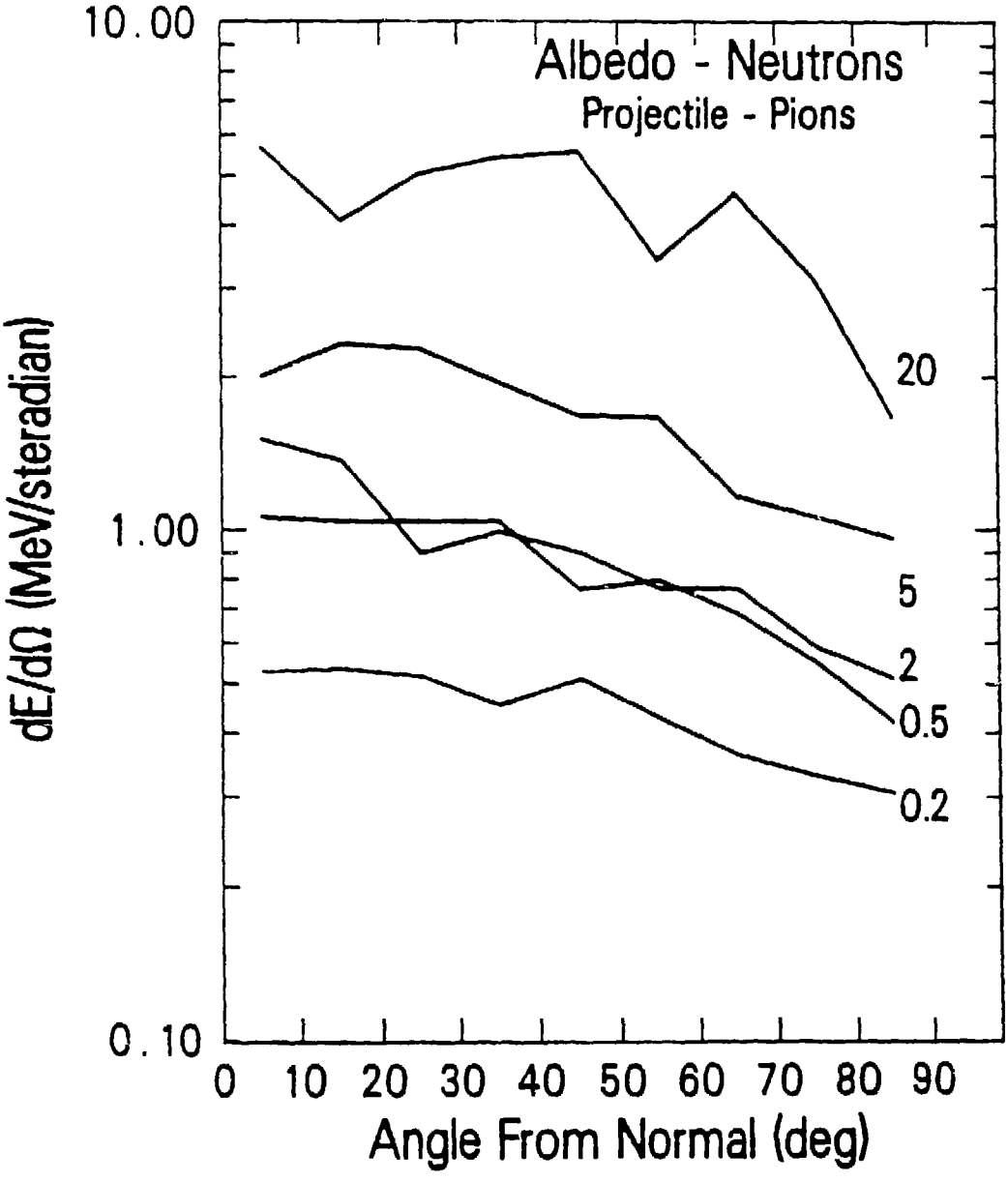

Fig. 8: Albedo neutron energy per unit solid angle. Projectile - pions. Curves are labelled by the projectile kinetic energy.

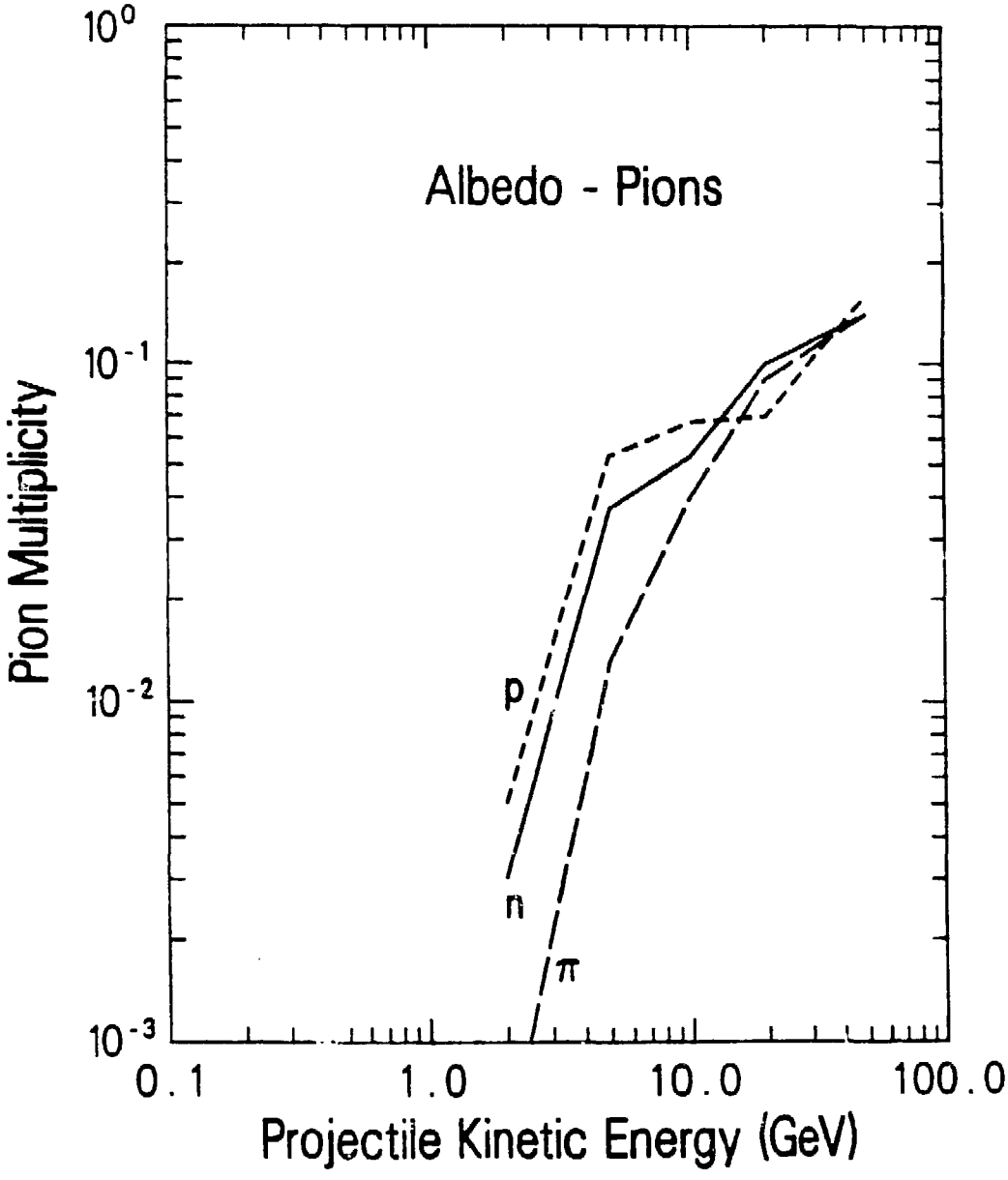

Fig. 9: Albedo pion multiplicity as function of projectile kinetic energy. Curves are labelled by type of projectile particle.

RESULTS AT 10 GEV/NUCLEON FROM THE E814 COLLABORATION*

K.L. Wolf
Cyclotron Institute
Texas A&M University,College Station, Texas 77843

Experiment E814 at the Brookhaven AGS covers a broad range of topics, as established by the title of the proposal " Study of Extreme Peripheral Collisions and the Transition from Peripheral to Central Collisions Induced by Relativistic Heavy Ions". The members are equally varied in background with a uniform distribution from low energy nuclear science, the Bevalac and high energy physics. Eight graduate students round out the group. The membership may be listed as : M.Fatyga, R.Hogue, D.Lissauer, T.Ludlam, L. Olsen, V. Polychronakos, I. Stumer, T. Throwe (BNL); V. Burkert (CEBAF); W.J. Willis (CERN); Z. Moroz, J. Wojtkowaka (Swierk); J. Boissevain, A. Gavron, B.V. Jacak, W.E. Sondheim, J.W.Sunier, H.Van Hecke (LANL); B.Bassalleck, J.Hall, N. Kominos, D.Wolfe (UNM); W.Cleland, J.Saladin, J. Thompson (U. Pittsburg); P.Braun-Munzinger, G.David, M.Herman, J.Jing, P.Paul, J.Stachel, L.Waters (Stony Brook); O.Benary, S.Dagan, Y.Oren (U. Tel Aviv); A.Farooq, H.L.Kent, A.Ray, J.K.Simon, J.P.Sullivan, K.L.Wolf (TAMU); D.G.Sarantites, T. Semkow (Washington Univ.); S.V. Green, B.Shivakumar (Yale).

The first beam time on the AGS used by the E814 collaboration has produced some interesting results. The primary purpose of the experiment was a test of detectors, but it became clear to us several months in advance that,in addition, a reasonable experiment could be performed. The experimental apparatus is relatively simple compared to the instrumentation of the other major heavy-ion groups, as is shown in Fig.1. An array of 600 NaI detectors coupled to vacuum photodiodes covered 144 towers of uranium- scintillator calorimeter. Both detector systems were used previously in experiments at CERN, before being reworked at Stony Brook and Brookhaven,respectively. The beam was directed into the center of the calorimeter, with a subtended angle of approximately 50 degrees. The NaI detectors formed an electromagnetic section of five radiation lengths. An extensive menu of triggers was used in the experiment, including several cuts on transverse energy, a type of multiplicity (R-counter), and a Bevalac Zow or leading particle type (S3). A plot of the calorimeter pulse height response for the 12 X 12 towers is shown in Fig.2, which was generated during the experiment. A silicon beam of 10 GeV/nucleon was used, corresponding to the maximum rigidity of the beam line. For analyzed and tagged beams of electrons, muons, pions, protons and deuterons the line performed well, and allowed extensive calibrations to be performed, which more than made up for the rigidity limit. The calibrations were extremely important for understanding the calorimeter response and the associated problems, and for making it possible to rapidly produce a first look at the heavy-ion data. The calibrations for nearly all particles from 150 MeV/c to 10 GeV/c produced a linear response in the calorimeter, which we believe to be the result of several compensating factors such as enhanced dE/dX response for low energies, balanced by light attenuation in the wavelength shifter

bars. An exception from linearity occurred for low energy deuteron beams, which gave an enhanced response, probably associated with neutrons from breakup.

Figure 3 shows the transverse energy distributions taken with 10 GeV/nucleon Si on Al, Cu, and Pb targets. These analyses are preliminary since the experiment was completed quite recently. The absolute values of the energy calibration may change slightly, and the overall cross section normalization may change, but for comparisions given here the data are valid. The shape of the transverse energy distributions is similar to the heavy-ion data taken at 200 GeV/nucleon, with a long plateau followed by a rapid fall off at high energies. This feature is interpreted as a pileup of the yield at high E_t for a relatively large range of central and near-central impact parameters. A more significant result from Fig.3 can be seen if the multiplicative factor of 5 is taken out of the cross section for the lead target, which results in a complete overlap of the distributions for the lead and copper targets at the high energy end. Results for the aluminum target are significantly lower. At face value, these results argue strongly for "complete stopping" of 10 GeV/nucleon silicon, with the copper nucleus furnishing enough matter in central collisions to stop the projectile. The heavier lead nucleus produces little additional stopping power, i.e. the extra matter is unnecessary. From a HIJET simulation, with the calorimeter geometry and response, a monotonic increase of the E_t with target mass should occur, thus arguing that finite acceptance is not the cause of the similarity between the two results.

The extension of the complete stopping condition from the Bevalac energy region to that of the AGS is an important result. With complete stopping, equation of state studies can be extended to AGS energies, in principle. Possibly, one-fluid hydrodynamic models can make semi-quantitative predictions about the energy flow and densities. In an extension of these calculations(1) significant flow is predicted, and densities of 5-10 times the normal value are attained. In addition, it may be possible to probe the mixed phase region of the quark-gluon plasma at the AGS. A careful study of the energy flow may produce a signature due to an associated softening of the equation of state. Another search for a signal from the high baryon density plasma involves the correlation of leading particles e.g. lambdas, with energy flow. Both of the methods mentioned here are well-suited to experiment E814 which will be performed in 1988. The layout of the experiment is shown in Fig.4. The large number of components necessary to complete the experimental apparatus is typical of these heavy ion experiments at high energies. A 4π calorimeter coverage, with an extensive forward spectrometer makes this experiment quite powerful for the correlation of leading-particle properties with stopping power and energy flow. The study of exotic excitations at projectile rapidities is another major goal. In the target rapidity region, complimentary information is provided by the target calorimeter which consists of 1000 NaI detectors and plastic scintillator paddles. The forward spectrometer features BNL-designed high resolution drift chambers (DC-1,2,3) which can operate in the high multiplicities

encountered in a one-degree cone around the beam axis. The multiplicity density is similar to the values that will be encountered at RHIC. The participant calorimeter is another device which is of interest for the design of RHIC detectors in the future. The space limitations along the beam axis require the minimization of the longitudinal dimension of the calorimeter, while covering the angular range of 1-45 degrees. This detector is in the design stage and will be constructed at LANL in collaboration with TAMU. It is a lead-plastic scintillator sampling device with two electromagnetic and two hadronic sections for a total of 3.7 absorption lengths. The angular segmentation corresponds to polar and azimuthal angles of 5 and 22.5 degrees, respectively,as shown in Fig.5. The quadrants can be reconfigured to provide a variable beam aperture. The unusual feature of this calorimeter is the wavelength-shifting fiber optic readout. Green-transmitting optical fibers run radially to the photomultiplier tubes at the edges of the box. Besides saving space along the beam, the fiber optic readout has two significant advantages over conventional designs. A uniform response is attained throughout the calorimeter, and the fibers essentially eliminate Cherenkov light contamination which can be a serious problem caused by particles rattling down WLS bars or rods. The combination of the uniform response, the elimination of Cherenkov light, and the longitudinal segmentation may result in an improved low energy response for the AGS and for RHIC. The disadvantage of the fiber optic method is the labor intensiveness, since optical fibers are bonded by hand into nearly 8000 plastic scintillator plates in the participant calorimeter. Fortunately this is a rather small device by high energy standards, as can be seen in Fig.6. This example of size is true also for RHIC detectors in the future. The segmentation may be large for some types, but the scale of the devices is relatively small, which should keep construction facilities and costs at a manageable level. It looks quite probable that the WLS and scintillating fiber designs will be employed at RHIC, and there is even a good probability that the participant calorimeter will be used at RHIC in the future.

* This work supported by the Robert A. Welch Foundation and by the Director, Office of Energy Research, Division of Nuclear Physics of the U.S. Department of Energy under contract DE-AS05-85ER40207.

Acknowledgements

We would like to thank the AGS staff for a successful effort and G. Rai for help in the setup of the GEANT 3.10 simulation.

References

1. H. Stocker and W. Greiner, Physics Reports 137,278(1986).

Figure 1. The layout of E814 test run at the AGS.

Figure 2. A leggo plot of the response of 144 towers of the uranium calorimeter.

Figure 3. Transverse energy distributions triggered by E_t levels for 10 GeV/nucleon Si on Al,Cu and Pb.

Figure 4. The experimental apparatus for experiment E814 as planned for experiments in September, 1988.

Figure 5. End view of the participant calorimeter.

Figure 6. A GEANT simulation drawing of the participant calorimeter.

AGS EXPT. 814 TEST

10 GeV/amu
SILICON & PROTON BEAMS

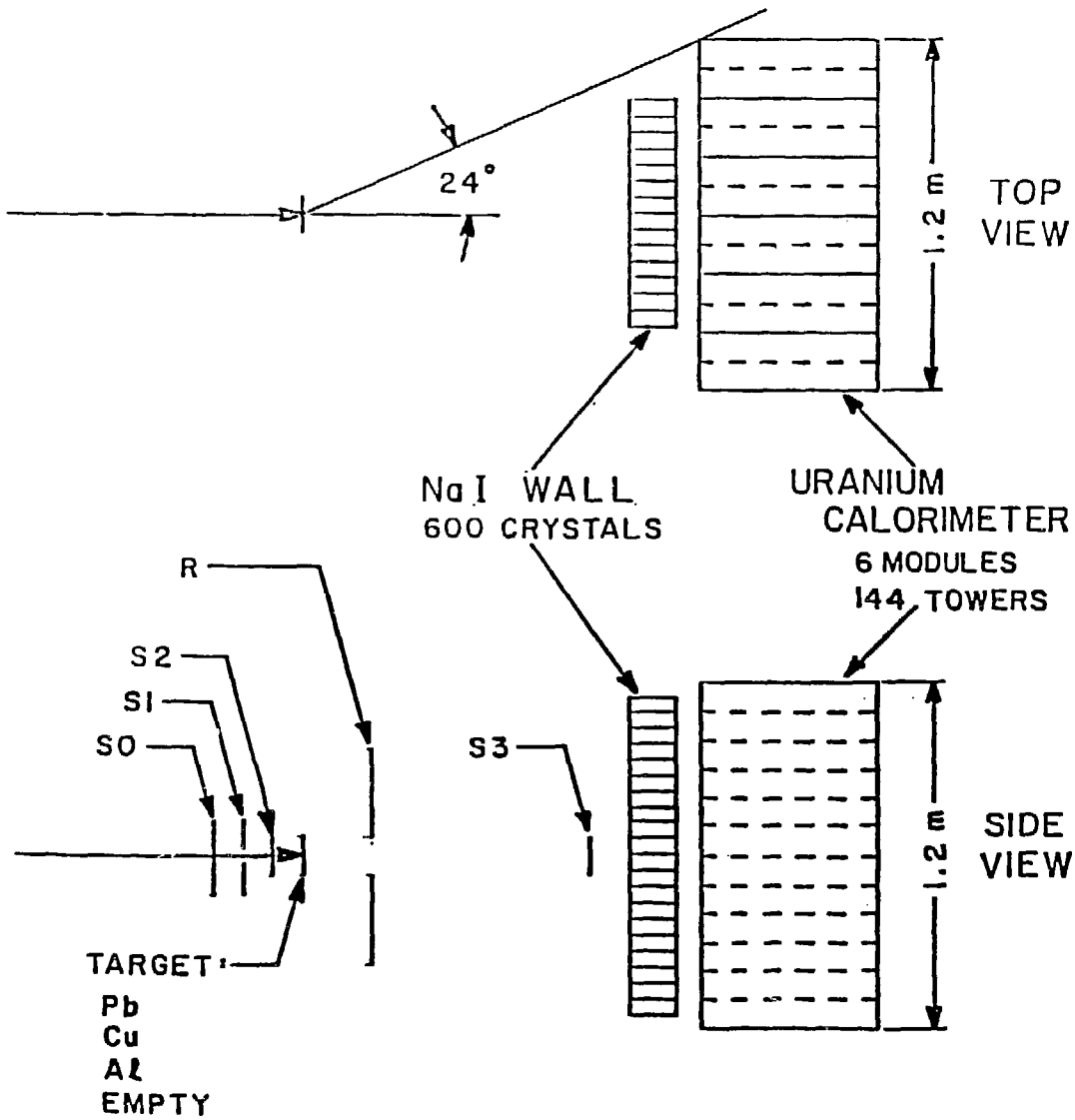

Figure 1

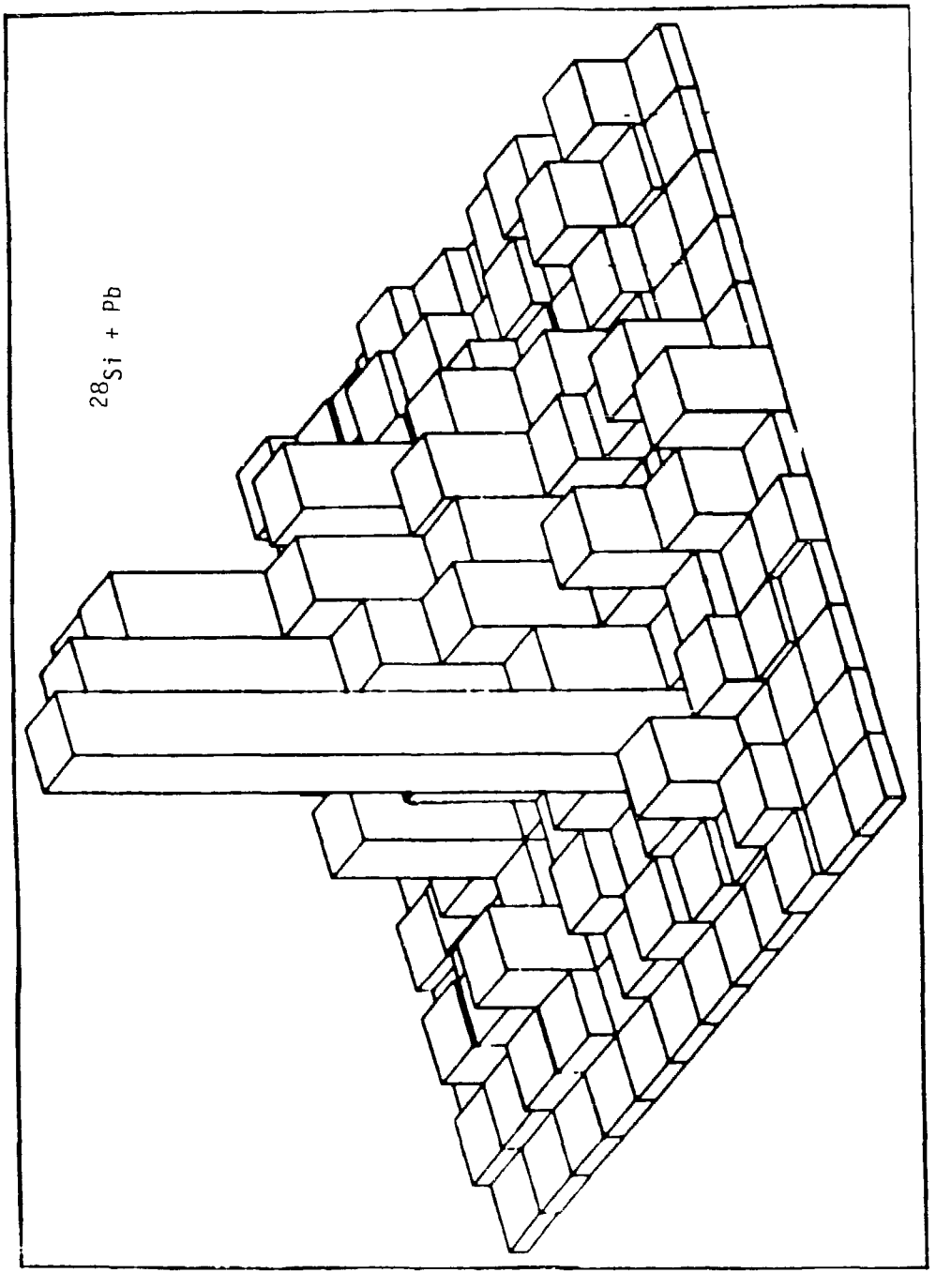

Figure 2

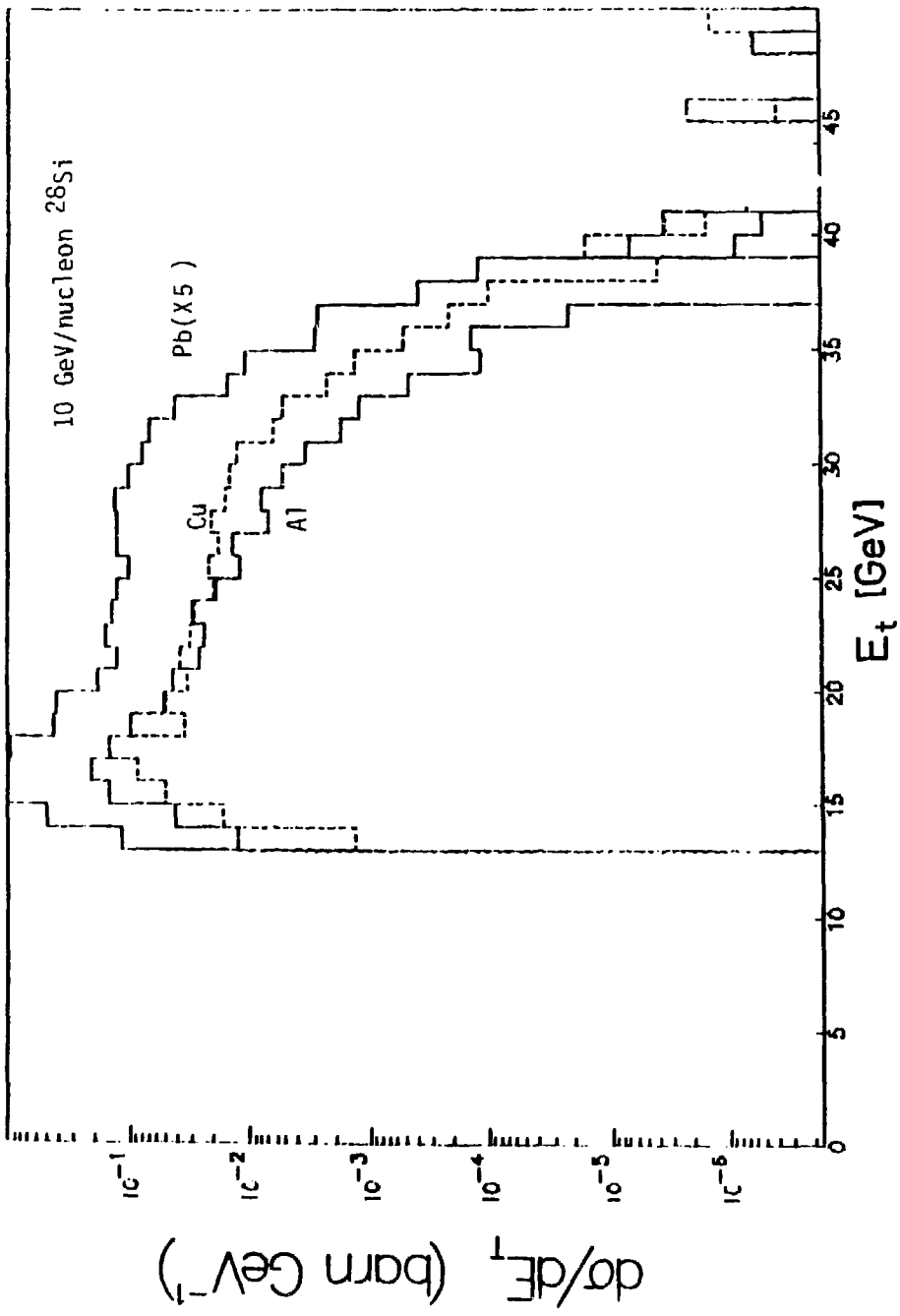

Figure 3

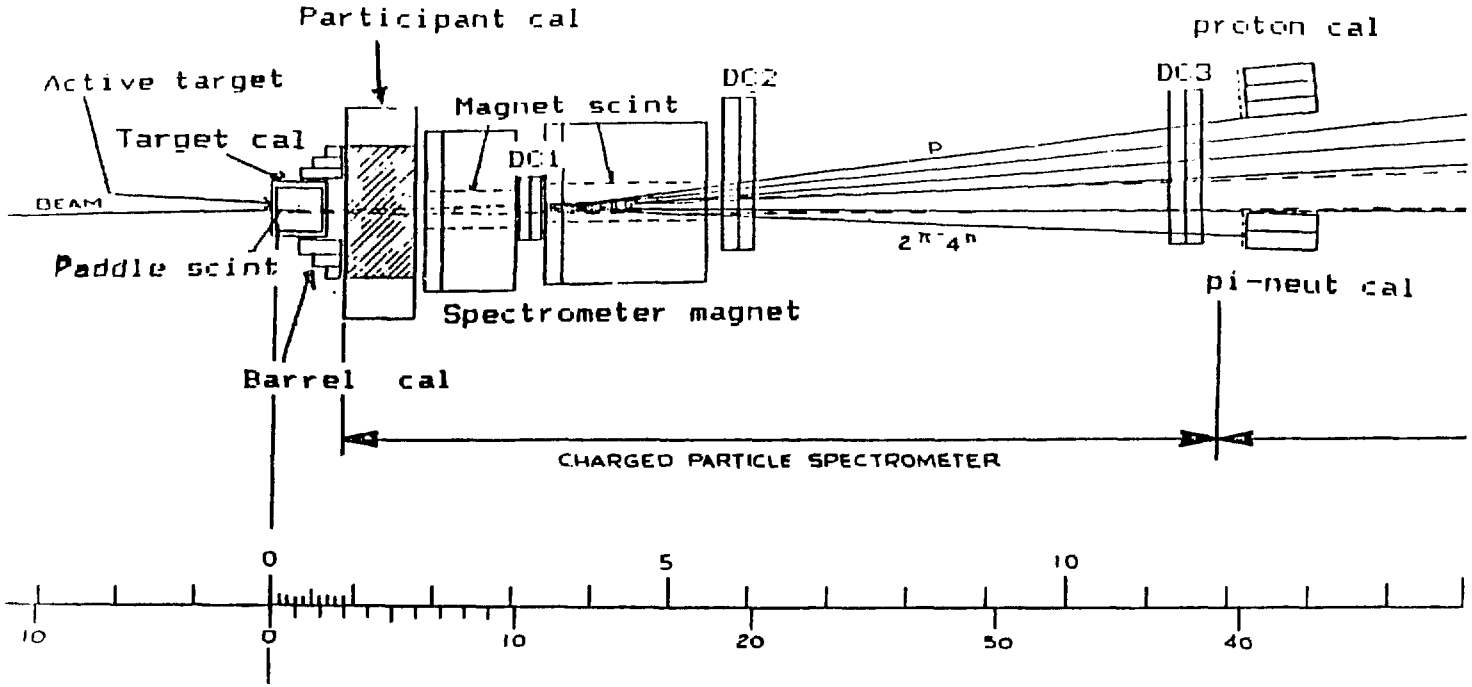
Participant cal
proton cal
Active target
DC2
DC3
Magnet scint
Target cal
DC1
p
BEAM
$2\pi^-4^n$
Paddle scint
pi-neut cal
Spectrometer magnet
Barrel cal
CHARGED PARTICLE SPECTROMETER
0
5
10
10
0
10
20
50
40

Figure 4

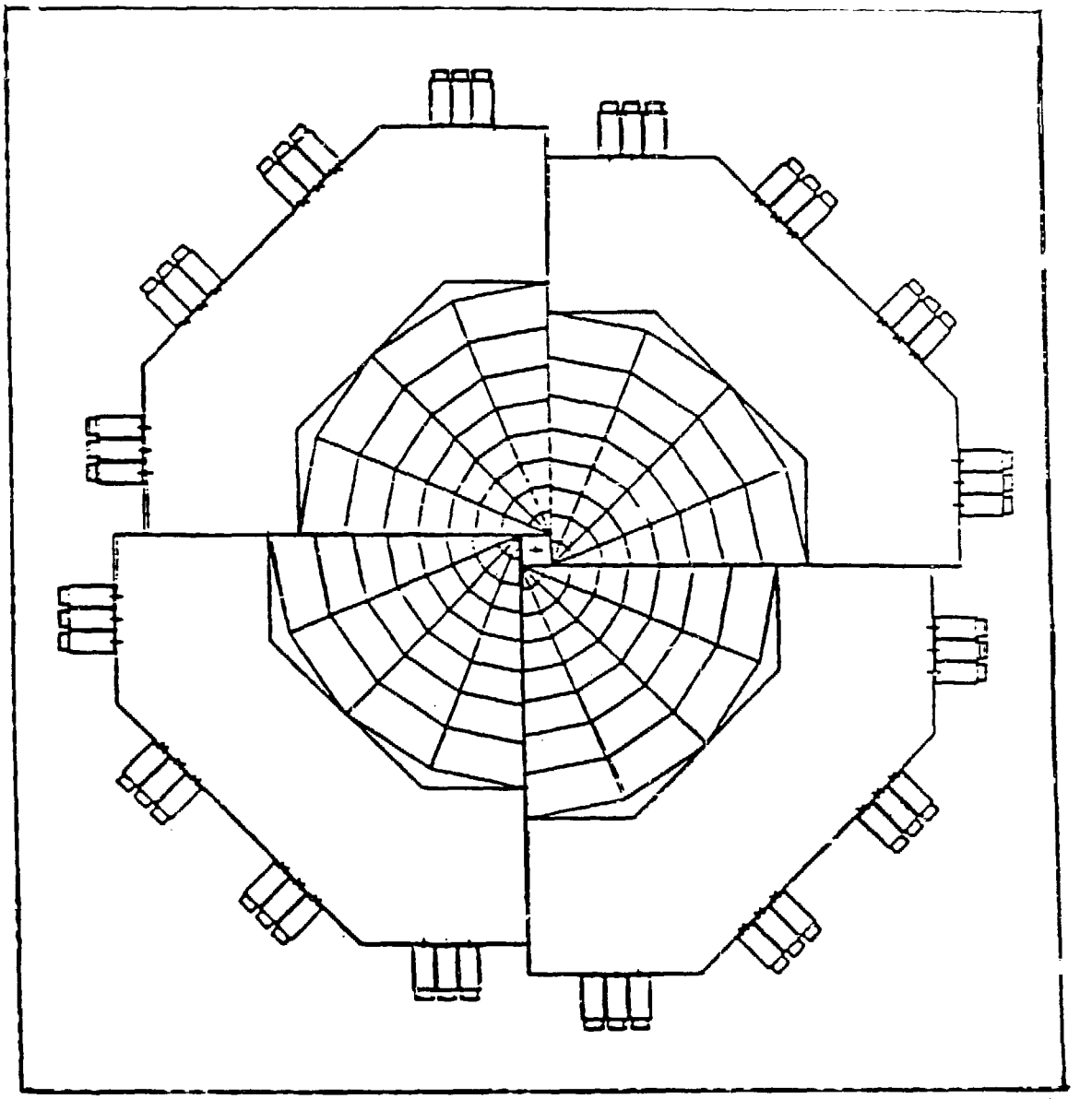

Figure 5

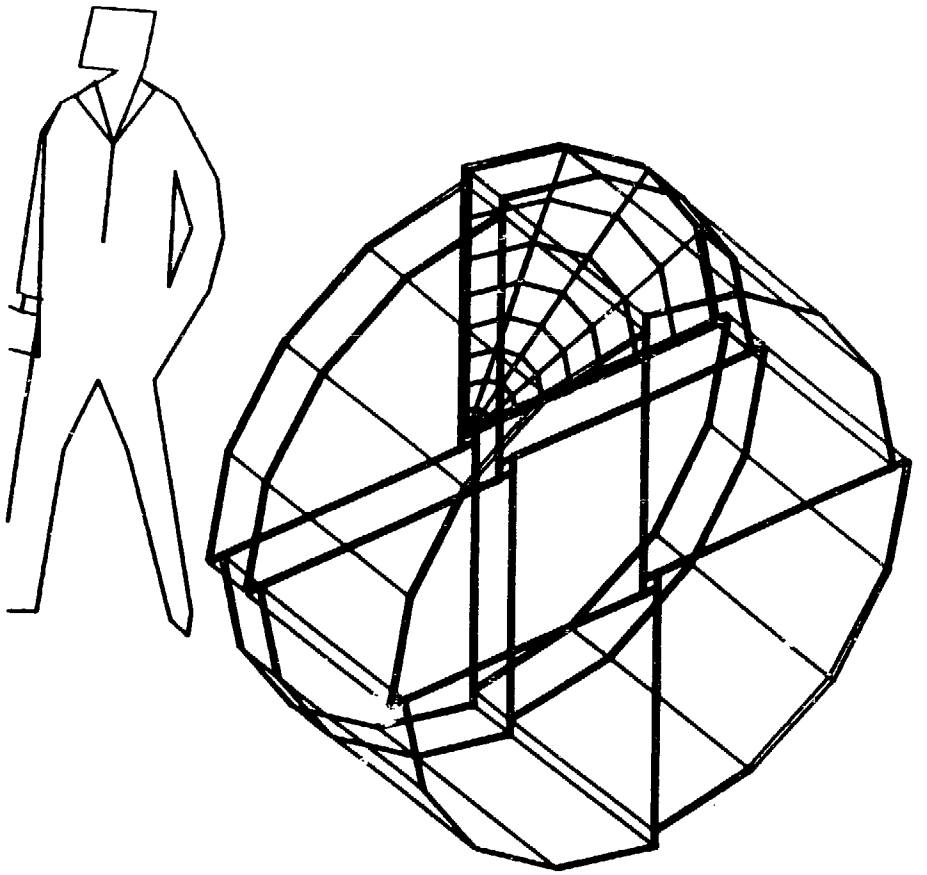

Figure 6

A POSSIBLE INTERACTION VERTEX POSITION DETECTOR

Arthur M. Poskanzer
Lawrence Berkeley Laboratory, Berkeley, CA 94720

A method to determine the position along the beam axis of the interaction vertex in a simple way, without tracking all the individual particles would be highly desirable. Because of the large interaction diamond in RHIC, a first guess at the interaction vertex would greatly help tracking and background reduction in an external spectrometer. Also, the information would be useful to determine when there are two interactions in the same beam crossing.

A detector is being considered consisting of scintillating fibers bent into rings and flattened to disks resembling mechanical washers. Many of these scintillating washers would be placed around the beam pipe so that the planes of the washers are perpendicular to the beam axis. Individual lucite light pipes would conduct the light externally where a pulse height measurement would be made for each washer. The idea is that with thousands of particles each washer would integrate azimuthally and only preserve the lateral information along the beam axis. The idea of making the scintillating rings flat is to present a large thickness to the particles nearby coming perpendicular to the beam axis and a small thickness to the other particles, thus increasing the localization of the response of the detector. This effect is compensated by the fact that many more particles at smaller angles to the beam axis hit the washers, both because of the larger solid angle they present to the vertex and also because the particles pass through more than one washer. Thus a calculation is required.

In the example studied the washers are one mm thick, and have an inner radius of 50 mm and an outer radius of 60 mm. Thus the cross section of the body of a washer is one mm by 10 mm. The washers are spaced every 10 mm along the beam axis. Thus the total mass is equivalent to a one mm thick cylinder of plastic around the beam axis. However, the results would be the same if all the dimensions were scaled by the same ratio. The present calculation has been done only in the forward hemisphere, with 50 washers, making the total detector one meter long. The response for one event with 500 particles in the forward hemisphere has been calculated. The particles

are assumed to be isotropic (distributed with a random cos theta). The path lengths of all the particles through each washer have been summed up and presented in the figure as a function of washer number. In this event the vertex is midway between the planes of two washers just off the axis to the left. Thus the figure may be reflected about the vertical axis and would then present a peak at the position of the vertex. The centroid of such a peak would determine the vertex position, and the narrowness of it would allow reasonable double interaction rejection. Assuming a dE/dx of 2 MeV/(gm/sqcm) the maximum signal would be about 20 MeV neglecting all losses of light.

However, the same graph for particles distributed randomly in pseudorapidity, is flat, without a peak, because of the much more pronounced forward-backward peaking of the particles. The next step clearly would be to do the calculation on events generated by a simulation program, such as Hijet. To really utilize the flat shape of the washers it would be necessary to discriminate against the many particles which contribute small pulse heights. Thus a possible great improvement would be to make the washers out of another material which introduced a time delay so that the small individual pulses would be below a discriminator.

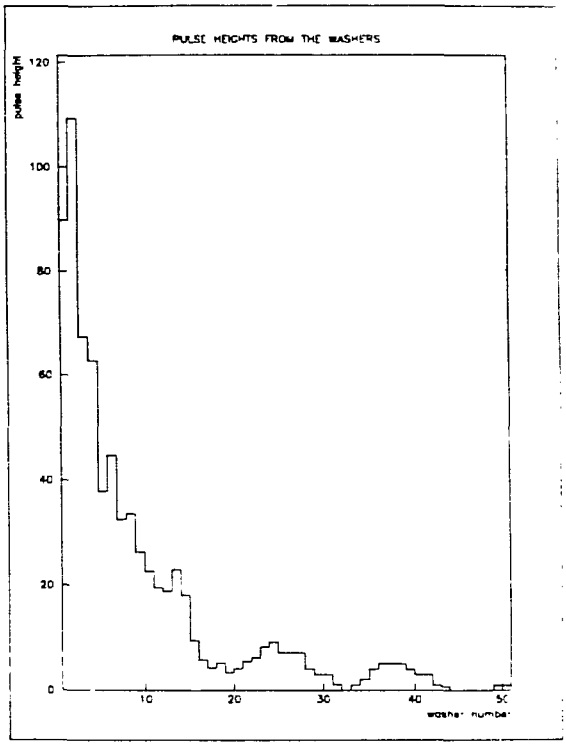

Figure Caption: The pulse heights for each scintillating washer summed for 500 particles distributed isotropically. The vertex is half a washer spacing to the left of the origin. The vertical scale is actually the sum of the path lengths in mm.

A 4π DETECTOR FOR THE STUDY OF NUCLEUS-NUCLEUS COLLISIONS

G. Rai, F. Bieser, S. A. Kleinfelder, G. Odyniec, H. G. Pugh,
P. A. Seidl, H. Wieman,

University of California
Lawrence Berkeley Laboratory
Berkeley, California, CA 94720

Abstract:

We present an outline of a proposed 4π tracking detector to study collisions between relativistic heavy ions at the Bevalac and describe the development of a prototype time projection chamber.

Introduction

Considerable progress has been made during the last two decades in studying collisions between relativistic heavy ions. Most of the pioneering work carried out at Bevalac placed special emphasis on probing the nuclear matter equation of state. The motivation stemmed primarily from the lack of knowledge on the behavior of nuclear matter when extrapolated from equilibrium p=0, T=0 (the realm of conventional nuclear physics) to extreme conditions p>>0 and T > 0. Understanding the equation of state is therefore fundamental in its own right and has implications in other fields of physics. It is important in the study of phase transitions - that is, the possibility of creating abnormal states such as pion condensate, delta matter, density isomers, hadron gas, and in neutron star stability, supernova dynamics, baryon rich quark-gluon plasma.

Experimentally, most of the information on the equation of state has been extracted from pion excitation functions, composite fragment yields and in-plane transverse momentum analysis, the latter establishing the phenomenon of nuclear collective flow. All of these observables are related to single particle inclusive differential cross sections and have been measured using the streamer chamber and the plastic ball. Both detectors have disadvantages. The streamer chamber has almost 4π acceptance but is a low statistics device. Multiparticle measurements entail scanning and digitizing film in three stereoscopic views and performing offline matching and reconstruction - a very time consuming process. The plastic ball, while highly segmented, only provides limited resolution and momentum space acceptance and thus, confines particle-ratios (d/p, t/p, etc.) measurements (entropy) to rather small overlapping regions of phase space. Because of the inadequate scope of present detectors, there is considerable experimental work pending, not the least of which is the systematic survey of the triple differential cross sections, urgently needed to test new theories.

At RICH energies, however, the focus of attention is directed towards studying the properties of the deconfined state of nuclear matter - the quark gluon plasma. Theoretical calculations predict charged particle multiplicities exceeding 4000 for the most violent Au+Au collisions. Rapidity fluctuations have been conjectured to occur as a result of hadronisation of plasma droplets. Such variations in topology on

an event by event basis requires a highly segmented 4π detector with 'JET' capability and capable of operating in a very high multiplicity environment. On the other hand, to carry out charged particle interferometry requires excellent two track separation and momentum resolution. The purpose of this paper is not to propose a specific design but to report on a few aspects of the TPC project at the Bevalac which are pertinent to the RHIC 4π detectors.

In 1986, we investigated the concept of a four-pi tracking detector with particle identification capability that would supersede existing streamer chamber at the Bevalac and meet the experimental challenges of handling and recording high multiplicity relativistic heavy ion collisions. A Time Projection Chamber (TPC) with novel features was considered to be the best practical solution. The project, named EOS, is described in detail in a preliminary design report [1].

The EOS Detector

A schematic view of the TPC is shown in Figure 1. It consists of a large volume of gas where electrons, produced by ionization along the the particle tracks, drift towards the end cap under the action of parallel electric and magnetic fields. The end cap, constructed in several sectors is covered with thin-gap multiwire proportional chambers. Track localization is achieved by recording with suitable electronics, as a function of time, the charge detected on the anode wires. For each segment of track the drift time (with respect to a common start) provides one coordinate, while the induced signals on the pad rows provide the coordinates in the plane of the MWPC. Since the TPC provides many position measurements along each track and also many samples of dE/dx, it provides excellent momentum resolution and particle identification.

The layout of the EOS detector is shown in Figure 2. A superconducting solenoid (3.6m long and 2.2m diameter) provides a homogeneous longitudinal magnetic field of 1.5T, in which a TPC of diameter 1.8m and length 2.0m is located. A uniform electric field gradient of 115V/cm is generated by the internal field cage, and a circular HV wire plane. The sensitive fiducial volume is filled with 91% Ar - 9% CH4 mixture maintained at 1 atm. A laser

calibration system is installed in the TPC to monitor variations in drift velocity as well as any global and local track distortions. The target is located in an evacuated carbon-beryllium beam pipe of diameter 20cm, which passes through the center of the TPC. This beam pipe serves to protect the TPC against the very heavy ionization which would occur if the beam passed through the TPC. It is made large enough to accommodate supplementary detectors at a later stage of the project. The TPC is complemented by a time-of-flight scintillator array which consists of two parts: the "barrel" scintillators which line the inside of the magnet and the "downstream scintillators which cover the exit face of the magnet. The EOS time projection chamber, in contrast to similar devices built for colliding beam experiments, is single ended. This enables us to minimize nuclear and electromagnetic interactions by placing the electronics upstream from the target, where there are few particles. The endcap has a sectored layout as in PEP4 [2] and DELPHI [3] but unlike, conventional TPCs, the end plane is entirely covered by cathode pads followed by three wire planes. The first plane of sense and field wires is placed in front of the cathode pads and create the avalanches. The second plane of wire serves to isolate the drift and the amplification volume while the third plane, called the gating grid, suppresses positive ion feedback. The pad layout has been optimized to accommodate Au + Au collisions at 1 GeV/A by giving special attention to two track resolution and multihit probability on the pads. The most economical approach without compromising the multihit and dE/dx performance led us to propose a pad layout in which the size of the pads varies from the inner to the outer radius of the TPC. The physical dimensions of the pads varies linearly from 0.5 x 0.5 cm^2 (at r = 10 cm) to 1.5 x 1.5 cm^2 (at r = 90 cm). This design requires 25,000 pads and about 1000 sense wires. Two possible methods of constructing a non-uniform pad and wire arrangement have been considered and are shown in Figure 3. The top figure depicts the variable gap and anode wire approach in which the wire gain M remains constant for equal wire radii and operating voltage provided the ratio s/g is kept constant. The bottom figure illustrates the resistive cathode readout scheme. This a simple way of adjusting the pad width and distance without modifying the basic wire plane construction. The principle is based on the observation that, if the cathode is made from a thin sheet of material having a large resistivity, the fast signal induced

on external pickup pads has roughly the same amplitude and distribution on identical pads internal to the chamber. This method of readout allows a flexible choice of the geometrical shape of the pads and to simplify construction.

The momentum resolution is expected to be dP/P = 0.7-0.9% for low momentum tracks and dP/P = 0.24 - 0.40%P for stiff tracks. These predictions are based on Monte Carlo simulations and extrapolation of PEP-4 results taking into consideration the realities of fitting tracks [4]. Energy loss, dE/dx, resolution depends on the number of samples, the ionization potential of the gas and pressure. Using the EOS parameters, the fwhm resolution is between 10.2 - 12.8 % assuming 80 samples obtained from measurements on the pads. The intrinsic spatial resolution of the EOS TPC is determined by the diffusion of the ionization electrons after they have drifted on to the end cap. The sigma for the transverse position coordinate (x-y pad plane) is expected to be 0.24 mm whereas the longitudinal accuracy is 1.75 mm.

Prototype Test TPC

A small TPC borrowed from the PEP4 collaboration is being modified tc test the practicality of the new ideas presented in the EOS design. The immediate goal is to demonstrate tracking and particle identification using only the pad information. Initially, a simple pad layout scheme will be used and afterward the more intricate variable pad designs mentioned earlier will be tested. Eventually, we plan to fabricate and test a complete EOS type sector.

The prototype TPC is essentially a development of the original LABTPC [5] used by the PEP-4 group to study electrostatic field cage distortions. Structural modifications were made to accommodate the readout of the additional cathode pads. The TPC is shown schematically in Figure 4. It has a rectangular geometry (approximately 40 x 40 x 40 cm) with a drift length of 30cm. The field shaping structures consist of a coarse field cage (CFC), a fine field cage (FFC) and a high voltage screen (HV). The CFC shields the FFC from the outer grounded wall. It consists of a series of 2.5mm wide copper lines spaced 5mm apart on a flat G10 (insulator) surface and 20mm pitch lines on the reverse side. The FFC has the same pattern but the dense pitch surface points into the TPC fiducial volume as

shown in Figure 5. A slightly conductive polyurethane coating has been applied to the FFC board to suppress electrostatic distortions.

A pulsed electron point source is located on moveable trolley mechanism above the HV plane. The electron source is made with a needle discharge from a platinum needle contained inside an Argon/Isopropyl flushed cavity. The source injects clusters of electrons through the HV screen and can be moved over the entire top surface of the drift region.

There are two wire planes located 30 cm below the HV screen. The first plane consists of 75 um wires spaced 1mm apart held at ground potential. This grid separates the drift and amplification region. Below the grid plane are located the 75 um field and 20 um sense wires with 2mm pitch. The cathode pads are situated beneath the field/sense wire plane. An array of 16 by 16, 0.5cm square, gold plated copper pads are fabricated on a 1mm thick flexible kapton sheet. There are 256 pads occupying a total area of 64 cm**2. The number of usable pads were restricted in this design by the allowable trace density. The pad array, as shown in Figure 6, is positioned in the center and is bounded by a 3 cm guard ring. The signals from the pads are conducted through vias onto the underside of the kapton and traced out to connectors mounted on the preamplifier motherboard (Figure 6-lower). The kapton sheet is bonded to a flat sheet of G10 insulator for mechanical support and the whole structure can be removed without disturbing the wire frames. Noise considerations are vital to the performance of all TPCs and for this reason the kapton sheet thickness was chosen to minimize the input capacitance to the preamplifier.

The gas handling system shown in Figure 7 supplies the TPC and the electron source with premixed gases. In addition, impurities in the TPC argon/methane mixture are controlled down to 1.2 ppm.

Electronics:

The readout of the EOS detector poses challenging data acquisition problems which are not unlike those facing similar new RICH and SSC detectors. It is clear that much of the information needs to be processed and reduced in real time before being passed onto the event builders. The data acquisition scheme must incorporate hardware intelligence at the beginning of the information flow path. While these ideas are being addressed in EOS, they are not so important to the Test TPC. However, as a

parallel program, we intend to test new electronic ideas and circuits currently being developed at LBL, using the prototype TPC.

To begin with, the test TPC is equipped 256 channels of PEP4 electronics. Signals from the cathode pads are fed to individual charge sensitive preamplifiers. The entire analogue history of a given sample is stored in a CCD delay line. This device consists of 455 storage cells. Charge (pulse height) information is shifted along this array at 20 MHz and read back at 10 KHz.

Improvements in the noise performance of the preamplifiers and dynamic range will be required to match EOS specifications. We intend to investigate alternative preamplifiers using present day technology such as those being manufactured for use in TPC detectors under construction at CERN and Tristan. Both ALEPH and TOPAZ preamplifiers have better noise performance than the PEP4.

There are a number of commercially available preamplifiers providing excellent noise immunity and low power consumption. Hybrid preamplifiers, with noise figures as low as 150 electrons (Cd < 5pf, risetime tr of the order of 10ns) are available. Also ultra low noise preamplifiers have been reported in research literature. Future plans may allow, capitalizing on existing R&D, the development of a new custom designed preamplifier.

The CCDs may be replaced by fast, high density storage devices. A new 16 channel fast analog switched capacitor array (FSCA) has been fabricated using CMOS VLSI technology [6]. The device consists of 128 storage capacitors per channel individually switched to either the input or buffered output pins as shown in Figure 8. The switches are controlled by internal shift registers for both the read and write cycles. Recurrent time sampling is accomplished by sequentially clocking the capacitor array switches. Under trial conditions, pulses have been recorded in the device at 50 MHz (20 ns) and read out at 3 MHz. In reality most of the 128 time samples will contain zeros, i.e., no hits. Real time zero suppression can be accomplished in a more complex design in which the capacitors are grouped or segmented. Each group stores contiguous time samples whenever the input signal exceeds a preset threshold. A digital memory stores the necessary information for time reconstruction [7].

Further development could permit multiplexed readout into a single ADC on the same chip. At present 10 MHz, 10 bit, multistep/pipelined ADCs can

be manufactured using CMOS. However, considerable progress has been made over the last two years in combining bipolar and CMOS technology. As a result, greater functionality can be incorporated onto a single chip such as complete front end data acquisition systems. VLSI chips containing the preamplifier, shaper, multiplexer and ADC have become available, albeit not yet meeting the demanding specifications of EOS. Some of the preceding ideas were inspired by the waveform sampling design of the SLD electronics and the microplex chip where the advantages of having VLSI has been fully exploited. A high degree of multiplexing immediately on the pad plane results in the reduction of cumbersome cabling and allows digital signal processing electronics to be managed in two or three racks.

Summary

A new four-pi detector for studying heavy ion collisions at the Bevalac was proposed and a prototype TPC is being assembled to study some of its unusual aspects. In the short term we hope to demonstrate tracking capability using pad information only. Elements of a new data acquisition system will also be tested.

References

[1] EOS: A Time Projection Chamber for the Study of Nucleus-Nucleus Collisions at the Bevalac
H. Pugh, G. Odyniec, G. Rai, and P. Seidl
LBL-22314 (1986).

[2] PEP4: Proposal for a PEP Facility Based on the Time Projection Chamber
A. R. Clark et al., (1976).

[3] DELPHI Collaboration
P. Delpierre
Nucl. Instr. Meth. 225 (1984) 566.

[4] Proceeding Bevalac-TPC Workshop LBL, April 1987 (unpublished)
G. Lynch

[5] Time Projection Chamber Workshop, TRIUMPF, Vancouver, B.C., Canada
M. Iwasaki, et al.
AIP Conference Proceedings 108 (1983).

[6] Development of a Switched Capacitor Based Multi-Channel Transient Waveform Recording Integrated Circuit
Stuart A. Kleinfelder
Presented at the IEEE Nuclear Science Symposium, San Francisco, October 1987.

[7] Stuart A. Kleinfelder, LBL, Private Communication.

Figure Captions

Figure 1: Side view schematic of the EOS Time Projection Chamber

Figure 2: Schematic layout of the EOS detector.

Figure 3: Alternative ways to vary pad size and gap spacing as a function of radius.

Figure 4: Schematic drawing of the prototype TPC (PEP4-LABTPC).

Figure 5: Expanded view of the field cage structures.

Figure 6: Top: Construction of the TPC pad array
Bottom: Printed circuit trace out on the underside of the kapton sheet.

Figure 7: TPC gas handling system.

Figure 8: Circuit diagram of the switched capacitor chip. Two channels of 32 sample and hold cells per channel shown. The I.C. contains 16 channels of 128 cells per channel.

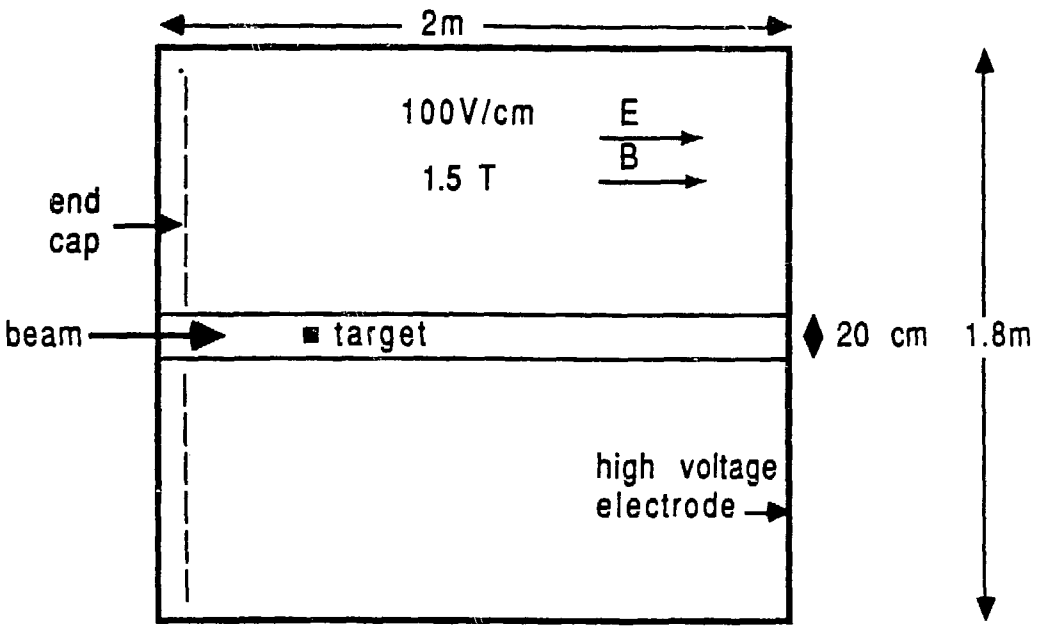
SCHEMATIC VIEW OF EOS TPC
2m
100V/cm
E
B
1.5 T
end
cap
beam
target
20 cm
1.8m
high voltage
electrode

Figure 1

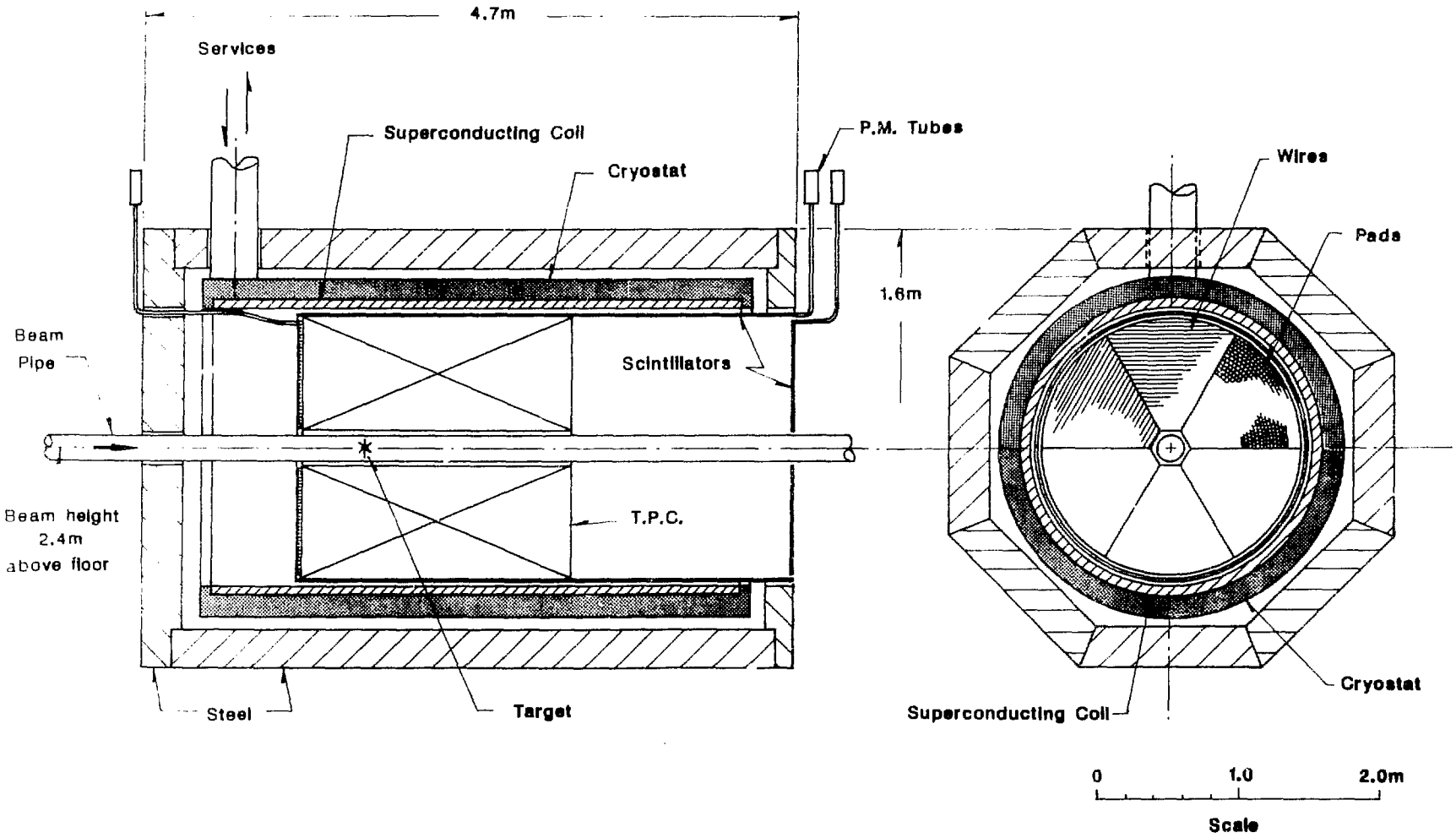
4.7m
Services
Superconducting Coil
Cryostat
P.M. Tubes
Wires
Pads
1.6m
Beam
Pipe
Scintillators
Beam height
2.4m
above floor
T.P.C.
Steel
Target
Superconducting Coil
Cryostat
0
1.0
2.0m
Scale

Figure 2

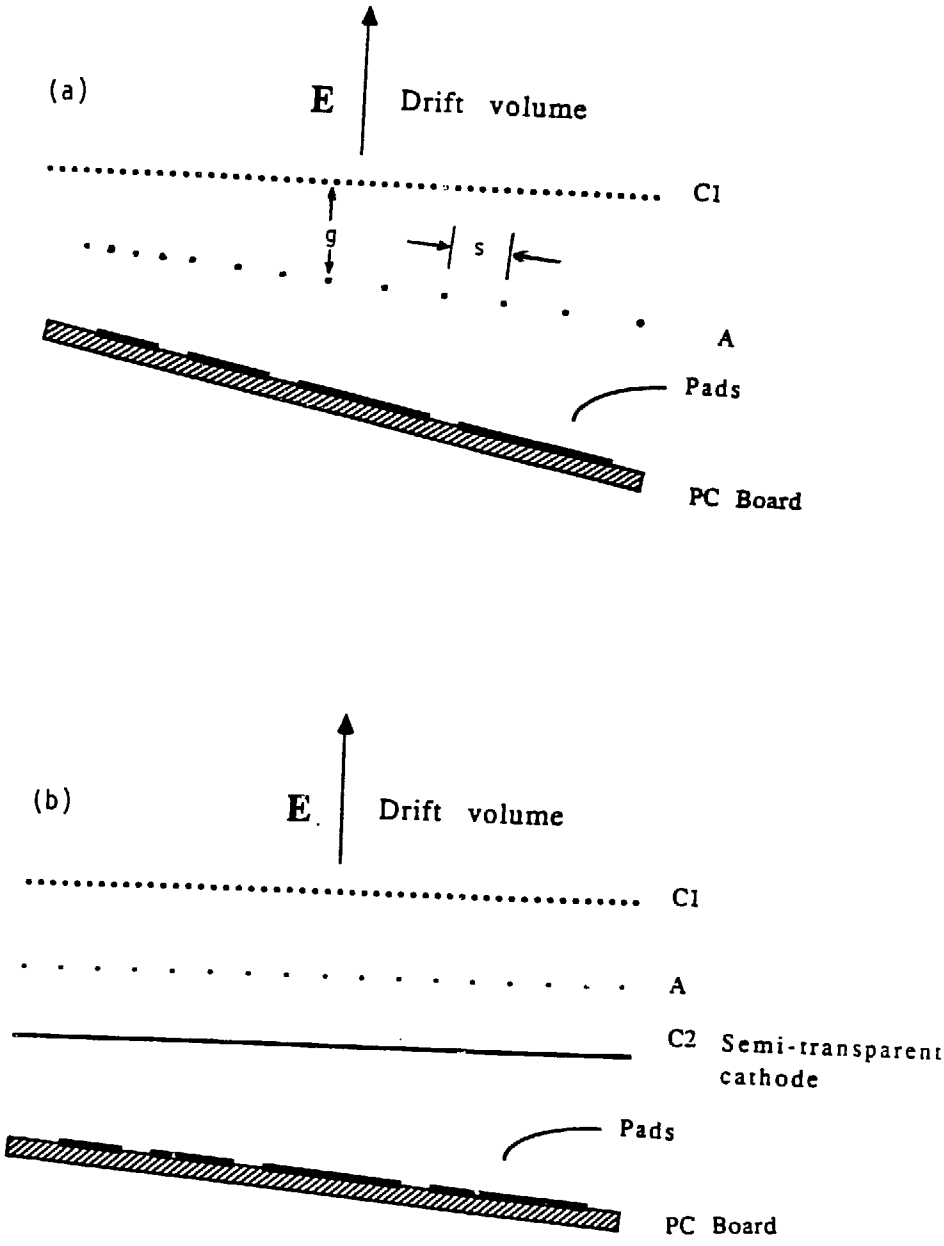
(a)
E
Drift volume
C1
g
s
A
Pads
PC Board
(b)
E
Drift volume
C1
A
C2
Semi-transparent cathode
Pads
PC Board

Figure 3

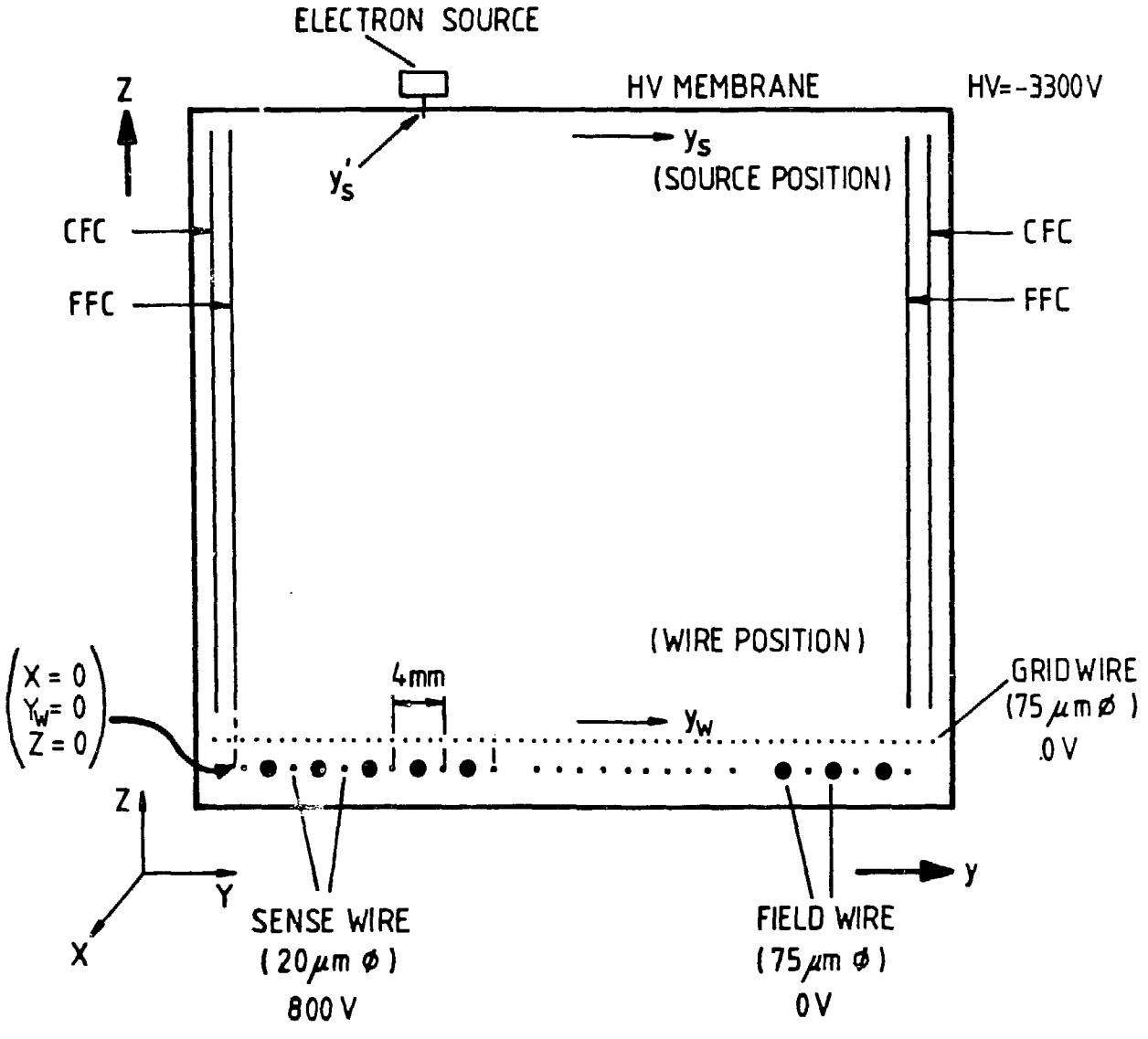
ELECTRON SOURCE
HV MEMBRANE
HV=-3300V
Z
y_s
(SOURCE POSITION)
y_s'
CFC
FFC
CFC
FFC
(WIRE POSITION)
X = 0
Y_w = 0
Z = 0
4mm
y_w
GRIDWIRE
(75 µm ø)
0 V
Z
Y
X
y
SENSE WIRE
(20 µm ø)
800 V
FIELD WIRE
(75 µm ø)
0 V

Figure 4

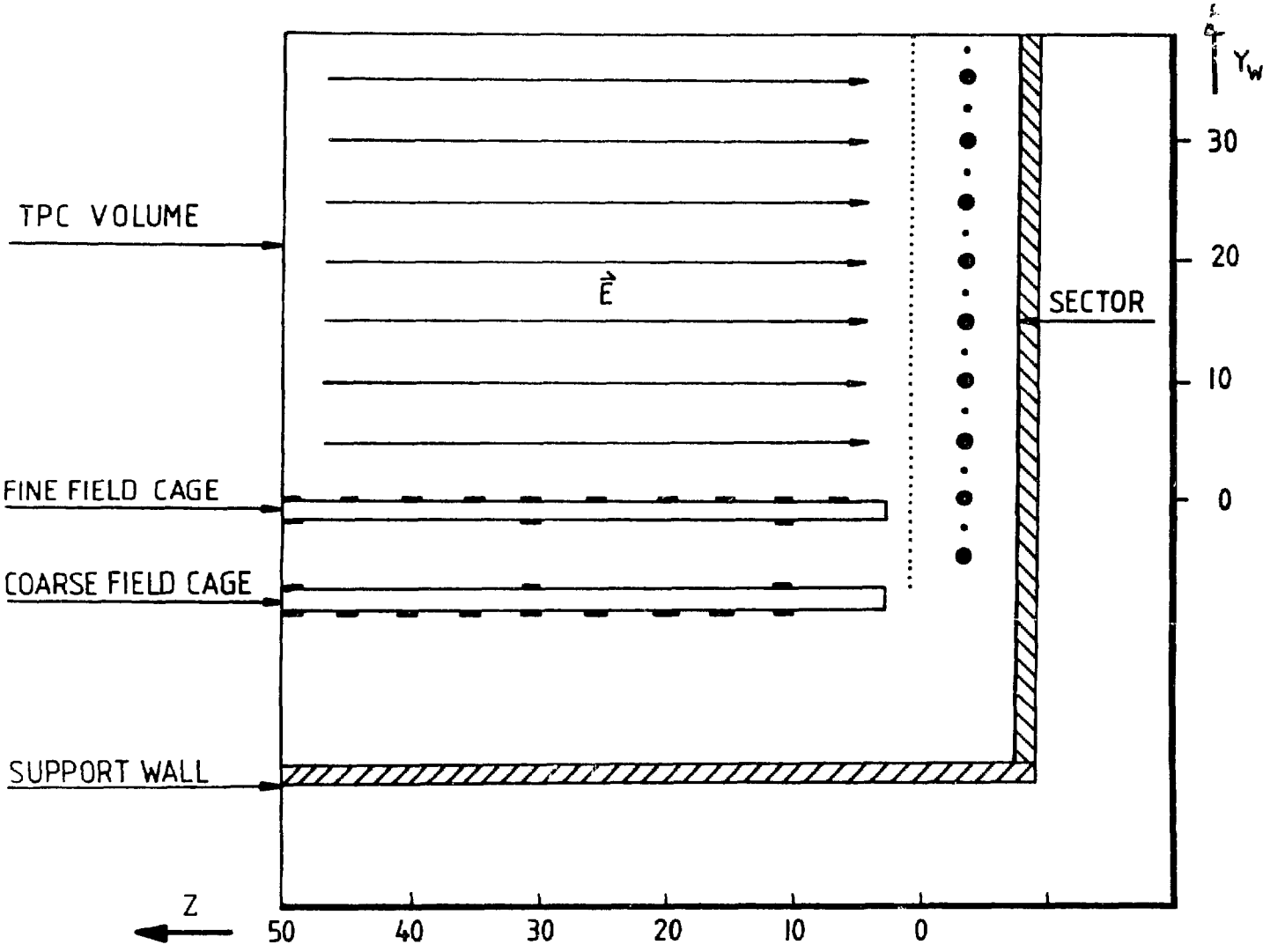
TPC VOLUME
$\vec{E}$
SECTOR
FINE FIELD CAGE
COARSE FIELD CAGE
SUPPORT WALL
Z
50
40
30
20
10
0
Y_W
30
20
10
0

Figure 5

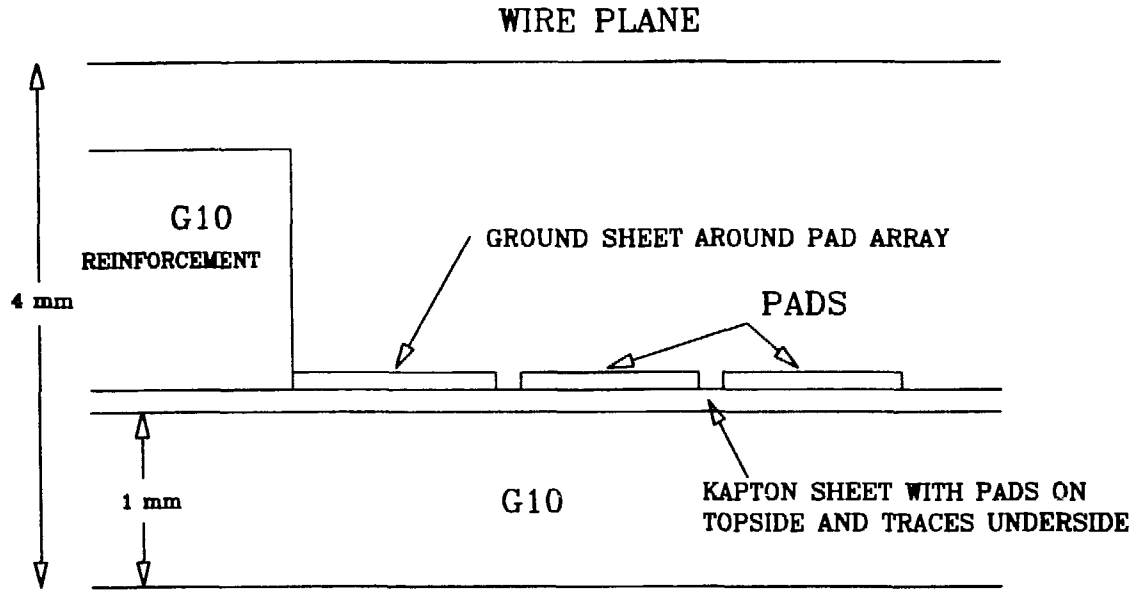
WIRE PLANE
G10
REINFORCEMENT
4 mm
GROUND SHEET AROUND PAD ARRAY
PADS
1 mm
G10
KAPTON SHEET WITH PADS ON
TOPSIDE AND TRACES UNDERSIDE
BASE

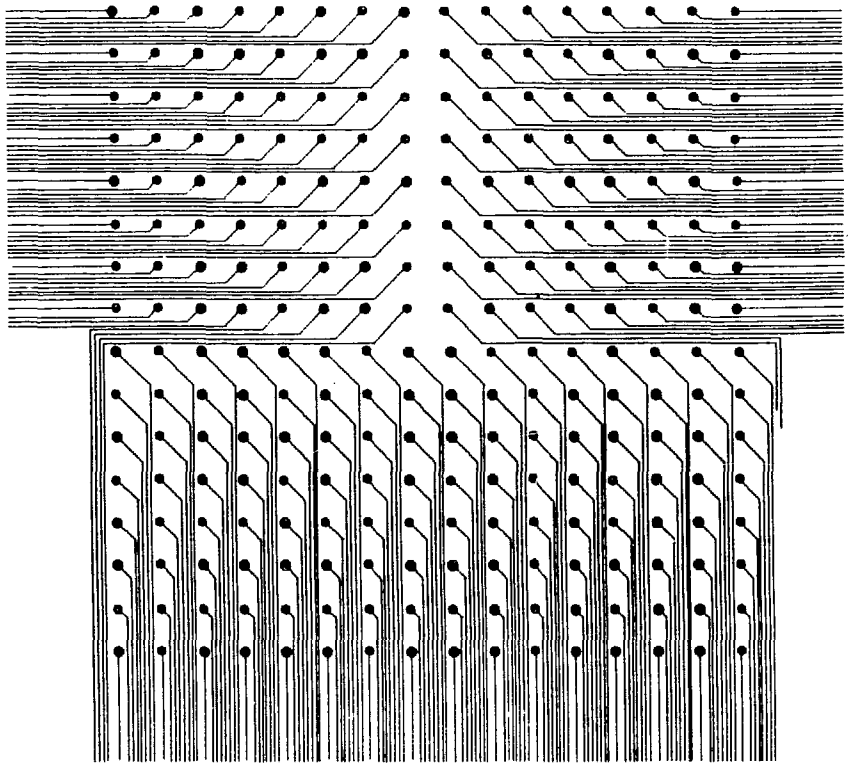

Figure 6

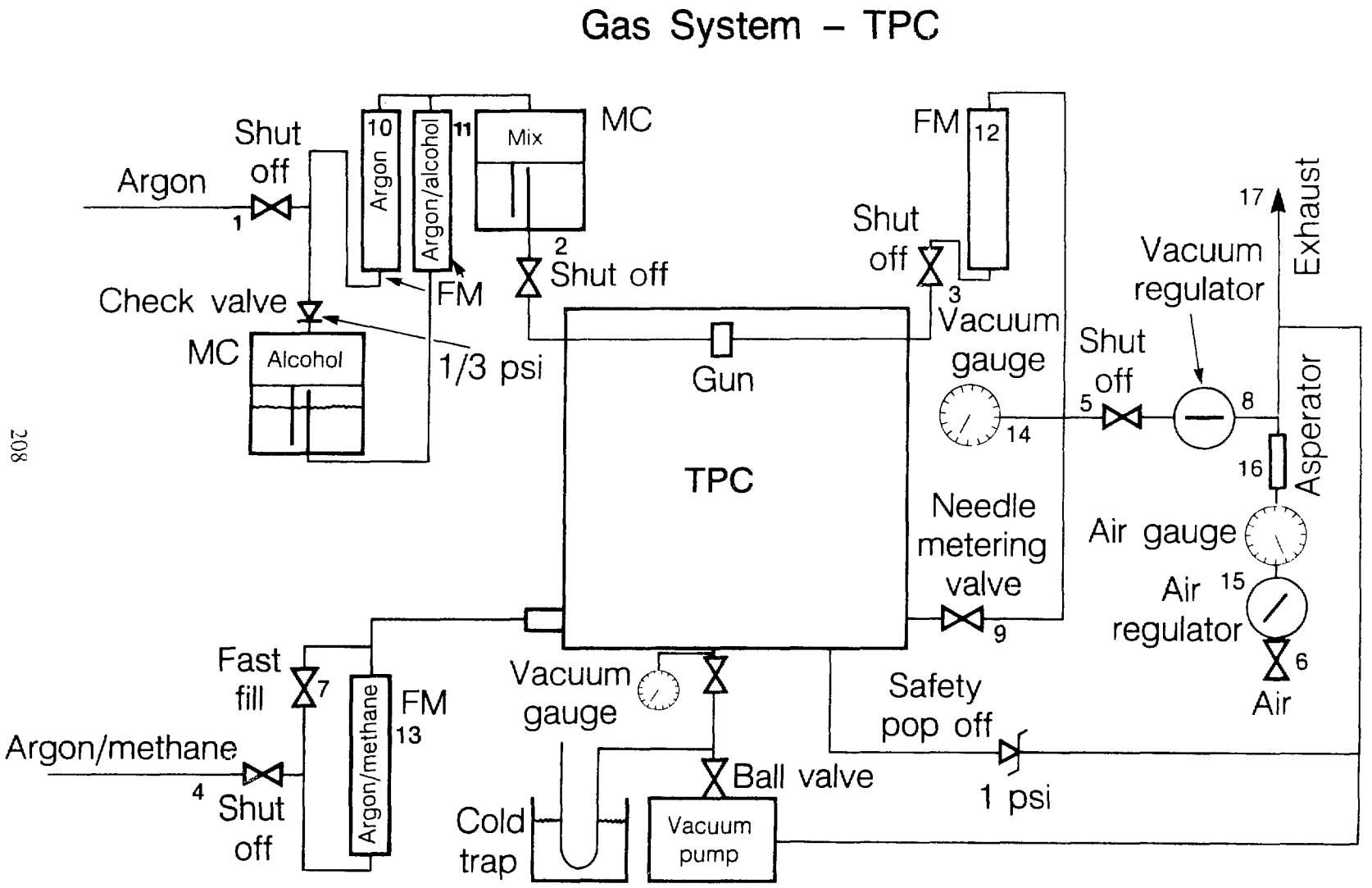
Gas System – TPC
Argon
Shut off
1
Check valve
MC
Alcohol
10
Argon
11
Argon/alcohol
Mix
MC
2
Shut off
FM
1/3 psi
Gun
TPC
FM
12
Shut off
3
Vacuum gauge
14
Shut off
5
Vacuum regulator
8
17
Exhaust
Asperator
16
Air gauge
Air regulator
15
6
Air
Needle metering valve
9
Fast fill
7
Argon/methane
4
Shut off
Argon/methane
13
FM
Vacuum gauge
Ball valve
Cold trap
Vacuum pump
Safety pop off
1 psi

Figure 7

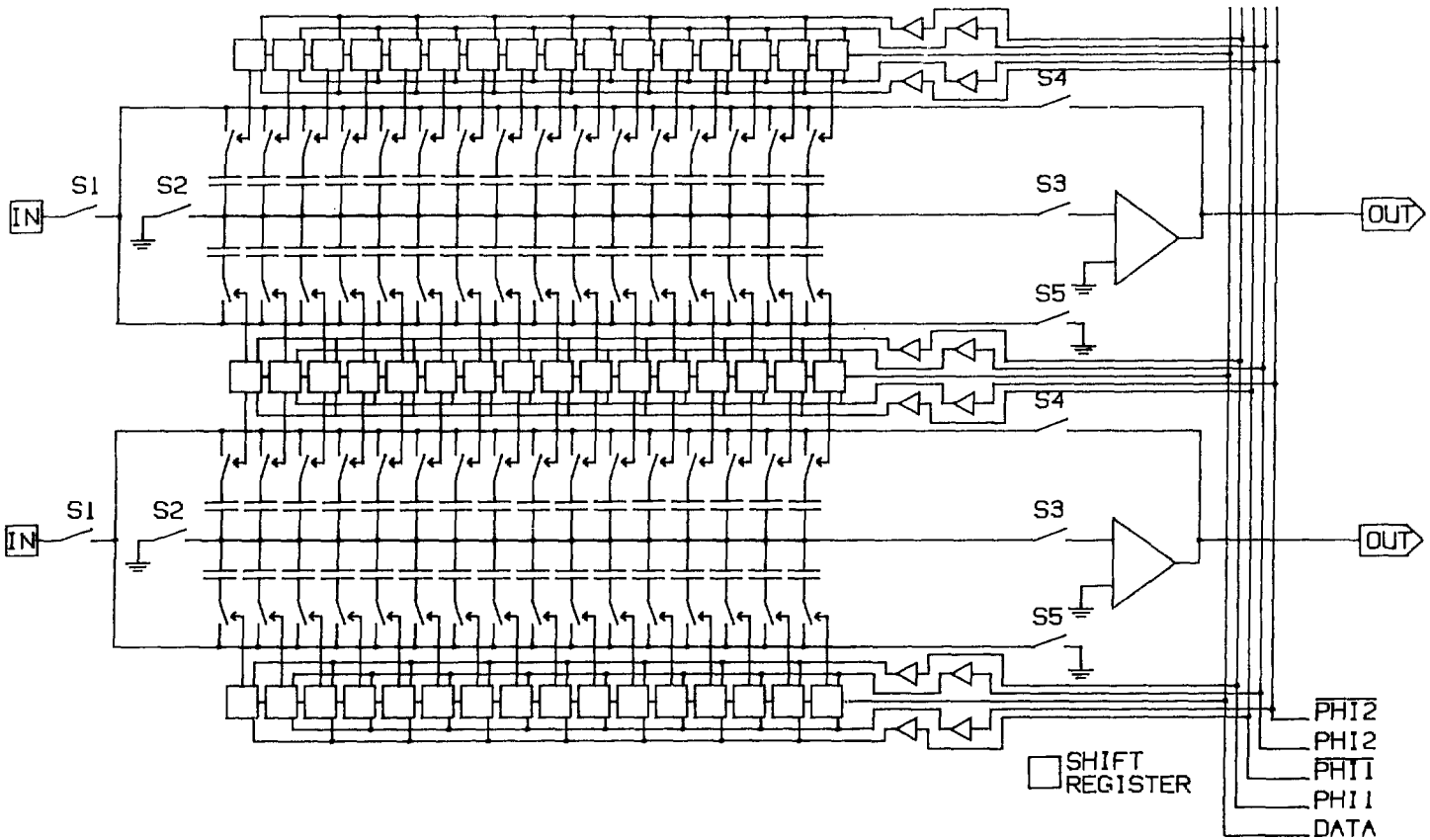
S1
S2
S3
S4
S5
IN
OUT
S1
S2
S3
S4
S5
IN
OUT
SHIFT REGISTER
PHI2
PHI2
PHI1
PHI1
DATA

Figure 8

THE NA36 TIME PROJECTION CHAMBER: AN INTERIM REPORT ON A TPC DESIGNED FOR A RELATIVISTIC HEAVY ION EXPERIMENT

G.E. Diebold*
Carnegie-Mellon University, Pittsburgh, PA 15213

NA36 Collaboration

P.D. Barnes, R. Blaes, H. Braun, B. Castano, M. Cherney, M. Cohler, G.E. Diebold, C. Fernandez, G. Franklin, C. Garabatos, J. Garzon, W.M. Geist, D.E. Greiner, C.R. Gruhn, M. Hafidouni, M. Heiden, J. Hrubec, D. Huss, J.P.M. Kuipers, P. Ladron de Guevara, A. Michalon, M.E. Michalon, Z. Natkaniec, J.M. Nelson, G. Neuhofer, E. Platner, P. Porth, B. Powell, B. Quinn, J.L. Riester, H. Rohringer, M. Rozanska, I. Sakrejda, P. Salz, J. Traxler, J. Turnau, Ch. Voltolini, Y. Xia, A. Yanez, P. Yepes, R. Zybert

Bergen, Berkeley (LBL), Birmingham, BNL, Carnegie-Mellon University, CERN, Chandigarh, Cracow, Madrid (JEN), Santiago, Strasbourg (CRNS), Vienna, York

I. INTRODUCTION

Since its conception[1] in the early 1970s, the TPC has found application in several areas of particle physics ranging from e^+e^- collider experiments[2-4] to rare decay studies of lepton nonconservation[5,6]. A new and promising area of application for the TPC is the study of relativistic heavy ion collisions (RHIC). Presented here is an interim report on the first TPC for this field of physics, the NA36 TPC, being developed by Berkeley (LBL) for RHIC at the CERN SPS. Emphasis is placed on the operational and design considerations implemented to optimize the performance of the NA36 TPC in the study of central rapidity strange baryons produced in RHIC.

The NA36 TPC volume is rectangular with an endcap area 0.5 m x 1.0 m and a maximum drift distance of 0.5 m. The drift volume is filled with Ar-CH_4 (9%) at one atmosphere. A total of 6400 channels of time digitizing electronics instrument 66% of the endcap in a wedge shaped area matched to fixed target kinematics.

II. RHIC PHYSICS

The most overwhelming characteristic of RHIC is the high particle multiplicity produced,

---

*Present address: CERN, EP Division

especially in central collisions. From this environment, event parameters such as transverse energy flow and particle rapidity distributions must be extracted in a way to allow for complementary correlations with proposed signals of quark-gluon plasma (QGP) such as the production of strange quarks, dilepton pairs and single photons. Without these correlations it will be difficult to make an interpretation of observed anomalies with any certainty. On this basis, one can see the need for detectors with information densities consistent with the particle multiplicities expected and which preserve correlations between event parameters.

III. GENERAL TPC CHARACTERISTICS - IMPLICATIONS FOR RHIC

In very general terms, a TPC consists of a large drift space filled with an appropriate gas mixture, together with an electric field, **E**, a magnetic field, **B**, and a fine grained two-dimensional spatial readout system. The two-dimensional readout system records the drift time of electrons produced in the gas by the passage of ionizing radiation through the drift volume. From the two spatially measured coordinates and the third time-inferred coordinate, three-dimensional space points lying on the path of the ionizing particle are determined with a spatial resolution approaching that of conventional chambers but without the usual associated ambiguities. Additionally, if pulse height information is retained from the charge measurements, good particle identification by dE/dx can be achieved by suitably averaging over many pulse heights for a given track.

From this general description of a TPC, certain advantages and disadvantages of its use in RHIC experiments become apparent.

ADVANTAGES:

1. High information density => high multiplicty capability.
2. Particle identification as well as tracking within the same volume.
3. Unambiguous three-dimensional space points greatly simplify the task of track identification. This makes the possibility of event reconstruction a reality even for the high track multiplicity of RHIC events.
4. Good imaging capability enables extraction of topological features of interest, such as particle decays, from a given event without complete event analysis.
5. The electronic nature of information from the TPC enables one to perform a high statistics topological analysis of (rare) physical processes.

DISADVANTAGES:

1. Long dead time (~10 μs) due to the large drift distances involved.
2. Space charge effects are aggravated by high multiplicities, high Z fragments and δ-rays. These effects will cause distortions in the TPC tracking and dE/dx measurements and may lead to other problems such as sparking and loss of gain.
3. Longitudinal diffusion of the drifting electrons can be quite large (~1cm). This limits the two track resolution which is important for complete event reconstruction.
4. For the very high multiplicity of RHIC, the probability of having two avalanches near each other within the same time bucket can be large. This will result in errors in the measured positions to the extent that a given measurement is influenced by nearby avalanches. For a "conventional" pad TPC this is on the order of 1cm. Two track separation is also limited by this effect.

IV. THE NA36 TPC

The experimental arrangement of NA36 is shown in figure 1. The goal of NA36 is to measure central rapidity strange baryon production in RHIC and correlate this to global event parameters such as transverse energy flow (E_t), dE_t/dy, and forward energy flow due to projectile fragments. The strange baryons produced will be identified solely by their decay topology as measured by the TPC in conjunction with large downstream tracking chambers. Strangeness production in RHIC is expected to be a sensitive signature of QGP (c.f. P. Koch et al., Phys. Rep. 142 (1986) 167).

The NA36 TPC was designed with regard to the aforementioned disadvantages of TPCs for use in a RHIC environment. An attempt has been made to minimize the limitations imposed by nearby avalanches and space charge effects. The problems associated with dead time and diffusion should not compromise the goals of NA36.

In order that position measurements are not affected by nearby avalanches, the NA36 TPC utilizes a two-dimensional readout array of 12mm x 20μ sense wires with a 2.54 mm pitch, as illustrated in figure 2. This is in contrast with the readout array of most other TPCs using long sense wires over (segmented) cathode pads. In this latter case, the second spatial coordinate is obtained from the centroid of induced pulses on the pads nearest the avalanche and will be perturbed if other avalanches occur nearby. For the NA36 TPC, the two spatial coordinates are determined entirely by the position of the sense wire on which the avalanche occurs, much in the

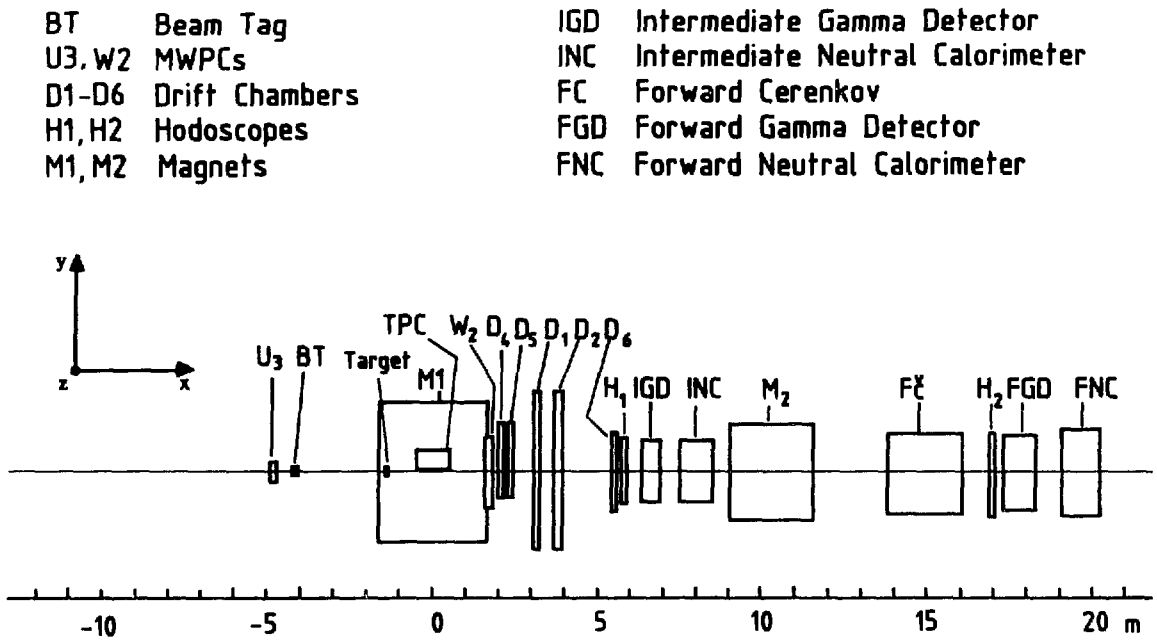

Figure 1. Plan view of Experiment NA36.

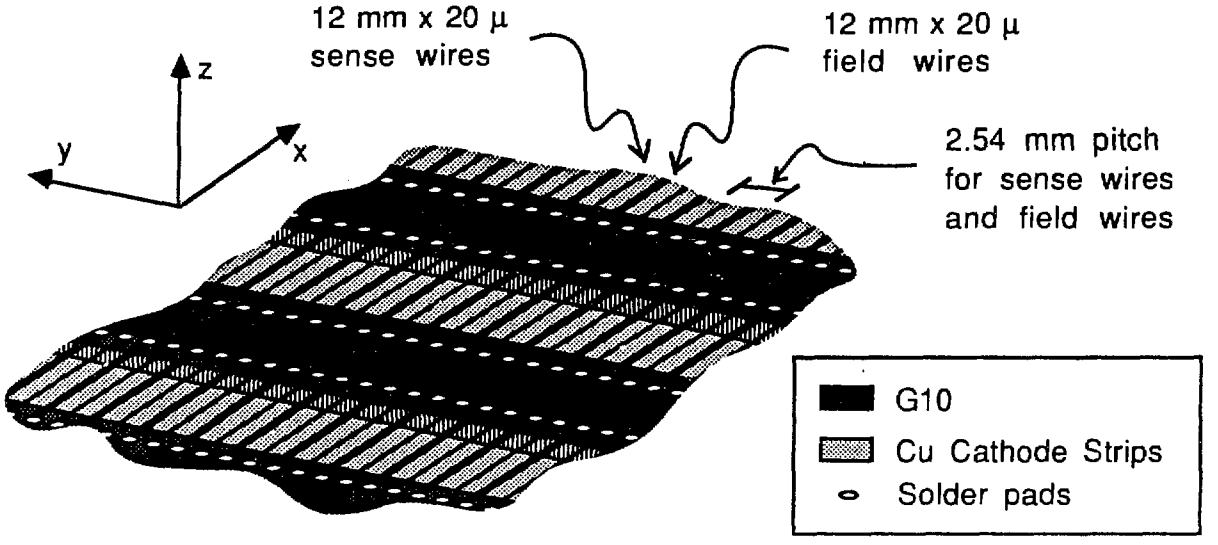

Figure 2. Close up view of the NA36 TPC sense wire array.

way that one-dimensional coordinates are determined from a MWPC. With this type of readout system, two hit separation in one coordinate is improved at the expense of single hit resolution. In the case of the NA36 TPC, this corresponds to a two hit separation in the y-coordinate of 2.54 mm with single hit resolution limited to 2.54 mm as well. Both of these quantities are determined by the sense wire pitch. Independent of this, the z-coordinate single hit resolution and two hit separation of the NA36 TPC are dependent on drift length, through diffusion, as is the case for conventional TPCs. Resolution in the z-coordinate of 1 mm may be possible, independent of drift length, if a detailed study of the TPC pulse shape is made. The two hit separation in z, limited by diffusion and efficiency tradeoffs due to signal shaping, varies between 2 and 15 mm depending on the drift distance. This may be improved by a careful correlation of pulse length and drift distance.

As pulse height information is not needed to make a position measurement in the NA36 TPC, design criteria critical to gain uniformity as well as detailed calibration studies can be relaxed if one gives up particle identification by dE/dx. Although this information would be useful for the goals of NA36, particle identification by dE/dx has been sacrificed in favor of the simplifications noted above. This was in part a matter of practicality in view of limited time and resources available.

It is well known that space charge effects from positive ions in the drift volume pose potential problems to TPC performance. This is especially true for TPCs used to study RHIC. To minimze these effects the NA36 TPC is positioned, relative to the beam and target, in such a way as to limit the number of "uninteresting" tracks passing through the TPC without unduly compromising the detection efficiency for central rapidity strange baryons. The NA36 TPC only looks at about 25% of the charged particles produced in a given event, due to limited geometric acceptance and sweeping of the low momentum particles by the M1 magnet. The target to TPC distance varies with the beam momentum and is chosen to optimize strange baryon detection efficiency by reducing the number of low momentum particles (mostly pions) that enter the TPC. This helps limit the amount of space charge produced in the drift volume in addition to simplifying the pattern recognition of decay topologies by reducing unwanted background tracks. The amount of space charge produced in the drift volume is further limited by positioning the TPC 2.5 cm above the beam line, keeping beam particles and projectile fragments from entering the TPC. Still, δ-rays and high Z fragments from interactions beneath the TPC can enter the drift volume and produce a large number of positive ions. A vacuum pipe mounted directly beneath the TPC is envisioned to supress these interactions by reducing the amount of material under the TPC.

To further reduce space charge effects, low gain TPC operation is attractive in order to minimize the number of positive ions produced in the avalanche. For the NA36 TPC, a gain of about $3x10^4$ is achieved at the sense wires. This is produced asymmetrically between the copper cathode strips and the wire cathode plane (figure 3). As a result, appoximately 66% of the positive ions produced in the avalanche drift to the copper cathode rather than toward the drift volume. Additionally, the wire cathode plane together with a passive gate plane collect about 98% of the remaining ions produced in the avalanche. In this manner the space charge reaching the drift volume should be less than 10^6 ions/track-meter, keeping space charge effects to a tolerable level.

V. THE NA36 M1 MAGNET

The NA36 TPC is situated in the **B** field of the superconducting magnet M1 of the CERN European Hybrid Spectrometer facility. This field differs from all previous **B** fields used for TPCs on two points. First, the central field value of M1 is 2.7T, the highest for any TPC constructed to date. This leads to a higher $\omega\tau$ ($\omega\tau \sim 20$) than that of any other TPC, thereby reducing distortions in the path of the drifting electrons due to **E** field nonuniformities and space charge effects.

Secondly, for all previous TPCs, the **E** and **B** fields are exactly parallel and extremely uniform with integrated nonuniformities kept to one part in 10^4. This eliminates **ExB** deviations in the electron drift path. The **B** field of M1, on the other hand, is very nonuniform with variations over the active volume of the TPC of about 0.8T for B_x, 0.6T for B_y and 1.5T for B_z. Because of these nonuniformities, deviations of the electron drift path from the **E** field can be as large as several centimeters. In fact, because of the high $\omega\tau$, the electron drift path will closely follow the **B** field. Precise reconstruction of three-dimensional space points, therefore, requires an accurate **B** field map to make appropriate magnetic optics corrections.

VI. TPC ELECTRONIC READOUT AND MONITORING

The readout system of the NA36 TPC amounts to the time digitization of 6400 waveforms over a 10 μs period. Differential analog signals are produced from the TPC by current sensitve preamplifiers which are mounted directly on the TPC endcap. These signals are sent over 18 m of twisted pair ribbon cable to a shaping and comparator circuit. The comparator produces a time-over-threshold digital signal which is time digitized by LeCroy 1879 pipeline TDCs in Fastbus. Data will be buffered during the SPS spill in two LeCroy 1892 Fastbus 4 Mbyte buffer memories

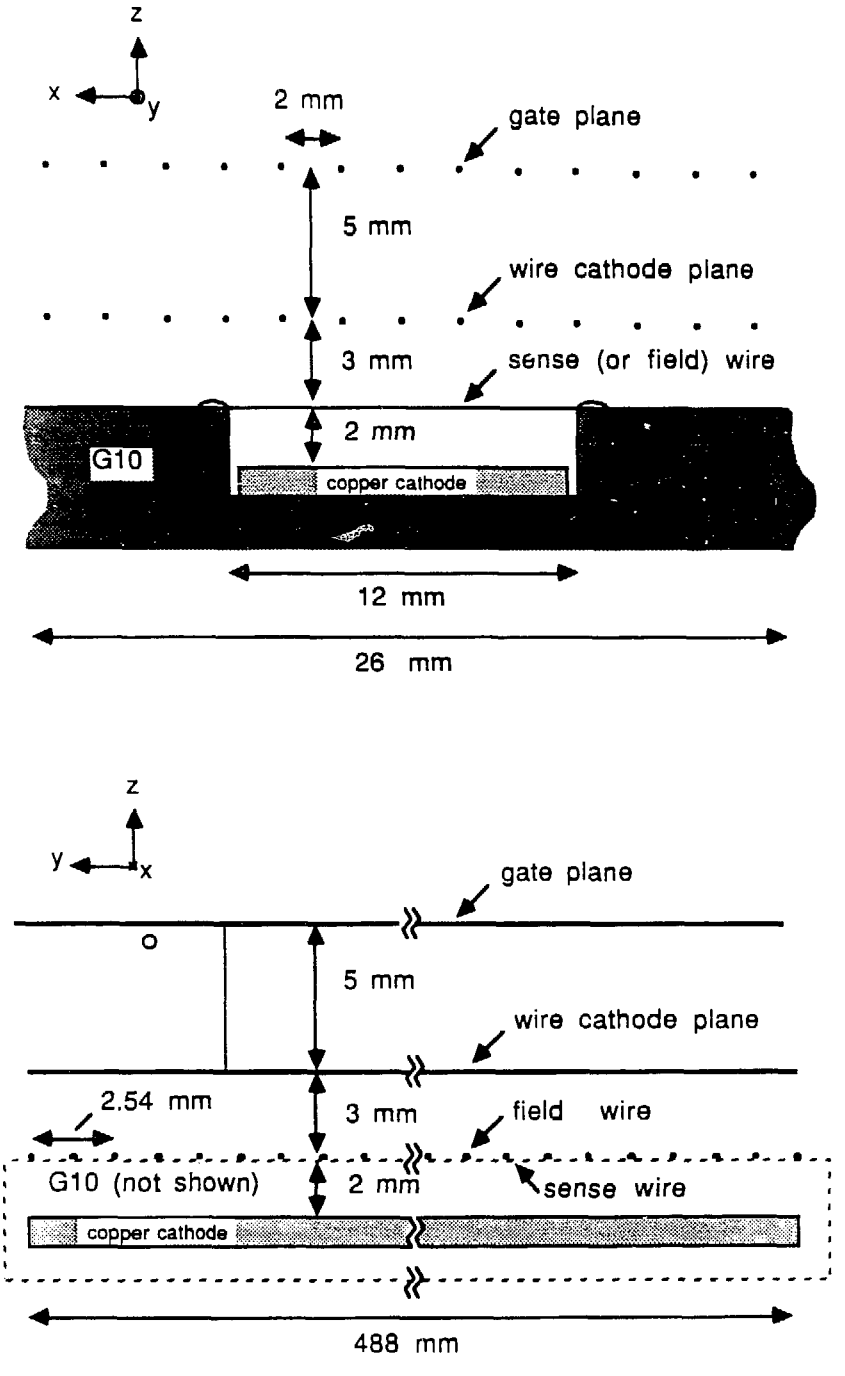

Figure 3. A schematic illustration featuring two orthogonbal views of the NA36 TPC cathode structure.

and then readout between spills. The expected event size for central collision events of 200 GeV/c/ A sulfur on gold is about 50 kbytes.

In addition to the readout electronics of the TPC, various monitoring devices are necessary for stable operation. The TPC operating potentials and leakage currents are monitored online through Fastbus ADCs. Temperature both internal and external to the TPC are monitored, as well as gas pressure and flow rate. Finally, as the readout electronics of the TPC retain no pulse height information, several channels of LeCroy 2261 and 2262 Image Channel Analyzers (ICA) are used as well as Fastbus ADCs to monitor uniformity of the chamber response under various operating conditions.

An example of 2261 ICA data is shown in figure 4. In figure 4a, five hits were detected with peak amplitudes ranging from 4 to 8 μA. In figure 4b, a plot of pulse heights verses event number is shown. When this data was taken, TPC operating potentials were being varied to investigate the chamber response, accordingly, marked changes in the pulse height distribution can be seen. The average signal for this set of data was 6.7 μA.

VII. PRESENT STATUS AND FUTURE TESTS

At this time, the NA36 TPC itself is entirely operational although a full complement of readout electronics will not be realized until June, 1987. In any event, cosmic ray tests are to begin in May starting with a limited number of readout channels. The experimental arrangement for these studies is shown in figure 5.

On the order of 100 cosmic rays/hr between 0.7 and 2.0 Gev/c are expected to pass through the spectrometer arrangement consisting of M1 together with the TPC, the "upstream" MWPCs and the large downstream tracking chambers. Tracks will be reconstructed from the external tracking chambers and compared with corrected TPC data. From these measurements, the calculated TPC magnetic optics corrections can be checked and an appropriate error matrix generated. Also, further studies of TPC gain and efficiency will be conducted for various operating conditions. In addition to the cosmic ray tests, similar studies are foreseen with muons in mid-June when the SPS is restarted.

By late August, NA36 will start taking its proton comparison data in final preparation for the first sulfur ion runs scheduled to begin in October.

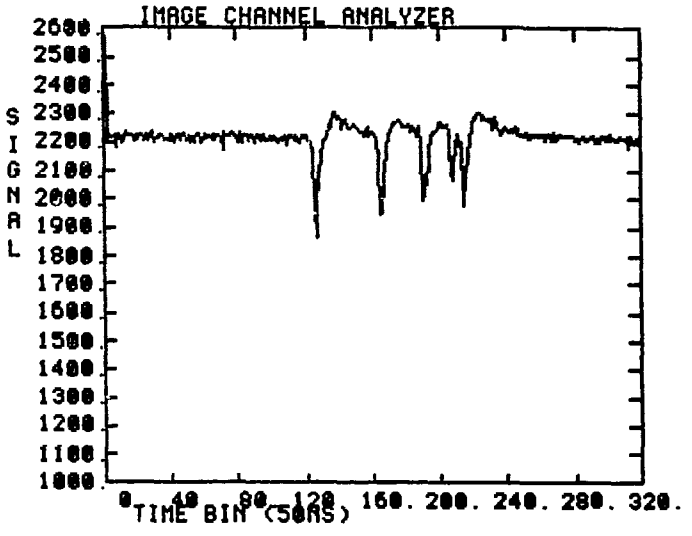

Figure 4 a. TPC waveform as recorded by the 2261 Image Channel Analayzer.

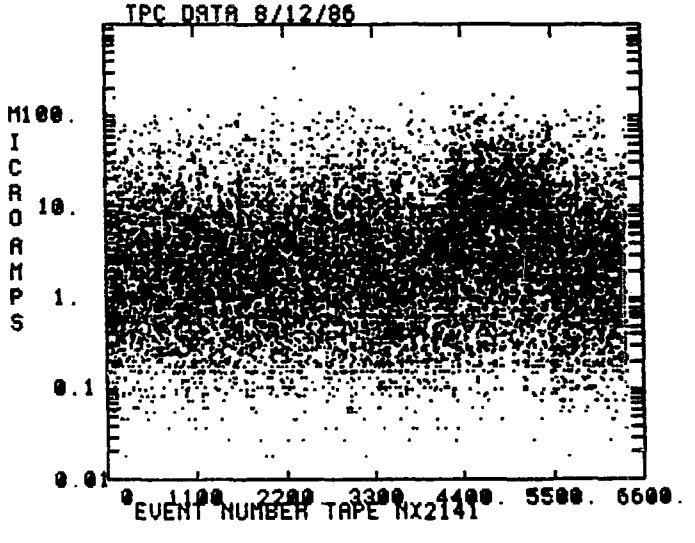

Figure 4b. TPC pulse height spectrum verses event number.

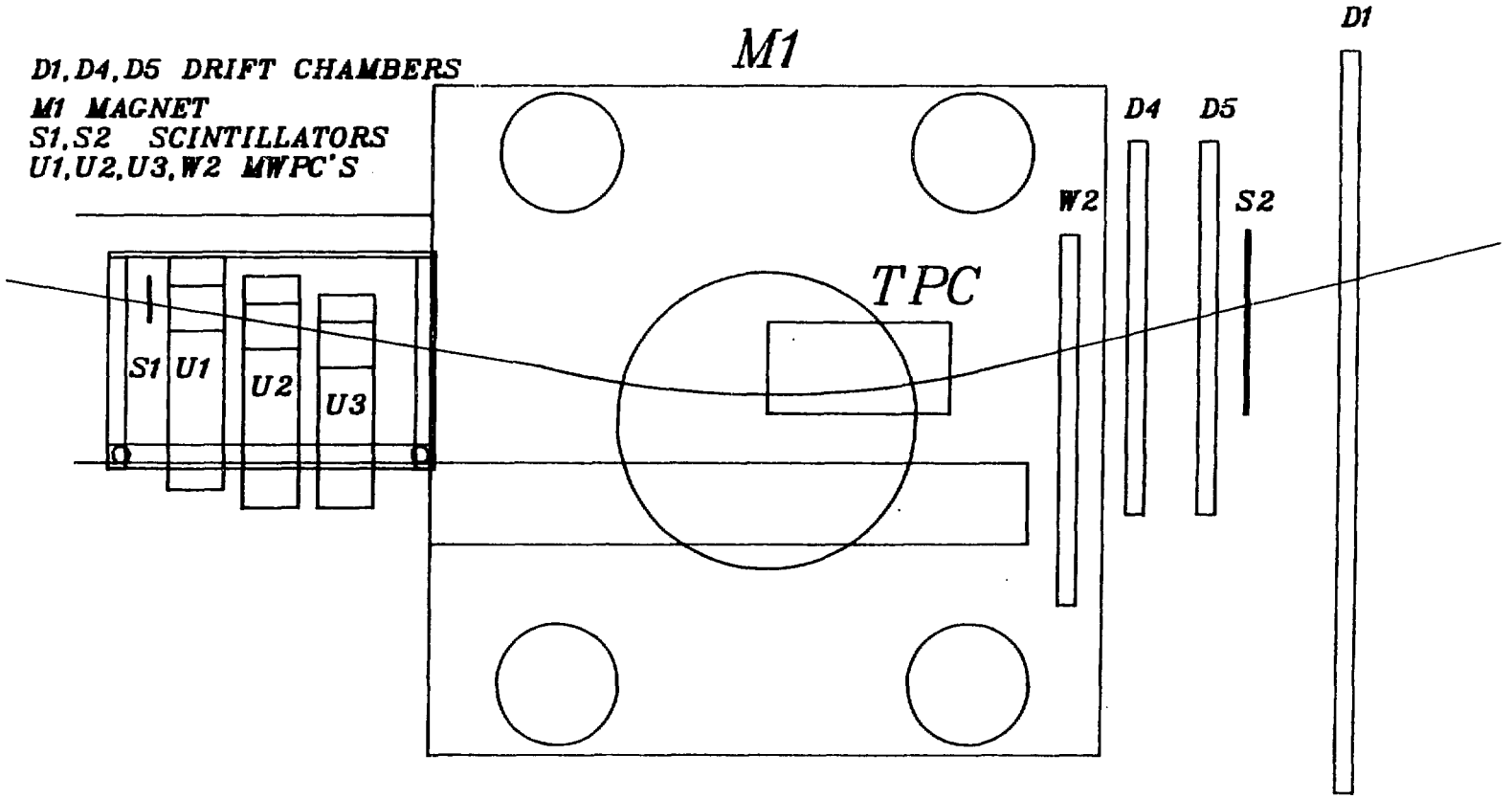

Figure 5. Experimental arrangement for cosmic ray tests.

VIII. CONCLUSIONS

The TPC, with its high track information density and good three-dimensional imaging capabilities, is a promising detector for the study of relativistic heavy ion collisions provided that measures are taken to minimize performance limitations due to very high multiplicities, space charge effects and diffusion. Design considerations and other efforts to reduce these drawbacks in the NA36 TPC have been presented, however there are certainly welcome improvements to be made. The benefits of particle identification by dE/dx, although not implemented in the NA36 TPC, should not be overlooked for other applications.

IX. ACKNOWLEDGEMENTS

The author would like to acknowledge the contributions of A. Klingler, W. Janczur (Cracow) and the technicians and machinists from Cracow for their efforts in the construction of the TPC, as well as J.C. Berset (CERN/EP) for his outstanding work on the TPC preamplifiers and many useful discussions concerning all aspects of the front end TPC electronics.

X. REFERENCES

1. D. R. Nygren, Proposal to Investigate the feasibility of a Novel Concept in Particle Detection, LBL internal report, February 1974.
2. Proposal for a PEP-4 Facility Based on the Time Projection Chamber, (1976).
3. ALEPH Collaboration, Letter of Intent, CERN/LEPC/82-3/I1, January 1982.
4. DELPHI Collaboration, Letter of Intent, CERN/LEPC/82-8/I6, January 1982.
5. M. Blecher et al., Search for Muon-Electron Conversion at TRIUMF, TRI-PP-81-32, July 1981
6. E. Bellotti et al., A proposal to investigate lepton conserving and non-conserving double beta decay with a xenon time projection chamber, CERN report 30/6/82.

Possible Future Performance Upgrades for RHIC

S.Y. Lee and A.G. Ruggiero*
Brookhaven National Laboratory
Associated Universities, Inc.
Upton, NY 11973

At this RHIC workshop several of the working groups have asked what is the maximum luminosity which can ultimately be expected from the machine. This is important from the point of view of the sensitivity of experiments to rare phenomena, as well as the particle-rate capability which must be designed into detector components. A related issue is the length of the interaction diamond: Most of the detector designs would like this length to be as small as possible. In order to assist in the design of large detectors, which should be able to take advantage of possible upgrades in the machine performance, the accelerator physics group has examined a plausible (although not guaranteed!) scenario for performance improvements after RHIC becomes operational.

The following six steps have been proposed as possible means for upgrading the performance of RHIC beyond the specifications of the Conceptual Design Report (CDR). While all of these steps are judged feasible, it is unlikely that they would be undertaken until after the machine has been operated successfully at its design specifications, and its detailed performance characteristics become well understood. The net result of these improvements would be, over the long term, about an order of magnitude increase in luminosity, and a reduction of the length of the interaction region to an average value during the beam lifetime of $\lesssim 20$ cm for head-on collisions. Further improvements might be achieved in special insertion regions (mini-beta), and also if it is possible to take full advantage of stochastic cooling (step 4 below).

A brute force method to increase the luminosity is to increase the beam bunch intensity. This method nevertheless has serious drawbacks. First there is the limitation of the heavy ion source which will be capable of delivering only a given amount of beam at some rate and quality. The injection into the Booster is an obvious bottleneck. Second, there is a limit on the intensity per bunch that cannot be exceeded without seriously altering the bunch dimensions or without causing beam losses due to a variety of instabilities. Finally the magnet, vacuum, rf and refrigeration systems have all to be capable from time zero to allow for the larger projected intensity, and this could eventually lead to a significant cost increase and to a more difficult mode of operation. Consider for example that a larger beam intensity translates in a larger overall energy that has to be absorbed by shielding, beam dump, rf cavities, etc.

Conversely, we thought it safer and more reliable to seek performance improvements also by preserving and reducing the beam dimensions. The six steps of improvement which we consider are as follows:

*Work performed under the auspices of the U.S. Department of Energy.

1. According to the CDR, each beam is made of 57 bunches. This provides a time interval between bunches of 200 nanoseconds, sufficiently larger than the rise-fall time of the injection kickers. It is possible to double the number of bunches to 114. This will provide an increase of the average current per each beam of a factor two and a corresponding increase of the luminosity by the same factor. It seems that the technology for a 100 nsec rise-fall time of the injector kickers is within reach. Nevertheless, one should research the engineering implications of the kicker design and provide a proof of existence. By doubling the number of bunches per beam, the Length of the Interaction Region (LIR), which is the length useful from the experiment point of view, remains unchanged, whatever is the crossing geometries.

2. If we take gold at 100 GeV/amu as reference, according to the CDR the number of particles per bunch N is 1.1×10^9. It is reasonably safe to consider the possibility to double also the number of particles per bunch, in this case, to 2.2×10^9. Again, the LIR will not change because of this upgrade, but the luminosity will increase by a factor of four, whatever is the crossing angle. We know that the beam bunch dimensions during collision are really determined by the intrabeam scattering effects, and the results of the study of this field are well documented in the CDR. More recent calculations of this effect have shown that, under the assumption of full coupling, the estimates of the beam dimensions actually correspond to a beam twice as intense, and moreover the dependence of the beam growth with the bunch intensity is far less than linear. Thus, doubling the intensity per bunch should not cause any significant increase of the bunch dimensions beyond those reported in the CDR. Moreover, the intrabeam scattering effects are believed to be less significant for the lighter ion species of the same electron current per bunch.

The combination of this step and the one above will provide an increase in the beam intensity of a factor of four. An increase beyond this is questionable, in our judgment. Large variation in bunch size can be expected from intrabeam scattering effects and from individual and bunch-to-bunch instabilities. The beam-beam tune-shift due to beam crossing will also increase accordingly. But, perhaps more important, there are several engineering considerations that are current dependent vacuum pipe heating from the beam, the beam loading on the rf cavity system, the total energy in the beam that has to be dumped in case of emergency and shielding.

The accelerator components of RHIC are being designed with the prospect of increasing the number of bunches to 114 and of doubling the intensity per bunch reported in the CDR. At the same time an effort will continue, in the Accelerator Physics research, to determine the beam stability and/or requirements at the ultimate intensity level thus proposed.

3. Because of the beam bunch dimensions increase due to intrabeam scattering effects, the average luminosity over a period of 10 hours is half the initial value. To recover a factor of two for the integrated luminosity, it has been proposed to apply stochastic cooling of the individual bunches during the same period of time collisions occur and experimental data are taken. During this step one requires only to preserve the initial bunch dimensions, thus stochastic cooling rates are to match the diffusion rates for intrabeam scattering. The required cooling times are therefore quite long, of

the order of the hour. For this step one can benefit of the experience of the SPS proton-antiproton collider in CERN, where stochastic cooling of proton beam bunches is planned under similar conditions.

To recover the factor of two for the integrated luminosity, it is sufficient to consider only stochastic cooling of the betatron oscillations in both planes. Momentum cooling can also be applied to preserve the initial momentum spread and, therefore, bunch length. Consequently, also the LIR will be preserved to the initial value which is 35 cm for head-on collision and 14 cm for crossing at 2 mrad.

4. As experience on the stochastic cooling techniques is gained, larger cooling rates can be applied, with the goal of reducing further the beam dimensions to enhance the luminosity and to reduce the LIR. We require a reduction of a factor of two in both horizontal and vertical beam emittances, which in principle can be achieved with a cooling rate twice as large as in the previous step. The luminosity for head-on collision would also increase correspondingly by a factor of two.

Similarly, by applying faster cooling also in the momentum plane the momentum spread of the beam bunches and, therefore, the bunch length could be lowered. Here too we require a factor of two for reduction with the consequence of reducing the LIR also by the same amount.

At the moment we believe that, with the present technology available, stochastic cooling of bunched beams at the rate thus specified is feasible, though a very detailed analysis and study of the method is required. Larger cooling rates are doubtful.

5. The length of the interaction region LIR depends on the bunch length. This in turn is given by the momentum spread in the beam and by the rf frequency wavelength. The momentum spread diffuses because of intrabeam scattering. It is important that the bucket height is large enough to accommodate the bunch size at any time, but the bunch length will not exceed the bucket length. Thus it is possible to double the rf from 26 MHz as specified in the CDR to 52 MHz. To provide the same bucket height, twice the rf voltage is required. The result is a bunch length twice as short. The original choice of 26 MHz for the rf was mainly due to beam dynamics considerations during crossing of the transition energy. This problem is being re-investigated again and may require a fast crossing of the transition with quadrupoles jump, in which case the beam dynamics would be independent of the rf.

By doubling the rf, as we have already said, the bunch length is a factor of two smaller. This will not cause any modification of the luminosity but only a significant reduction of the LIR by a similar amount.

6. Finally, it is possible to increase the luminosity by reducing the value of β^* at the crossing point. In the CDR the free space region around the crossing point has been chosen to be $\pm$ 10 m which will allow a β^* value of no less than 3 m. The free space region has to be reduced in length in order to reduce the β^* value further. Also common quadrupoles are then required which will not allow operation with colliding beams of different momenta. If the free space region is reduced down to $\pm$ 5 m then it is possible to obtain

$\beta^* = 1.5$ m. This will increase the luminosity by a factor of two but will have negligible consequences on the LIR.

Of the six steps proposed step 1 and 5 are the easiest to accomplish with present technology.

Step 2 requires a careful and detailed analysis of the performance of the heavy ion source, of the multiturn injection and of the rf capture capability in the Booster. There are still some unknowns about the best strategy for ion stripping in the Tandem and between the Tandem and the Booster that ought to be explored. A possible conclusion, already reached by an internal committee at BNL, is that one might replace the Tandem with a more powerful source in a second phase.

A mini-beta insertion to provide a β^* as small as 1.5 m has already been designed which in principle can be accommodated at any time with no known adverse consequences to the beam stability. This is an item that, if required can also be considered from the start of the project. What is required is the willingness of the experimentalists to limit their research to colliding beams with equal momenta and to a narrower free space allowed to their detector.

Finally, steps 3 and 4 rely on an exotic technique that only recently has been proven to work according to predictions. The major concern here, though, is that we require cooling of tight bunches and therefore we need large bandwith device. Nevertheless there are good expectations since to SPS collider in CERN seems also definitively committed to this technique for the same reasons. This is clearly the element of the upgrade program proposed that requires a longer range investigation and that probably will be included in an advanced stage of the RHIC project.

COMPUTING ISSUES FOR LARGE DETECTORS

S. C. Loken
Lawrence Berkeley Laboratory
University of California, Berkeley, CA 94720

Abstract

We review the computing issues which will affect planning for experiments at RHIC.

1 Introduction

It is traditional in workshops on new facilities to discuss the computing requirements for the experiments. Usually this discussion will focus on the number of MIPS (Million Instructions Per Second) needed to analyse the data tapes and, perhaps, the number of Terabytes of data storage. These are important parameters for planning new facilities. They are, however, only two of the features that define the computing requirements for new experiments. In this paper, I will discuss a broader range of computing issues and indicate how the problems of large experiments might be addressed on the time-scale of RHIC.

In this discussion, I will draw on the experiences of high energy physics groups working at colliding beam facilities, especially the Tevatron and LEP. In the colliding beam experiments, it has become increasingly important to consider the computing system as a component of the full detector system. The computing system includes online and offline computers, workstations, networks and mass-storage. It also includes software, both commercial and experiment-specific.

In the next section, I will review recent developments in computing equipment as well as mass storage and networks. In the following section, I turn to the problems of software development, testing and maintenance.

2 Hardware

The computing system for a large experiment includes many items: online computers, trigger processors, offline computers, workstations and terminals, networks and mass storage. The balance among these elements is an important aspect of the design for a large experiment. While the cost of computing hardware is typically a small fraction of the total

cost of the detector system, the computer system has a very large impact on the scientific productivity of an experiment.

2.1 Online Computer Systems

The online computer controls the running of the experiment, logs data onto tape, and monitors the data to ensure that the detector is working properly. For the colliding beam experiments, the online computer also serves as the controller for a large network of small computers which function as part of the trigger system for the experiment.

The trigger/data-acquisition system for any of the large colliding-beam experiments in high energy physics consists of a fast analog trigger and a system of microprocessors to implement higher level trigger functions [1]. In a separate contribution to this workshop, Sunier [2] has reviewed the existing or proposed systems and has compared them to the system needed for RHIC experiments. He concludes that the systems planned for high energy physics experiments will satisfy the RHIC requirements.

These trigger/data-acquisition systems are, in fact, computer networks and can be modeled, and optimized, using tools that have been developed for the computing industry. Cutts and van Ingen [3] have carried out a simulation of a trigger farm for an SSC experiment. They find that variations in bus-bandwidth and buffer size can have a significant impact on performance of the trigger system.

Hardware and software issues for online computer systems are similar in many respects to those for offline systems. The software is often shared; the algorithms developed for offline analysis are incorporated into the trigger processors. The requirements for debugging and monitoring the software, however, are even more severe than for offline software since events that are lost at the trigger level can not be recovered by rerunning the data tapes.

2.2 Offline Computer Systems

For most experiments, the main offline computing facility is located at the laboratory where the experiment is located. This facility usually provides a significant fraction of the CPU cycles for the experiment to reduce raw data tapes to data summary tapes (DST) and to simulate events for acceptance and background calculations. The central facility usually maintains the databases and program libraries for the experiment as well.

Most experiments also use computer facilities at the home institutions of the collaborators. The balance between central computing and distributed computing varies but with few exceptions, collaborations make significant use of their local facilities. This use must be planned early in the experiment as it has important implications for networking, software compatibility, library maintenance and database organization.

The choice of central computer is often outside the control of a single experiment. It typically consists of a large mainframe computer with a single scalar processor, a closely-coupled array of scalar processors, or single or multiple vector processors. The trend in

Figure 1: The cost of computer processing power as a function of time

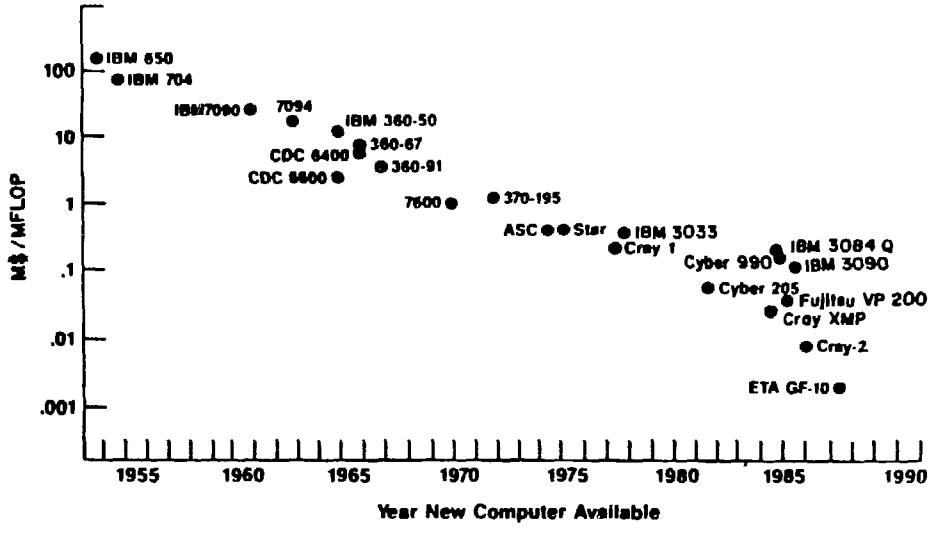

computing costs over the last three decades is illustrated in Figure 1. The cost of CPU power, measured in Millions of FLoating-point Operations Per Second (MegaFLOPS), has decreased by about four orders of magnitude. A more subtle feature is that since about 1980, two distinct lines appear. The decrease in cost has been achieved by the use of vector architecture (Cray, CYBER 205, ETA, and Fujitsu). The conventional scalar processing is significantly more expensive. To respond to this, the manufacturers of scalar computers (IBM and CYBER 990) are adding vector processors to achieve higher performance for many applications. In the future, all mainframe computers will be a closely coupled system of scalar and vector processors.

In general, the problems of experimental high energy physics, and of relativistic heavy ion physics, are not well matched to vector supercomputers. There has been some success in vectorizing simulation codes [4]. Here, the components of the vector correspond to different events. There has been much less success in using vector processing techniques for the analysis of data from colliding beam experiments. The techniques have been applied to a relatively simple fixed-target geometry and there is an effort to vectorize the analysis of one of the LEP experiments [5]. Clearly, the installation of a Cray-XMP at CERN and the vector upgrade of many of the IBM 3090 computers will give a boost to vectorization efforts.

If the move to vectorization is successful, it will likely come from the development of completely new algorithms. This means that the analysis code may exist in two different versions, one for the vector machines and another for the smaller computers at the home

institutions and on the online trigger system. This will significantly increase the problems of program maintenance for experiments. With these problems in mind, many groups look to other alternatives for inexpensive computing power.

2.3 Emulators, Micros, and all that

A very successful technique for supplying the CPU cycles needed for data analysis and simulation is the use of emulators or micro-computers. These are arranged in a parallel array, usually called a farm, with one event processed in each CPU. The computing time for each event is large compared to the time to move an event between the host and the processor. The technique is widely used for both online and offline computing and there is a broad range of processor options.

Emulators are special processors that have the same instruction set as mainframe computers. The 3081/E developed by SLAC and CERN, and the 370/E produced by Rutherford and the Weizmann Institute both execute code developed on an IBM host.

The Advanced Computer Program (ACP) at Fermilab uses commercial microprocessor chips on specially designed boards. The current choice is the Motorola 68020 with math co-processor but the approach is quite flexible and will accept newer and more powerful chips as they become available. The system was designed to provide offline computing and is being integrated into the Fermilab computing center. The ACP is also being integrated into the online trigger systems for experiments such as CDF at Fermilab and MEGA at Los Alamos.

A third approach is to use complete micro computer systems like the MicroVAX. D0 at Fermilab will use an array of MicroVAXs coupled by Ethernet to a VAX online computer as part of its trigger system. The same configuration has been used for D0 event simulation. The integration of microVAXs into a local area cluster is supported by the VAX/VMS operating system and makes it straightforward to add additional computing power at significantly less than the typical mainframe cost.

Another approach with potentially great promise is the use of transputers. These are powerful VLSI processors with I/O ports that have been designed to permit building large multiprocessor arrays. Such arrays have been built and used on simulation code [6]. A commercial computer system built of transputers is available from Meiko Computer. Good software support is only now becoming available and the impact of the transputer is yet to be felt.

2.4 Mass Storage

Based on Sunier's estimate for a typical event size [2], one experiment running for a year at RHIC might produce 5-10 Terabytes of raw data, or 35-70 thousand 6250 bpi tapes. The analysis output is typically the same size and even the "data summary" for a year's run could be 10-100 Gigabytes. The problem of mass storage needs to be addressed.

Unfortunately, the technology has not advanced in this area as rapidly as in some others.

For years, optical disks have been just around the corner. They are still not a viable system although they have many attractive features: they may be a random-access device; each disk holds 1 or more Gigabytes per side; they are easily handled remotely; the lifetime is significantly longer than magnetic media. There are also many problems: the devices are slow; the current generation disks cannot be erased; the disks are more expensive than tape; there is no standard format; no major computer vendor offers a system for his computer. Many experts expect that rewritable disks with capacities of up to 10 Gigabytes will be available in 2-3 years. At this time, the most we can say is that optical disks may be just around the corner.

In the meantime, the only alternative to the standard 6250 bpi tape appears to be the IBM 3480 cartridge tape. A single cartridge holds about the same amount of data as a standard reel but the unit is smaller and easier to handle with a remote loading device. The density is expected to increase by a factor 2-4 in the near future. IBM is committed to this technology and has dropped reel tapes entirely. DEC is expected to announce soon whether they will offer cartridge tapes. In the meantime, third party devices are available for both IBM and DEC. The silo system from Storage Technology can be expanded to satisfy the needs of any experiment or laboratory. It is the likely choice at most of the major laboratories in the United States and Europe.

2.5 Networks

Computer networks have become indispensible for scientific research. Local area networks at major laboratories and at universities provide communication between computers and workstations. Wide area networks permit access to program libraries and databases at the major laboratories and elsewhere and provide for the transfer of mail and files anywhere in the world.

Networking includes a broad spectrum of services. These include the following:

- Direct terminal connection
- Virtual terminal access
- Mail
- Phone
- File transfer
- Remote job entry
- Remote printing and graphics

- Distributed databases and libraries
- Process to process communication
- Telefax
- Video conferencing

All but FAX and video conferencing are widely used today and are required for the running of experiments or the development of software. Future collaborations will make even more use of networking in planning and proposing new experiments, and in developing a complete design for their software before they begin developing code.

The networks used by high energy and nuclear physics today have grown as a result of many individual initiatives to satisfy the needs of experiments. In 1985, a subpanel of the High Energy Physics Advisory Panel (HEPAP) [7] recommended the establishing of a national network (HEPNET) to coordinate the ongoing activity and to provide high-speed trunk lines between the major laboratories. Shortly afterward, the Office of Energy Research (OER) of the US Department of Energy established the Energy Science Network (ESNET) to provide central management of all OER networking. The two main efforts to be brought together in ESNET are HEPNET and MFENET, the network supporting the Magnetic Fusion Energy program. New sites will be added to ESNET to satisfy the needs of other OER programs.

By the end of 1987, ESNET will provide 56 Kbaud lines from SLAC/LBL to Fermilab/ANL to Brookhaven and MIT. There will be a 64 kbaud line from Fermilab to CERN in early 1988. These lines will run the X.25 protocol and will support terminal traffic, DECnet, and Coloured Books, an international, multivendor protocol for file transfer, mail and terminal access. The MFENET will run in parallel, with different protocols, but the two will merge in about 2 years to form the single network shown in Figure 2.

Similar network initiatives are supported in other government agencies in the United States. The National Science Foundation has established NSFNET to link the NSF-supported supercomputer centers and to link regional networks around the United States. NASA has established the NASA Science Network. Both of these, and the ESNET, will use the internet protocols, TCP/IP, developed for the ARPANET. There is already a government initiative to bring all these networks into a single internet. The networks will evolve towards a new networking standard, OSI (for Open Systems Interconnection) sponsored by the International Standards Organization (ISO). At the same time as we move to more interconnectivity, the speed of the individual links must be increased to accomodate additional traffic and to supply entirely new functionality. (see Figure 3).

2.6 Workstations

High performance personal workstations are a relatively new feature but are already have a significant impact on our research. As their performance continues to improve, and as

Figure 2: Major sites of the Energy Science Network (ESNET)

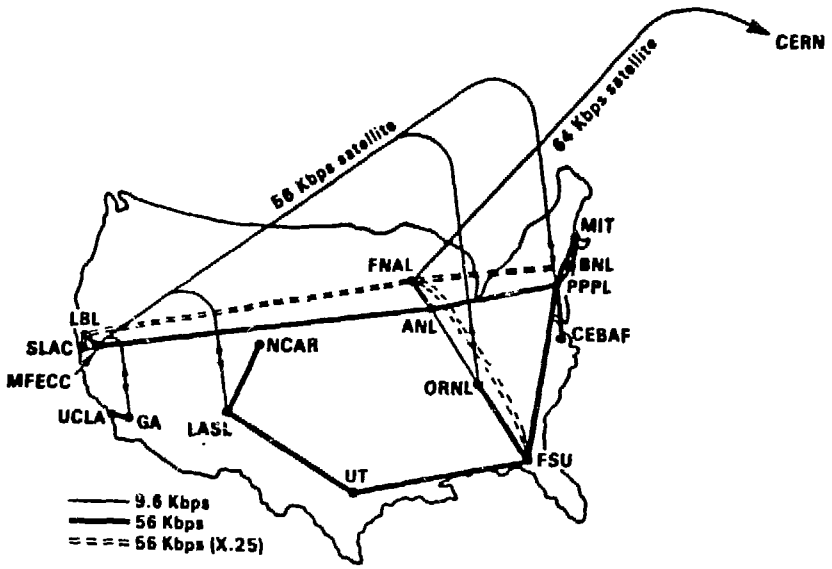

costs continue to decrease, they will revolutionize physicists' work habits.

The appeal of workstations is the gain in personal productivity. This, in turn, comes from the use of windows to keep track of multiple processes at the same time, often on different computers, and the use of high performance graphics. The workstations can provide high-resolution monochrome or color graphics and, by using the main CPU and custom graphics chips, can quickly rotate and zoom on 3D images.

These workstations provide significant computing power and storage for the individual user. For larger problems, it is possible to use the network support software to submit jobs to a remote processor or to reference a remote database. These facilities will give the workstation a role in interactive data analysis that is only now being appreciated [8].

Closely related to the workstation is the high performance 3D graphics terminal. They share the same capability to store 3D images and to zoom and rotate as desired, often using the same VLSI chips. They differ in that the graphics terminals have no general-purpose operating system. The graphics support software resides in the host computer and uses a device driver to send the image to the terminal. Different device drivers can be used with a variety of terminals form the most sophisticated 3D device to the lowliest dumb terminal. This permits the same graphics program to be used by the full collaboration.

Finally, I should point out that almost all of the workstations use the UNIX operating system. In addition, the network software used to support them is TCP/IP, a system that is integrated into the UNIX operating system in a way that is very different from its implementation in other operating systems. The growing attractiveness of workstations

Figure 3: Data Transmission Nomogram.

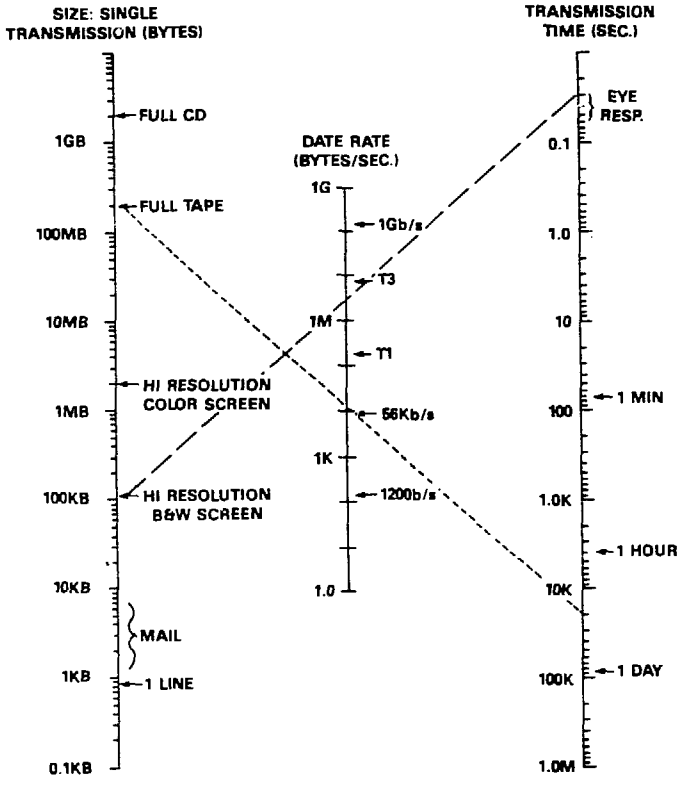

and network services will force a new look at UNIX by a large community that has rejected it almost unanimously in the past. The choice of operating system is only one of many software issues facing detector designers. I turn to other aspects of the software problem in the next section.

3 Software

It is traditional that software problems receive less attention than hardware, especially in the early phases of an experiment. This has been a serious problem for the current generation of high energy physics experiments and the problem will be even worse in the future.

Each of the current generation of colliding beam experiments is developing a software base of $3 - 5 \times 10^5$ lines of code. This development will take an effort of 300–500 man-years. The developers are typically not professional programmers and they have little, if any, training in computer science. They are not located in one place and, for the most part, do not devote full time to their software responsibilities. When a physicist who is

working on the design of a hardware component needs additional help, he often turns to and engineer or a technician. It is extremely rare that physicists will enlist professional help during any phase of the software development effort.

This situation is now changing. Recognizing the effort that software development will require, many groups are beginning to use software development methods that have been standard in the computing industry for many years. Many are using specialized systems to maintain data structures within FORTRAN programs and to use database management tools to maintain constants. While it is still too early to assess the success of these efforts, the indications are that the software will be better and that it will be easier to maintain.

3.1 Traditional Development Methodology

Up to now, most experiments have followed a "bottom-up" strategy for software development; the software is put together from components which were written for isolated studies during the design phase of the experiment. The result is a system with little design documentation. There is agreement on a general outline but individuals work on components with little intercommunication. Little attention is paid to integration of modules until after they are complete.

3.2 The Software Life Cycle

A modern approach to the problem of software development for experiments begins by recognizing that the software project will have a long and complex life and that each phase must be planned in detail. In fact, the approach is very similar to the engineering of any hardware component of an experiment. The phases of the software life cycle are the following:

- Requirements analysis
  - Define what the software is to do without consideration of how it is to do it or what the hardware configuration will be.
  - Build a logical model of the software system.
- Design
  - Define details of the software.
  - Create a physical model which describes the implementation.
  - Subdivide the problem into processing units, then into tasks, and finally into modules within tasks.
- Coding

- Write code, test and document modules.

- System Integration
  - Assemble modules and test.

- Acceptance Test
  - Demonstrate system performance

- Operation and Maintenance
  - Install in sites.
  - Update as necessary.

The formal structure emphasizes the early phases of the development cycle. Many studies have showed that the cost to fix an error increases significantly in later phases of the project (see Figure 4). In the early phases, the group working on the project is smaller. The effort to create a new model is much less than the effort to recode, compile and retest a module.

It is important to recognise that there are real costs associated with software errors. These are not measured by the same criteria as in the commercial world. The cost, however, can be measured in terms of lost beam-time, the expense of rerunning data tapes, missed discoveries, or incorrect results. It is very much worth the effort to get it right.

3.3 Structured Analysis/Structured Design

One of the formal methodologies for the first two phases of the project is Structured Analysis/Structured Design or SA/SD [9]. This methodology has been adopted by the ALEPH collaboration at CERN [10] and the D0 experiment at Fermilab[11]. While it is too early to determine whether the software for these experiments will be significantly better than that developed using traditional methods, both groups agree that they are developing programs that are different from what they would have done without SA/SD.

In the analysis phase, SA/SD uses three graphical tools to model the software system. These tools describe the software in much the same way that engineering drawings model a hardware object. A Data Flow Diagram models the flow and transformation of data in the system (see Figure 5). A State Transition Diagram (Figure 6) describes the time dependence and is especially useful for online programs or control systems. The Entity Relationship Diagram (Figure 7) defines the data elements of the system and the relationships between them. Together, these three tools describe the character of what is to be

Figure 4: The relative cost to fix an error or to make a change in software as a function of the time in the project.

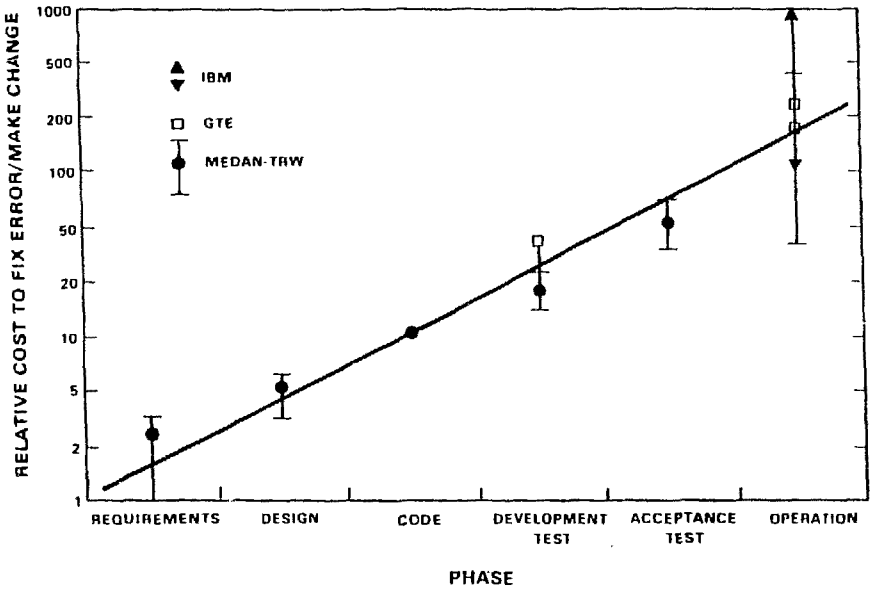

built. The graphical tools are augmented with textual specifications such as the Data Dictionary which specifies the characteristics of the stored data and Minispecs which describe the transformations in the diagrams.

The diagrams developed in the analysis phase are useful for describing the software system to people outside the development team. They should be the subject of a formal review, often called a Walkthrough. An error found by a review at this stage is usually fixed much more easily than later in the development cycle. There may be many ways to describe a system with the graphical tools. To choose the best model, or to refine a model, there are a number of criteria that may be applied. The most important of these is correctness. In addition, it is useful to simplify the interconnections in the system. The result of the analysis phase is a logical model of the system.

In the design phase, the constraints on the software are added. Pieces of the logical model will be allocated to various computers. The details of the human interaction will be incorporated. The elements of the logical model are assigned to modules and a physical model for the software is developed. The primary tool for the design phase is the Structure Chart. This is again a graphical tool and models the hierarchy, the partitioning and the interfaces of modules within a single program (see Figure 8). The Structure Chart should also be reviewed in a Walkthrough. There are also techniques to evaluate and refine this physical model of the software.

Figure 5: An example of a Data Flow Diagram taken from the ALEPH software [10].

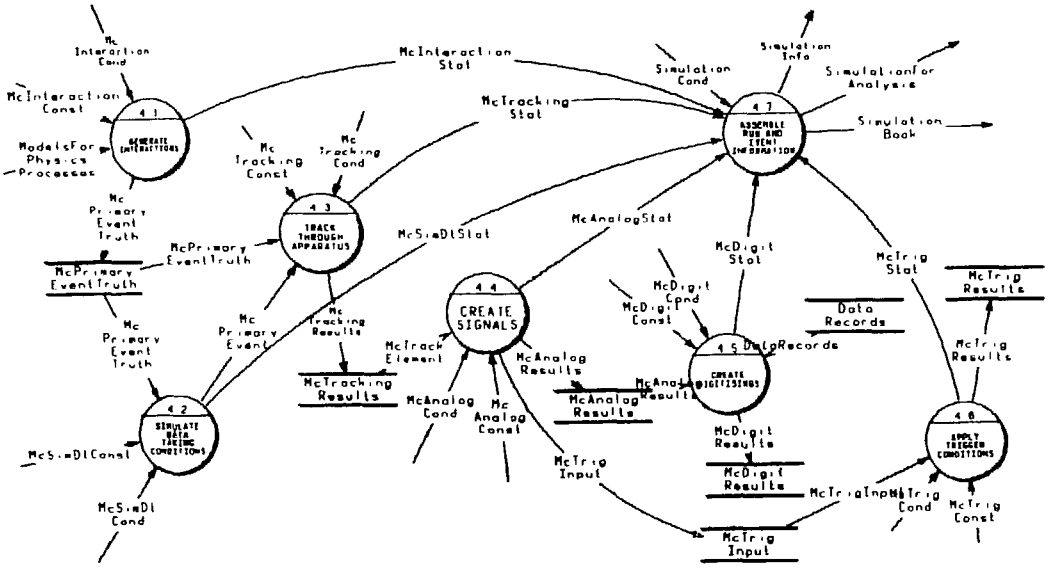

Figure 6: A State Transition Diagram taken from the D0 calibration software [11].

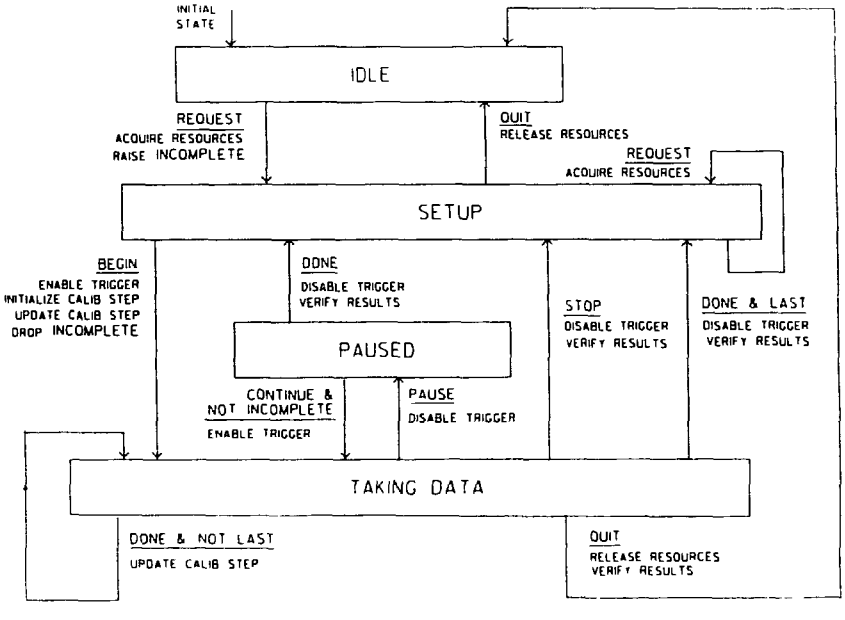

Figure 7: An Entity Relationship Diagram taken from the ADAMO data management system for ALEPH [10].

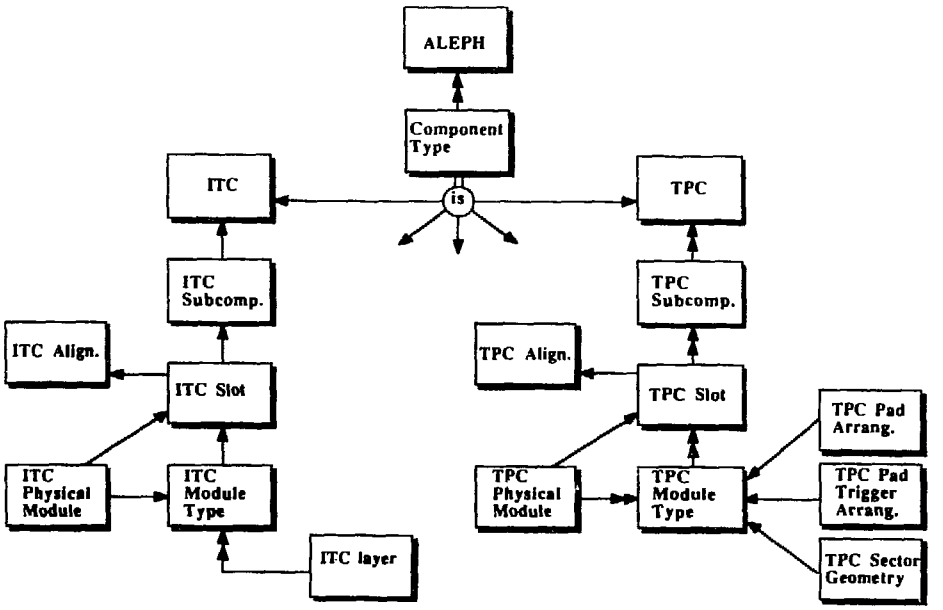

Figure 8: An example of a structure chart taken from ALEPH software [10].

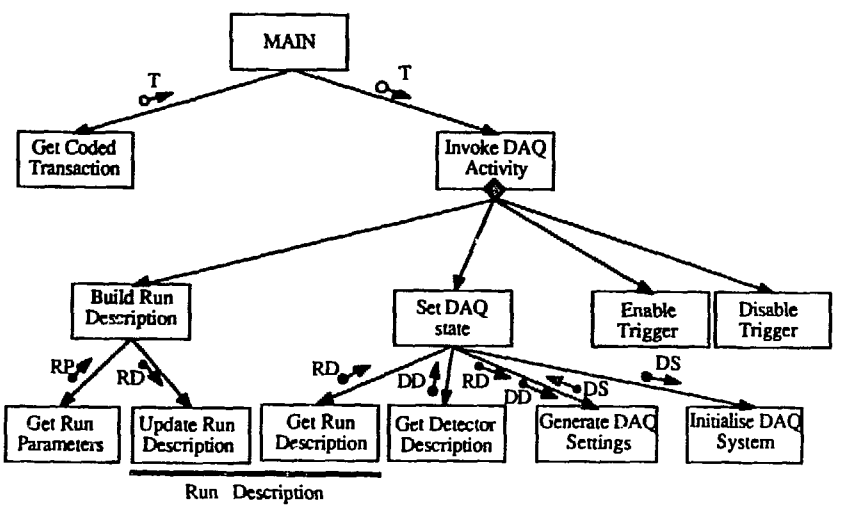

3.4 Computer-Aided Software Engineering

The commercial interest in software development methodologies has spurred the development of new tools to support what is now called Computer-Aided Software Engineering (CASE). Many of these products support SA/SD. The tools include programs to draw the diagrams of SA/SD. There are routines to check the consistency of various diagrams and to ensure that there is a complete specification of each data element or transformation. The tools store the diagrams and specifications in databases which are available over a network from remote computers.

These commercial have improved substantially in the last year. The two experiments which have committed to SA/SD were not able to find products that would satisfy their requirements even two years ago and have developed some tools themselves. D0 has recently undertaken an evaluation of available products and will try to put existing documentation into a new system. ALEPH has developed a set of tools which use the MacIntosh to manipulate Entity Relationship Diagrams in their ALEPH DAta MOdel (ADAMO)[12] . The ADAMO package goes beyond many commercial products and provides FORTRAN tools to manipulate data within the analysis code.

3.5 Code Management

During the development cycle, the software library must be carefully managed. Stable versions must be distributed to all developers so that new software can be tested with the rest of the system. There must be a full record of changes and there must be set of rules to ensure that new versions in the library are fully tested and documented. In fact, the problems of management begin earlier in the project. The same considerations apply to the requirements documents and the design documents.

The development of software for an experiment presents some challenges which are often not found in a commercial organization. The software continues to evolve over the history of the experiment as the apparatus is upgraded, our knowledge of the detector improves, or our physics interests change. There are many people involved in the project and they are at many sites. There are often many different computers.

The problem of code management is a difficult one and there is no simple solution. The PATCHY system developed at CERN can run on many computer systems but is not adapted to interactive access and is not widely used in the United States. Its replacement at CERN is a commercial product, HISTORIAN, but it is expensive for groups outside CERN and has not been widely adopted, even by LEP experiments. Many groups in the United States have decided to manage their software only on the VAX computer systems. The VAX products, CMS (Code Management System) and MMS (Module Management System) provide most of the functionality needed for experiments and support library management over a network with DECnet. There is a significant problem, however, for groups that have other computer systems at their home institutions.

4 Software Testing

No one developing software would dispute the need to test new software. The problem comes as the program is changed. Each change is tested to ensure that it does what it is expected to do. Seldom is the program subjected to all the tests that were run at earlier stages to ensure that old problems have not been reintroduced or that the change did not have some unexpected impact. To do this requires maintaining a series of test scripts that are run on each new version before it is distributed for general use. A set of standard output files must be maintained with the scripts so that a new file can be verified. Such a product is available as part of the VAX software system, DEC Test Manager (DTM) but again it works only for programs which run on the VAX computers.

Another aspect of testing that seldom gets the attention it deserves is the need to follow all possible paths through the program. A single program may have many thousands of possible paths depending, for example, on the nature of a complicated event. Often, these paths are not tried until a real event provides the set of parameters. If the program does not handle it properly, it is necessary to rerun the tape and chase the problem. It is more efficient to minimize the number of possible paths by the use of structured programming techniques, and then design the testing to ensure that all paths have been tried.

Various studies in the computer industry have indicated that up to half of the effort in a large project may be spent in testing programs. This statistic by itself should make it a high priority to improve the efficiency of software testing. The book by Myers [13] provides useful guidance for all aspects of software testing.

5 Conclusions

Computing for a large experiment is an effort that is comparable to that for any other aspect of the experiment. The design of the hardware system and of the software must be given the same attention that is given the other components.

Software development for a large experiment poses special challenges. New methodologies promise to significantly improve the productivity of the physicists and programmers and to improve the quality of the software product. Groups should begin immediately to gain experience with these modern methods so as to be able to use them effectively in the next generation of experiments.

References

[1] A.J. Lankford and G.P. Dubois. Overview of data filtering/acquisition for a 4π detector at the SSC. In R. Fenner B. Cox and P. Hale, editors, *Proceedings of the Workshop on Triggering, Data Acquisition and Computing For High Energy/High Luminosity Hadron-Hadron Colliders*, page 216, 1985.

[2] J.W. Sunier. *Comparison of Existing and Proposed HEP Data Acquisition Systems and their Suitability for RHIC.* , Los Alamos National Laboratory, 1987.

[3] D. Cutts and C. van Ingen. Modeling microprocessor farms for SSC data acquisition. In R. Fenner B. Cox and P. Hale, editors, *Proceedings of the Workshop on Triggering, Data Acquisition and Computing For High Energy/High Luminosity Hadron-Hadron Colliders*, page 216, 1985.

[4] K. Miura. Vectorization of EGS4 on vector processor system. In P. Kunz and T. Schalk, editors, *Computing in High Energy Physics: Proceedings of the International Conference on Computing in High Energy Physics, Asilomar, 2-6 February 1987*, page 127, 1987.

[5] D. Levinthal. Experimental HEP supercomputing at FSU. In P. Kunz and T. Schalk, editors, *Computing in High Energy Physics: Proceedings of the International Conference on Computing in High Energy Physics, Asilomar, 2-6 February 1987*, page 137, 1987.

[6] I. Glendinning and A. Hey. Transputer arrays as FORTRAN farms for particle physics. In P. Kunz and T. Schalk, editors, *Computing in High Energy Physics: Proceedings of the International Conference on Computing in High Energy Physics, Asilomar, 2-6 February 1987*, page 367, 1987.

[7] *Computing for Particle Physics: Report of the HEPAP Subpanel on Computer Needs for the Next Decade.* DOE/ER-0234, Department of Energy, 1985.

[8] R. Bock et al. PAW-towards a physics analysis workstation. In P. Kunz and T. Schalk, editors, *Computing in High Energy Physics: Proceedings of the International Conference on Computing in High Energy Physics, Asilomar, 2-6 February 1987*, page 181, 1987.

[9] S.J. Mellor and P.T. Ward. *Structured Development for Real-Time Systems*, Yourdon Press, New York, 1986.

[10] G. Kellner. Development of software for ALEPH using structured techniques. In P. Kunz and T. Schalk, editors, *Computing in High Energy Physics: Proceedings of the International Conference on Computing in High Energy Physics, Asilomar, 2-6 February 1987*, page 229, 1987.

[11] J.J. Linnemann et al. The use of SA/SD methods in D0 software development. In P. Kunz and T. Schalk, editors, *Computing in High Energy Physics: Proceedings of the International Conference on Computing in High Energy Physics, Asilomar, 2-6 February 1987*, page 245, 1987.

[12] Z. Qian et al. Use of the ADAMO data management system within ALEPH. In P. Kunz and T. Schalk, editors, *Computing in High Energy Physics: Proceedings of the International Conference on Computing in High Energy Physics, Asilomar, 2-6 February 1987*, page 283, 1987.

[13] Glenford J. Myers. *The Art of Software Testing.* Wiley-Interscience, New York, 1979.

Comparison of Existing and Proposed HEP Data Acquisition Systems and their Suitability for RHIC

Jules W. Sunier
Los Alamos National Laboratory

1. Introduction

A variety of recent topical conferences,[1,2] symposia,[3] and dedicated workshops[4,5] have reviewed the data acquisition (DACQ) existing or proposed for major detectors at High Energy Physics (HEP) collider facilities.

In this note, a summary of these DACQ systems is presented for UA1, MARK II, D0, CDF, and SLD, focussing on the data acquisition stages and trigger rates. The suitability of these systems for a RHIC calorimeter detector with ports is then discussed.

Although these DACQ systems have their individuality, they all use the common approach, illustrated in Fig. 1, of a multi-level trigger that reduces the rate and volume of the data to be recorded, in a number of appropriate steps. The first level trigger is analog, operates in the 1 μsec range, and has the purpose to reduce the interaction rate to a manageable rate of 10^5 Hz or less. While a second level trigger is being formed, in a time range as short as 10 μsec for SSC detectors, the data can be compressed (zero suppression, pedestal subtraction, etc.) and is buffered. The second level trigger has usually some intelligence, in the form of programmable logic or micro-processors. The third level trigger is done by software. At this stage, it is current practice to employ a processor "farm" to assemble full events and implement the reconstruction necessary to perform the final event selection, prior to archival on tape or optical disc.

The nature and amount of data processing performed at each level is flexible and depends on the application. The differences between the specific systems described below reside in:

- interaction rate and raw event size,
- type of primary data acquisition hardware and read-out scheme,
- choice of busses and processor farms.

2. The UA1-VME Scheme

Originally using a REMUS-CAMAC parallel read-out scheme, UA1 has now implemented a new VME based read-out system that supports REMUS, FASTBUS and Streamer Tube ADC Readout (STAR), with generalized use of the CPUA1 microprocessor. The event filtering is carried out by a farm of six 68E emulators. A group of 3081E emulators is planned to perform on-line and off-line analysis. Experiment control is well supported, through VME, by MacIntosh /68000 personal computers.

The data acquisition stages and rates are given in Fig. 2. The main bottleneck in the system is the enormous volume of data produced by the Central Drift Chamber, that is reduced and read-out in 25 ms. The first and second level trigger must therefore, without use of the central drift chamber information, reduce the trigger rate to well below 40 Hz.

3. MARK II for SLC

The DACQ system is a predominantly FASTBUS system, with SLAC Scanner Processors (SSP) used as Segment Interconnect (SI). The overall trigger rate is ~2 Hz with a modest ~40 KBytes per event. A set of on-line 3081E emulators are used to process Flash ADC data, assemble the event and place data in final format to tape. Full "off-line" event reconstruction can be run on-line to monitor detector performance. A SLAC FASTBUS controller (SFC) has been placed in the FASTBUS system crate to supervise the data transfer from the acquisition segments to the processor segment. Another SFC is used to monitor (in parallel with the VAX host) the general instrumentation electronics. SFC application programs are written in FORTRAN, to share code with the more complex VAX monitor programs.

4. The D0 System

A pretrigger (Level-0) initiates data collection at a rate of 50 kHz. To avoid dead-time, the Level-1 trigger must operate within the interval of 3.5 μsec between beam crossings. It uses signals from the calorimeter, an electron tag from the TRD system, and a muon signal from the muon proportional drift-tubes. It passes full events, at the rate of 200-400 Hz, to the second level trigger that consists of a MicroVax II supervisor and 50 parallel analysis nodes, also MicroVax II processors. The level-2 trigger operates, on the average, 100,000 instructions to completely filter one event. It delivers to tape an average event size of 200 KBytes, with a 1-2 Hz rate. The DACQ and online computer system are illustrated in Fig. 3.

The D0 DACQ was designed on the basis of two key concepts:

- a single event should be handled entirely by one processor (no splitting or rebuilding should be done)
- use of commercial hardware and software should be maximized.

The read-out section is coupled to the analysis nodes through 8 daisy-chained cables, with an aggregate throughput of 320 MBytes/sec. The input channels feed dual ported memories of 64 KBytes. The data is fed to the nodes private memory concurrently with the event analysis in progress. The Host Vax has Ethernet connections to the event processor nodes (running on VAXELN, a software product dedicated to real-time systems) as well as to equipment monitoring computers (more MicroVax II) and μVax workstations. It is interesting to note that the off-line processing needs of DO are estimated to be 50 to 100 VAX 780 years. The on-line system has 50 VAX 780 equivalents.

5. The CDF System

The primary trigger rate is 50 kHz and a typical event size is 100 KBytes. Three levels of triggering pass events for recording at a rate of 1–5 Hz. The Level-1 trigger, deadtime less, operates on mostly calorimetric information and reduces the trigger rate to 5 kHz. The Level-2 trigger uses the same information as Level-1, with more sophistication. It takes from 20–100 μsec and reduces the trigger rate to ~100 Hz. Intelligent Readout Scanners perform the digitization in 1–4 μsec, each scanner having storage space for 4 events. The system is shown in Fig. 4.

A Buffer Manager (μVax II) directs the Event Builder that is responsible for the accumulation of all data from the scanners. Two trigger supervisors (TS) are used to allow calibration and diagnostics to run concurrently with the data taking. The Level-3 trigger, a multiprocessor system with a processing power of ~10 VAX 11/780, reduces the event rate from 100 Hz to 1–10 Hz to be available for consumer processes on the VAX online computers. Each of these computers (1 primary VAX 11/785 Host, 3 secondary VAX 11/750 for monitoring and control, 1 alarm monitoring VAX 11/730 with serial CAMAC) is connected to FASTBUS through a UNIBUS processor interface, allowing each of them simultaneous access to the events in the Level-3 farm.

The CDF DACQ system runs on the concept of independent multiple partitions, sections of the detector that function independently of other sections. Each partition has its own read-out scanners and can receive independent triggers. The buffer manager and event builder operate on all partitions, with appropriate readout lists. This concept is very powerful for parallel debugging or calibration. The partitions are dynamic, down to the basic unit of a single readout scanner.

6. The SLD System

The low 180 Hz repetition rate of SLC allows for a very "simple" software trigger (5.5 msec between crossings), performed by SSP's processing coded hit information from the drift chambers and the energy sums of the liquid argon calorimeter, which are digitized in ~1 msec. Triggered events are fully digitized in ~50 msec and buffered into the SSP memory of each FASTBUS crate. Further processing (~200–400 msec) is done by the SSP's, prior to passing full events to a μVaX processor farm, at the trigger level of 1–2 Hz. Finally, events are logged and sampled by the host computer. A typical event size of 100 KBytes is obtained from 96 MBytes of digitized data.

7. Suitability of Described Systems for a RHIC Detector

According to the proceedings of the Workshop on Experiments for RHIC,[6] the major components of a calorimeter, with a slit spectrometer for the central region, are:

a. ~2300 Electromagnetic and Hadronic cells in the central part of the calorimeter, 800 Electromagnetic and 200 Hadronic cells in each of the end caps, or a total of ~6600 channels of data.

b. A multiplicity detector (DC with pad-read outs, silicon pads, streamer tubes?) with about 10^5 cells.

c. A port equipped with an inside TPC (10^4 channels), a RICH detector (5×10^2), external tracking chambers (10^3) and TOF counters (225).

In addition a Vertex Detector is required, due to the spatial extent of the interaction region. This detector could easily have 10^5–10^6 channels.

The above very approximate numbers lead to a final event size of the order of 100 kBytes, while the uncompressed event could be of the order of several megabytes. Table I summarizes the trigger and event rates, as well as the taped event size of the detectors described above. One can easily see that the RHIC calorimeter under study will have DACQ requirements quite similar to those of UA-1, D0 and CDF.

8. Conclusions

This study has shown that the RHIC detectors will require DACQ systems with performances equal or better than the DACQ of the large detectors presently used in HEP hadron colliders. This means that the DACQ of the detectors will be a significant part of their design effort and cost. Much can be learned from the experience gained by the HEP detectors, particularly in terms of balanced systems that optimize data throughput and instrument monitoring. While specific hardware/software choices can only be finalized when the detectors are designed, the complexity of the RHIC detectors suggests that the DACQ be incorporated to the detector design at the earliest feasible stage.

References

1. Fourth Conference on Real Time Computer Applications in Nuclear and Particle Physics, Chicago, May 20-24, 1985. IEEE Transactions on Nuclear Science, Volume NS-32, No. 4, August 1985.

2. VME bus in Physics Conference, CERN, Geneva, Oct. 7-8, 1985. CERN 86-01, January 1986.

3. 1985 Nuclear Science Symposium, San Francisco, October 23–25, 1985. IEEE Transactions on Nuclear Science, Volume NS-33, No. 1, Feb. 1986 (see also 1983, 1984, 1986 NS Symposia).

4. Proceedings of the FNAL Workshop on Triggering, Data Acquisition and Computing for High Energy/High Luminosity Hadron-Hadron Colliders (March 1986).

5. Report of the Task Force on Detector R&D for the SSC, SSC Central Design Group, June 1986.

6. RHIC Workshop: Experiments for a Relativistic Heavy Ion Collider, BNL, August 15–19, 1985. Report BNL 51921.

TABLE I
Event Rates, Trigger Rates and Recorded Event Size for Various HEP Detectors Compared to a RHIC Calorimeter with Slit Spectrometer

Detector	Pre-Trigger Rate (Hz)	Level-1 Trigger (Hz)	Level-2 Trigger (Hz)	Level-3 Trigger (Hz)	Event Size (kbyte)
UA-1	1.5×10^5	100	20	5	120
MARK II	2×10^2			2	40
D0	5×10^4	2–400		1–2	200
CDF	5×10^4	5000	100	1–10	$\sim$ 100
SLD	2×10^2			1–2	100
RHIC CALO/SLIT	$10^4 - 10^5$			$\sim$ 5	$\sim$ 100

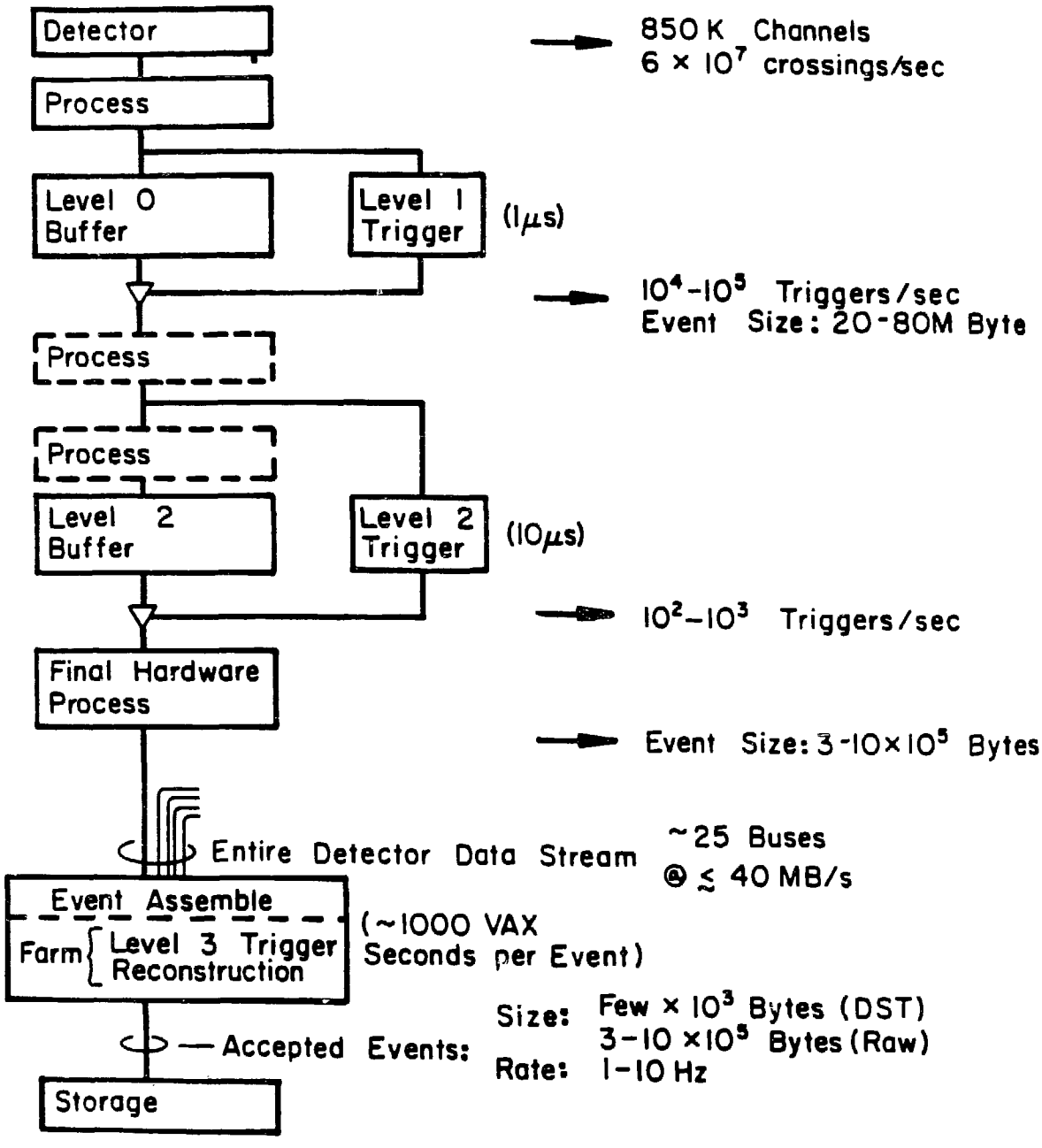

Figure 1. General model of data flow through levels of the data acquisition (from A. J. Lankford and G. P. Dubois, Ref. 4)

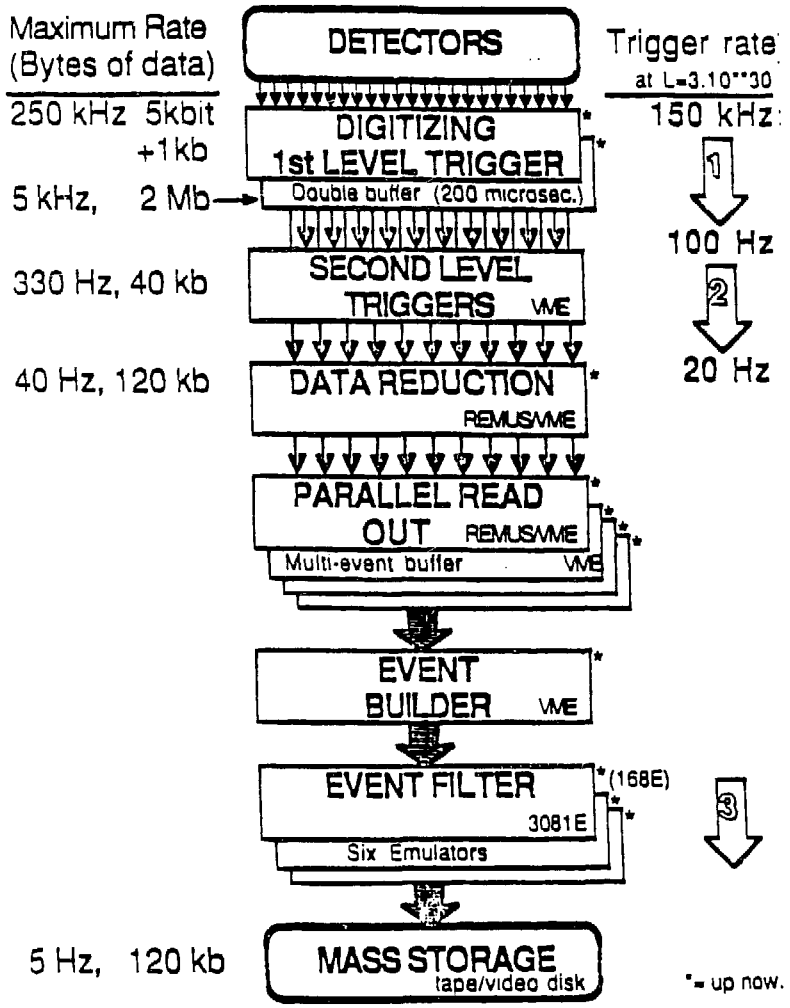

Figure 2. Schematic of the UA1 data acquisition system (from S. Cittolin, Ref. 2)

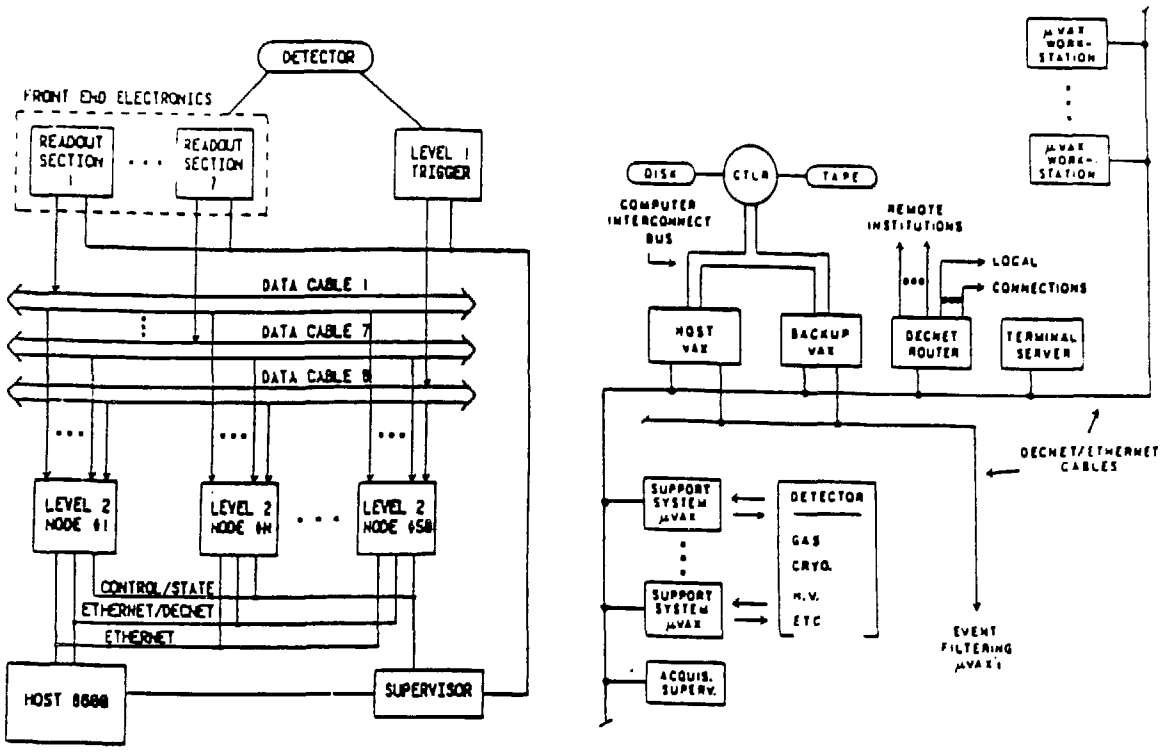

Figure 3. Data acquisition and online computer system at DO (from D. Cutts, et al., Ref. 1)

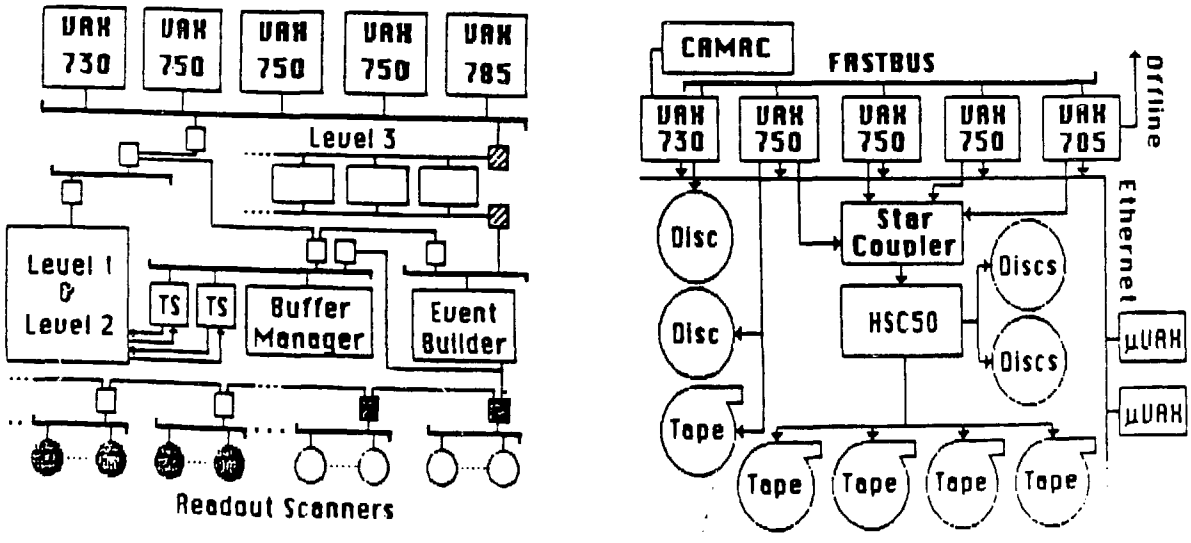

Figure 4. Data acquisition and online computer system at CDF (from D. Quarrie, Ref. 1)

On the Charm Production in Ultra-relativistic Heavy Ion Collisions *

T. Matsui

Center for Theoretical Physics
Laboratory for Nuclear Science and Department of Physics
Massachusetts Institute of Technology
Cambridge, Massachusetts 02139 U.S.A.

There are several reasons why it is important to measure the charm production cross section in ultrarelativistic heavy ion collisions.

1) Charm carries an information of the very early stage of the collision process: Since the charm quark is so massive (m_c = 1.5 - 1.8 GeV), it is likely that its creation takes place only at the very beginning of the whole collision process and the charm quark abundance will be essentially frozen in the later stage of the matter evolution. Hence it can be used to probe the early stage of matter formation and to test dynamical models of particle production.

2) If there is a strong enhancement of charm production in heavy ion collisions, in comparison with non-charm particle production, it would spoil some interesting signals of the plasma formation: J/ψ suppression by the plasma screening effect[1] will be compensated by the enhanced recombination of $c\bar{c}$ into the J/ψ during the hadronization stage; semileptonic decay of charmed mesons produces a large background for the dilepton signals from the plasma[2].

In this short report, I will first make a crude and rather conservative estimate of the expected charm abundance in nucleus-nucleus collisions based on the measured charm production cross section in pp interactions, and then discuss a possible coherent soft process which would lead to a further enhancement of the charm production in the case of heavy ion collisions. This talk is based on the work which is presently in progress in collaboration with Larry McLerran and Ben Svetitsky.

A rough conservative estimate:

The measured charm (D-meson) production cross section in pp interactions at $\sqrt{s} = (20 - 30)$ GeV is $d\sigma_c/dy \sim d\sigma_D/dy = (5 - 10)$ μb in the central rapidity region[3]. For non-charm particles, mostly being pions, the corresponding cross section is $d\sigma_\pi/dy = \sigma_{inel} \times (3/2) \times dn_{ch}/dy \sim 100$ mb. This gives the average D/π ratio in pp interactions $(D/\pi)_{pp} = (.5 - 1.) \times 10^{-4}$.

Let us assume that in pp interactions the charm quarks are produced in pair by the annihilation of hard partons like Drell-Yan process. In fact, the measured charm cross section[3] is reasonably consistent with the theoretical prediction based on the parton model[4]. If this is so even in heavy ion collisions, we may expect that the

* This work is supported in part by funds provided by the U. S. Department of Energy (D.O.E.) under contract # DE-AC02-76ER03069.

charm production yield will increase in proportion to $A^{1/3} \times A^{1/3} \times A^{2/3} = A^{4/3}$ for the case of central collisions of two identical nuclei of mass number A. On the other hand, most of the secondaries are supposed to be produced by the soft process, and the multiplicity will grow in proportion to A in central AA collisions. Hence we may expect a slow increase of D/π ratio in heavy ion collisions.

$$(D/\pi)_{AA} = (.5 - 1.) \times 10^{-4} A^{1/3} \tag{1}$$

Now let us compare the above number with the equilibrium ratio in a hot hadron gas. In the ideal gas of pions and D-mesons in complete chemical equilibrium, this ratio is given by

$$\begin{aligned}(D/\pi)_{eq} &= \frac{4 \times 1/(8\pi^2)\Gamma(1/2)(2Tm_D)^{3/2} \exp(-m_D/T)}{3 \times \frac{1}{\pi^2}\zeta(3)T^3} \\ &= 0.70(m_D/T)^{3/2} \exp(-m_D/T)\end{aligned} \tag{2}$$

Here we have used the non-relativistic Boltzmann approximation for the D-meson density and neglected the finite pion mass. The above formula gives

$$(D/\pi)_{eq} = 1.7 \times 10^{-3} \tag{3}$$

at temperature $T = 200$ MeV. Hence the observed D/π ratio in pp interactions and its extrapolation to AA collisions are about one order of magnitude smaller than the equilibrium ratio.

Given the expected D/π ratio, we next estimate the statistical recombination rate of free $c\bar{c}$ to form the J/ψ. To do this, we suppose that the phase space distribution of the charm quarks produced in a heavy ion collision obeys the statistical law determined by the temperature of the surrounding medium (thermal bath) of light quarks and gluons. Since there is a shortage in the number of charm quarks compared with its equilibrium value, this implies in thermodynamics that charm quarks and D-mesons acquire a non-zero (negative) chemical potential. If we assume that the chemical potentials of non-charm quarks are zero, then the charm quark chemical potential, $\mu_c = \mu_D$, are determined by the relation $(D/\pi) = (D/\pi)_{eq} \exp(\mu_c/T)$. Under the same conditions, the J/ψ chemical potential μ_ψ is related to the charm quark chemical potential by $\mu_\psi = 2\mu_c$ and hence we obtain

$$\begin{aligned}(\psi/\pi)_{rec} &= \frac{3 \times 1/(8\pi^2)\Gamma(1/2)(2Tm_\psi)^{3/2} \exp[-(m_\psi - 2\mu_c)/T]}{3 \times \frac{1}{\pi^2}\zeta(3)T^3} \\ &= (\psi/\pi)_{eq} \left(\frac{(D/\pi)}{(D/\pi)_{eq}}\right)^2\end{aligned} \tag{4}$$

where $(\psi/\pi)_{eq} = 0.52(m_\psi/T)^{3/2} \exp(-m_\psi/T)$ is the equilibrium ψ/π ratio in the hadron gas. Suppose that all J/ψ are formed by the statistical recombination at the hadronization temperature $T_H = 200$ MeV, then the above formula gives

$$(\psi/\pi)_{rec} = (0.5 - 2.) \times 10^{-7} A^{2/3} \tag{5}$$

which grows as A increases rather fast and becomes comparable for large nuclei, say uranium ($A^{1/3} = 7$), with the observed ψ/π ratio in pp interactions scaled with the A dependence expected from the hard-process-dominance for J/ψ production:

$$(\psi/\pi)_{AA} \sim (\psi/\pi)_{pp} A^{1/3} = 1. \times 10^{-6} A^{1/3} \tag{6}$$

Note that the equilibrium ratio $(\psi/\pi)_{eq} = 0.59 \times 10^{-4}$ is about two order of magnitude larger than the observed ratio.

Charm production in the flux tube model:

We shall now examine another mechanism to create heavy quarks efficiently in heavy ion collisions. It is one of the interesting consequences of the flux tube model which we have been studying as a dynamical model of energy deposition and plasma formation in ultrarelativistic nucleus-nucleus collisions[5-7]. Similar models have been proposed and discussed by many others[8].

This model assumes that the two colliding nuclei are color charged by random color exchange when they overlap. This leads to the formation of strong color field in between two separating nuclear disks which are oppositely color charged. The field decays subsequently by the pair creation of $q\bar{q}$ and gluons, and thus yields an enormous energy deposition creating a rapidly expanding hot quark-gluon plasma in the mid-rapidity region[5,6]. The long range color force acting on the color charged nuclei causes a deceleration and diffusion of the baryon number in the two nuclear fragmentation region as well[7]. As already pointed out[9], the intense color field should also result in some enhancement of heavy quark pair production in heavy ion collisions since the pair creation rate p (per unit volume) depends on the particle mass m as[10]

$$p_{f/b}(m) = \gamma \frac{(gE)^2}{8\pi^3} \sum_{n=1}^{\infty} \frac{(\pm)^{n+1}}{n^2} \exp\left(-\frac{\pi n m^2}{gE}\right) \tag{7}$$

where the subscript f/b stands for fermions and bosons, respectively, g the effective coupling constant and γ the degeneracy factor.

In pp interaction where the octet flux tube would dominate, namely $gE = (9/4)^{1/2} 0.2$ GeV^2, the above formula predicts very small charm production due to the very small exponential suppression factor; $\exp\left(-\frac{\pi m_c^2}{gE}\right) = 5.9 \times 10^{-11}$ where we have used $m_c = 1.5$ GeV. This strong suppression, however, heals very rapidly as the field intensity E grows. For example, if the effective string tension gE becomes ten times greater than the above octet string tension, as may well happen in a head-on collision of two uranium nuclei, this suppression factor is only 0.1! Unfortunately this is an over estimate since we have not taken into account the evolution of the field whose intensity decreases rapidly as a result of the pair creation.

To estimate the total charm production in the decaying flux tube we need to integrate the rate equation for the charm quark. If one neglects the change of charm

quark abundance by the collision process and only takes into account the production mechanism by the pair creation from the background field, it is written as

$$\partial_\mu n_c^\mu = p_f(m_c) \tag{8}$$

where $n_c^\mu = n_c u^\mu$ is the charm quark current density and we set $\gamma_c = 2 \cdot 3 \cdot 2 = 12$ for the spin, color and particle/antiparticle degeneracy factor of charm quark. Since $\partial_\mu(n_c u^\mu) = (1/\tau)d(\tau n_c)/d\tau$ in one-dimensional scaling hydrodynamic expansion, the total charm quark numbers produced per unit rapidity ($\frac{dN_c}{dy} = n_c \tau \pi R^2$) is given by

$$(n_c \tau)_{\tau=\infty} = \int_0^\infty d\tau \tau p_f(m_c) \tag{9}$$

Note that the factor τ in the integral which comes from the longitudinal extent of the available volume suppresses the contribution from the large field strength and enhances the contribution from the weakened field. Since light particles dominate the pair creation, the field attenuation may well be described by the formula[5]

$$E(t) = \frac{E_0}{(1 + \tau/\tau_0)^2} \tag{10}$$

where $\tau_0 = 2/(\kappa E_0^{1/2})$. The numerical constant κ is given in terms of the effective coupling strength $g_{f/b}$ and the degeneracy factor $\gamma_{f/b}$ of fermion/boson as $\kappa = (1.34/16\pi^3)(\gamma_b g_b^{5/2} + (1 - 2^{-3/2})\gamma_f g_f^{5/2})$. In using (10), we neglect the effect of the finite electric conduction in the produced matter which causes faster (exponential) attenuation of the field.

In the case of one dimensional expansion, the total entropy produced per unit rapidity ($dS/dy = \sigma \tau \pi R^2$), which is related to the final particle multiplicity by $dN/dy \sim 0.25 dS/dy$, can be calculated by integrating the entropy equation[6]

$$\frac{d(\sigma\tau)}{d\tau} = \frac{\tau E(\tau) J_{\rm ind}(\tau)}{T(\tau)} \tag{11}$$

where $J_{\rm ind}$ is the strength of induced current and T is the local temperature. If we again neglect the effect of finite electric conduction in the produced matter, the induced current is given by $J_{\rm ind} = \kappa E^{3/2}$. In this case, the asymptotic value of the entropy is written in a compact form:

$$(\sigma\tau)_{\tau=\infty} = 0.64(a^{1/4}/\kappa)E_0 \tag{12}$$

where $a = (\pi^2/30)(\gamma_b + \frac{7}{8}\gamma_f)$ is the Stefan-Boltzmann constant. Note that the entropy, hence the resultant particle multiplicity, is proportional to the total flux $E_0 \pi R^2$ of color field initially contained in the giant flux tube.

To estimate the charm to entropy ratio according to the above formulae (9) and (12), we need to specify the effective degree of freedom, $\gamma_{f/b}$, and the effective coupling strength $g_{f/b}$. If we use $g_f = 2$ and $g_b = 3$ taking into account the ratio of the Casimir

operator 9/4, and set $\gamma_f = 36$ for light quarks including strange quarks and $\gamma_h = 16$ for gluons, we find $\rho_c/\sigma = 0.7 \times 10^{-3}$ for $g_f E_0 = 3$ GeV^2. If the hadronization takes place adiabatically at $T_h = 200$ MeV, this implies $D/(\pi + K) = 1.4 \times 10^{-3}$ and $\psi/(\pi + K) = 3.8 \times 10^{-6}$. These numbers are as high as the equilibrium ratios in the hadron gas at $T = 200$ MeV and hence two orders of magnitude greater than the conservative estimate based on the parton model.

In conclusion, we have made a simple estimate of the charm production yield in ultrarelativistic heavy ion collisions based on two different mechanisms. The results suggest that the relative charm yield could be very large in real heavy ion collision so that more careful study is needed to clarify whether a clear detection of the proposed signatures of plasma formation are not hindered significantly.

I thank Larry McLerran, Vesa Ruuskanen, Helmut Satz, Asher Shor and Ben Svetitsky for helpful discussions and useful comments.

REFERENCES

1. T. Matsui and H. Satz, Phys. Lett. **178B** (1986) 416.
2. This problem is presently being studied by Asher Shor (private communication).
3. For recent data, see Aguilar-Benitez et al., Phys. Lett. **189B** (1987) 476.
4. H. M. Georgi, S. L. Glashow, M. E. Machacek, and D. V. Nanopoulos, Ann. Phys. **114** (1978) 273; B. L. Combridge, Nucl. Phys. **B151** (1979) 429.
5. A. Kerman, T. Matsui and B. Svetitsky, Phys. Rev. Lett. **56** (1986) 219; K. Kajantie, and T. Matsui, Phys. Lett. **164B** (1985) 373.
6. G. Gatoff, A. Kerman and T. Matsui, Phys. Rev. **D36** (1987) 114.
7. T. Matsui and J. Zingman, to be published; a preliminary result was reported by Jonathan Zingman in this workshop.
8. H. Ehtamo, J. Lindfors and L. McLerran, Z. Phys. **C18** (1983) 341; T. S. Biro, H. B. Nielsen and J. Knoll, Nucl. Phys. **B245** (1984) 449; A. Bialas and W. Czyz, Phys. Rev. **D31** (1985) 198; M. Gyulassy and A. Iwazaki, Phys. Lett. **165B** (1985) 157.
9. A. Bialas and W. Czyz, Phys. Rev. **D31** (1985) 198.
10. J. Schwinger, Phys. Rev. **82** (1951) 664· E. Brezin and C. Itzykson, Phys. Rev. **D2** (1970) 1191; A. Casher, H. Neuberger and S. Nussinov, Phys. Rev. **D20** (1979) 179.

CHARM PRODUCTION AND THE DILEPTON BACKGROUND FROM DECAY OF CHARMED HADRONS IN ^{197}Au + ^{197}Au COLLISIONS AT 200 GeV/A*

Asher Shor

Brookhaven National Laboratory
Associated Universities, Inc.
Upton, NY 11973

Abstract: A calculation is performed to determine the level of charm production and the background to the dilepton mass distribution from the semi-leptonic decay of charmed hadrons for ^{197}Au + ^{197}Au collisions at 200 GeV/A. The calculation incorporates HIJET for the systematics of nucleus-nucleus collisions, ISAJET for computing the cross section and hadron spectra for charm production, and a Monte-Carlo code which combines these results and generates lepton pairs from the decay of charmed hadrons. A mean multiplicity of 3.3 charmed hadrons is found for a central gold on gold collision. This brings about an appreciable level of background for lepton pairs above a mass of about 2 GeV. The dilepton background from charm decay can be significantly reduced with appropriate cuts on the polarization angle of the lepton pairs.

Dilepton production has long been accepted as one of the most promising tools for probing the interior of the quark gluon plasma. Dileptons are produced by the annihilation of a quark and anti-quark in the hot primordial plasma. Once produced, the dileptons, owing to their purely electroweak coupling, emerge from the interior of the plasma without further interaction and thus carry with them information on the properties of the plasma.

The above favorable scenario relies on the plasma as being the dominant source of dileptons, at least over a specified range of dilepton masses. The question of single lepton and dilepton production from the semi-leptonic decay of charmed hadrons in high energy p-p collisions has received a considerable amount of attention, and it is known to be a significant background

*Work performed under the auspices of the U.S. Department of Energy.

at masses of 1-3 GeV [1,2] and $P_T \sim 1$ GeV/c [3]. It can be readily shown that the charm background for dileptons becomes more severe in the case of nucleus-nucleus collisions. In p-p collisions, at most one $D\bar{D}$ pair can be produced per collision, with each D-meson having approximately a 10% chance to decay to, say, a muon, or approximately a 1% probability for both D's to decay to a $\mu^+\mu^-$ pair. For high energy nucleus-nucleus collisions, more than one pair of charmed hadrons could be produced in a single collision. For example, at 200 GeV, the charm cross section is approximately 0.5% of the total inelastic N-N cross section. Assuming an $A^{4/3}$ dependence for charm production, a central gold-on-gold collision can yield more than 2 pairs of charmed hadrons. There are now several combinations of charm pairs that can decay to lepton pairs. A further complication results from the rapidity separation of the charmed hadrons. In p-p collisions, a charm pair is correlated and is produced with a separation of typically less than one unit in rapidity, which can result in a decay to dileptons with mass of 0.5 to 2 GeV. For nucleus-nucleus collisions in which there are more than one charmed pair, a $\mu^+\mu^-$ can come from the decay of uncorrelated charmed hadrons which can have a separation of several units of rapidity and will result in a larger invariant mass for the $\mu^+\mu^-$ pair. Although like sign subtraction is an obvious solution to the problem of background from uncorrelated charmed hadrons, this solution becomes less attractive as the background begins to dominate the plasma signal.

To obtain an estimate for the dilepton background from charm decay, we develop a Monte-Carlo calculation which generates multiplicity distributions for charmed hadrons assuming purely conventional sources. The calculation allows for semi-leptonic decay of the charmed hadrons, and produces spectra for dilepton mass distributions. We focus primarily on the reaction Au + Au at 200 GeV/A, which is the design criterion for the proposed RHIC accelerator. We first describe the Monte Carlo code and the assumptions that go into it. Next, we show that the results of these calculations are compatible with experimental data on single lepton and dilepton production in p-p collisions. Most of our discussions will center on the results of the calculations for gold-on-gold collisions at 200 GeV/A. The question of which experimental cuts are necessary to reduce the charm background is important in the designing of detectors to measure dileptons at RHIC.

Description of Monte-Carlo Calculation

The calculation is organized into three stages. The first step involves generating 50 HIJET events for central collisions of Au + Au at 200 GeV/A. For each event, the 4-momenta of the N-N c.m. system is recorded for every N-N interaction. The second step uses ISAJET to compute the charm cross section in p-p collisions and to record the 4-momenta of the charmed hadrons for 1000 events at each of the following energies: 10, 20, 30,...., 190, and 200 GeV. The third step involves a Monte-Carlo code which utilizes the results of the first two stages. The Monte-Carlo calculation determines the charm multiplicity for each gold-on-gold collision, and randomly allows the charmed particles to decay to leptons.

The Monte-Carlo calculation begins by randomly selecting one of the 50 HIJET events. For each event, it cycles through the N-N interactions, and randomly determines whether a charm pair is created. The probability for creating a charm pair in an N-N interaction is given by

$$\frac{\sigma^{p-p}_{charm}(E_{cm})}{\sigma^{p-p}_{inelastic}}$$

If a charm pair is created, the 4-momenta for the charmed hadrons is randomly selected from one of the 1000 charm events from the file previously created at the E_{cm} closest to the invariant mass of the relevant N-N interaction. The charmed hadrons generated in this fashion are then allowed to decay to leptons according to known branching ratios and lepton momentum distributions. The leptons are Lorentz transformed first to the N-N frame and finally to the lab frame.

The scheme outlined above relies on the fact that the charm cross section is small and does not noticeably alter the evolution of the nucleus-nucleus collision. Although many events are required to generate dilepton mass spectra, continuous selection from only 50 HIJET events is acceptable for this study since each N-N interaction has at most a 0.5% probability for producing charm. The variation in momenta of the charmed hadrons, along with the variation in the lepton momenta following charm decay, further smear out the distribution and provide for a statistically significant calculation.

HIJET: Hijet [4] is an event generator for high energy nucleus-nucleus collisions. For our application it is ideal since it treats each N-N collision individually and thus we are able to construct our perturbative scheme for charm production. Figure 1 shows the distribution for the number of individual N-N interactions per central gold-on-gold collision. The mean is about 550 which implies a scaling from p-p of about $A^{1.2}$.

ISAJET: The charm cross section and charmed hadron momenta are computed using the ISAJET [5] high energy event generator. ISAJET assumes that charm production occurs via a hard scattering of the partons from the colliding nucleons. The charm cross section is determined by calculating the lowest order QCD graphs for the process $gg \rightarrow c\bar{c}$ and $q\bar{q} \rightarrow c\bar{c}$, and by the structure functions of these partons in the colliding nucleons. The distributions for the outgoing charmed hadrons are also affected by the fragmentation functions for the charmed quarks.

The effective mass of the charm quark is taken as a variable parameter. This is justifiable since charm production is not strictly in the perturbative regime since the Q^2 required is relatively low. The value for M_c was adjusted so as to obtain agreement with total charm cross sections recently measured by the LEBC collaboration [6] for p-p interactions at E_{cm} of 27 and 39 GeV. Figure 2 shows a comparison of the experimental cross sections with those computed by ISAJET for various values of M_c. Very good agreement is obtained for M_c=1.2 GeV. This is consistent with values obtained by other workers [7]. The value for M_c is taken to be 1.2 GeV for all subsequent calculations. Figure 3 shows the charm cross section as a function of E_{cm} as computed by ISAJET. Note that at E_{cm}=200 GeV the charm cross section is 150 μb, or 0.5% of the inelastic n-n cross section. The $c\bar{c}$ pair produced in ISAJET fragment mostly into D-$\bar{D}$. Occasionally D_s and charmed baryons are also produced.

Semi-leptonic Decay of Charmed Hadrons: The semi-leptonic decays of D-mesons are taken from R. Baltrusaitis et. al. [8]. They are

$$D^+ \rightarrow e^+ + X \qquad \text{b.r.}=17\%$$
$$D^0 \rightarrow e^+ + X \qquad \text{b.r.}=7.5\%$$

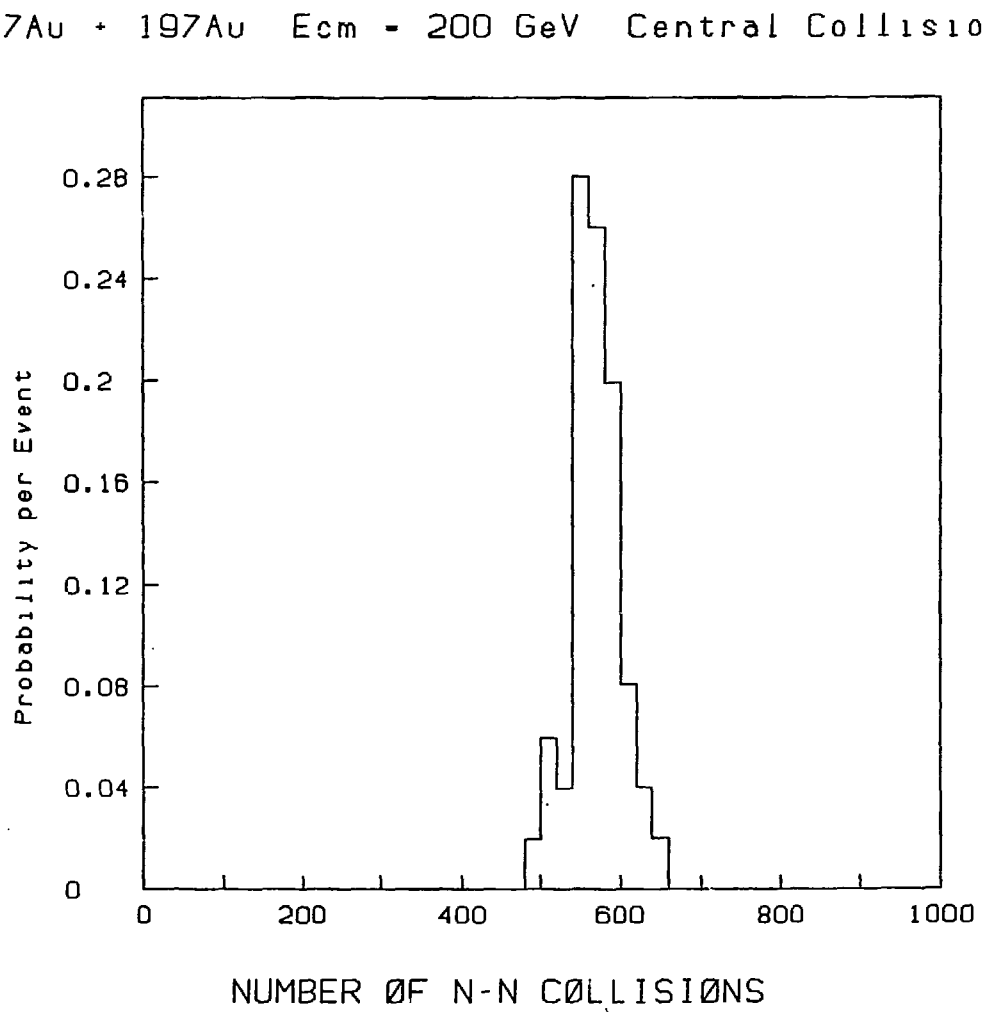

Fig. 1. HIJET calculations: number of N-N interactions per central Au + Au collisions.

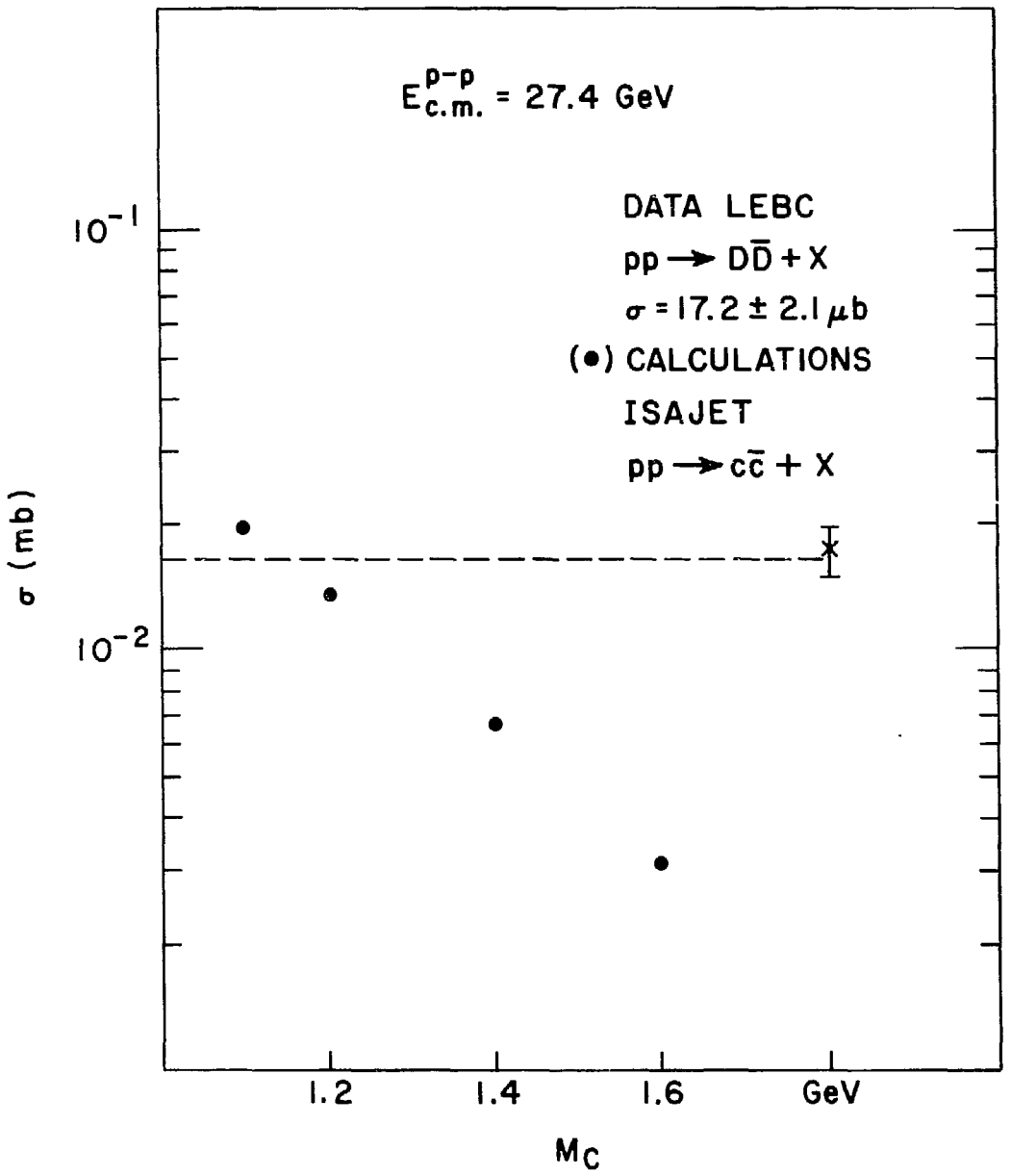

Fig. 2. Charm cross section in p-p collisions at /s = 27 GeV. Comparison of data (ref. 6) with ISAJET for several values of the charm quark mass.

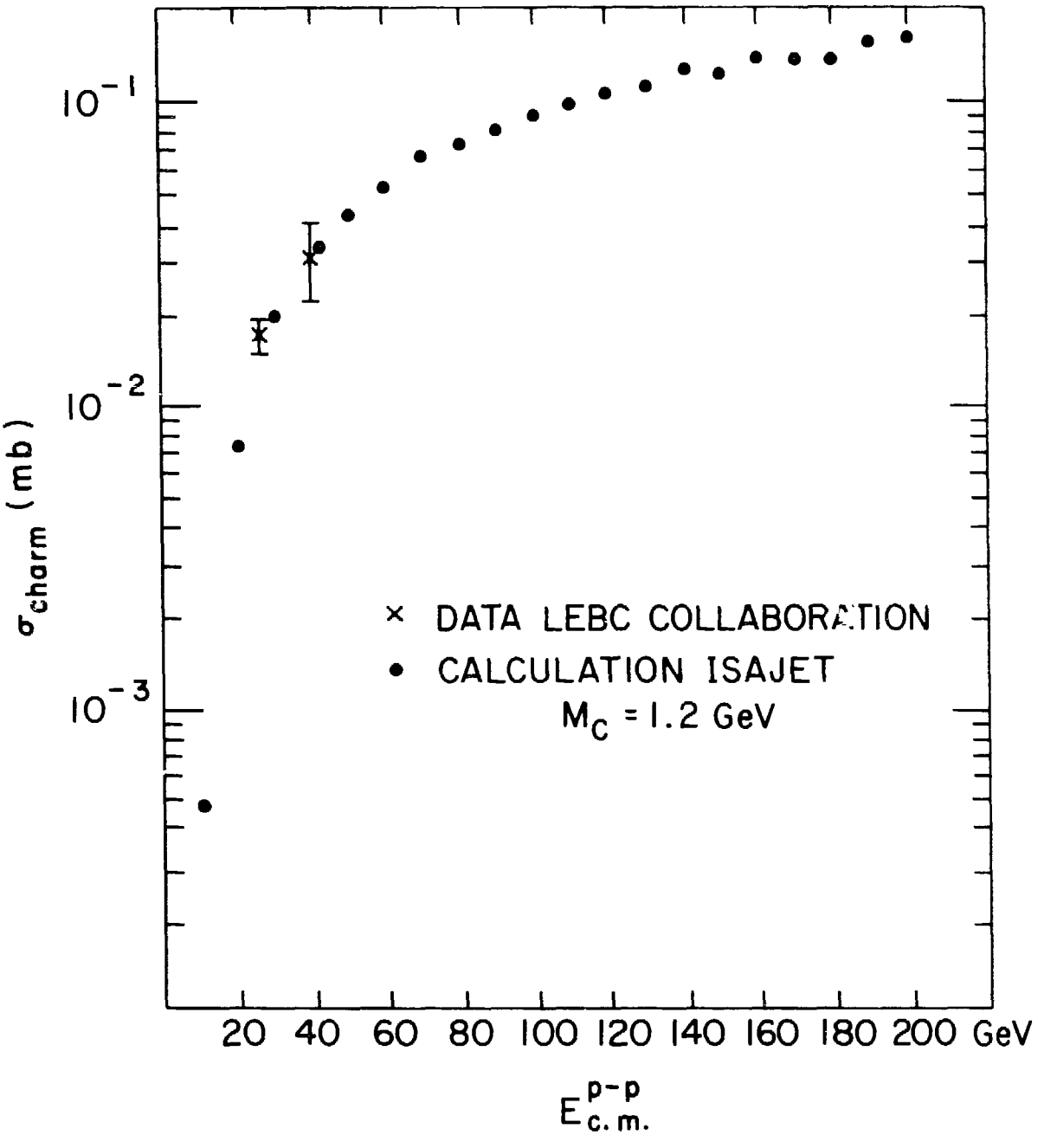

Fig. 3. ISAJET calculations: Charm cross section as a function of /s for M_c = 1.2 GeV.

The momentum distributions of the electrons in each case is consistent with equal probabilities for the following decays

$$D \rightarrow Ke\nu$$

and

$$D \rightarrow K^{*}e\nu,$$

with the energy sharing determined by phase space. We assume the decay of the D_s is also given by phase space and has a branching ratio of 10%. The branching ratio for $\lambda_c \rightarrow e^{+} + X$ is measured at 4.5% [9]. We assume equal probability for

$$\lambda_c \rightarrow pe\nu$$

and

$$\lambda_c \rightarrow \lambda e\nu$$

and a similar decay for Σ_c.

Comparison with Single Lepton and Dilepton

Production in P-P Interactions

For this calculation to be deemed reliable, it must produce results on single lepton and dilepton production compatible with experimental data for p-p interactions. Estimates on the single lepton and dilepton yields from charm decay have been made by several authors. This background has been found to account for a large fraction of the prompt lepton yields at low P_T observed at the ISR [3]. Assuming reasonable values for the charm cross sections, several authors have been able to almost saturate the observed dilepton yields for masses of 1-3 GeV [2].

A comparison of our calculation with ISR data is shown in Fig. 4 for prompt single electron production at low and moderate values of P_T [10]. We are able to reproduce quite well the direct electron yields for values of P_T below 1 GeV/c. Figure 5 shows a comparison with di-electrons observed at the ISR [11]. The calculated yields almost saturate the experimental results for masses of 2-4 GeV.

It is quite interesting that a substantial range of P_T for single lepton and mass for dilepton production can be accounted for by the mechanism of charm production and decay. This issue has been discussed by others and will not be further pursued here.

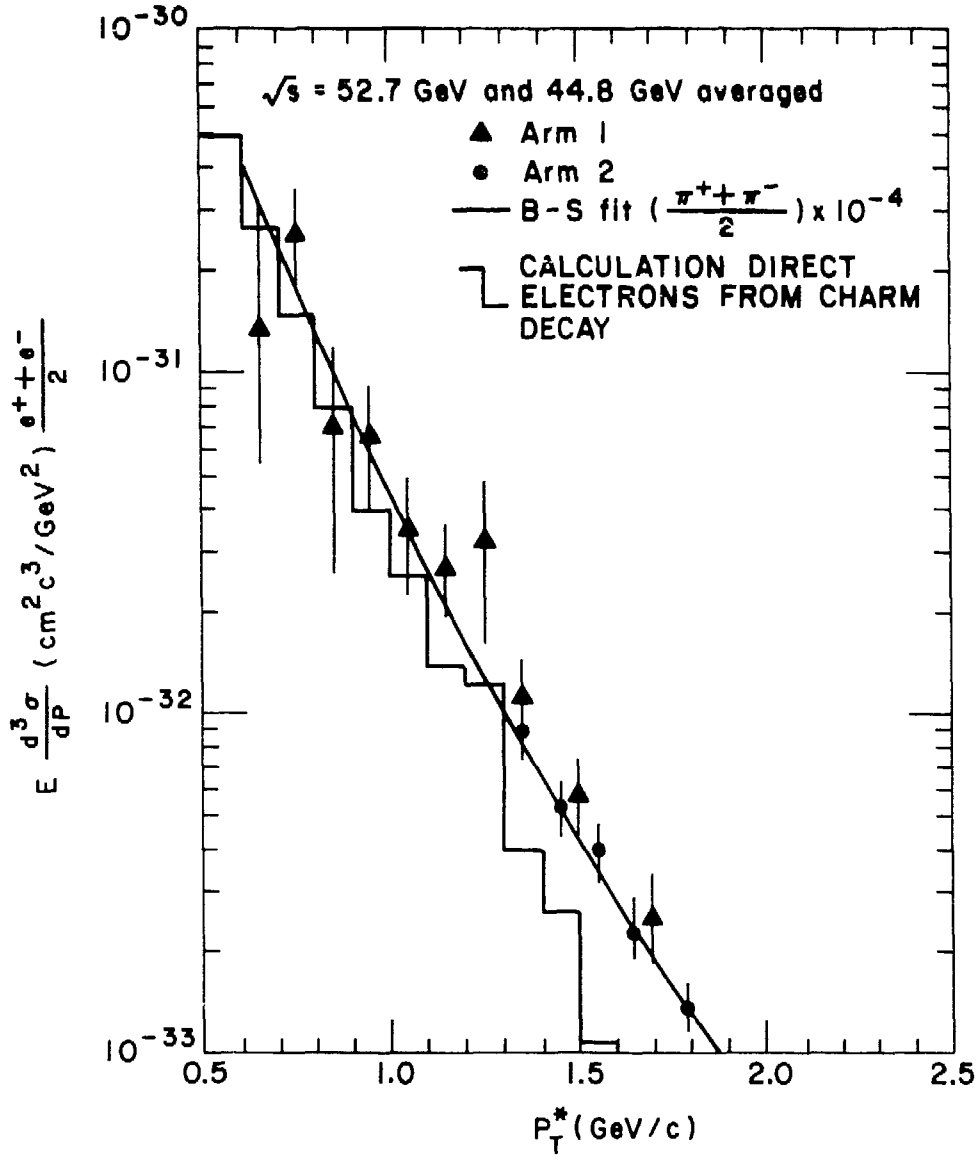

Fig. 4. Direct electron production at the ISR: Comparison of experimental data (ref. 10) with calculations for electron production from decay of charmed hadrons.

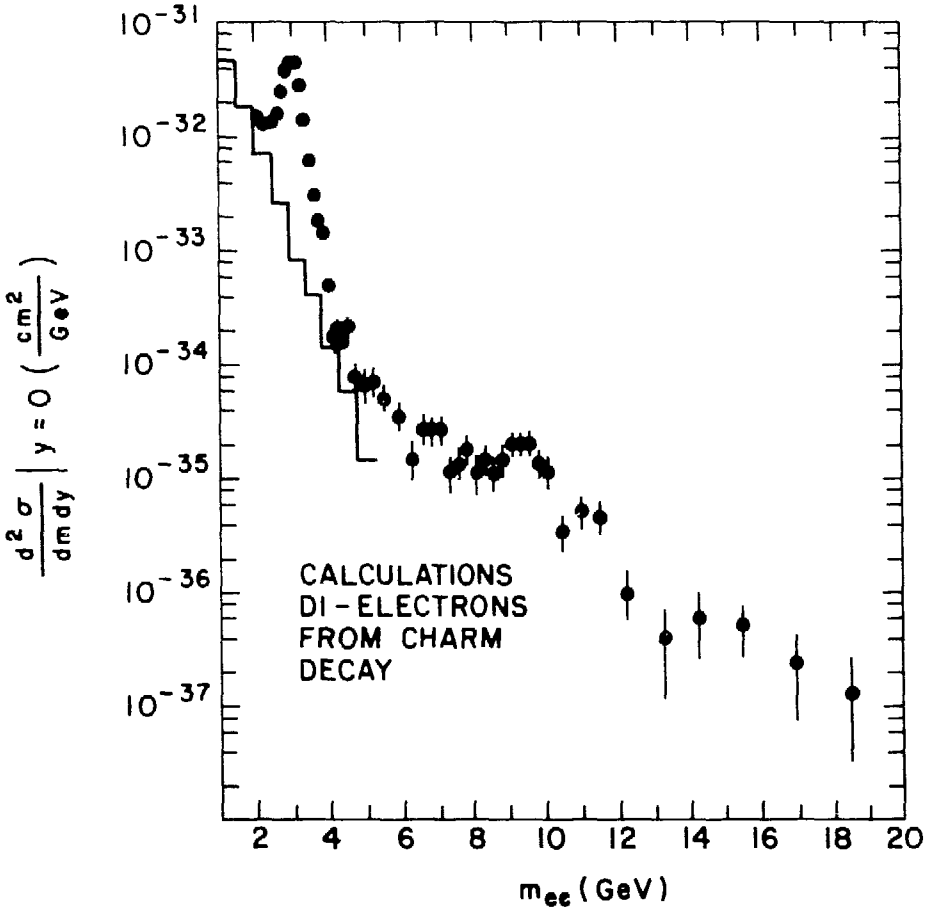

Fig. 5. Di-electron production at the ISR: Comparison of experimental data (ref. 11) with calculations for di-electrons from charm decay.

Results for $^{197}Au + ^{197}Au$ at 200 GeV/A

The bulk of the calculations were performed for central collisions of gold-on-gold at 200 GeV/A. One million events were generated using the prescription described above.

The multiplicity distribution for charmed hadrons is shown in Fig.6. The mean value is 3.3 charmed hadrons per event, although some events contain as many as 20 charmed particles. Figure 7 shows the rapidity gap between charm pairs. Note that this is a much wider distribution than that for p-p collisions at 200 GeV shown in Fig. 8. The large rapidity gap in gold on gold collisions comes primarily from uncorrelated pairs, whereas only correlated pairs are produced in p-p collisions. This will bring about larger lepton pair masses in nucleus-nucleus collisions.

The multiplicity of muons produced by decay of charmed hadrons is shown in Fig. 9. Note that 1/4 of the events contain at least one muon produced by charmed particles. Figure 10 shows the P_T distribution of these muons. The transverse momenta of these muons are relatively low and so acceptance for thermally produced muons could be enhanced with appropriate cuts on P_T.

The invariant mass distribution ($d^2N/dMdY$ per event for central Au + Au at 200 GeV/A) for di-muons produced by charm decay in central gold-on gold collisions is shown in Fig. 11 for several values of rapidity of the pair. Figure 12 shows a comparison between the like sign and opposite sign dimuons at y=0. Note that the two curves become almost the same for masses above 2 GeV. This represents the fact that most of the higher mass dimuons come from uncorrelated charmed hadrons.

Figure 13 shows a comparison of the charm induced dimuons with results of calculations performed by Kajante, Kapusta, McLerran, and Mekjian [12] for dimuons produced from a hot plasma. The contribution from charm decay appears to be at the same level as the signal from the plasma at the relavant pair masses. Note that the calculation for dimuons produced by the plasma are for very high initial plasma temperatures. For lower initial plasma temperatures, the background of dimuons from charm decay will begin to overwhelm the signal from the plasma. This appears to be very discouraging, but we will show that there are very powerful cuts that can be made to significantly reduce the dileptons from charm decay.

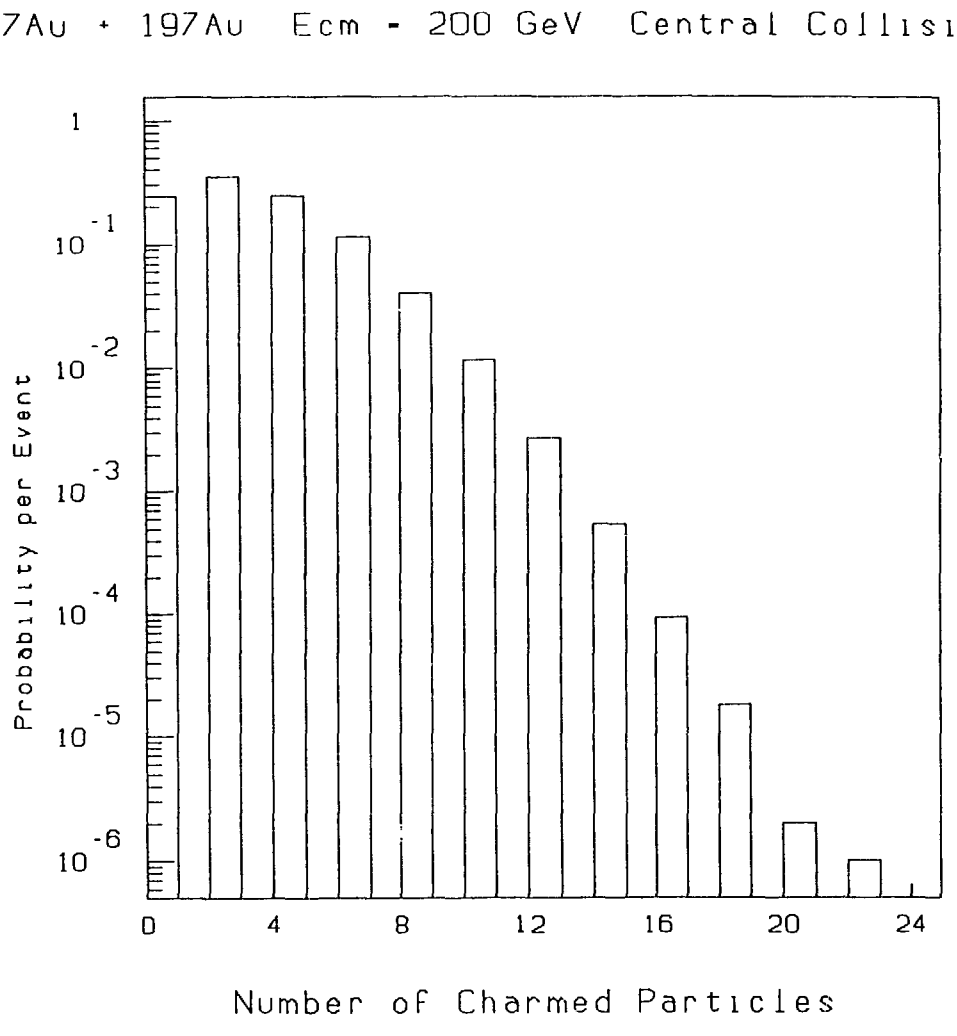

Fig 6. Calculated multiplicity distribution for charmed hadrons in central Au + Au collisions at E_{cm}/A = 200 GeV.

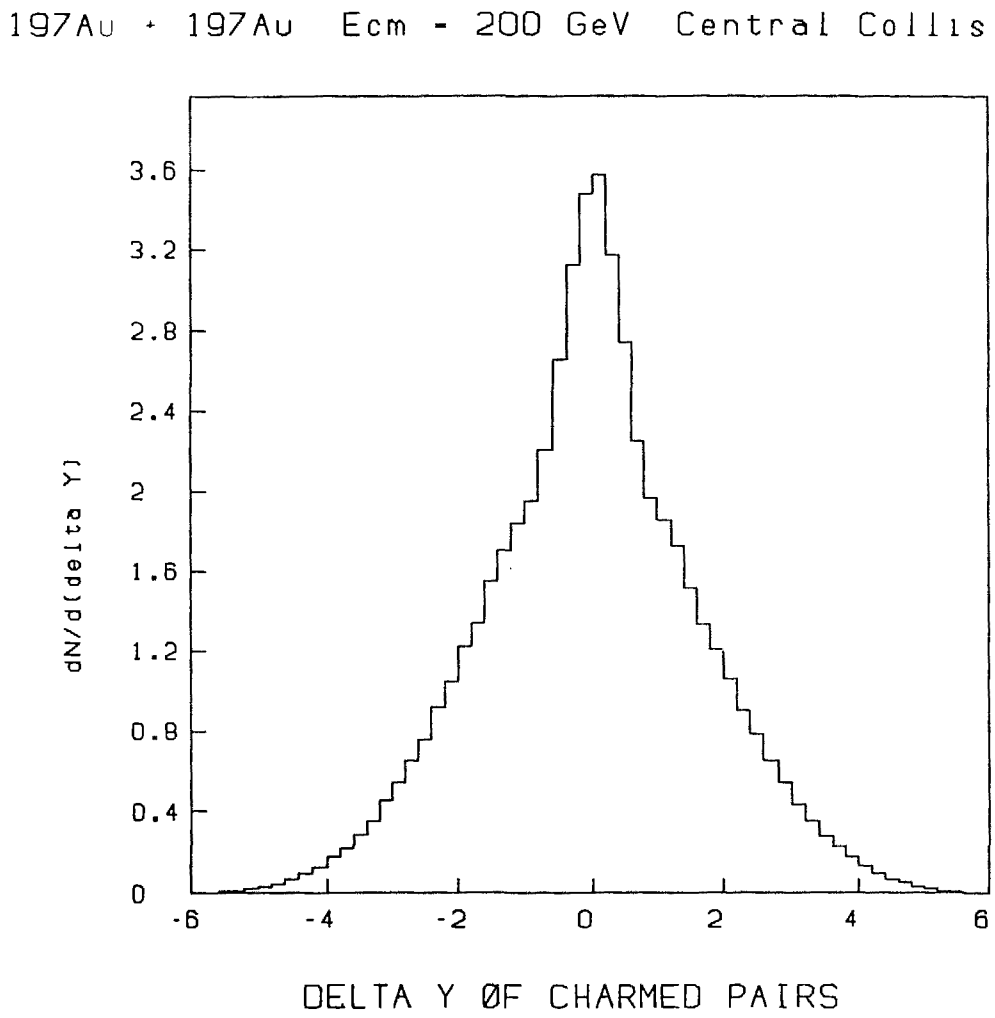

Fig. 7. Rapidity separation between pairs of charmed hadrons in central Au + Au collisions at 200 GeV/A.

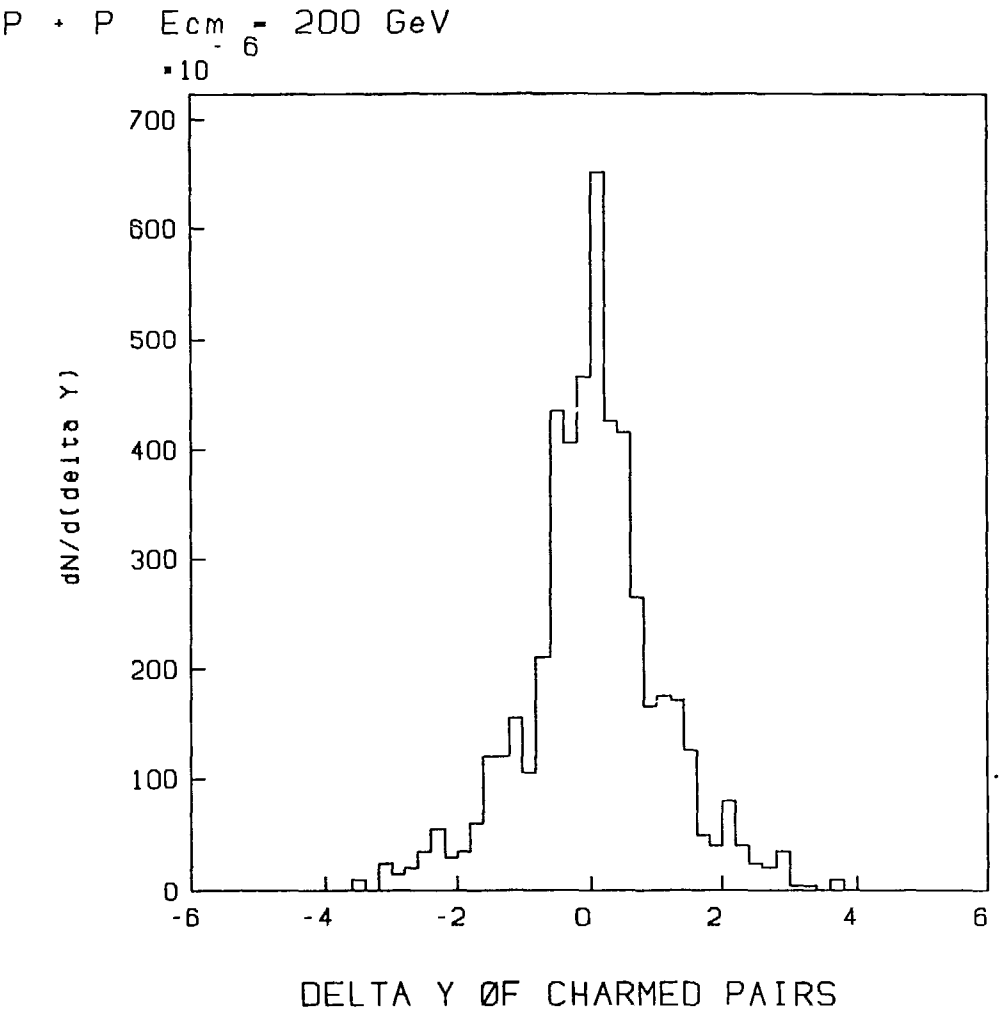

Fig. 8. Rapidity separation between pairs of charmed hadrons in p-p collisions at 200 GeV.

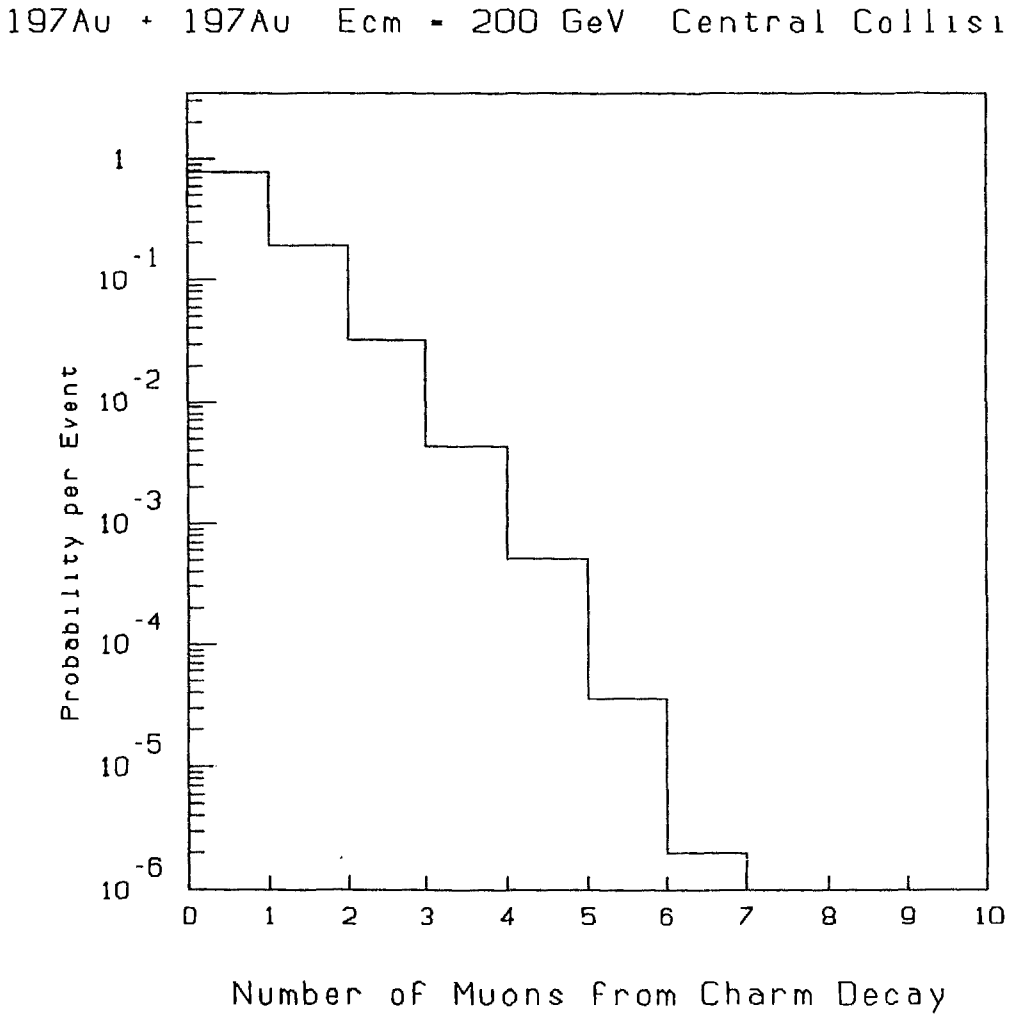

Fig. 9. Multiplicity distribution for muons produced by decay of charmed hadrons in Au + Au collisions at 200 GeV/a.

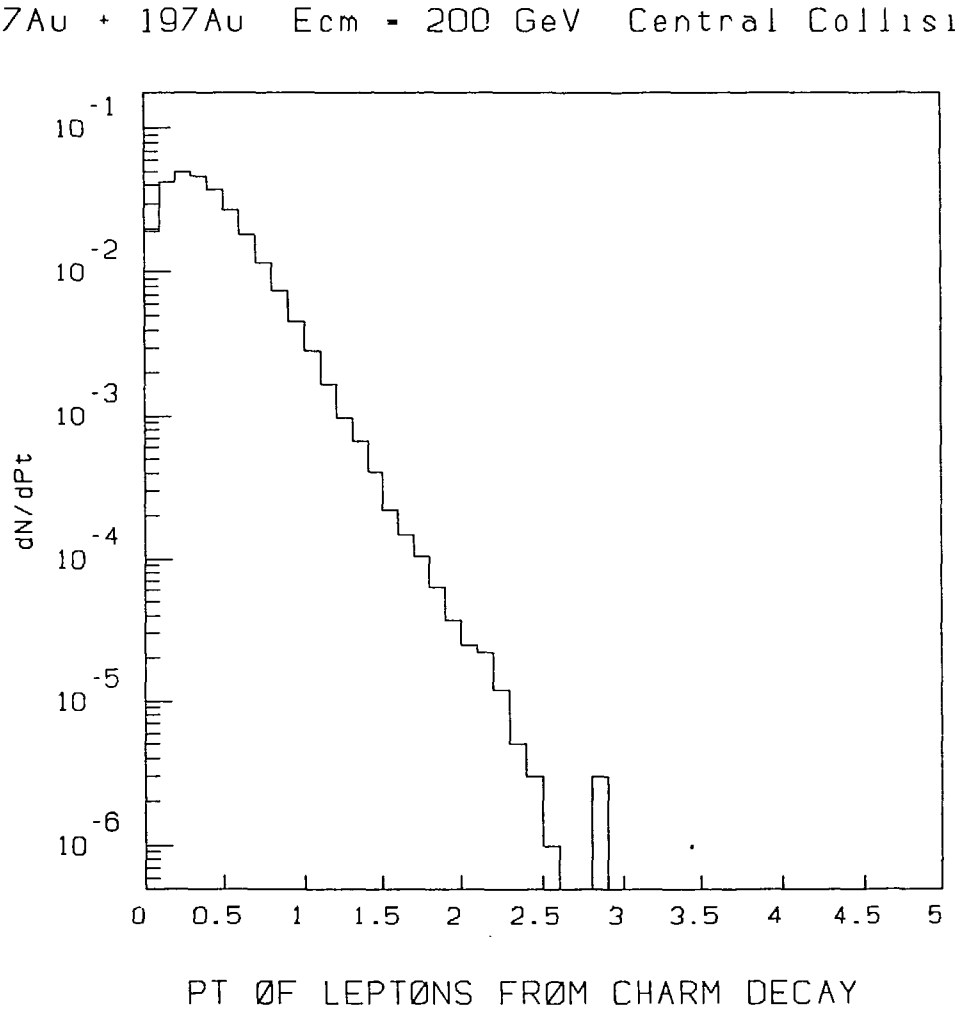

Fig. 10. P_t distribution for muons from charm decay in Au + Au collisions at 200 GeV/A.

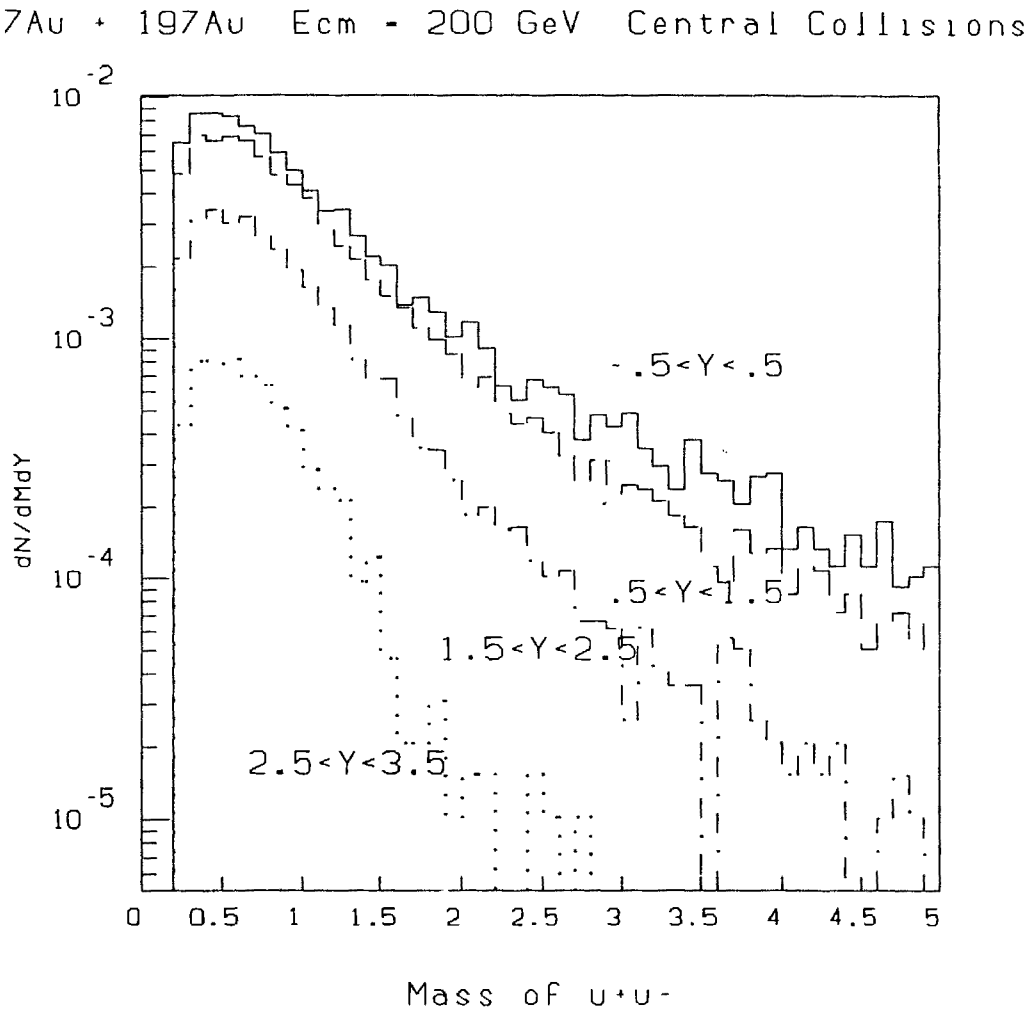

Fig. 11. Invariant mass distribution for di-muons from charm decay in Au + Au collisions at 200 GeV/A for several values of the rapidity of the pair.

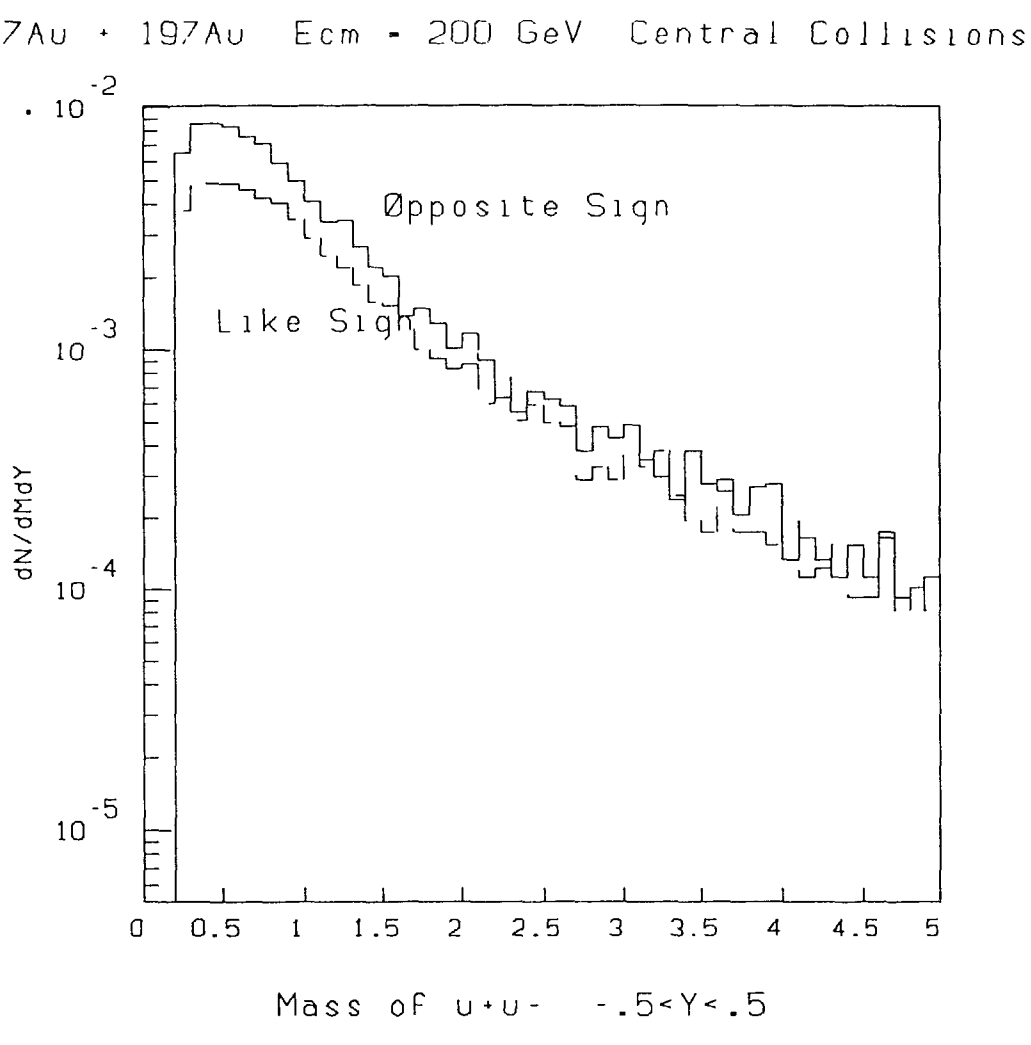

Fig. 12. Comparison of opposite sign and like sign dimuons from charm decay.

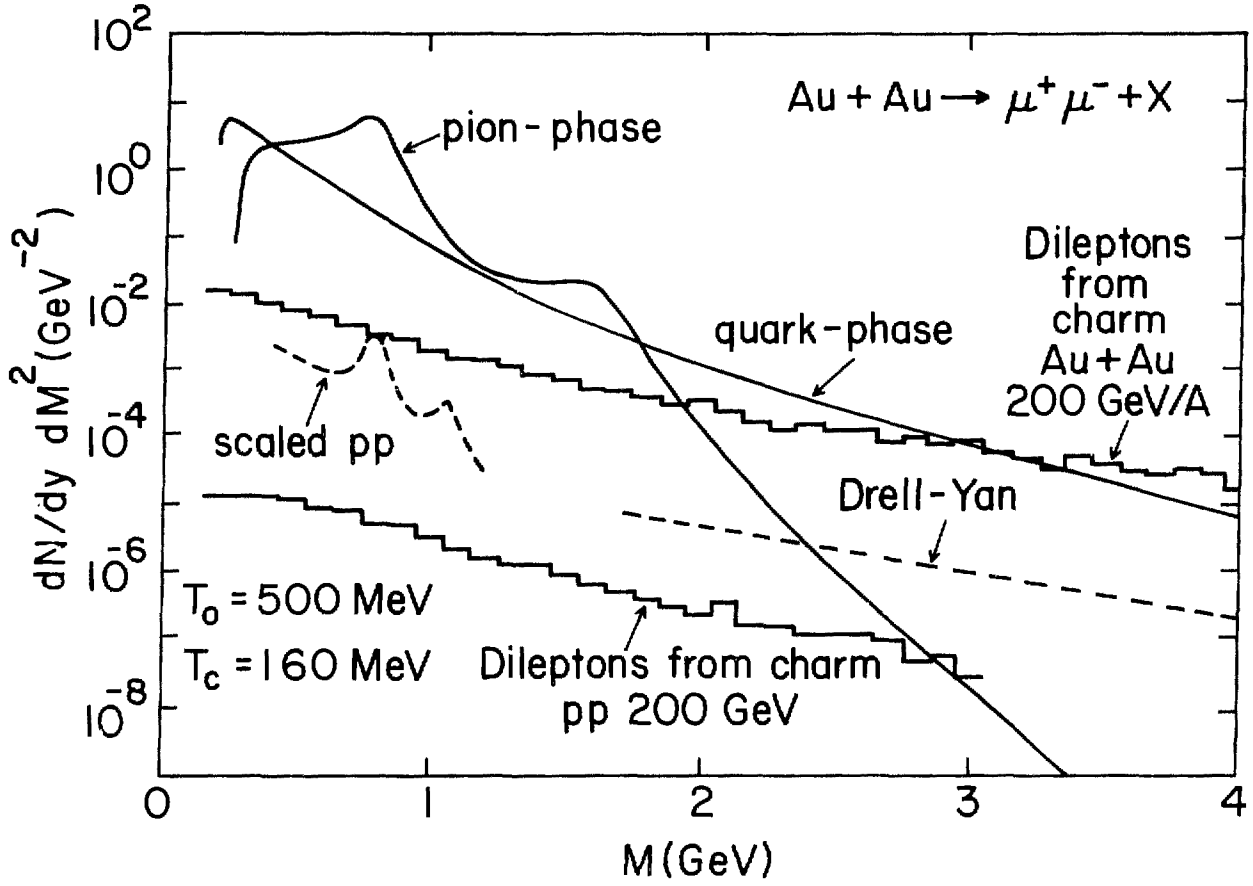

Fig. 13. Comparison of charm induced dimuons for Au + Au at 200 GeV/a with results of calculations for plasma production of Kajante, Kapusta, McLerran, and Mekjian (ref. 12).

Recall that the larger dilepton masses for charm induced dileptons result from a large rapidity separation between uncorrelated charmed hadrons. These leptons, however, still have a relatively low value for P_T. The separation between these leptons are in the longitudinal rather than the transverse direction. These dileptons would then exhibit a sizable degree of polarization in the longitudinal direction. Dileptons produced by a thermal souce, i.e., the quark-gluon plasma, would be isotropically produced and not contain any polarization.

Figure 14 contains a scatter plot of the polarization of the dimuons as a function of the dimuon mass. Theta * is defined as the angle of the dileptons with respect to the longitudinal direction in the dilepton c.m. system. Note that for larger values of dilepton massses, the polarization of the pair becomes more severe. At values of $\cos\theta^*$ less than abs (0.7), very few dileptons at masses above 2 GeV are produced. Placing such cuts on the experimental data, in addition to performing like sign subtraction, will quite significantly reduce the dilepton bcakground from charm decay. Figure 15 shows invariant mass distributions for di-muons at Y=0 for various cuts on θ^*. The solid line shows the $\mu^+\mu^-$ distribution with no cuts. The dashed line shows the dimuons with θ^* star larger than 25 $^\circ$ (i.e., the angle of each muon with respect to the longitudinal direction in the dimuon c.m. system is larger than 25°). Note that the yield for dimuons of mass of 3 GeV is an order of magnitude smaller when θ^* star is required to be larger than 25 $^\circ$. The dashed-dotted line represents dimuons with θ^* larger than 45°. Clearly, appropriate cuts on θ^* helps to reduced the dimuon of larger masses that are the result of charm decay.

Discussions

The Monte-Carlo calculation described above yields a sizable multiplicity for charmed particles in central gold-on-gold collisions at 200 GeV/A. These calculations take into account purely conventional sources of charm production and do not include new mechanisms such as strong color fields due to color charge buildup which may occur in heavy ion collisions [13]. The charm multiplicity is essentially poisson in shape, with a mean multiplicity of 3.3 charmed particles. Given such relatively large charm multiplicities, questions such as recombination of a c and $\bar{c}$ quark to form a J/ψ need to be

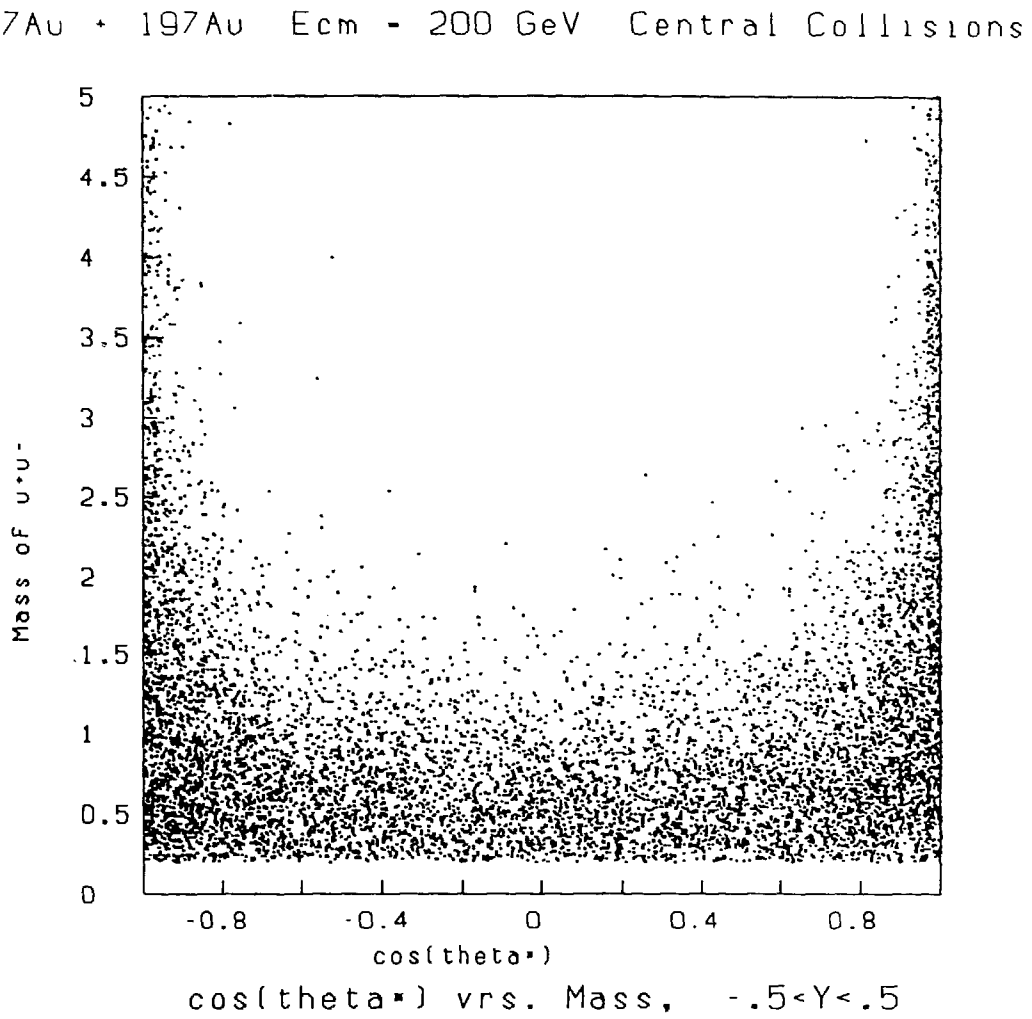

Fig. 14. Cosine of θ^* (angle w.r.t. the longitudinal of dimuons in the dimuon c.m.) as a function of dimuon mass.

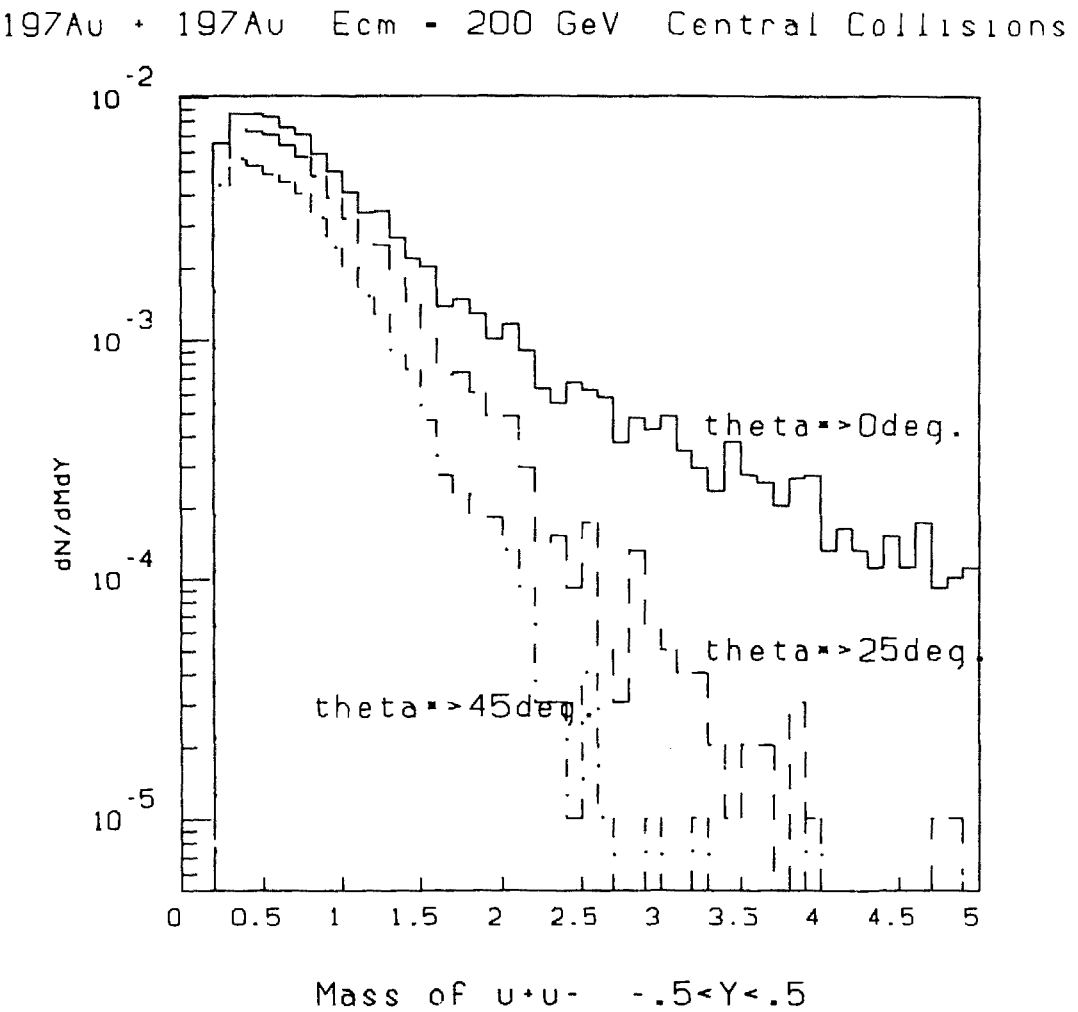

Fig. 15. Invariant mass distribution for dimuons from charm decay with several cuts on θ^*.

explored to confirm the validity for some of the signals proposed for detecting the plasma [14].

Since the charm multiplicities for central gold-on-gold collisions can be several pairs of charmed hadrons, the dilepton yield increases by a larger factor than the typical A or $A^{4/3}$ scaling for central collisions. Even more problematic is the relatively large mass for lepton pairs which are the decay products of uncorrelated charmed hadrons. We have discussed the feasibility for a substantial reduction of the dilepton background from charm decay by placing appropriate cuts on the polarization angle of the lepton pair, in addition to performing like sign subtraction. For large initial plasma temperatures, this prescription should be sufficient to reduce the charm background to well below the dilepton signal from the quark-gluon plasma.

References

1. M. Bourguin and J.-M. Gaillard, Nucl.Phys.B114 (1976)334.
2. H.G. Fisher and W.M. Geist, Z.Phys.C19(1983)159 and S.N. Ganguli et al., Phys.Rev.D32(1985)1104.
3. W.M. Geist, "Moriond Workshop on New Flavours", 1982, ed. J. Tran Thanh Van, L. Montanet, p. 407.
4. HIJET: a Monte Carlo Event Generator for High Energy Nucleus-Nucleus Collisions Based on ISAJET, T.Ludlam et al.,RHIC Workshop 1 BNL-51921.
5. ISAJET: a Monte Carlo Event Generator for pp and $p\bar{p}$ Interactions, F.E. Paige and S.D. Protopopescu.
6. LEBC-MPS Collaboration, R. Ammar et al.,Phys.Lett.183B (1987)110.
7. J.R. Cudell et al.,Phys.Lett.175B91986)227 S.N. Ganguli et al., Z. .Phys.C19(1983)83.
8. R.M. Baltrusaitis et al.,Phys.Rev.Lett.54(1985)1976.
9. Review of Particle Properties,Rev.Mod.Phys.56(1984).
10. F.W. Busser et al.,Nucl.Phys.B113(1976)189.
11. C. Kourkoumetis et al.,Phys.Lett.91B(1980)475.
12. K. Kajante et al.,Phys.Rev.D34(1986)2746
13. G. Gutoph, A. Kerman, and T. Matsui,Phys.rev.D36(1987)114.
14. T. Matsui and H. Satz,Phys.Lett.178B(1986)416.

PULSED ELECTROMAGNETIC PRODUCTION OF LEPTONS*

C. Bottcher and M. R. Strayer
Physics Division
Oak Ridge National Laboratory
Oak Ridge, TN 37831

It seems likely that significant heavy lepton production and emission will occur from the electromagnetic fields which arise in relativistic heavy-ion collisions. This possibility was first suggested several years ago by Gould,[1] based on estimates using the Weizsäcker-Williams method. The technique can be derived from perturbation theory, as discussed by Soff[2] in the context of electron pair production in relativistic collisions of uranium. In such collisions, the near-zone electromagnetic field becomes very large, transverse, and very sharply pulsed.

In our studies, which are nonperturbative, we find large cross sections from this mechanism, much larger than from the Drell-Yan mechanism, which has been suggested as a possible means of diagnosing the transition from hadronic matter to a quark-gluon plasma in such collisions.[3] Positron production in slow, heavy-ion collisions has been the subject of intense experimental and theoretical investigation for over a decade.[4] Preliminary investigations using nonperturbative techniques have extended the theory to relativistic energies[5,6] and necessitate the accurate calculation of all of the particle-antiparticle states which are excited out of the vacuum in the presence of the strong transient fields. For each state, the time-dependent Dirac equation must be solved in three space dimensions, which is very difficult and expensive. In this paper, we address the production of lepton pairs out of the vacuum using these methods and a local field model. The formal details of this are given elsewhere.[7,8] In our current work, we shall apply the model and discuss in detail the production cross sections as a function of the transverse momentum, the invariant mass, and the rapidity.

For simplicity, we consider the symmetric collision of two bare, heavy nuclei of charge Z and mass A at relativistic velocities. We shall work in an inertial frame fixed in one of the nuclei, referred to as the target; in units

*Research sponsored by the U.S. Department of Energy under contract DE-AC05-840R21400 with Martin Marietta Energy Systems, Inc.

of the nucleon mass, the kinetic energy of the projectile in this frame is γ-1. The collision is assumed to occur at a fixed impact parameter b, and we shall also assume complete nuclear transparency between the two nuclei, even when b is less than the interaction radius of the nuclei. This assumption will be discussed later. The motion of the projectile nucleus creates an intense electromagnetic pulse which is treated classically, and which excites pairs out of the vacuum.[5-9]

The local equivalent field model, as employed here, is a variation of a model attributed to Schwinger, in which pairs are excited in a given region of space by the local electric field, supposedly uniformly over the region. This model has an extensive literature,[4] and we find that for arbitrary time dependence, there are nearly integrable solutions. Our results indicate that most of the production occurs near the Compton wavelength of the lepton. Thus, muons are produced partially inside, and tauons are produced entirely inside the nucleus.

The lepton pair production cross section predicted by the Weizsäcker-Williams method is given by

$$\sigma_W = 2\pi \int_{2m_\ell c^2}^{\gamma m_\ell c^2} \frac{d\omega}{\omega} \int_{\lambda\!\!\!^{-}}^{\infty} b\,db\, F(b,\omega) \left(\frac{S(b,\omega)}{h^2}\right) \qquad (1)$$

where F is the flux of virtual photons and S is the cross section for photon-induced pair production. The integral requires a cutoff at small values of the impact parameter, usually taken as the Compton wavelength, $b = \lambda\!\!\!^{-}$. In the high-energy limit, σ_W scales with lepton mass, m_ℓ, with the charges, Z_1, Z_2, and with the bombarding energy per nucleon, γ-1,

$$\sigma_W \sim \left(\frac{Z_1 Z_2}{m_\ell}\right)^2 \ln^3(\gamma) \qquad (2)$$

Equation (2) is incorrect in the high-energy limit, since it violates the Froissart limits for cross sections,[10]

$$\sigma < \sigma_0 \ln^2(\gamma)$$

The nonperturbative model has associated with it a dimensionless parameter, κ, which, in simple systems, behaves as the expansion parameter for pair production via time-dependent perturbation theory.[6]

$$\kappa = (\omega/m_\ell)\, E/E_0. \tag{3}$$

In (3) E_0 is the critical field for a lepton of mass m_ℓ,

$$E_0 = m_i^2/e,$$

and ω is the frequency of the interacting field of strength E. We have evaluated κ for collisions of U+U at the AGS and at RHIC, and we find that $\kappa >> 1$ for muon production at the AGS and tauon production at RHIC. This suggests that perturbative methods of calculation are probably not applicable.

In the nonperturbative method, the effective Lagrangian coupling leptons of mass m_ℓ to an external classical electromagnetic field, A^μ, is

$$\mathscr{L}(x) = \overline{\psi}(x)\left[\gamma_\mu(i\partial^\mu - A^\mu) - m_\ell\right]\psi(x) \tag{4}$$

Note that this Lagrangian separately conserves electron, muon, and tauon number. For our purposes here, we assume that A^μ is completely specified by the classical motion of the heavy ions. For each species of lepton, a semi-classical action is defined by

$$\mathscr{S} = \int d^4x \; \langle 0(t) \,|\, : \mathscr{L}(x) : \,|\, 0(t)\rangle \tag{5}$$

where $|\, 0(t)\rangle$ denotes the many lepton-antilepton state which evolves from the vacuum. The normal ordering is taken with respect to the vacuum. The parameters labeling this state constitute dynamical coordinates which are varied to make the action stationary. This procedure yields a set of time-dependent single-particle equations,[5-8]

$$\left[(\vec{\alpha}\cdot(\vec{p}-\vec{A}) + \beta m + A_0) - i\partial_t\right] |\, \psi_\lambda^{(s)}(t)\rangle = 0 \tag{6}$$

the label $s = (+,-)$ denotes states which evolve from single lepton or single antilepton states, and λ denotes all of the other necessary quantum numbers. The solution to (6) for particular field configurations yields the inclusive number of negatively charged leptons as

$$N_s = \sum_{\lambda,\,\mu} \left| \langle \psi_\lambda^{(+)}(-\infty) \,|\, \psi_\mu^{(-)}(+\infty)\rangle \right|^2. \tag{7}$$

The summation is over indices which cover all available positive- and negative-energy single-particle states. The emission of pairs of leptons from the projectile and target nuclei is incoherent, in part due to the classical motion of the heavy ions, and in part due to the intrinsic time delay for the

emission. Thus, we work in a frame at rest in the target nucleus, and only consider the time-varying fields from the projectile. In this frame, the total inclusive singles cross section can be written as

$$\sigma_S = 2\pi \int_0^\infty bdb \; [2\, N_S(b)], \tag{8}$$

where the states in (7) are restricted to those of the target atom, and where we shall only consider symmetric projectile and target combinations. The above equations are evaluated using a local equivalent field approximation which is discussed in Ref. 8. The results of calculations for colliding beams of U+U, (solid curves), and Kr+Kr, (dashed curves) are shown in Fig. 1 for e^-, μ^-, and τ^- total cross sections. The dot-dashed curve is the e-pair uranium-induced cross section evaluated using the Weizsäcker-Williams formula, (1), which is included for comparision purposes. There are several noteworthy features in Fig. 1. At low energies the e-pair cross section is approximately the same as the Weizsäcker-Williams result. However, at energies per nucleon of about 100 GeV, these differ by about a factor of 100. This difference is principally due to the unphysical $\ell n^3(\gamma)$ energy scaling of the perturbative method.

In contrast, the results for muons and tauons are dominated by the finite size of the nucleus, for which reason the Weizsäcker-Williams formula as usually quoted is completely invalid. Note that the mu and tau cross sections increase with energy as $\ell n(\gamma)$, and at 100 GeV are, respectively, 100 and 10 mb. The dashed curves display the cross section as a function of bombarding energy for collisions of Kr+Kr and show qualitatively similar features as those of U+U.

In Fig 2 the cross section is shown as a function of the lepton mass at a bombarding energy of 100 GeV per nucleon in U+U. This figure illustrates the effects of a number of assumptions: In (a) both the positive- and negative-energy continuum states of the target are assumed to be plane waves, in effect assuming a coherent field over the entire nucleus. This result is clearly unphysical and is included for illustration. In (b), Coulomb distortion factors are included and averaged over the nuclear volume, in effect assuming that the field is coherent over distances the size of nucleons. In (c), these factors are treated without any averaging, yielding a field which is approximately coherent over distances comparable to the impact parameter. The result (d) is for point nuclear charges with none of the above effects treated, and

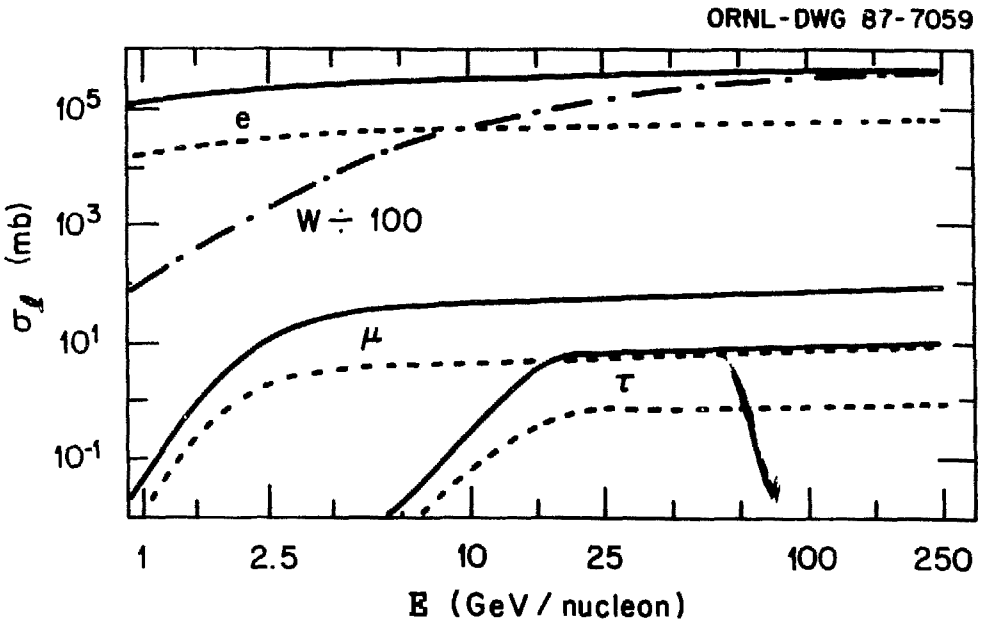

Fig. 1. Total inclusive singles cross sections vs beam energy in a collider computed for electrons, muons, and tauons. Full curves refer to the symmetric collision of uranium, and the dashed curves to the symmetric collisions of krypton. The curve labeled W is the production of electrons from a Weizsäcker-Williams model divided by one hundred.

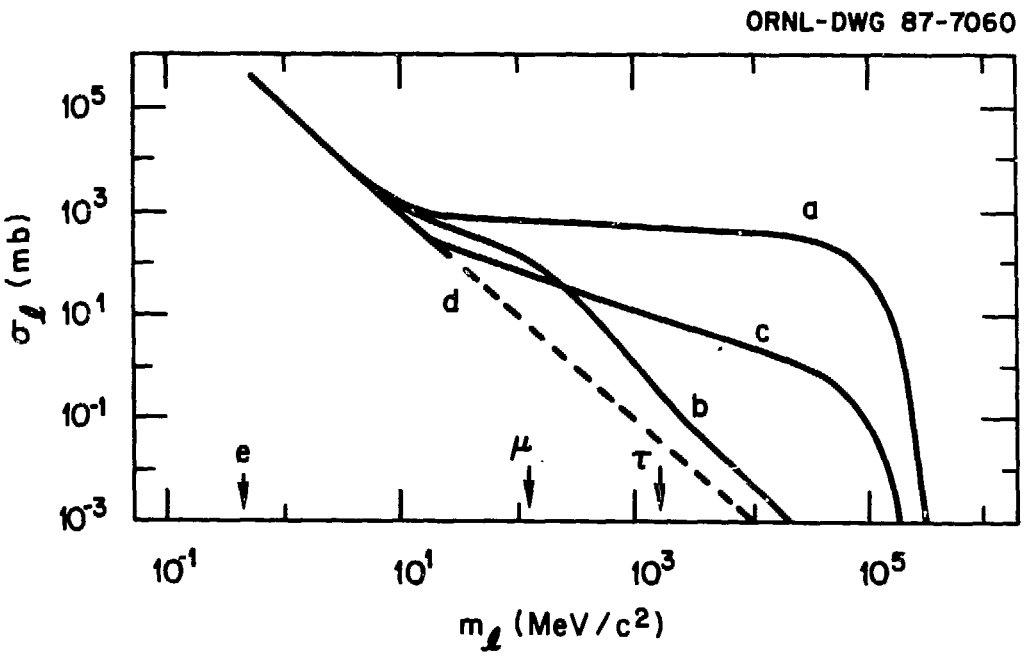

Fig. 2. Total cross section vs lepton mass for collisions of uranium at an energy per nucleon of 100 GeV. A range of assumptions yielding the curves labeled (a)-(d) are described in the text.

this case scales as m_ℓ^{-2}.

The differential cross sections, in terms of transverse momentum and rapidity, can be obtained from (7) and (8) by noting the relations

$$\sigma_s = \int_{-\infty}^{\infty} dY \int_0^{\infty} dP_\perp \frac{d\sigma}{dY dP_\perp} \tag{9}$$

with

$$Y = \frac{1}{2} \ln \left(\frac{P_o + P_\parallel}{P_o - P_\parallel} \right) \tag{10}$$

and where $P = (P_o, \vec{P})$ is the four vector associated with the positive-energy continuum state in (6). The vector $\vec{P}$ is decomposed into parts which are transverse, $\vec{P}_\perp$, and longitudinal, $P_\parallel$, to the beam direction. The transverse part is averaged over the azimuthal angle in order to simplify the computations in (9). The resulting e^- differential cross section is shown in Fig. 3 for the fixed target collision of Au+Au at an energy per nucleon of 4.2 GeV. This is an experiment that could be realized at the AGS. In Fig. 3 are given the contours of the inclusive cross section in (9), as a function of the transverse momentum, $P_\perp$, in units of $m_\ell c$, and of the rapidity. The cross section is given in units of $mb/m_\ell c$, and the contours are labeled by their exponent to the base 10. In this collision, the projectile rapidity is approximately 2.4, as indicated in the figure. Note the sharp side peaking at the projectile and target rapidity, reflecting the transverse character of the fields producing the pairs. Also, note that the distribution is a maximum for values of $P_\perp$ near the Compton momentum, $m_\ell c$, and has a broad distribution which decreases by three orders of magnitude as $P_\perp$ increases to about 20 $m_\ell c$.

The total inclusive pair cross section is another invariant which can be easily computed in our model. Since the time-evolved vacuum state is a Slater determinant, the multiplicity at fixed impact parameter for producing a lepton of momentum $\vec{k}$ and an antilepton of momentum $\vec{q}$ is

$$(2\pi)^6 \frac{dN_p}{d^3k d^3q} = \sum_{q<0} \left| \langle \psi_k^{(+)}(-\infty) \mid \psi_q^{(-)}(+\infty) \rangle \right|^2 \sum_{k>0} \left| \psi_k^{(+)}(-\infty) \mid \psi_q^{(-)}(+\infty) \rangle \right|^2$$

$$+ \left| \sum_{q<0} \langle \psi_k^{(+)}(-\infty) \mid \psi_q^{(-)}(+\infty) \rangle \langle \psi_q^{(-)}(+\infty) \mid \psi_q^{(-)}(-\infty) \rangle \right|^2$$

where again we emphasize that the states $\psi^{(-)}$ are the negative-energy continuum states, and the states $\psi^{(+)}$ are the positive-energy continuum states,

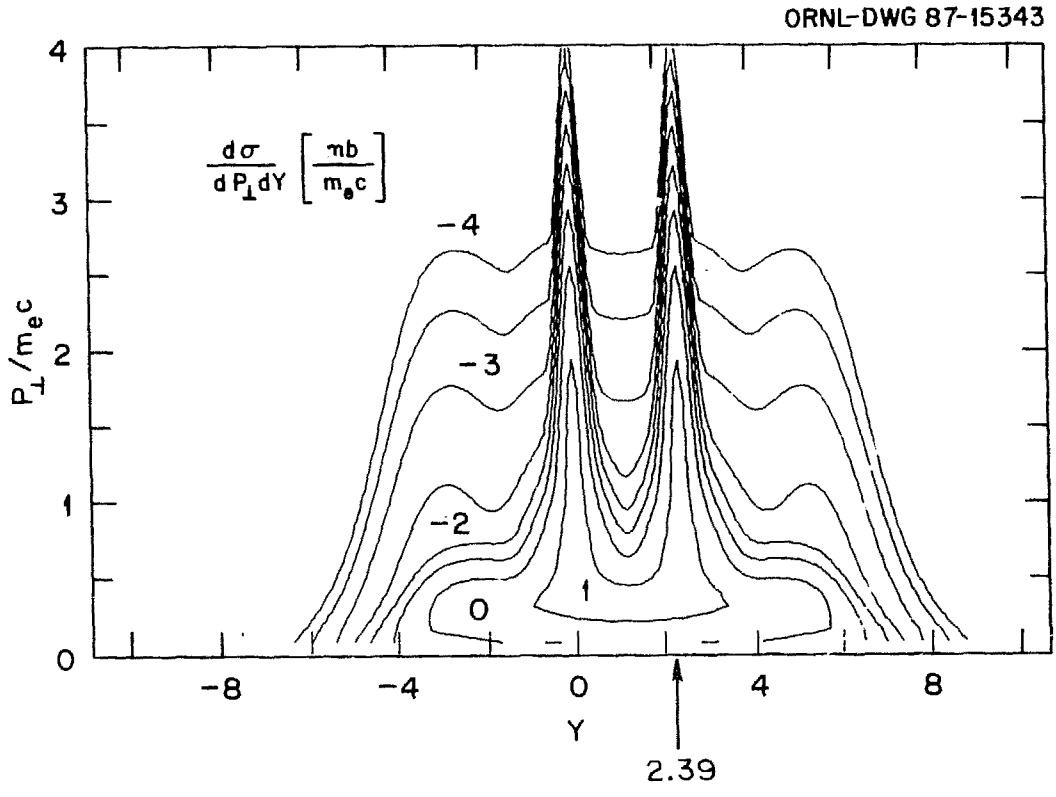

Fig. 3. Contours of the inclusive electron singles production cross section for the fixed target collision of Au+Au at an energy per nucleon of 4.2 GeV as a function of the electron transverse momentum and rapidity. The beam rapidity, 2.39, is indicated by the arrow. Log_{10} of the contour values are included as labels.

and the time labels either the initial states, $t = -\infty$, or the final states, $t = +\infty$. Detailed derivations are given in Refs. 6 and 8. Since $\vec{k}$ and $\vec{q}$ label single-particle momentum of the pair, it is straightforward to transform (11) and obtain the dependency on the total four momentum of the pair,

$$P = (k+q)$$

the invariant mass,

$$M^2 = [P_o{}^2 - \vec{P}^2]$$

and the total rapidity of the pair,

$$Y = \frac{1}{2} \ell n \left(\frac{P_o + P_{\parallel}}{P_o - P_{\parallel}} \right)$$

Again we note that these results are obtained in Ref. 8 and will not be discussed here. The contours of the e-pair cross section as a function of the total transverse momentum of the pair, and of the total rapidity of the pair are shown in Fig. 4 for the Au+Au collision discussed in Fig. 3. Note that the pair distribution is much broader in comparison to the singles distribution shown in Fig. 3. This is, in part, due to the correlations arising from the second term in (11). The pair cross section as a function of the rapidity and the invariant mass for the same collision is given in Fig. 5. Here we clearly see that most of the cross section comes from invariant masses which can be as large as 2×10^3 lepton masses. This is also shown in Fig. 6, again for the same Au+Au collision, however, as a function of the transverse momentum and the invariant mass. In this collision, the total pair cross section is $\sigma_p \sim 116$ b.

Returning to the singles cross section in Fig. 3, the same features are apparent in Au+Au collisions at 100 GeV, as shown in Fig. 7. However, the transverse momentum and rapidity distribution is very broad in rapidity, reflecting the extreme violence of the collision. Note that the cross section still has a maximum for $P_{\perp}$ near the Compton momentum and decreases by about three orders of magnitude at about $P_{\perp} \sim 20\ m_{\ell}c$. In this particular case, the beam rapidities are ± 5.4, and the total singles cross section yield is about 1260 b.

We have also studied these distributions for the production of muons and tauons, reaching the following conclusions:

i) The production of heavy leptons occurs mainly within the interior of

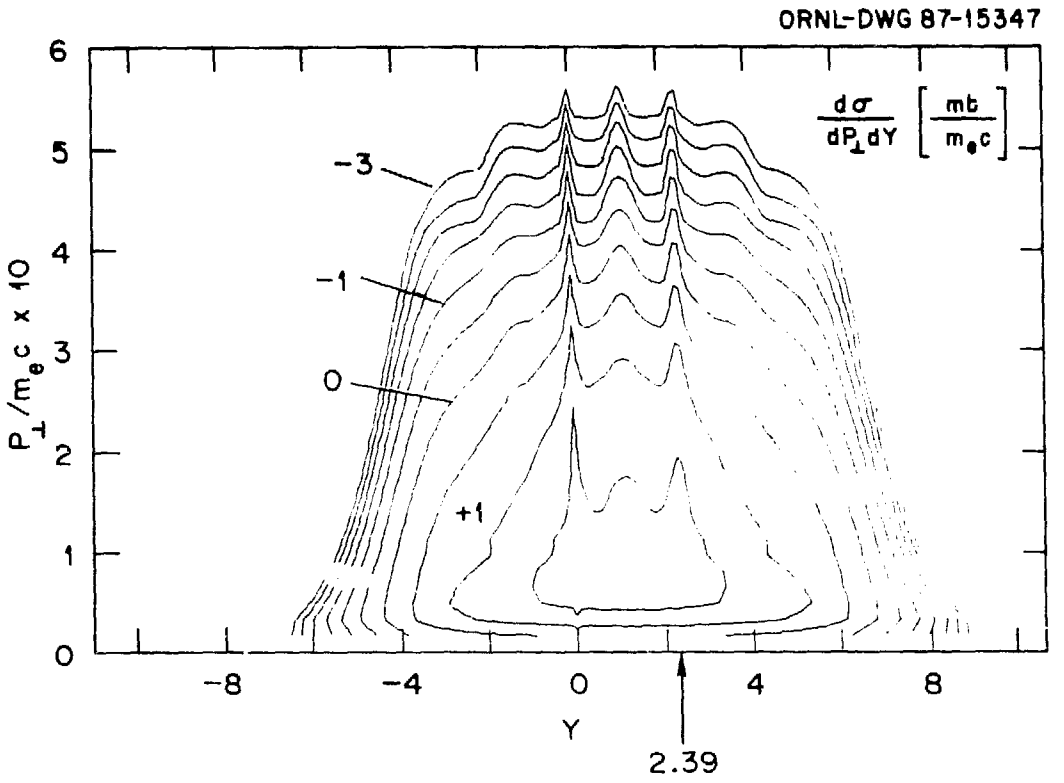

Fig. 4. Contours of the inclusive electron pair production cross section for the collision in Fig. 3 as a function of the total transverse momentum of the pair and the total rapidity. The beam rapidity, 2.39, is indicated by the arrow. Log_{10} of the contour values are included as labels.

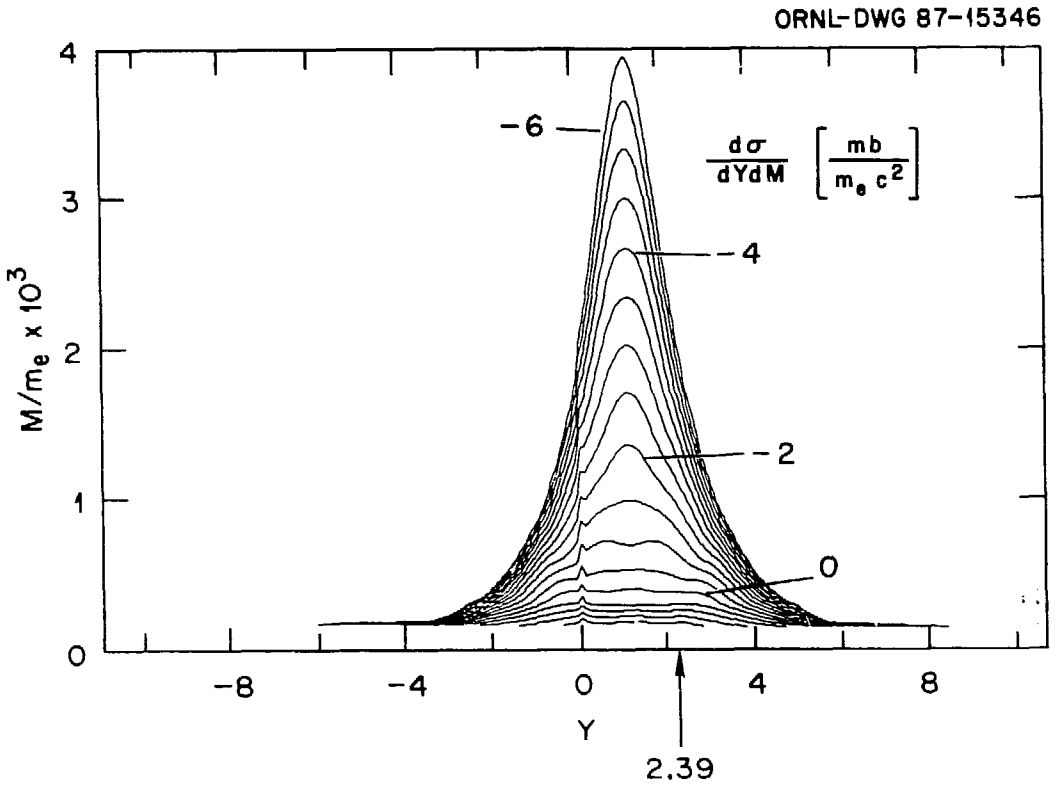

Fig. 5. Contours of the inclusive electron pair production cross section for the collision in Fig. 3 as a function of the invariant mass of the pair and the total rapidity. The beam rapidity, 2.39, is indicated by the arrow. Log_{10} of the contour values are included as labels.

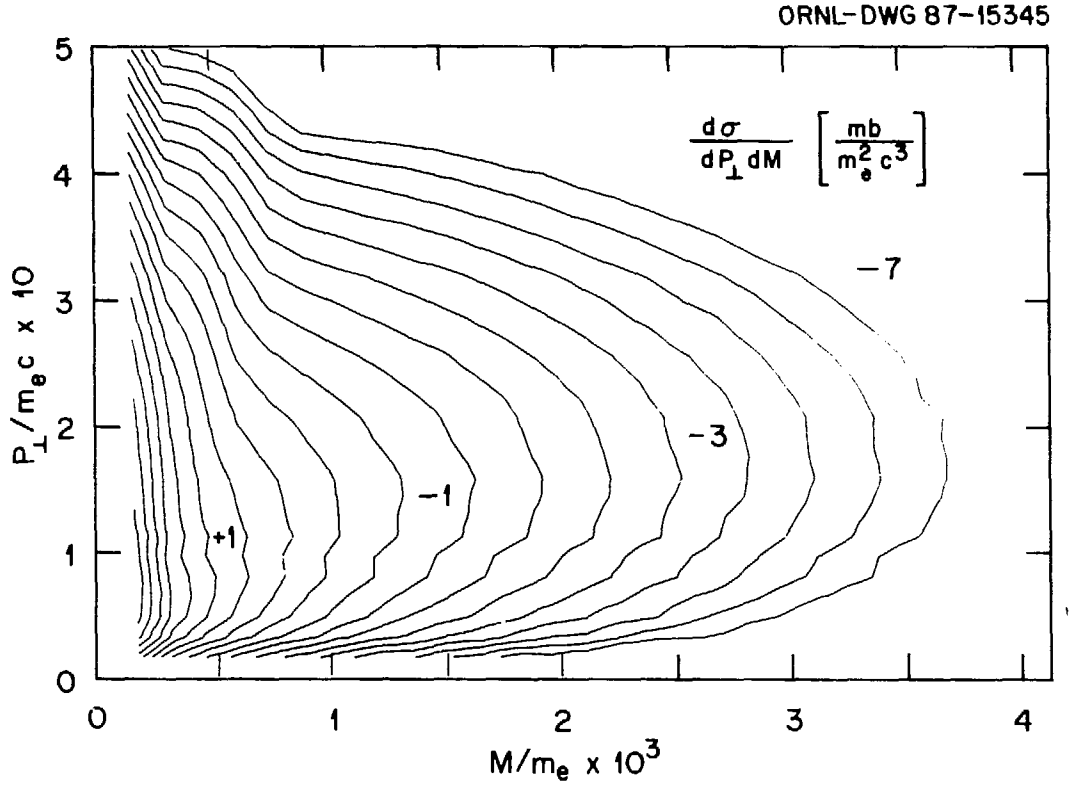

Fig. 6. Contours of the inclusive electron pair production cross section for the collision in Fig. 3 as a function of the total transverse momentum of the pair and the invariant mass. Log_{10} of the contour values are included as labels.

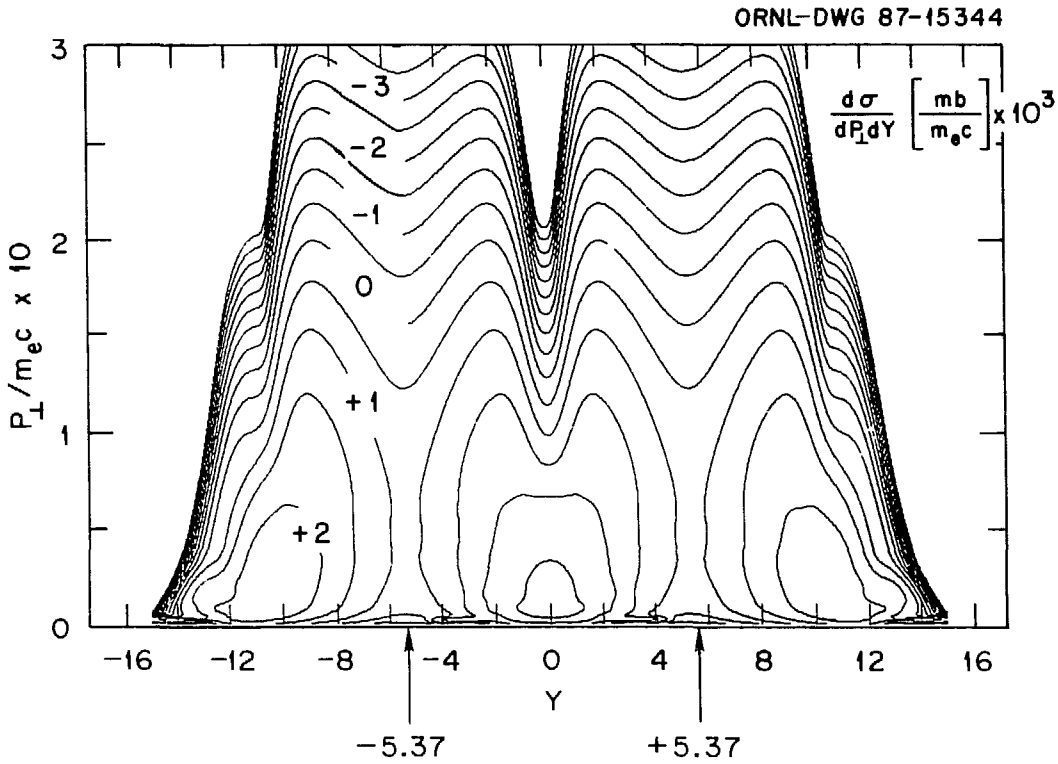

Fig. 7. Contours of the inclusive electron singles production cross section for the collision of Au+Au at a collider energy per nucleon of 100 GeV as a function of the electron transverse momentum and rapidity. The beam rapidities, ±5.37, are indicated by the arrows. Log_{10} of the contour values are included as labels.

the nuclei, and is sensitive to details of the nuclear charge distribution. Because of the relatively small Compton sizes of the mu and tau, it is probably important to give the nuclear charge form factor in terms of the quark distributions in the nucleus.

ii) The cross section yields for muons and tauons are large compared to those predicted by the Weizsäcker-Williams process, due to the coherence developed during the time evolution in the interior of the nucleus. The differential cross sections are strongly peaked at the projectile and target rapidity and have a spread in the transverse momentum variable on the order of the Compton momentum of the produced lepton.

In conclusion, we should like to emphasize that other particles should readily be produced by this mechanism, including the J/ψ and W-pairs, and possibly even magnetic monopoles.[11] There is some evidence that central collisions of heavy ions in this energy range will undergo tremendous deceleration forces. If this is the case, then the production of leptons as we have discussed will be substantially enhanced.

References

1. H. Gould, in "Proceedings of the Atomic Theory Workshop on Relativistic and QED Effects in Heavy Atoms", Gaithersburg, Maryland, May 1985, AIP Conf. Proc. No. 136, American Institute of Physics, New York, 1985.

2. G. Soff, Thesis, University of Frankfurt, 1976, unpublished.

3. K. Kajantie, J. Kapusta, L. McLerran, and A. Mekjian, Phys. Rev. D 34, 2746 (1986).

4. "Quantum Electrodynamics of Strong Fields", ed. W. Greiner, Plenum Press, New York 1983.

5. C. Bottcher and M. R. Strayer, Phys. Rev. Lett 54, 669 (1985).

6. C. Bottcher and M. R. Strayer, Ann. Phys. 175, 64 (1987).

7. C. Bottcher and M. R. Strayer, in "Proceedings of the NATO International Advanced Course on Physics of Strong Fields", ed. W. Greiner, Plenum Press, New York 1987.

8. C. Bottcher and M. R. Strayer, in preparation.

9. V. N. Bair, V. M. Katkov, and V. M. Strakhovenko, Nucl. Inst. and Meth. B16, 5 (1986).

10. A. K. Kerman, private communication.

11. E. Teller, in "Proceedings of the Ninth International Conference on the Application of Accelerators in Research and Industry", ed. J. L. Duggan, North-Holland, Amsterdam, 1986.

AN EVENT GENERATOR FOR ULTRARELATIVISTIC PROTON PROTON COLLISIONS: A MULTISTRING MODEL

K. Werner
Brookhaven National Laboratory
Upton NY 11973

We present a multistring model for low p_t proton proton collisions. The process is divided into two independent steps: formation of color strings and subsequent fragmentation of strings. We take into account diffractive and nondiffractive contributions, each contribution consisting with a certain probability w_i of $2i$ strings. The $i>1$ contributions correspond to "multi-Pomeron exchange."

One of the major problems in ultrarelativistic heavy ion physics is the question of how to detect a phase transition into a quark gluon plasma (QGP) phase if such a transition occurs. Also, the transition is not expected to represent the average event; most probably the majority of all events is of "normal", uncollective nature, whereas transition events require large fluctuations. In order to disentangle normal and QGP events a profound understanding of the "normal" behavior is necessary.

As a first step toward this direction we investigate low p_t proton proton collisions between few and 540 GeV cm energy. We present a model consisting of formation and subsequent fragmentation of color strings. The calculations are carried out on event generator basis. The fragmentation of strings is compatible with deep inelastic lepton scattering and e^+e^- results.

The model is based on an extension[2] of the dual parton model (DPM) of Capella et al[1]. Unlike other event generators based on DPM[3,4,5] our model provides in a limited energy range a unified description of e^+e^-, νp, $\bar{\nu}p$, μp as well as nondiffractive and diffractive pp scattering (see ref. 6). The fragmentation is treated differently making use of the quark counting rules as elementary input. Other event generators like HILUND[7] and ISAJET[8] are less predictive concerning the formation of strings.

Color exchange is assumed to cause the formation of color strings: i exchanges of color between quarks of the projectile and target proton result in $2i$ strings. The relative weight of i color exchanges is named w_i, thus cross sections can be written as

$$\sigma = \sum_{i=1}^{\infty} w_i \sigma_i \,, \tag{1}$$

This work has been supported by the U. S. Department of Energy under contract no. DE-AC02-76CH00016.

σ_i being the contribution consisting of $2i$ strings.

We first describe the dominant $i = 1$ contribution, i.e. the formation of two strings. Color exchange between a quark of the projectile and a quark of the target rearranges the color structure of the pp system; instead of two protons in singlet states we find two singlets each consisting of a diquark and a quark of the other nucleon (see fig. 1(a)). We explicitly treat the case in which one (or both) of the quarks participating in the color exchange is accompanied by an antiquark such that the $q\bar{q}$ pair is color neutral, because in this case the diquark quark (qq–q) string is replaced by an q–$\bar{q}$ string and a baryon. In figs. 1(b,c,d) we show this for the case when the projectile quark (b), the target quark (c), or both quarks (d) are part of colorless $q\bar{q}$ pairs. We generate quarks with and without $\bar{q}$ partners with probabilities w and $1-w$, so the relative weights of the contributions 1(a,b,c,d) can be expressed in terms of the parameter w (in a complicated way because certain events have to be discarded as unphysical). So far we treat neither color exchange between antiquarks nor color exchange between gluons. Gluons are only spectators, in the sense that diquarks are implicitly assumed to be "dressed", i.e. to contain gluons.

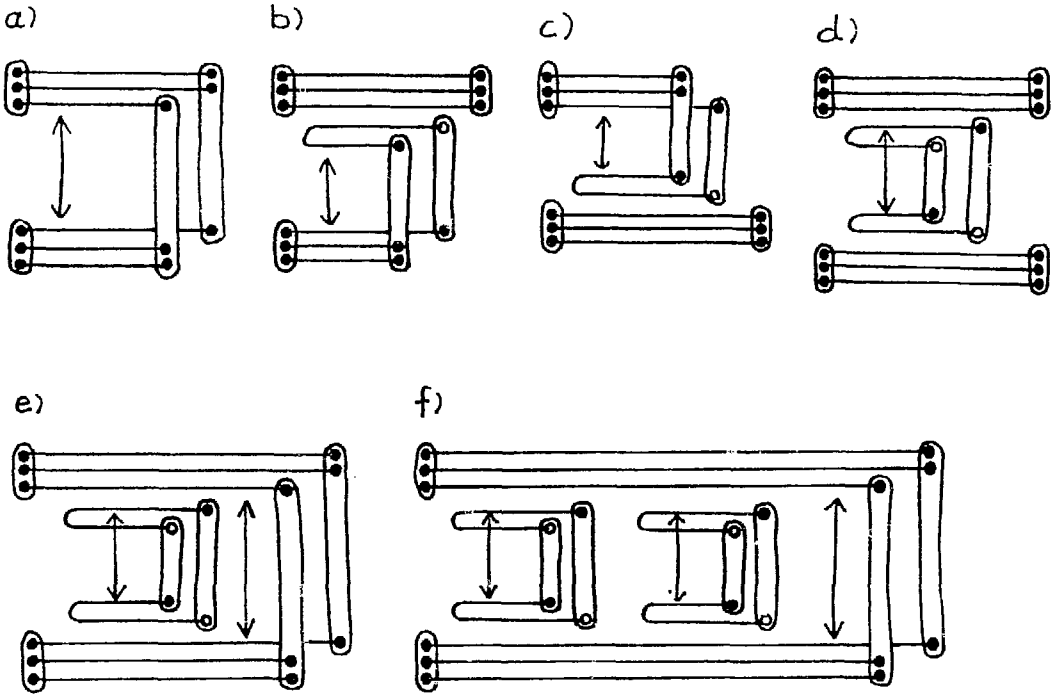

Figure 1

Looking at figures 1(a) and 1'd) indicates already a possible generalization: the color exchange between quarks being part of white $q\bar{q}$ pairs 1(d) may occur in addition to the nondiffractive color exchange of fig. 1(a) leading to the $i = 2$ (2 color exchanges)

contribution with $2i = 4$ strings shown in fig. 1(e). Two color exchanges of the type 1(d) in addition to the exchange of type 1(a) leads to a $i = 3$ contribution with six strings (see fig. 1(f)) and so on. The same generalizations apply to the contributions 1(b), 1(c) and 1(d). This expansion in terms of the number of color exchanges (i.e. in terms of the number of strings) corresponds to the multi-Pomeron exchange picture of Abramovskii, Kancheli and Gribov[9] and is also used by other authors (ref. 4 and references therein).

How do we determine energy and momentum (and so the mass) of a string? We want to choose a frame in which both protons are fast and moving in opposite directions, so we take the pp cm system. According to the quark parton model, the longitudinal momentum distribution of a parton i in a fast-moving proton is given as $q_i\left(Q^2, x\right)$, where x is the longitudinal momentum fraction of the parton and Q^2 the momentum transfer involved in the process measuring q_i. These parton distribution functions (or structure functions) $q_i\left(Q^2, x\right)$ have been parametrized analysing lepton scattering data[10]. We generate flavor and momenta of the quarks involved in the color exchange and of the antiquarks according to these structure functions. The distribution functions q_i also determine the relative weight of valence and sea quarks; yet, in the case of a quark accompanied by an antiquark, we always assume the quark to be a sea quark and the pair to be flavor white (some further study of $pp \to nX$, for example, is necessary to justify or reject this last assumption). By momentum conservation, the momentum of a diquark is $1 - x$ when the quark has momentum fraction x. For reasons discussed in ref. 6 we take x to be the energy rather than the momentum fraction, which amounts to the same for large x.

What about transverse momenta? Since the partons are confined to the proton size R, the uncertainty principle requires a finite transverse momentum:

$$< p_t > \approx \frac{1}{R} . \tag{2}$$

We generate transverse momenta for the quarks according to the exponential distribution

$$f\left(\vec{p}_t\right) = \frac{2}{\pi < p_t >^2} e^{-2p_t/<p_t>} . \tag{3}$$

To preserve momentum the diquark corresponding to a quark with momentum $\vec{p}_t$ assumes a transvere momentum of $-\vec{p}_t$. The strings are now fully determined, since we assume the string constituents (quarks, antiquarks, and diquarks) to be massless.

In the following we describe how strings formed according to the above fragment. In fact, it is more general if one assumes that string fragmentation depends only on the parton content and the energy-momentum of the string, and not on the way it has been formed. In fact, the weak Q^2 dependence compared to the W^2 dependence (W = energy of all produced particles) observed in muon proton scattering[11] supports this assumption, and

therefore we are going to use exactly the same fragmentation procedure which has proven successful already for e^+e^-, νp, $\bar{\nu}p$, and μp scattering[6]. We describe the fragmentation in the frame where the total string momentum vanishes (string cm), and also the p_t of the string constituents, so in general we have to make a Lorentz boost and a rotation. We use the independent fragmentation scheme of Field and Feynman[12], i.e. the string constituents (jets) fragment independently of each other. The fragmentation cascade is iteratively defined by elementary vertices: a jet $(q, \bar{q}, qq, \overline{qq})$ produces a primary hadron, leaving a new jet particle with reduced momentum. Figure 2 shows the vertices we take into account: (a) a quark jet producing a meson, leaving a quark jet; (b) a quark jet producing a baryon, leaving an antidiquark jet; (c) a diquark jet producing a meson, leaving a diquark jet; and (d) a diquark jet producing a baryon, leaving an antiquark jet (vertices for antiquark and antidiquark jets are obtained by exchanging quarks and antiquarks).

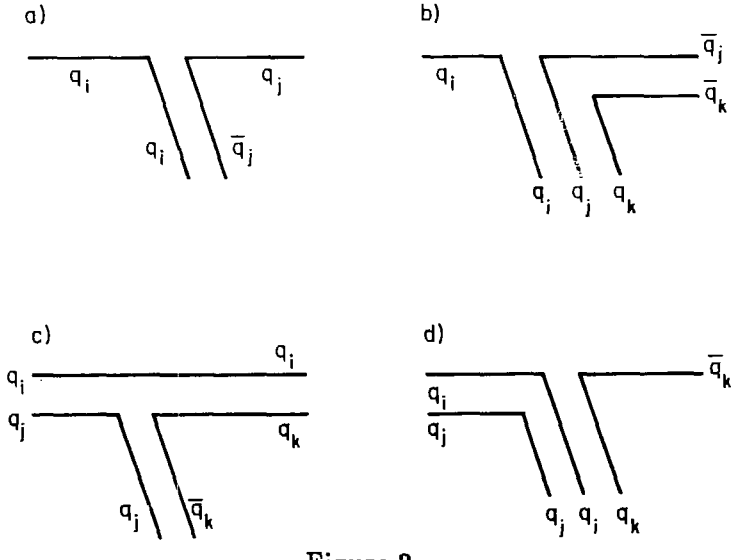

Figure 2

The energy of a primary hadron relative to the energy of the corresponding jet is generated according to so-called splitting functions $f_q^m(x)$, $f_q^b(x)$, $f_{qq}^m(x)$, and $f_{qq}^b(x)$ for the four vertices of fig. 2. For reasons explained in ref. 6 we use (up to normalization factors)

$$\begin{aligned} f_q^m(x) &= (1-x) \\ f_q^b(x) &= x^\alpha (1-x)^3 \\ f_{qq}^m(x) &= (1-x)^3 \\ f_{qq}^b(x) &= x^\alpha (1-x) \,. \end{aligned} \tag{4}$$

We discussed earlier the necessity of finite $< p_t >$ for partons in nucleons. For similar reasons, the production of $q\bar{q}$ pairs as part of the fragmentation process should require a finite $< p_t >$ for both q and $\bar{q}$. So we generate a transverse momentum $\vec{p}_t$ for the quark according to the same exponential distribution in eq. 3, using the same parameter $< p_t >$ (which is certainly not necessary, but both $< p_t >$ should be of the same order). The antiquark assumes $-\vec{p}_t$.

The jet fragmentation cascade is terminated when the jet energy is too small to produce further particles. In order to achieve flavor conservation (and thus baryon number conservation) we combine the two remaining partons of two corresponding jets to make a primary hadron.

All the parameters determining the fragmentations are fixed by comparing with e^+e^- and deep inelastic scattering data[6]. The momentum transfer Q^2 entering the structure function is taken to be $Q^2 = 4\text{GeV}^2$. The probability w, that in a pp collision an interacting quark is accompanied by an antiquark, is fixed such that the fraction of events involving one such $q\bar{q}$ pair matched the ratio $\sigma_{\text{diffr}}/\sigma_{\text{inel}}$, which has, over a wide energy range, the value 0.2[13]. This prescription is explained in ref. 2. For the mean transverse momentum $< p_t >$ of quarks in the proton, we use $< p_t >= 0.5$ GeV. The multicolor exchange probability w_i entering eq. 1 provides in principle an infinite number of parameters. On the other hand, the results we will discuss in this paper are rather insensitive to higher than the first moment of w_i, and this first moment

$$< i >= \sum i w_i \tag{5}$$

is fixed to give correct mean multiplicities. In the actual calculations we use an exponential distribution

$$w_i = \frac{1}{< i >} \left(\frac{< i > -1}{< i >} \right)^{i-1} . \tag{6}$$

(Using a Poisson distribution instead of (6) leads to quite similar results.) It is obvious from this discussion of parameters that pp collisions are essentially (with very few additional parameters) expressed in terms of string fragmentation.

In the following, we compare Monte Carlo results with data. In all plots we use the following convention: open dots are data, full dots are Monte Carlo results, lines may be either of them. In fig. 3 we display the rapidity (y) distribution of negative particles and of charged particles, integrated over p_t (data from ref. 18). Figure 4 shows transverse momentum distributions of pions in the central region ($y=0$) and in the projectile fragmentation region ($x = 0.3$) (The latter distribution is normalized to one.). The steeper central distribution reflects the fact that the small energy of particles in the central region

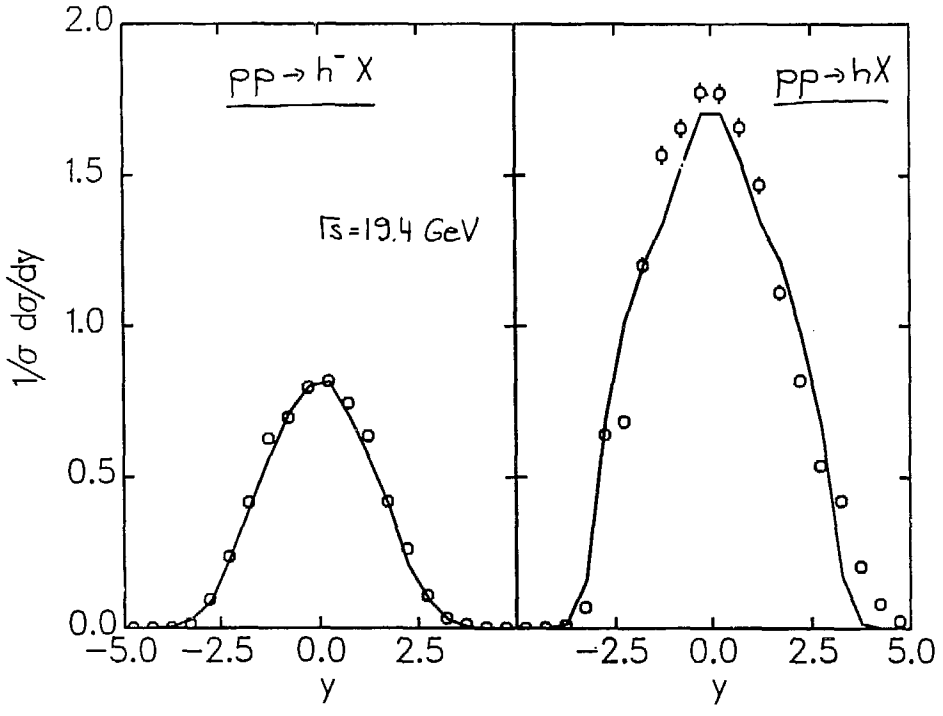

Figure 3

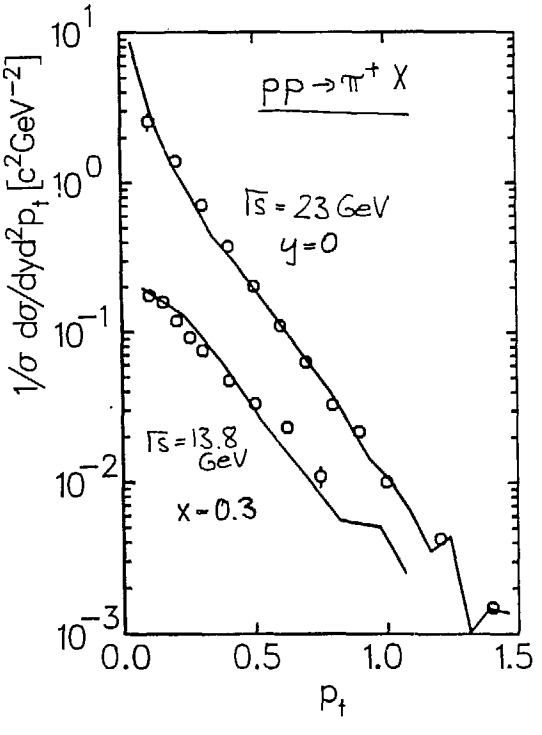

Figure 4

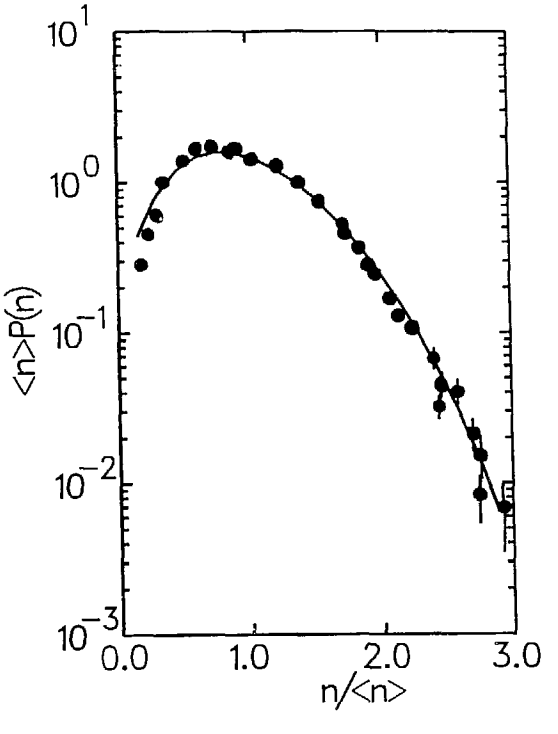

Figure 5

requires also small p_t. The data are from refs. 16 and 17. In fig. 5 finally we plot multiplicity distributions. It is known for many years already that multiplicity distributions $P(n)$ for pp collisions in a wide energy range scale, i.e.

$$< n > P(n) = \Psi\left(\frac{n}{< n >}\right)$$

with a universal energy independent function Ψ. The curve in fig. 5 represents the parametrization of Ψ according to ref. 15. The Monte Carlo results for pp collisions with cm energies of 14, 23, and 53 GeV are very close to the experimental curve. Scaling behavior means that with increasing energy the width exceeds more and more the width of a Poisson distribution with the same $< n >$. There are two reasons for such a behavior: (1) the distribution w_i gets wider with increasing energy ($< i >$ increases) leading to larger multiplicity fluctuations and (2) with increasing energies the effective cutoff for structure functions (due to a necessary cutoff for string masses) decreases as s^{-1}. Consequently, because of the x^{-1} divergence of the structure functions, sea quarks dominate more and more over valence quarks with increasing energy. This also leads to increasing multiplicity fluctuations because strings with sea quarks involved show larger fluctuations than strings which contain valence quarks.

We presented a model for soft pp collisions based on independent string formation and string fragmentation. Diffractive and nondiffractive processes contribute, each contribution containing at least two strings, yet with a certain probability w_i also $2(i-1)$ additional $q\bar{q}$ strings. Rapidity, transverse momentum, and multiplicity distributions can be reproduced quite well for pp collisions at ISR energies.

I acknowledge helpful discussions with F. E. Paige, S. H. Kahana, and A. M. Matheson.

REFERENCES

1. A. Capella and J. Tran Thanh Van, Z. Phys. C10, 249 (1981).
2. K. Werner and M. Kutschera, Phys. Lett. 183B, 385 (1987).
3. J. Ranft and S. Ritter, Z. Phys. C27, 413 (1985).
4. P. Aurenche, F. W. Bopp, and J. Ranft, Z. Phys. C23, 67 (1984).
5. J. P. Pansart, Preprint DPhPE 86-06 (1986).
6. K. Werner, BNL 39726, submitted to Phys. Lett. B.
7. B. Erlandson, preprint HELIOS note 164 (1986).
8. F. E. Paige and S. D. Protopopescu, BNL 38034 (1986).

9. V. A. Abramovskii, O. V. Kancheli, and V. N. Gribov, in XVI International Conf. on High Energy Physics, Batavia IL, 1973, Vol. 1, p. 389.
10. D. W. Duke and J. F. Owens, Phys. Rev. D30, 49 (1984).
11. EMC. M. Arneodo et al, Z. Phys. C31, 1 (1986).
12. R. D. Field and R. P. Feynman, Nucl. Phys. B136, 1 (1978).
13. A. Wroblewski, Proc. of the 14th International Symposium on Multiparticle Dynamics, Granlibakken, 1983, eds. P. Yager and J. F. Gunion, World Scientific Publ. Co.
14. Z. Koba, N. B. Nielsen, P. Olesen, Nucl. Phys. B40, 317 (1970).
15. P. Slattery, Phys. Rev. Lett. 29, 1624 (1972).
16. A. E. Brenner et al, Phys. Rev. D26, 1497 (1982).
17. B. Alper et al, Nucl. Phys. B100, 237 (1975).
18. C. De Marzo et al, Phys. Rev. D26, 1019 (1982).

A SIMPLE MODEL FOR HEAVY ION COLLISIONS

Hans Bøggild
The Niels Bohr Institute

In this note I want to describe briefly a simple model for heavy ion collisions developed by A.D.Jackson and myself[1], based on an approach by G.Baym et al[2]. The model is essentially geometrical describing the collision between two nuclei as the interaction between two extended objects (consisting of protons and neutrons), having the impact parameter as the main parameter. At a given value of b the calculation of the overlap of the two colliding objects leads to a certain expected mean number of independent nucleon-nucleon interactions each producing a certain multiplicity, E_T etc. The actual number of collisions is assumed to be Poisson distributed around the mean. The nucleon-nucleon collision physics is assumed to be known and is essentially treated as a "black box".

In the simple version of the model described in ref.1, where E_T distributions are discussed, the only parameter is ϵ_0, the mean E_T per pp-collision at a given c.m.s. energy and for a given rapidity interval. For several reasons the value of ϵ_0 is usually different from the corresponding value in real pp collisions, the most important reason being the so-called "energy degradation", i.e. the loss of energy of the nucleon (or excited nucleon) as it penetrates the nucleus making a number of successive collisions. This will be discussed later. Another effect is rescattering, i.e. interactions of secondary particles (not the leading baryon system) before leaving the nucleus. Basically the model neglects this assuming that the secondary particles, building up E_T, hadronizes outside the nucleus.

In summary the simplest version of the model describes a heavy ion collision as the superposition of a number of independent nucleon-nucleon collisions, where

a) Each nucleon interacts with all the nucleons it meets on its way through the other nucleus (drills a cylinder).

b) A number of secondary particles are released and leave the nucleus without interacting. In the simple version a distribution of E_T is used in the calculation.

c) The leading baryon or rather baryon system continues ready for new interactions. (Degradation of the interaction energy is described by a change in the mean energy ε_o).

Clearly this model is closely related to other models on the market like e.g. HIJET. However, it has the virtue of having essentially 1-2 parameters and of being in an analytic form.

As an illustration of how the number of pp-interactions depends on the atomic numbers of the two nuclei fig.1 shows the maximum (b=0) number of interactions for different nuclei on gold reaching up to $\sim$1000 for gold on gold (RHIC scenario). Fig.2 illustrates the impact parameter dependence for different relative sizes of the nuclei.

The agreement with data is illustrated, fig.3, by a fit to data from the Helios Collaboration, ref.3, at the CERN SPS, where 60 and 200 GeV/nucleon Oxygen ions are colliding with Tungsten and Silver targets. In this case an extra parameter was introduced to take into account the result of various smearing effects neglected in the simple model; the extra parameter, w , is the variance of the E_T distribution from the individual pp collisions and tends to be somewhat larger than in the simple model. It should be noted that the curves which indeed reproduce the data well are <u>not</u> using the same ε_o and w and thus do not represent a completely consistent description of the data.

<u>Event generator</u>

A Monte Carlo event generator of the model exists, called HIM (Heavy Ion Model). The heart of this model, besides the geometry described previously, is the p-p generator, which attempts to make realistic proton-proton collisions at a given c.m.s. energy. The generator makes pions and protons and is not perfect but fast. A new and improved version which will treat the energy

degradation (see later) will probably soon be available.

Further developments

A new version of the model including the effects of energy degradation is turning out to be quite successful in describing the qualitative features of E_T-spectra for different targets, energies and rapidity ranges, ref.4. In this approach the energy per pp collision is not a parameter but is taken from pp collisions at the relevant energies. The only parameter is the energy degradation factor k , and the model assumes this to be a constant (independent of c.m.s. energy) which turns out to be $\sim$2/3 for the SPS energy range.

Extrapolation to RHIC

Fig.4 shows the prediction for RHIC for Gold on Gold collisions at 200 GeV/n for a central rapidity interval of -1.5 to 1.5. The solid curve shows the result for $\varepsilon_0 = 2/3 \cdot \langle E_T \rangle_{pp}$ at that energy, and the dashed curve is a result of the improved version of the model including energy degradation (k = 2/3).

References

1) A.D.Jackson and H.Bøggild. Nucl Phys A470 (1987), 669

2) G.Baym, P.Braun-Munzinger and V.Ruuskanen.
Phys Lett 190(1987) 29

3) T.Akesson et al.: The Transverse Energy Distribution in ^{16}O-Nucleus Collisions at 60 and 200 GeV/nucleon.
CERN Preprint To be submitted to Z.Phys.C.

4) Work in progress by author.

Figure Captions

Fig 1 Number of pp collisions at b=0 for A-Au collisions.

Fig 2 Number of pp collisions vs impact parameter for $R = (A_1/A_2)^{1/3}$ = 0.1, 0.3, 0.5 and 1.0

Fig 3 Transverse energy distribution for O-W and O-Ag collisions at 200 GeV/nucleon for $-.1 < \eta_{lab} < 2.9$. The curves are described in the text and in more detail in ref.3.

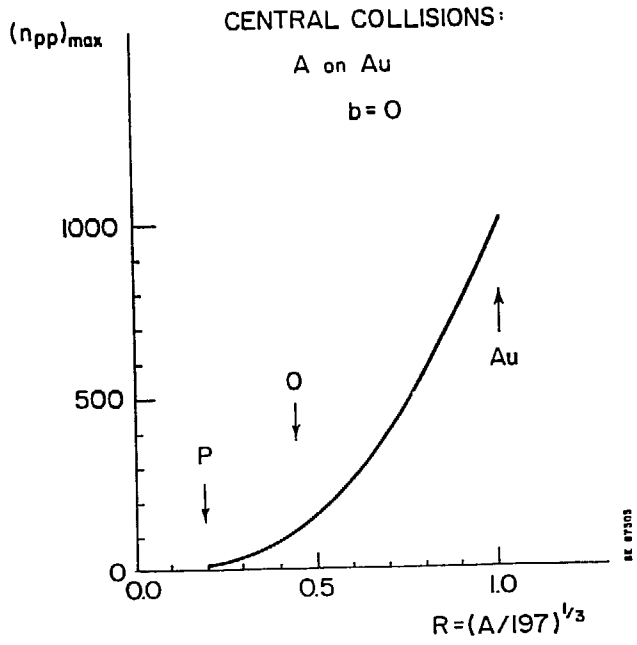
CENTRAL COLLISIONS:
A on Au
b = 0
$(n_{pp})_{max}$
1000
500
0
0.0
0.5
1.0
P
0
Au
$R=(A/197)^{1/3}$

Fig 1

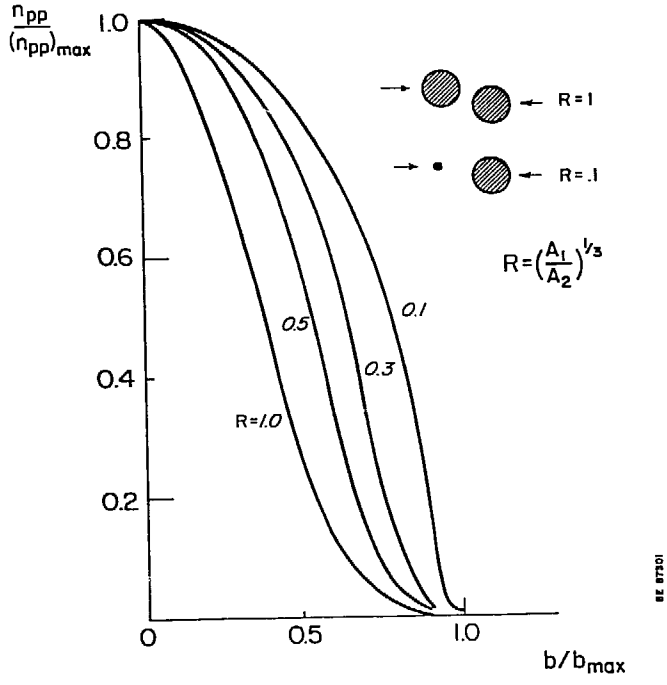
$\frac{n_{pp}}{(n_{pp})_{max}}$
1.0
0.8
0.6
0.4
0.2
0
0.5
1.0
b/b_{max}
R = 1
R = .1
$R=\left(\frac{A_1}{A_2}\right)^{1/3}$
0.1
0.3
0.5
R=1.0

Fig. 2

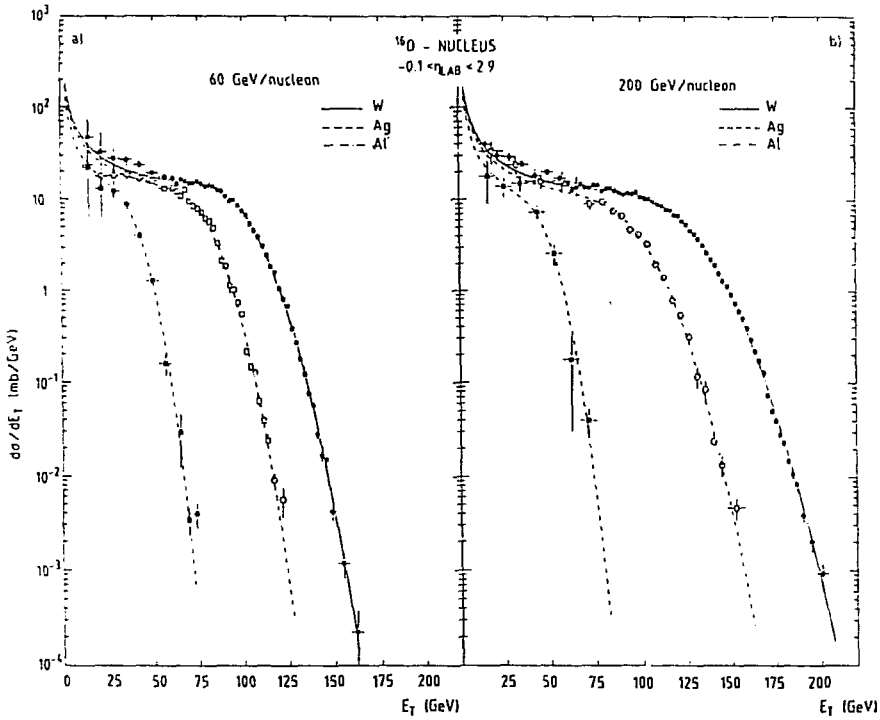
a)
^{16}O - NUCLEUS
$-0.1 < \eta_{LAB} < 2.9$
60 GeV/nucleon
W
Ag
Al
b)
200 GeV/nucleon
W
Ag
Al
$d\sigma/dE_T$ (mb/GeV)
E_T (GeV)
E_T (GeV)

Fig 3

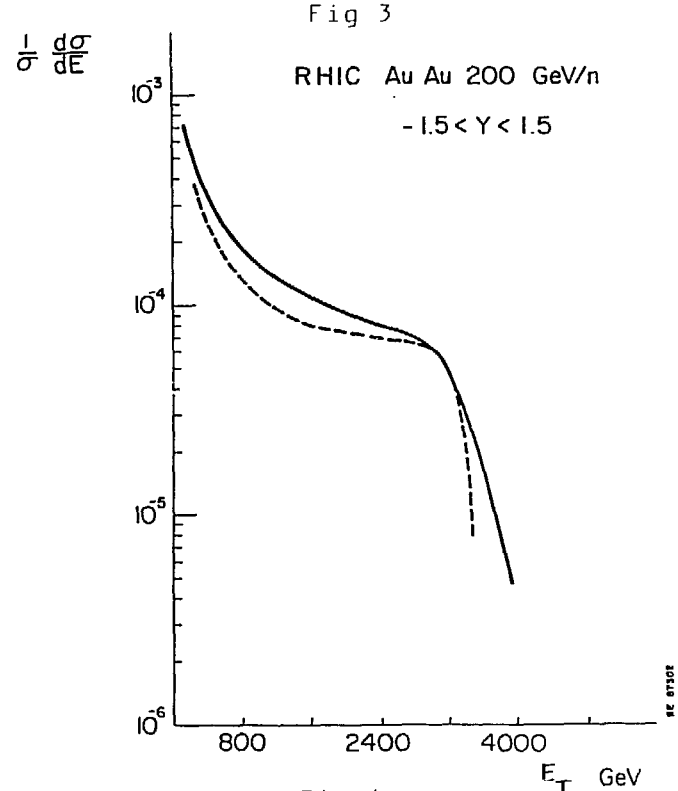
$\frac{1}{\sigma}\frac{d\sigma}{dE}$
RHIC Au Au 200 GeV/n
$-1.5 < Y < 1.5$
10^{-3}
10^{-4}
10^{-5}
10^{-6}
800
2400
4000
E_T GeV

Fig 4

NUCLEAR STOPPING AND ENERGY DEPOSITION INTO THE CENTRAL RAPIDITY REGION

J. A. Zingman*

Lawrence Livermore National Laboratory, Livermore, Ca, 94550

Abstract

Nuclear stopping and energy deposition into the central rapidity region of ultrarelativistic heavy-ion collisions are studied through the application of a model incorporating hydrodynamic baryon flow coupled to a self-consitent field calculated in the flux tube model. Ultrarelativistic heavy ion collisions are modeled in which the nuclei have passed through each other and as a result are charged and heated.

Introduction

The possibility of forming a quark-gluon plasma in the collision of extremely high energy nuclei has recently become a topic of great interest to theorists and experimentalists alike. The generally held theoretical view is that the central rapidity region, the part of phase space near the rapidity of the center of mass,will be the most likely place for the formation of the quark-gluon plasma.[1] In this region, high energy densities are expected with low baryon number since induced by the reaction will deposit energy there. While energies at the CERN and AGS heavy-ion programs are probably too low for this physics to occur, it should be quite important at RHIC energies.

The processes that can lead to the formation of the quark-gluon plasma can be modeled in the following way. Because ultrarelativistic nuclei are extremely Lorentz

*This work was supported in part by the U.S. Department of Energy under Contract No. W-7405-Eng-48.

contracted, the interaction time for these collisions is very short. Thus the nuclei are thought to be nearly transparent to one another. Even on this time scale, however, soft gluon exchanges typical of those in p-p collisions are possible, and will result in the formation of color flux tubes as the nuclei separate. The large number of interactions due to the presence of many nucleons should lead to much larger energy densities than are found in p-p collisions. As the flux tubes elongate, the energy in the tubes increases until pair production occurs, leading to energy deposition in the central region. At the same time, the fragmentation regions are likely to undergo expansion and diffusion of baryon number in phase space, as they dissipate the energy gained from collision processes. Because of conservation of energy, the transfer of energy from the fragmentation regions' initial kinetic and internal energies to the central region must lead to slowing down of the nuclei as well as to the diffusion mentioned above. This change in baryon number distribution through the collision is what we will refer to as nuclear stopping.

We have developed a model which incorporates all this physics in a simple and transparent fashion. In this model, we use the flux-tube model of color interactions to describe the field and its deposition of energy, and relativistic hydrodynamics to handle the motion of the baryonic fluid.[2] We consider only one-dimensional hydrodynamics of the fluid, and hence the fields are taken to be longitudinal. To simplify the calculations, the fields are assumed Abelian as well. This work has been developed along with Tetsuo Matsui and Arthur Kerman of MIT and will be presented in more detail in a forthcoming paper.[3]

Formulation of the model

In the first part of this section, we will describe the ideas underlying our model, and present the model itself. As sketched above, we assume the initial part of ultrarelativistic collisions occurs as the two nuclei pass through each other with nearly complete transparency to baryon number. Thus the initial phase of the collision results in very little baryon number diffusion, and the nucleon distribution immediately following the transit of one nucleus across the other is almost the same as the initial one. However, there are soft gluon interactions during this time, and already some energy must be deposited in the field. We assume that this exchange of energy results in a bulk slowing down of the nuclei.

The energy distribution, however, is quite different now than before the collision.

Before, all the nucleons(or quarks) had an energy distribution that merely resulted from the boosting of a nucleus to the collision frame. Now that the gluonic interactions have deposited energy into the large nuclear bag, the quarks will assume a thermal distribution corresponding to the amount of energy deposited. Hence while the two nuclei are overlapped, they gain color charge and internal energy, and slow down.

We use relativistic hyperbolic coordinates as in Ref. 4,

$$s = \ln\sqrt{t^2 - z^2}/\tau_0$$

$$\eta = \frac{1}{2}\ln\frac{t+z}{t-z} \qquad (1)$$

By considering the center-of-mass frame, one finds that the overlap between the nuclei ends at an event occuring at the proper time $\tau_0 = 2R/\sinh y_{cm}$, where R is the nuclear radius, and y_{cm} is the rapidity of the nuclei in this frame. Our choice of τ_0 is thus significantly different from that used previously, where τ_0 is given by the pion formation time of ~1 fm/c.[4,5] In the center of mass frame, the overlap will end along the z=0 axis and hence the hyperbola of constant proper time will go through later coordinate time for all points along z. In the rest frame of one nucleus, however, since the origin is defined by the event in which the nuclei first make contact, the point of last contact will not occur for z=0, and hence the hyperbola of constant proper time actually passes through earlier coordinate time. Thus by starting our calculation at this proper time, for large rapidity, we are investigating the nuclei soon after one has passed through the other. Also, our assumption that very little has happened before the initiation of the calculation is seen to be justified.

The initial conditions we impose are that very little has taken place other than the charging and heating of the nuclei and the establishment of the color fields. While some studies have suggested that the charging of the fluids is likely to take place in a random walk fashion,[6,7] for simplicity we assume that as the nuclei separate, they are uniformly and oppositely charged. Since we are not modeling the actual charging process, we are not concerned with how such charge separation could be achieved, and take this just as an important assumption. Further studies in more than 1+1 dimensions may be able to relax this somewhat, but we do not feel this is a limitation to the model.

The amount of heating is also an assumption. Here we can use some physical input to determine its nature. First of all, since we are considering symmetric collisions, we expect the amount of energy deposited in each nucleus to be the same. Since the same random walk-type interaction rates are resulting in both the charging and heating of the nuclei, we expect the initial energy distribution to be smooth as well, and we assume it is uniform over the nucleus. From scaling the equations to remove dimensionful quantities, it is seen that what is important in describing the strength of the electric field is the ratio of the square of the initial field energy density to the initial baryonic energy density. This parameter, called γ below, has been varied in our calculations to gauge its effect on the flow of matter, and is important mostly in determining the amount of compression that will occur.

Thus our scenario starts with two charged, heated fluids separating at some rapidity slightly below that with which the nuclei started. Since we are investigating the fragmentation regions as well as the central region, we cannot make one assumption that has often been used in similar studies. We do not assume Bjorken scaling[1] of the central region, and hence all thermodynamic quantities are functions of η as well as s.

We assume that the field is Abelian, and hence its dynamics are controlled by Maxwell's equations. Since we are interested in the effect of pair production, Maxwell's equations are coupled to a current source. Not only that, but since the pair production produces charged particles, the current conservation equation is also coupled to a source. Note that, since no net baryon number is created, the baryon current is conserved, in contrast to Ref. 4. In Ref 5, the baryon current was conserved, but they did not calculate a self-consistent field as we do through the coupling of the field and matter. Note also that their calculation is of the flow of the matter after 1 fm/c, the pion production time, rather than from our initial time of $2R/\sinh y_{cm}$.

This model is called electrohydrodynamics, since it describes the evolution of coupled matter and field, and has been discussed previously in ref. 2. The hydrodynamical part of the equations starts with the ideal stress-energy tensor,

$$T^{\mu\nu} = u^\mu u^\nu(\varepsilon + p) - g^{\mu\nu} p. \qquad (2)$$

Here u^μ=(cosh y, sinh y) is the 4-velocity of the matter, y is the rapidity, ε is the internal energy, g is the metric and p is the pressure. The velocity is also used to calculate the baryon current, $j^\mu_b = u^\mu \rho_b$ where ρ_b is the baryon number density. In general, we will use an ideal gas equation of state, so that $\varepsilon = c_s^2 p$.

The field is described by the Maxwell tensor $F^{\mu\nu}$, whose dynamics are controlled

by the charge current j^μ_c . This current is the source of the new physics in our model. It contains terms for the charge distributions as well as for the charge that is created and interacts with the field. The first term is the ordinary flow of charged matter, given by $j^\mu_t = u^\mu \rho_c$, where ρ_c is the charge density. The second term can be viewed as arising from the polarization of the vacuum by the intense fields generated by the stretching of the tubes. We assume that the pair is created at a single point, and hence there is no charge created in the rest frame of the produced pair. This means that the current specifying the vacuum polarization, j^μ_V, must be space-like as opposed to the time-like flow of ordinary current. The latter must be timelike since there is a frame in which there exists only charge. The charge density must include the produced charge as well and will be seen to decrease when the vacuum polarization is turned on.
The only normalized spacelike vector that can be used for this current is $\sigma^\mu = (\sinh \eta, \cosh \eta)$. The pair production rate can be derived most simply by considering the pair as tunneling through a barrier to enter the vacuum.[8,9] By dimensional arguments, the current must be proportional to $E^{3/2}$, where E is the field strength. In 1+1 dimensional electrodynamics, there is no magnetic field, so E is also the only non-zero component of the Maxwell tensor. We define $F^{03} = -E$ and $F^{30} = E$. Combining the two terms above, we will define the color current as[2]

$$j^\mu_c = u^\mu \rho_c + \kappa E^{3/2} \sigma^\mu. \qquad (3)$$

Here κ is a parameter scaling the rate of pair production.

Now that the current has been written down, we can write the equations of electrohydrodynamics. First of all, the total charge current must be conserved:

$$\partial_\mu j^\mu_c = 0. \qquad (4)$$

Since charge is created by pair production to nullify the initial field, only <u>total</u> current is conserved. Given the current, Maxwell's equations specify the dynamics of the field:

$$\partial_\mu F^{\mu\nu} = j^\nu_c . \qquad (5)$$

The hydrodynamic equations are given by the divergence of the stress-energy tensor. Total energy must be conserved, so any energy or momentum given up by the fluid must be taken up by the field and vice versa. This is equivalent to the stress-energy tensor of the system as a <u>whole</u> being conserved. The stress-energy for a Maxwell field is given by $1/4\ F^{\mu\nu} F_{\mu\nu}$, and using Maxwell's equations above gives

$$\partial_\mu T^{\mu\nu} = F^{\mu\nu} j_{\mu c} . \qquad (6)$$

Finally, the baryon flow is given by the conservation of its current,

$$\partial_\mu j^\mu_b = 0. \qquad (7)$$

Eqs(4-7), along with the corresponding definitions of the quantities entering them, form the equations of electrohydrodynamics.

In 1+1 dimensions, these equations specify six differential equations. There are, however, only five dynamic equations. One of the Maxwell's equations corresponds to Gauss' law, and hence yields no dynamic information. We will use this equation to specify the initial field given the initial charge density, and it serves as a check on the accuracy of our integration of the dynamics afterwards. These five dynamic equations yield the five unknown functions that will describe the physics of our system, E, ρ_c, ε, y, and ρ_b. The pressure is determined by the equation of state, which is also not dynamic since it does not specify the time evolution of the pressure. The equation for baryon number conservation, eq(7), only contains the baryon density and the rapidity, and hence is coupled to the other equations only through the latter quantity. It is exactly this coupling that leads to baryon number stopping.

Solution of the Model

Since there is no intrinsic length scale to these equations, it is useful to scale them by dividing out all dimensionful quantities. When this is done, there are two dimensionless parameters which characterize the model. The first, mentioned above, is denoted by γ. This is the ratio of the initial field strength squared to the initial baryon energy density at η=0. This parameter thus describes the field intensity. The second parameter relates the two time scales of the problem, τ_0, and τ_{pair}, the pair production time. In the absence of the vacuum polarization, the pair production time is infinite, and hence we define $\alpha = \tau_0 / \tau_{pair}$. The form of the equations, when cast into our coordinates, suggests a Lagrangian numerical solution. However, since there is no central region initially, a Lagrangian solution would only examine the fragmentation regions. An Eulerian solution, in which matter flows through a grid fixed in space, will handle all of space, including regions which are inaccessable to the initial flow lines. We have calculated the solutions to the electrohydrodynamic equations both ways, with the Lagrangian solutions as a check on the accuracy of the Eulerian ones. Numerical solutions to the equations are possible for a wide range of α and γ.

We can look first at the fluid flow lines in order to see the nature of the flow and to understand when pure hydrodynamic behavior unaffected by the presence of the field starts. In our coordinates, uniform streaming motion is given by a flow line at constant η. This is always seen after the field has dissipated. Fig. 1 presents an

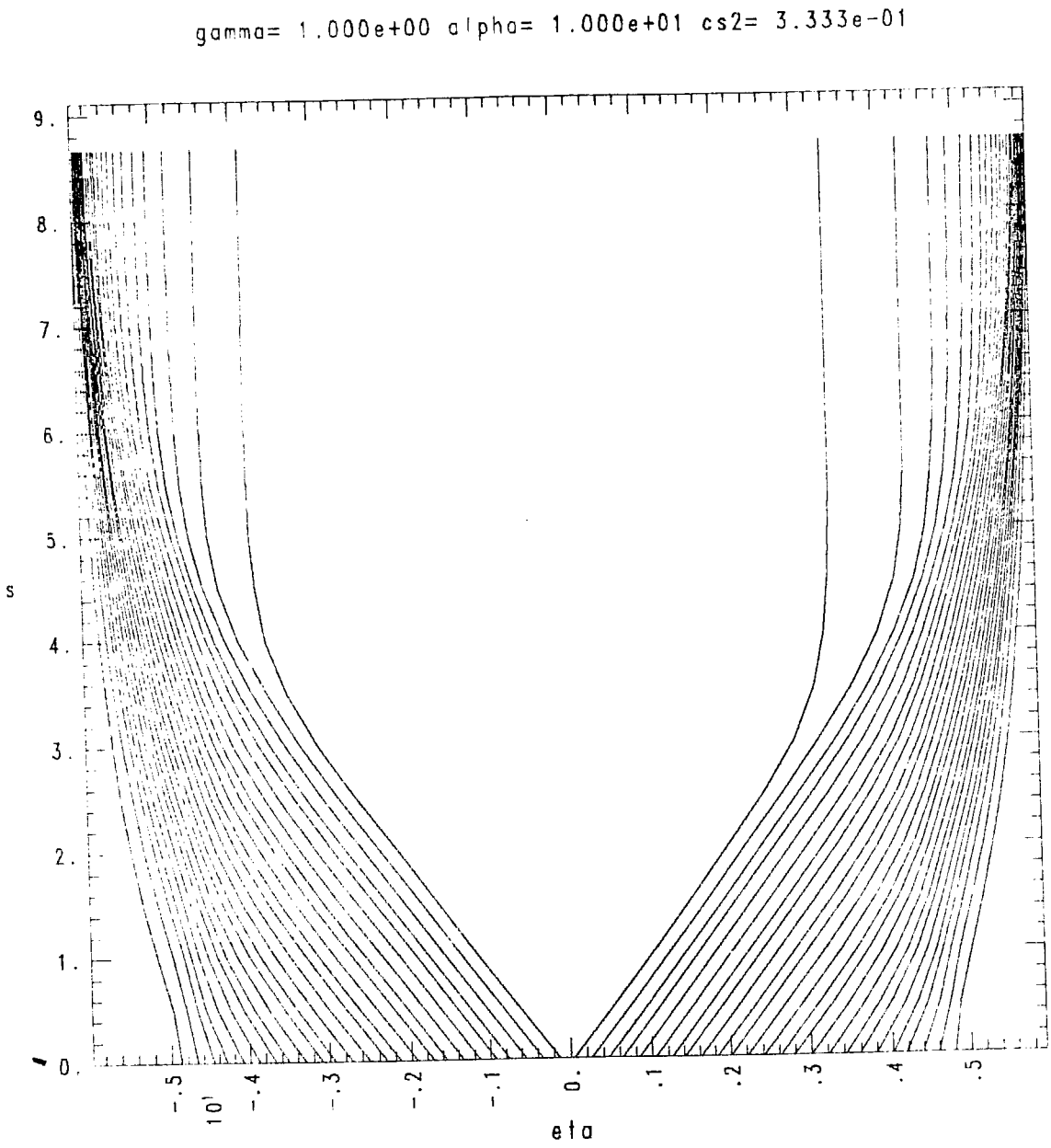

Figure 1. Flow pattern in s-η space for a typical calculation. When the lines proceed at constant η, then the field has been nullified, and the fluid is free streaming.

example of such a flow pattern. Most cases are quite similar to this, and this provides more of a check of the numerics than an experimentally observable result.

Heavy ion experiments can measure particle and energy distributions in rapidity, and we can extract analogous quantities from our model. Since our color charge dissipates, it yields no observable. Baryon number, on the other hand, is conserved, and we can integrate it to verify this. However, since we are no longer in ordinary space, we must include the Jacobian. $\tau \cosh(y-\eta)$, in the integral. It is in fact this Jacobian times the energy or baryon number density that is related to the experimental quantities and which we will present in the figures below. Note that at late proper times, since the velocity of the flow, $\tanh (y-\eta)$, must vanish, $y \rightarrow \eta$ and the Jacobian tends to 1.

In Figs 2 and 3, we present final energy and baryon number distributions for different choices of parameters. In both cases, we choose $y_{cm}=5$. We do not specify what nucleus we are calculating, since we will solve the equations in their scaled form, and hence these same results could be applied to several different nuclei. In all calculations, we also take $c_s^2 = 1/3$. In Fig 2, we have $\alpha=10$ and $\gamma=1$. This corresponds to a fairly weak, quickly decaying field. The baryon number is clustered around the beam and target rapidities, but has dispersed somewhat. Since there was a small field, and it did not have a long time to pump energy into the central region, most of the energy also lies near the original beam and target rapidities.

Figure 3 shows the case where again $\alpha=10$, but now $\gamma=10$ as well, corresponding to a much stronger initial field. In this case, it takes approximately 20% longer for the field to decay, since there is so much more energy in the field initially. The baryon number distribution is similar, but skewed slightly towards the central rapidities. The major difference in the two examples, however, is the energy distribution. In the latter case, a great deal more energy has been deposited into the central region, and hence there is a peak near zero rapidity that was much less pronounced previously. In a full calculation, this energy will go into all of the degrees of freedom, and hence will contribute to the transverse as well as the longitudinal expansion. Hence the calculated energy at late s should be an indication of the $dE_{\perp}/dy$ distribution expected.

Conclusions

We have developed a unified model of the formation of the quark gluon plasma.

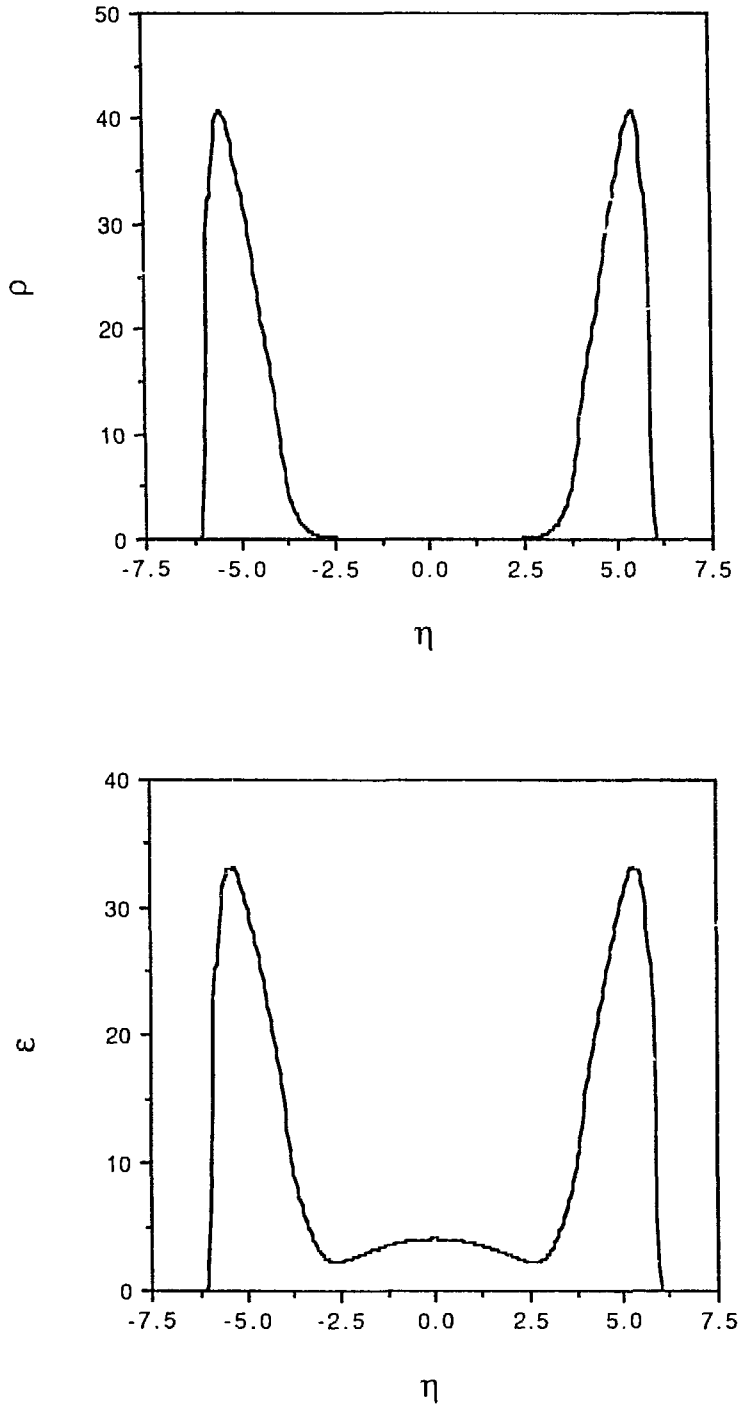

Figure 2. Final baryon number(top) and energy(bottom) distributions. These are shown as a function of η, which at late times approaches y. Here, $y_{cm} = 5$, $\alpha = 10$, $\gamma = 1$, $c_s^2 = 1/3$.

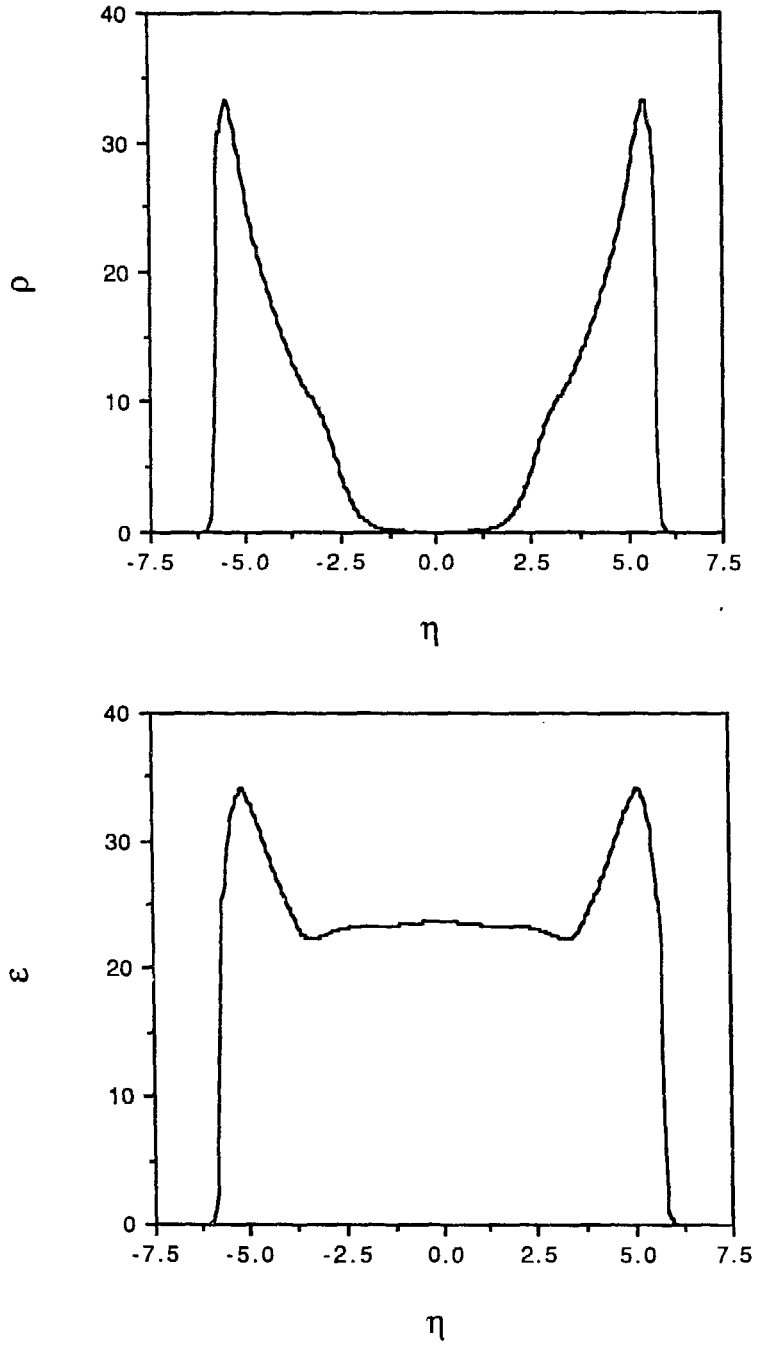

Figure 3. As in Fig 2, but with $\gamma = 10$.

NUCLEAR STOPPING AND ENERGY DEPOSITION

We couple one-dimensional relativistic hydrodynamic baryon flow to an electric field which can create pairs as its energy increases. In this way, we self-consistently calculate the energy deposition into the central region and the extinction of the color fields. Already we can extract dN_b/dy and $dE_\perp/dy$ distributions for a wide choice of our parameters, and are analyzing the available data in order to have the most realistic parameter set. While currently all of our equations are ideal, we are implementing finite electric conductivity terms and considering the extension of the model to more space dimensions in order to make the calculations more realisitic.

References

1. J. D. Bjorken, Phys. Rev. D27 (1983) 140.
2. G. Gatoff, A.K. Kerman, T. Matsui, Phys. Rev. D36 (1987) 114.
3. T. Matsui, J.A. Zingman, in preparation.
4. K. Kajantie, R. Raitio, P.V. Ruuskanen, Nucl. Phys. B222 (1983) 152.
5. M. Gyulassy, L.P. Csernai, Nucl. Phys. A460 (1986) 723.
6. A.K. Kerman, T. Matsui, B. Svetitsky, Phys. Rev. Lett. 56 (1986) 219.
7. H. Ehtamo, J. Lindfors, L. McLerran, Z. Phys. C18 (1983) 341; T.S. Biro, H.B. Nielsen, J. Knoll, Nucl. Phys. B245 (1984) 449.
8. A. Casher, H. Neuberger, S. Nussinov, Phys. Rev. D20 (1979) 179.
9. J. Schwinger, Phys Rev. 82 (1951) 664; E. Brezin, C. Itzykson, Phys. Rev. D2 (1970) 1191.

BEYOND THE PRODUCTION OF THE QUARK-GLUON PLASMA

J. BOGUTA
Advanced Nuclear Concepts
Pier 70
San Francisco, CA 94107

August 3, 1987

Abstract

Quark-gluon plasma is a highly unstable state of matter. In the hadronization process all energetically available nuclear structures should be produced. The plasma can be a gateway to new nuclear structures. Three exotic excitations, HENS, HADRODS and STRINGS are discusses from relativistic nuclear field theory point of view.

A. INTRODUCTION

The natural domain of nuclear physics is the production and study of nuclear structures. Stable nuclei are found naturally; unstable ones can be made in a collison process. There are many ways of doing this— nucleus-nucleus collision, photon or meson nucleus collisions or by fragmentation of the projectile. The required energy scale, in the laboratory, to excite these structures ranges from a few MeV, just above the coulomb barrier, to several hundreds of MeV. The central idea is to infuse sufficient amount of energy to excite a new state without categorically destroying the ordered nature of the nucleus itself.

In the production of the quark gluon plasma the complete destruction of the ordered nature of the colliding nuclei is required. Indeed, the aim is to produce such a violent nuclear collision that even the basic degrees of freedom describing nuclear interactions— those of baryons and mesons— are melted, exposing the underlying quarks and gluons in a hot and dense conglamorate called the quark-gluon plasma.

The main theoretical focus over the last few years has been the assessment of the conditions under which this plasma could be produced and to pinpoint signatures which herald its production. These efforts have been well summarized in a number of conferences [1]. The aim of this contribution is quite different. Simple minded calculations, to be given below, show that if in nuclear collisions there were sufficient stopping power then the quark-gluon phase of hadronic matter can be produced at relatively low energies. Indeed, collision energies available at CERN or Brookhaven's AGS might already be sufficient for the production of this new phase of matter. So let's assume that the long sought plasma is being produced, not worry about the perennial questions of its signatures and focus our attention on the next question: *to what use can such a plasma be put to?*

The quark gluon state of hadronic matter is a highly excited state and unstable. The color degrees of freedom will be momentarily deconfined, persist for a very brief moment and then explode in a stupendous blast releasing its stored energy in the form of more stable baryonic and mesonic states. What kinds of final states will emerge? Most of them will be known nuclei and mesons, of course. But many other structures will also emerge, such as excited states of known nuclei, vibrating and rotating in all sorts of imaginable ways. In the plasma phase of hadronic matter there is no memory of nuclear structure, thus in the violent hadronization process of the plasma one would expect that all nuclear structures that can exist will be produced, though fleetingly. The plasma phase of hadronic matter can be a hot hadronic crucible which serves as a gateway to new nuclear structures. In the debris of exploding quark-gluon plasma one might find exotic physics.

What exotic physics can be in this debris? That is unkown. The aim of this work is to contribute toward the elucidation of this questions. To prevent caprecious thought, it is desirable to restrict the range of speculation. We will require that at the very minimum the candidate exotic structures should emerge from reasonable nuclear theories. Three types of exotic excitations will be considered—HENS, Hadroids and Strings [2]. The former excitation involves the interplay of mesonic and baryonic degrees of freedom to yield a highly exotic nuclear structure. The latter structures are non-perturbative excitations of mesonic degrees of freedom.

B. PLASMA PRODUCTION

Dense and hot nuclear matter is relativistic. The theoretical framework describing such a system should also be relativistic. The only known way of treating the mesonic and baryonic degrees of freedom in a relativistic way is through a field theory. One aim of theoretical nuclear physics over the last twenty years was to predict the properties of nuclear matter from the known nucleon-nucleon potential. This is a hard task. What we want is something more modest— a field theory of nuclear interactions which is flexible enough to parametrize the known properties of nuclear matter, such as its saturation density, binding enery per particle and the compressibility modulus. Such a field theory was given some time ago and its properties extensively studied [3]. Here we use this field theory to investigate hot and dense nuclear matter with the aim of inferring the conditions under which the quark-gluon plasma will be produced.

The relativistic nuclear field theory is given in terms of a Lorentz vector field ω_μ, which gives the short range repulsion, and a Lorentz scalar field σ, together with its self interactions $U(\sigma) = a/2\sigma^2 + b/3\sigma^3 + c/4\sigma^4$, which will give the desired attraction. The nuclear Lagrangian is

$$\begin{aligned}\mathcal{L} = &-\bar{\psi}\Big(\gamma_\mu\left(\partial_\mu - ig_v\omega_\mu\right) + M_n + g_s\sigma\Big)\psi \\ &- \frac{1}{2}(\partial_\mu\sigma)^2 - U(\sigma) \\ &- \frac{1}{4}F_{\mu\nu}F_{\mu\nu} - \frac{1}{2}m_v^2\omega_\mu\omega_\mu\end{aligned} \tag{1}$$

where

$$F_{\mu\nu} = \partial_\mu\omega_\nu - \partial_\nu\omega_\mu \tag{2}$$

The field equations are

$$\begin{aligned}\bar{\psi}\left(\gamma_\mu\left(\partial_\mu - ig_v\omega_\mu\right) + M_n + g_s\sigma\right)\psi &= 0 \\ \partial_\mu\partial_\mu\sigma - a\sigma - b\sigma^2 - c\sigma^3 &= g_s\bar{\psi}\psi \\ \partial_\nu\partial_\nu\omega_\mu - m_v^2\omega_\mu &= ig_v\bar{\psi}\gamma_\mu\psi\end{aligned} \tag{3}$$

The field equations, in the mean field approximation are given by

$$\begin{aligned}a\sigma + b\sigma^2 + c\sigma^3 &= -g_s\rho_s \\ m_v^2\omega_0 &= g_v\rho_v \\ \omega_i &= 0\end{aligned} \tag{4}$$

The expression for the energy density and pressure are

$$\epsilon = \frac{1}{2}\left(\frac{g_v}{m_v}\right)^2 {\rho_v}^2 + \frac{4}{(2\pi)^3}\int d^3k\sqrt{k^2+m^{*2}} + U(\sigma)$$
$$p = \rho_v^2 \frac{d(\epsilon/\rho_v)}{d\rho_v} \tag{5}$$

In the above ρ_s and ρ_v are the scalar and vector particle densities obtained from the plane wave solutions of the Dirac equation with the σ and ω_0 as the background fields. The eigenvalues of these solutions are

$$E = g_v\omega_0 + \sqrt{k^2+m^{*2}} \tag{6}$$

The effective mass of the nucleon is given by $m^* = M_n + g_s\sigma$.

The above model of nuclear matter has the advantage of being flexible enough to account for know properties of nuclear matter at saturation and also of being thermodynamically consistent. It satisfies the The Hugenholtz -van Hove theorem, which was proven for a complete solution of a field theory [4].

$$E_F = \frac{(\epsilon + p)}{\rho_v} \tag{6}$$

Here E_F is the Fermi energy. This relation is valid, surprisingly, also in the mean field approximation, as can be readily checked by the use of the field equations for infinite nuclear matter.

The above equations yield a thermodynamically consistent description of nuclear matter. The Hugenholtz-van Hove theorem relates the value of the nucleon effective mass, at saturation to the vector coupling constant g_v. From the field equations, and the expression for the Fermi energy, one can see that the energy dependence of the optical potential is also directly related to the same vector coupling constant. From the observed energy dependence of the nuclear optical potential the effective mass of the nucleon can be computed and is given by $m^* = 0.64\, m_n$ [5]. Taking nuclear matter compressibility modulus to be $K = 240$ MeV [6], all of the parameters of the self-coupled nuclear field theory are fixed and the equation of state for all densities and temperatures can then be computed, in the mean field approximation. In *Fig.*(1) the cold, symmetric, nuclear matter equation of state is shown. This corresponds of taking $C_s = (g_s/m_s)\, m_n = 18.4$ and $C_v = (g_v/m_v)\, m_n = 14.5$.

In the laboratory one does not produce nuclear matter at a desired density and/or temperature, but through the collision of nuclei. One needs to know, given the initial bombarding energy, what densities and temperatures will be reached in the compressed zone of nuclear matter. The state of hot and dense nuclear matter in this zone can be approximated by the Rankine-Hugoniot shock condition [7].

$$\left(\frac{\rho}{\rho_0}\right)^2 = \frac{\epsilon\,(p+\epsilon)}{\epsilon_0\,(p+\epsilon_0)} \tag{7}$$

The Lorentz contraction γ is given by

$$\gamma = \frac{\epsilon/\rho}{\epsilon_0/\rho_0} \tag{8}$$

where p and ϵ are the pressure and energy density in the compressed zone and ϵ_0 the energy density of the incoming projectile.

Hot and dense nuclear matter will not consist of nucleons alone, but resonance excitations will also be preset. The importance of the delta resonance has been emphasised [8]. It leads to a isomeric nuclear state. Resonances can be included in the self-coupled theory in a simple way by just counting the new degrees of freedom and effectively coupling them to the sigma and omega fields to yield the corresponding energy functional. The coupling to the vector field is universal, since the omega field couples to the total baryon current. Care needs to be excersized in choosing the scalar coupling constant. It must be taken in a way so that the effective masses of the resonances remain positive, otherwise spurious physics is induced [9]. The simplest prescription for the coupling constant of the resonance R is

$$\frac{g_s^N}{g_s^R} = \frac{m_N}{m_R} \tag{9}$$

This assures that all of the masses are positive and chiral symmetry is restored for all the particles at the same time, as it should be. In Fig.(2) the achieved nuclear matter densities, as a function of the bombarding energy, is shown with several resonances included. The inclusion of resonances does not make a dramatic difference in the density reached. It does affect the temperature significantly, as shown in Fig.(3).

The above calculations are, no doubt, just a crude approximation of the actual situation. But it serves their purpose. At a bombarding energy of about 20 GeV/A extreme state of nuclear matter can be reached: densities of about eight times those of normal nuclear matter and temperature of about 200 MeV. At such high densities and temperatures one expects that the baryonic and mesonic degrees of freedom will melt and hadronic matter goes into the quark-gluon plasma phase. If the collision energy is increased by a factor of ten, say, as contemplated for the Relativistic Heavy Ion Collider (RHIC), it is hard to imagine how the production of the quark gluon plasma can be avoided.

C. HADROIDS

The quark-gluon plasma, as produced in a nuclear collison process, will be extremely hot and have a very high energy density. The violent nuclear collision will produce a hadronic holacaust, obliterating all nuclear degrees of freedom. Hadronic matter will burn violently and from this hadronic furnace completely new nuclear structures could emerge. Baryons could coalesce in new ways and mesonic fields fluctuated to reach non-perturbative configurations.

Let's turn to the study of these non-perturbative mesonic excitations. As noted in the introduction, the study of these excitations must be based on phenomenologically reasonable field theories. A phenomenologically succesful field theory with non-linearly realized chiral invariance was given by Weinberg [10]. The $SU(2)_L \times SU(2)_R$ chiral model is broken to diagonal $SU(2)_V$. Because chiral symmetry is realized non-linearly, this theory can be embedded into a field theory with secret gauge invariance [11] in the diagnal symmetry group. In this theory massive gauge fields are produced by swallowing all of the Higgs degrees of freedom. Let the dynamical variable be U(x), which is valued in $SU(2)$. The theory can be parametrized by functions ξ_L, ξ_R constrained to satisfy

$$U = \xi_L^\dagger(x)\xi_R(x) \tag{10}$$

They transform under $g_L \in SU(2)_L, g_R \in SU(2)_R$ and $h \in SU(2)_V$ in the following way

$$\xi_{L(R)} \rightarrow h(x)\xi_{L(R)}(x)g_{L(R)}^\dagger \tag{11}$$

The rho field can be introduced as a connection, transforming in the usual way

$$V_\mu(x) \rightarrow h(x)V_\mu h^\dagger(x) + ih(x)\frac{\partial}{\partial x_\mu}h^\dagger(x) \tag{12}$$

where $V_\mu = \frac{\vec{\tau}}{2}\cdot\hat{\rho}_\mu$. The Weinberg Lagrangian for $\rho-\pi$ interactions can be written in a gauge invariant way. The kinetic energy of the $\hat{\rho}_\mu$ field is given in terms of $\hat{F}_{\mu\nu}$ given in eq.(15*b*). The kinetic energy of the pion and the interaction terms are expressible in terms of the quantity $\alpha_\mu^\pm$, given by

$$\alpha_\mu{}^\pm = (D_\mu\xi_L\xi_L{}^\dagger \pm D_\mu\xi_R\xi_R{}^\dagger)/2i \tag{13}$$

The Lagrangian is

$$\mathcal{L} = -\frac{1}{4}\hat{F}_{\mu\nu}\hat{F}_{\mu\nu} - f_\pi^2\, Tr\left(\alpha^-\right)^2 - 2f_\pi^2\, Tr\left(\alpha^+\right)^2 \tag{14}$$

where

$$\hat{D}_\mu = \frac{\partial}{\partial x_\mu} - ig\frac{\hat{\tau}}{2}\cdot\hat{\rho}_\mu \tag{15a}$$

and the field strength tensor is

$$\hat{F}_{\mu\nu} = \frac{\partial\hat{\rho}_\nu}{\partial x_\mu} - \frac{\partial\hat{\rho}_\mu}{\partial x_\nu} + g\hat{\rho}_\mu\times\hat{\rho}_\nu \tag{15b}$$

This model gives an accurate description of low energy $\rho-\pi$ interactions. Its non-perturbative excitations are hence of particular interest. The Weinberg chiral theory has infinite number of topologically non-trivial solutions in the Wu-Yang form, all having the topological index of unity [12]. It also has a solution outside the Wu-Yang form This solution to the Euler-Lagrange field equations can be obtained by giving the rho field the form

$$g\rho^a_c = \epsilon_{abc}x^b\,G(r)/r^2 + (\delta_{ac} - \frac{x_a x_c}{r^2})H(r)/r + \frac{x_a x_c}{r^2}K(r) \tag{16}$$

The energy is given by

$$\begin{aligned} E =& \frac{4\pi f_\pi^2}{m_\rho}\int d\xi\,[\,\frac{1}{2}(\xi^2F'^2 + 2\sin^2F) + 2\{(G+\cos F-1)^2 + H^2 + \frac{1}{2}\xi^2K^2\} \\ &+ \frac{1}{2\xi^2}((G-1)^2+H^2-1)^2 + (G'-HK)^2 + (H'+(G-1)K)^2] \end{aligned} \tag{17}$$

The Euler-Lagrange field equations field equations, for the case when the pion is trivial, are [13]

$$\begin{aligned} f'' &= \frac{2}{\xi^2}(2f-1)\left(f(f-1)+\beta^2+\xi^2\sigma^2+\frac{1}{16}\xi^2\right) + 4\beta'\sigma + 2\beta\sigma' + \frac{1}{8} \\ \beta'' &= \frac{4\beta}{\xi^2}\left(f(f-1)+\beta^2+\xi^2\sigma^2+\frac{1}{16}\xi^2\right) + 4f'\sigma + (2f-1)\sigma' \\ \sigma &= \frac{(2f-1)\beta' - 2f'\beta}{4\beta^2+(2f-1)^2+\xi^2/8} \end{aligned} \tag{18}$$

where $G = 2(1-f)$, $2\beta = -H$, $2\delta = -K$, $\sigma = \delta/\xi$ and $\xi = m_\rho r$. The field equations are solved under the boundary conditions: $G(0) = G(\infty) = 0$, $H(0) = H(\infty) = 0$.

The energy of this solution is found numerically to be

$$E = 5.18\frac{m_\rho}{g^2/4\pi} \tag{19}$$

The field profiles, for $g^2/4\pi = 3$, and $m_\rho = 780$ MeV are shown in fig.(4). A solution to a similar set of equations in a technicolor model, with a Skyrme type stabilization term, was reported in ref.(14). This stabilization term violates known $\rho-\pi$ phenomenology and is not considered here.

The above solution of the Weinberg theory cannot be shown to be ustable using the non-contractible loop argument [16]. It can be unstable in the pion direction, due to the attractive nature of the $\rho - \pi$ interactions. The second variation of the energy with respect to the pion field is obtained from eq.(17) and is

$$\delta^2 E = \frac{4\pi f_\pi^2}{m_\rho} \int d\xi \, [\, \frac{1}{2}\xi^2 (\delta F')^2 - (2 + 4(G + \cos F - 1)\cos F)(\delta F)^2] \tag{20}$$

A detailed analysis of stabilizing a solution of the Weinberg model in the Wu-Yang form against the variation along the non-contractible loop has been reported[16]. This involves the addition of quartic terms, given in terms of gauge covariant quantity $\alpha^{\pm}$. There are six such terms. The choice of these terms should be consistent with known pion and rho phenomenology. Terms contributing to $\pi - \pi$ scattering, or to ρ decay should be excluded, because the Weinberg model accounts for these data quite well. A judiciuos choice of the stabilization term against variations in the pion direction is obtained by recognizing the source of the instability: the pion couples to the rho field through a term $(G + \cos F - 1)^2$. This gives the instability in the pion direction. A desirable stabilizing term would be the one which couples other components of the rho field to the pion, such as H(r), thus making it more dear to excite it, but not increasing the total mass—just its second variation. A term which is allowed, is gauge invariant and suits the purpose, is

$$L = \epsilon \int d\xi \left(\frac{H^2 \sin^2 F}{\xi^2} + \frac{1}{2}(F' K \xi)^2 + \frac{1}{\xi^2} \sin^2 F \, (G + \cos F - 1)^2 \right) \tag{21}$$

This corresponds to the anti-commutator between α^+ and α^-. This term will stabilize the hadroid against pionic fluctuation by increasing the energy of the fluctuation.

For the physically reasonable value of the coupling constant $g^2/4\pi = 3$ the energy of the hadroid is about 1.4 Gev. After quatization of the classical solution there will be a whole tower of states satisfying the rule that the spin of the state is equal to its isospin. This hadroid has a mixed parity, as can be seen from the ansatz in eq.(16).

The above considerations were for the case when chiral symmetry was realized non-linearly. There exists another possiblity for realizing $SU(2)_L \times SU(2)_R$. This is a linear realization. The chiral quartet of fields $(\sigma, \hat{\pi})$ transforms under chiral transformations as

$$\begin{aligned} \sigma' &\rightarrow \sigma \\ \hat{\pi}' &\rightarrow \hat{\pi} - \hat{\epsilon} \times \hat{\pi} \end{aligned}$$

and

$$\begin{aligned} \sigma' &\rightarrow \sigma + \hat{\eta} \cdot \hat{\pi} \\ \hat{\pi}' &\rightarrow \hat{\pi} - \hat{\eta}\sigma \end{aligned} \tag{22}$$

The nucleon field transforms as

$$\begin{aligned} \psi' &\rightarrow (1 - \frac{i}{2}\hat{\tau} \cdot \hat{\epsilon})\psi \\ \psi' &\rightarrow (1 + \frac{i}{2}\hat{\tau} \cdot \hat{\eta}\gamma_5)\psi \end{aligned} \tag{23}$$

The chirally invariant Lagrangian is given by

$$\begin{aligned} \mathcal{L} = &- \bar{\psi}\Big(\gamma_\mu (\partial_\mu - i g_v \omega_\mu) + g_s(\sigma + i\gamma_5 \hat{\tau}\hat{\pi})\Big)\psi \\ &- \frac{1}{2}(\partial_\mu \sigma)^2 - \frac{1}{2}(\partial_\mu \hat{\pi})^2 - \frac{\lambda}{4}\left(\hat{\pi}^2 + \sigma^2 - \sigma_0^2\right)^2 \\ &- \frac{1}{4}F_{\mu\nu}F_{\mu\nu} - \frac{g_v^2}{2}\left(\hat{\pi}^2 + \sigma^2\right)\omega_\mu \omega_\mu \end{aligned} \tag{24}$$

The equations of motion for the spherically symmetric solution involving the σ, ω_0 and the fermion field ψ are

$$\begin{aligned} \frac{d^2\sigma}{dr^2} + \frac{2}{r}\frac{d\sigma}{dr} - \lambda\left(\sigma^2 - \sigma_0^2\right)\sigma - g_v^2 \sigma \omega_0^2 &= g_s \sum \left(F_\kappa^2 - G_\kappa^2\right) \\ \frac{d^2\omega_0}{dr^2} + \frac{2}{r}\frac{d\omega_0}{dr} - g_v^2 \sigma^2 \omega_0 &= g_v \sum \left(F_\kappa^2 + G_\kappa^2\right) \\ \frac{dF_\kappa}{dr} - \frac{\kappa}{r}F_\kappa &= \left(E_\kappa - g_v\omega_0 - m^*\right)G_\kappa \\ \frac{dG_\kappa}{dr} + \frac{\kappa}{r}G_\kappa &= \left(m^* + E_\kappa - g_v\omega_0\right)F_\kappa \end{aligned} \tag{25}$$

The functions F_κ, G_κ are the upper and lower components of the Dirac wave function ψ and κ denotes the usual angular quantum number. With the interaction parameters fixed by the

properties of normal nuclear matter, the above field equations can be solved for a finite spatial configuration by fixing its baryon content and the shells into which the baryons are to be arranged. Here a baryon four nuclear structure is studied. Nuclear structures with a higher baryon content can be obtained by arranging the baryons in higher orbital shells. Three solutions, corresponding to the above determined coupling constants, are found. In Fig.(5) the results of the calculation for the sigma, omega field configurations, as well as the density profiles, are shown. The first solution is volume dominated and qualitatively appears like the density profile of a normal ^4He nucleus. The sigma field, as well as the omega field, is similar in shape to the field configurations found in heavier, closed shell nuclei. The sigma field is positive throughout the nucleus and corresponds to an excitation around the vacuum state $+\sigma_0$. The other two solutions are quite different. The sigma fields are kinked. In the third solution, the interior of the structure corresponds to the second vacuum state of the theory ($\sigma = -\sigma_0$). Surprisingly, this kinky solution is lowest in energy. The binding energies of the three solutions are -40 MeV, $+43$ MeV and -74 MeV respectively. The reason for this is that in the abnormal solution, the nucleons are very tightly bound (about 300 MeV). The introduction of an explicit symmetry breaking term, such as $c\sigma$, can shift the energy of the kinked solutions significantly upwards making the normal nucleus to be the ground state.

An interesting apsects of the HENS considered here is the removal energy of the nucleon itself. In a normal nucleus, the removal energy of a lowest lying nucleon in a nucleus is about -50 MeV. In the abnormal nucleus considered above, the removal energy is about -300 MeV. This enormous binding energy is compensated by the huge amount of energy stored in the mesonic degrees of freedom. The nucleons sit in a very deep potential, as can be seen from the sigma field configuration shown in Fig.[1]. Such a deep potential for the nucleons allows for exotic combinations of neutrons and protons in an abnormal nucleus. In particular, the field equations can be solved for a baryon four system, where the four baryons are all neutrons or protons. Symmetry energy is overcome by the strong sigma field. A multi proton resonance state is thus another consequence of the chiral field theory.

The purview of nuclear physics has been nuclear structures with a non vanishing baryon content. The HENS, though exotic in their nature, still fit into this picture. A relativistic field theory of nuclear interactions can have hadronic structures which have no baryon content at all. One example of a nuclear glue ball is the hadroid, considered above. This is a three dimensional excitation of an isovector, Lorentz vector $\hat{\rho}_\mu$ field. The chiral nuclear Lagrangian considered here also possesses a purely mesonic excitation. It has cylindrical symmetry. To find this solution take the Nielsen-Olesen form for the omega field [17]

$$\begin{aligned} \omega_x &= -\frac{y}{g_v r^2} f(r) \\ \omega_y &= +\frac{x}{g_v r^2} f(r) \\ \omega_z &= 0 \\ r &= \sqrt{x^2 + y^2} \end{aligned} \tag{26}$$

The field equations for the functions $f(r)$ and $\sigma(r)$ are given by

$$\frac{d^2\sigma}{dr^2} + \frac{1}{r}\frac{d\sigma}{dr} - \lambda\left(\sigma^2 - \sigma_0^2\right)\sigma - \frac{f^2\sigma}{r^2} = 0$$

$$\frac{d^2 f}{dr^2} - \frac{1}{r}\frac{df}{dr} - g_v^2 \sigma^2 f = 0 \tag{27}$$

The above field equations are solved with the following boundary conditions $\sigma(\infty) = \sigma_0$, $f(\infty) = 0$, $\sigma(0) = 0$ and $f(0) = 1$

The energy density is given by

$$\epsilon = \frac{1}{2g_v^2 r^2}\left(\frac{df}{dr}\right)^2 + \frac{1}{2}\left(\frac{d\sigma}{dr}\right)^2 + \frac{\lambda}{4}\left(\sigma^2 - \sigma_0^2\right)^2 + \frac{1}{2}\frac{f^2\sigma^2}{r^2} \tag{28}$$

In Fig.[6] the functions f(r) and $\sigma(r)$ are shown as a function of the cylindrical radius r. The energy per unit length is computed to be about 190 MeV/fm.

A vortex solution of this kind was first discovered by Nielsen and Oleson for a $U(1)$ gauge field theory with a Higgs field. This theory is a relativistic generalization of the Ginzburg-Landau model. In our case a string solution exist without gauge invariance. The reason for this is that the $U(1)$ gauge field theory, in a fixed gauge (taking the Higgs field to be purely real) reduces to field equations given above.

E. CONCLUSIONS

The production of the quark-gluon plasma and its experimental detection is a important problem in nuclear physics. This experimentation is possible due to the many-body nature of the nucleus. Through the collision process energy density, mass and temperature can be built up to the point where the usual nuclear degrees of freedom are destroyed and the underlying forces of nuclear physics-quarks and gluons-are revealed. Thus it is tempting to think that ideas about nuclear structure are not all that important here. A return to the problems of nuclear structure is made in the hadronization phase of the plasma. The very nature of the plasma is such that it will violently exlope immediately after its production. In this most violent explosion all available nuclear configurations, both mesonic and baryonic should emerge. In the debris of exploding quark-gluon plasma could lie new and exotic hadronic structures. Models of three such possible structures were considered here. No doubt these models are just a probing in the dark, seeking for yet unimagined structures which will emerge from the quark-gluon plasma.

The author thanks T. Matsui and L. McLerran for discussions.

Bibliography

[1] Qaurk Matter Formation and Heavy ion Collisions: proceedings of the Bielefeld Workshop, May 1982 /edited by M. Jacob and H. Satz. (World Scientific, 1982)
Quark Matter '83 :proceedings of the Third International Conference on Ultra-Relativistic Nucleus-Nucleus Collisions, Brookhaven National Laboratory, September 1983/ edited by T. W. Ludlam and H. E. Wegner. (North Holland, 1984)
Quark Matter "84: proceedings of the Fourth International Conference on Ultra-Relativistic Nucleus-Nucleus Collisions, Helsinki, Finland June, 1984 /edited by K. Kajantie. (Springer, 1985)

[2] J. Boguta, Phys. Lett. **128B** (1983) 133
J. Boguta, HENS and STRINGS, SSL preprint, Feb.,1987
J. Boguta, Phys. Rev. Lett, **50** (1983) 148
J. Boguta, HADROIDS. ANC preprint, July, 1987

[3] J. Boguta and A. R. Bodmer, Nucl. Phys. **A292** (1977) 413
J. Boguta and H. Stöcker, Phys. Lett. **120B** (1983) 289

P. -G. Reinhard, M. Rufa, J. Maruhn, W. Greiner and J. Friedrich, Z. Phys. **A323** (1986) 13
T. Nakai and S. Takagi, Prog. Lett. **71** (1984) 1184
A. Bouyssy, S. Marcos, and Pham Van Thieu, Nucl. Phys. **A422** (1984) 541

[4] N. M. Hugenholtz and L. Van Hove, Physica **24** (1955) 363

[5] J. Boguta, Nuclear Optical Potential and the Equation of State, ANC preprint July, 1987

[6] J. -P. Blaizot, D. Gogny and B. Grammaticos, Nucl. Phys. **A265** (1976) 315

[7] W. J. M. Rankine, Trans. Roy. Soc. **160** (1870) 277

[8] J. Boguta, Phys. Lett **109B** (1981) 251

[9] S. I. A. Garpman, N. K. Glendenning and Y. J. Karant Nucl. Phys. **322A** (1979) 382

[10] S. Weinberg, Phys. Rev. **166** (1968) 1568

[11] A. P. Balachandran, A. Stern and G. Trahern, Phys.Rev. **D19** (1979) 1109
M. Bando, T. Kugo, S. Uehara, K. Yamawaki and T. Yanagida, Phys. Rev. Lett. 54 (1985) 1215
Ö. Kaymakcalan and J. Schecter, Phys. Rev. **D31** (1985) 1109

[12] J. Boguta and J. Kunz, Phys. Lett. **166B** (1986) 247

[13] R. F. Klinkhamer and J. Boguta, Weak Skyrmions and Sphalerons, LBL-23197Rev. June, 1987

[14] J. Ambjorn and V. A. Rubakov, Nucl. Phys. **256** (1985) 434

[15] J. Burzlaff, Nucl. Phys. **B233** (1984) 262
Z. F. Ezawa and T. Yanagida, Phys. Rev. **33** (1986) 247

[16] Y. Igarashi, A. Kobayashi, H. Otsu and S. Sawada, On the Chiral Soliton Model with rho meson DPNU-87-02-Rev

[17] H. B. Nielsen and P. Olesen, Nucl. Phys. **61** (1973) 45

Figure Captions

Fig.(1)

Predicted nuclear matter equation of state when the energy dependence of the optical potential is adjusted to the experimental value. The solid line is for $K = 240$ MeV, the dashed line is for for $K = 300$ MeV.

Fig.(2)

The density of nuclear matter reached as a function of the incident energy of the projectile, as predicted by the Rankine-Hugoniot shock condition. The energy is given in the lab as well as in the center of mass.

Fig.(3)

The temperatures reached as a function of the incident energy of the projectile, as predicted by the Rankine-Hugoniot shock condition. Notice the strong effect of the resonances.

Fig.(4)

The function G(r), in dashed line, and H(r) in solid, for the hadroid in the general spherical ansatz. The distance is in Fermis, $g^2/4\pi = 3$ and $m_\rho = 780$ MeV.

Fig.(5*a*)

Particle density for the three solutions of the field equations. Number one corresponds to normal He^4, while the other two are abnormal nuclei.

Fig.(5*b*)

The sigma field, in units of σ_0, as a function of radius. The first solution corresponds to a normal nucleus, while the other two are abnormal solutions.

Fig.(5*c*)

The omega field for the three solutions in units of σ_0 .

Fig.(5*d*)

Hadronic vortex field configurations F(r) and $\sigma(r)$ as a function of the cylindrical radius.

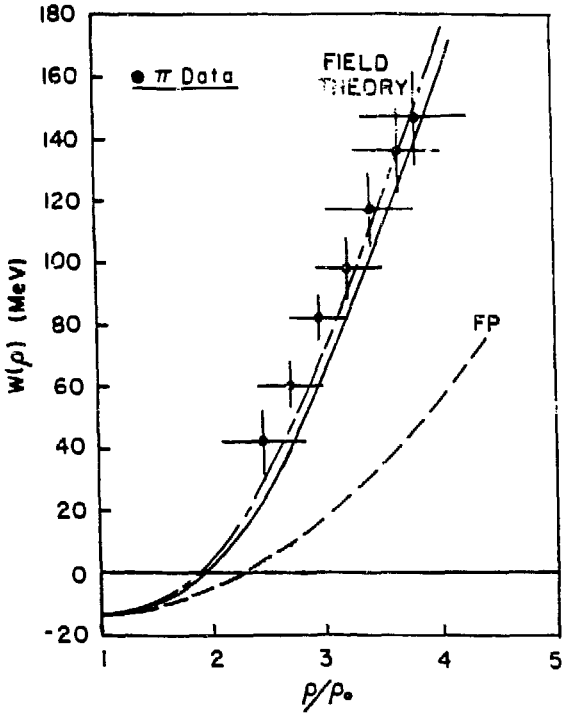

Fig. (1)

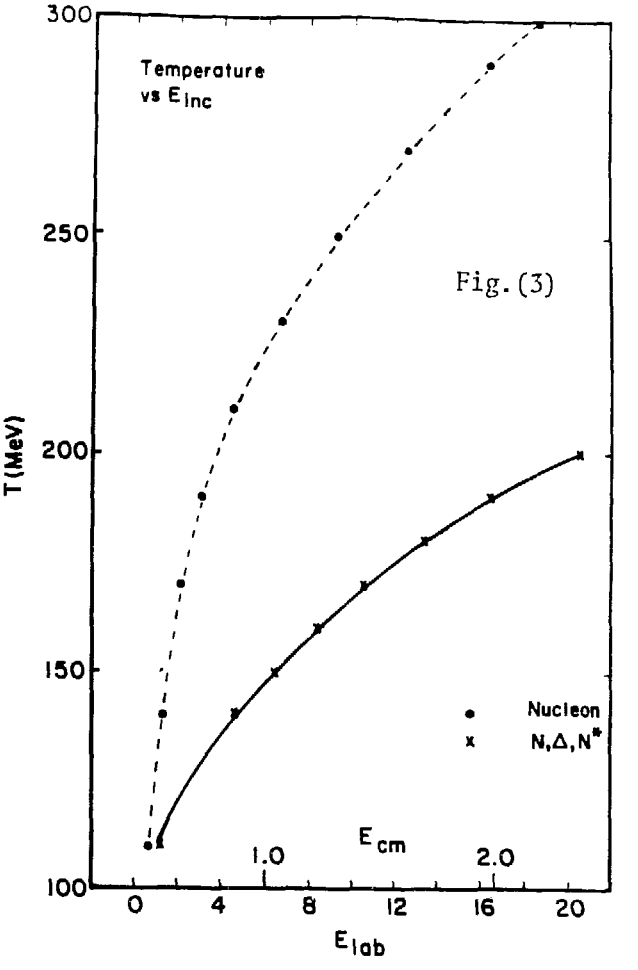

Fig. (3)

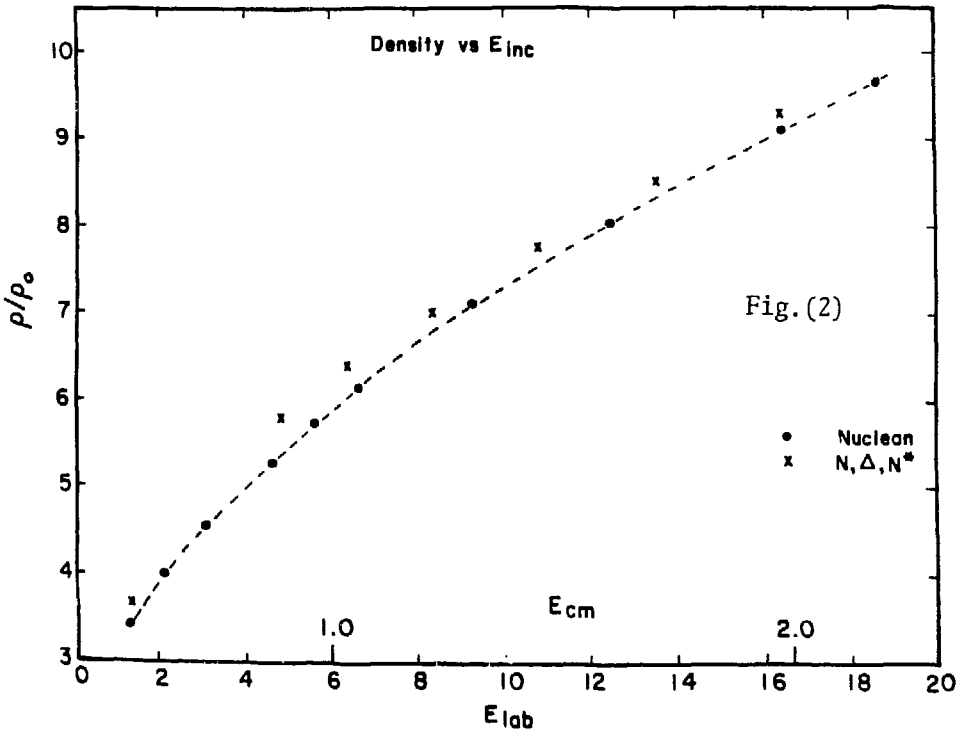

Fig. (2)

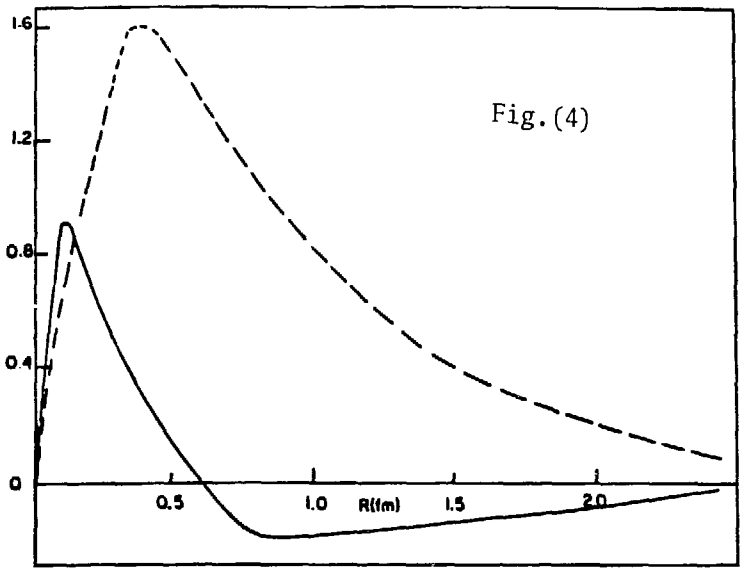
1.6
1.2
0.8
0.4
0
0.5
1.0
R(fm)
1.5
2.0

Fig. (4)

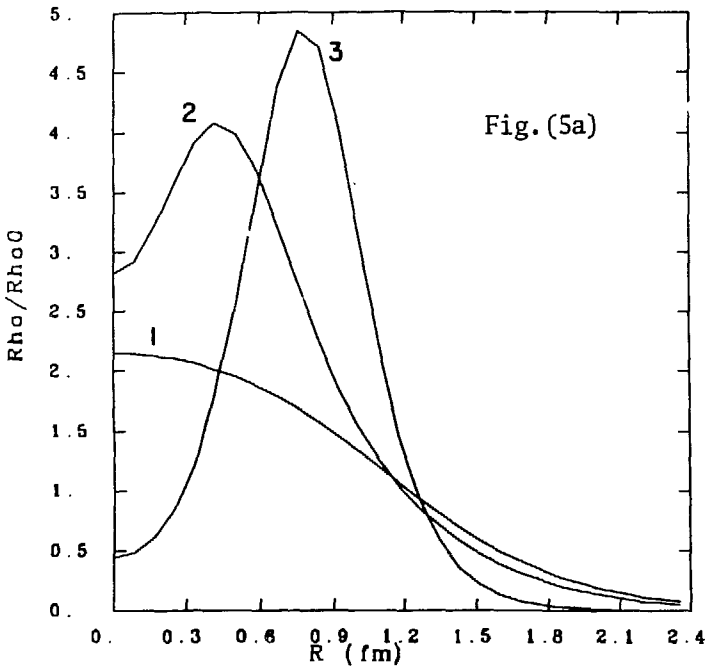
5.
4.5
4.
3.5
3.
2.5
2.
1.5
1.
0.5
0.
Rho/Rho0
1
2
3
0.
0.3
0.6
0.9
1.2
1.5
1.8
2.1
2.4
R (fm)

Fig. (5a)

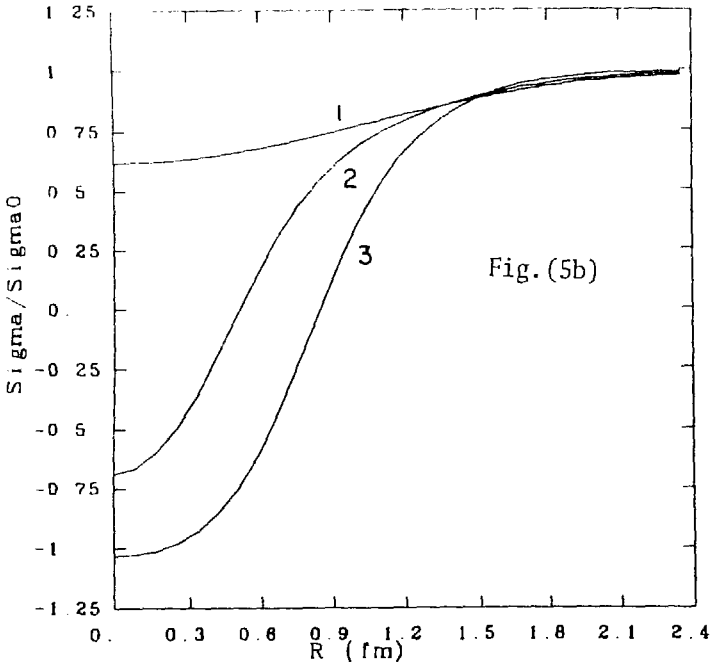

Fig. (5b)

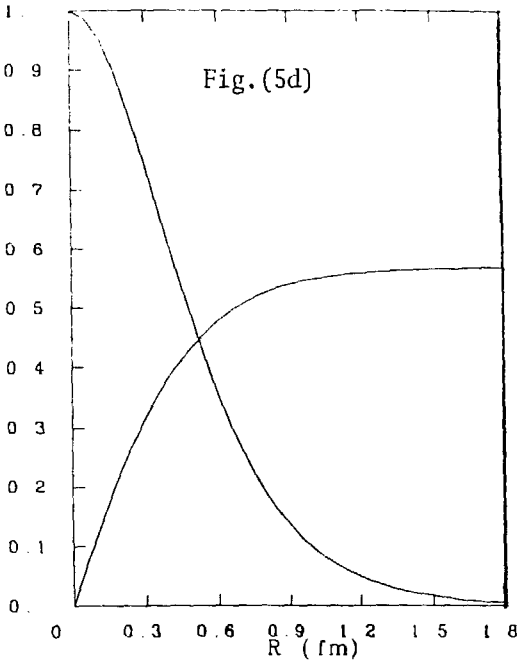

Fig. (5d)

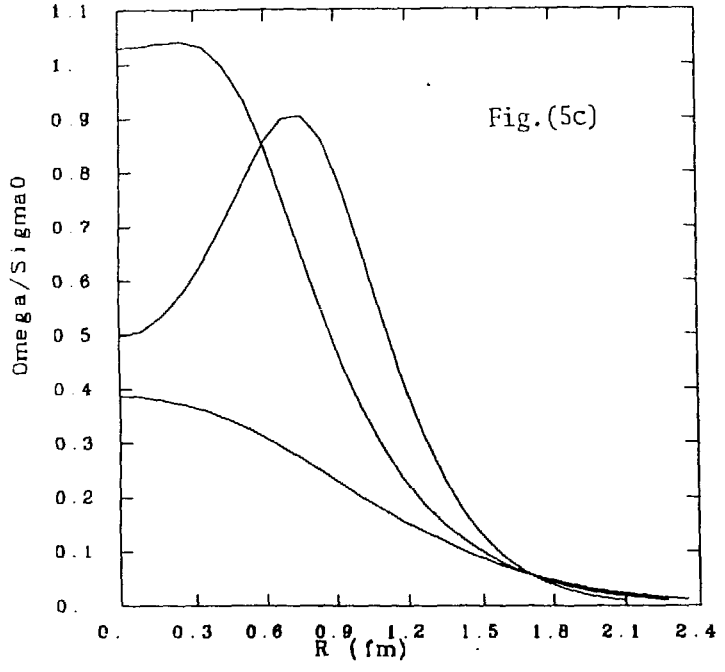

Fig. (5c)

☆U.S GOVERNMENT PRINTING OFFICE:1 9 8 8-5 8 6 9 8 7/9 9 0 8 8